UNIVERSITÉ DE STRASBOURG

ÉCOLE DOCTORALE DES SCIENCES CHIMIQUES

Institut de Chimie, UMR 7177

THÈSE présentée par

Yaokang LV (LU)

soutenue le : **1er décembre 2021**

pour obtenir le grade de: **Docteur de l'université de Strasbourg**
Discipline/ Spécialité : Chimie

Novel materials based on polyoxotitanate clusters

THÈSE dirigée par :

M. RUHLMANN Laurent	Professeur, Université de Strasbourg, Strasbourg
M. BONNEFONT Pierre-Antoine	Maitre de conférences, Université de Strasbourg, Strasbourg

RAPPORTEURS :

M. MIALANE Pierre	Professeur, Université de Saclay/Université Versailles Saint-Quentin, Versailles
M. LEMAITRE Frédéric	Professeur, Université PSL Paris Sciences et Lettre, ENS, Paris

EXAMINATEURS :

M. SAVINOVA Elena	Professeur, Université de Strasbourg, Strasbourg
M. BLANCHARD Sébastien	Maitre de conférence, Sorbonne université, Paris

ACKNOWLEDGEMENTS

I first want to acknowledge all the members of the jury for agreeing to evaluate this thesis:

Prof. Laurent RUHLMANN, Université de Strasbourg

Prof. Elena SAVINOVA, Université de Strasbourg

Prof. Pierre MIALANE, Université de Saclay

Prof. Fréderic LEMAITRE, Université PSL Paris Sciences et Lettre

Dr. Pierre-Antoine BONNEFONT, Université de Strasbourg

Dr. Sébastien BLANCHARD, Sorbonne Université

I want to thank the Zhejiang Ai-shan Green and Technology Research Institute for its financial support throughout the study and live in France.

I sincerely thank my supervisors for their advice, support and mentorship during my PhD. I sincerely thank Prof. Dr. Laurent RUHLMANN to carry out PhD at University of Strasbourg and giving me chance to work in his reseach group. I really enjoyed the scientific, academic, and friendly environment in his research group. His encouragement and personal care and advice were very important for me. I would also like to thank Prof. Dr. Pierre-Antoine BONNEFONT for his advice and suggestions which helped me to complete the thesis work on time.

I need to thank Prof. Dr. Dominic S. Wright working in university of Cambridge, Prof. Dr. Cheng Zhang working in Zhejiang University of Technology, and my coworkers: Dr. Gang Liu (PhD student), Mr. Jun Chen (postgraduate student), Mr. Xing Yang (postgraduate student), Mr. Hu Wang (postgraduate student), Mr Cong–Ze Wang (postgraduate student) and Miss Yi-

yao Shen, without their contributions, I can't complete my thesis on time.

I would like to thank all the members of the research group for day to day support and their friendly behaviour. I would also like to sincerely thank my parents and my wife Fang CHEN for their unconditional love and support throughout this endeavour.

Yaokang LV

CONTENTS

Résumé

1. Introduction

Les clusters du type polyoxotitanate (**POT**) sont des complexes polynucléaires de titane, qui appartiennent à la famille des polyoxométallates (**POMs**) [1-4]. Les **POT** peuvent non seulement être considérés comme des systèmes modèles pour étudier le dioxyde de titane TiO_2, mais sont également utiles en tant que précurseurs solubles de taille nanométrique pour la construction de nouveaux matériaux [5-10].

Les polymères conjugués ont attiré une grande attention pour une variété d'applications dans les dispositifs électroniques organiques, y compris les cellules photovoltaïques, les diodes électroluminescentes organiques, les transistors à effet de champ organique, les capteurs chimiques, les dispositifs électrochromes, les batteries et les supercondensateurs. La mauvaise stabilité des polymères conjugués reste cependant un obstacle majeur à leurs applications.

La préparation de composites inorganiques-organiques est un moyen efficace d'obtenir de nouveaux matériaux aux propriétés uniques. Cependant, les performances globales notamment électrochimiques des matériaux composites sont toujours limitées du fait de leur hétérogénéité à l'interface et de leur dispersion inégale.

Au cours des travaux de recherche de cette thèse, nous avons conçu, synthétisé et caractérisé des séries de nouveaux matériaux à base de **POT** : matériaux composites **TiO_2/C** ; matériaux composites **$CeTi_xO_y$/PEDOT** (**PEDOT :** poly(3,4-éthylènedioxythiophène)) ainsi que des nouveaux matériaux copolymères **Poly-(EDOT-POT)** et **Poly-(porphyrin-POT)**. Nous avons étudié les liens intrinsèques entre les microstructures et les propriétés électrochimiques de ces nouveaux matériaux.

Résultats et discussions

2.1. Synthèse et caractérisation d'une série de POT

Comme le montre la **Figure 1**, une série de **POT** avec des nucléarités différentes a été synthétisée et structurellement caractérisée. Leur diversité structurelle et leurs sites de coordination ajustables les rendent prometteurs en tant que précurseurs nanométriques ou blocs de construction pour de nouveaux matériaux.

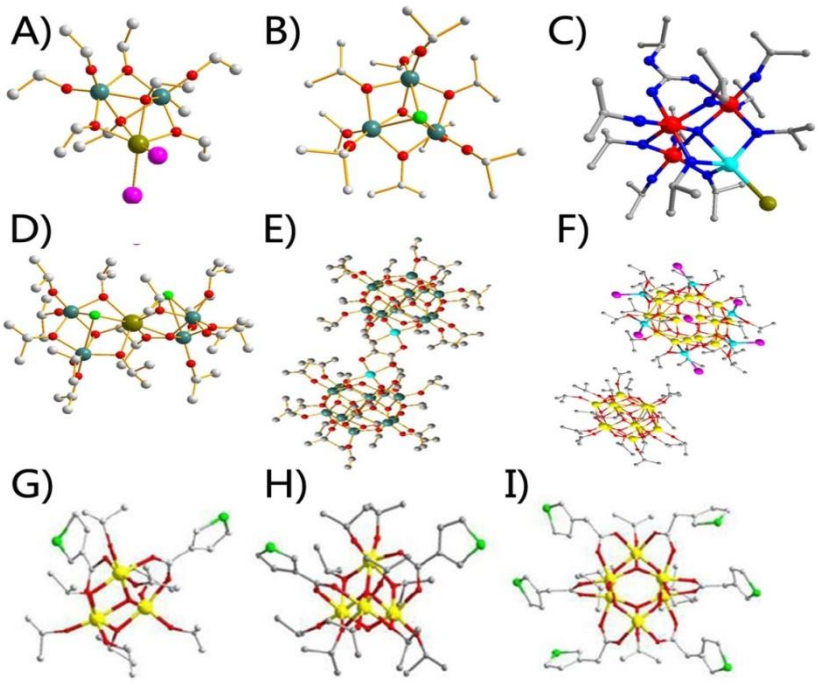

Figure 1. Structures des clusters du type **POT** syntétisés, A) $[Ti_2(OEt)_9InI_2]$, B) $[Ti_3O(O^iPr)_9Cl]$, C) $[Ti_3CO_2(O^iPr)_{10}CoBr]$, D) $[Ti_4O_2(O^iPr)_{14}CeCl_2]$, E) $[Ti_{22}O_{28}(C_2O_4)(O^iPr)_{34}Cu]$, F) $[Ti_{12}O_{15}(O^iPr)_{17}]^+[(ICo)_6Ti_{15}O_{24}(O^iPr)_{18}(I)]^-$, G) $Ti_3O(TC)_2(^iPrO)_8$, H) $Ti_4O(TC)_2(^iPrO)_{10}$, I) $Ti_6O_6(TA)_6(^iPrO)_6$. TC = thiophène-3-carbonate, TA = thiophène-3-acétate.

2.2. Préparation et propriétés des nouveaux matériaux composites dérivés des POTs

En utilisant les **POTs** comme précurseurs nanométriques, comme nous nous y attendions, une série de nouveaux matériaux composites a pu être obtenue. Comme le montre la **Figure 2**, la composition de ces composites peut être radicalement modifiée par les conditions précises de calcination, telles que la température de calcination et la composition de l'atmosphère.

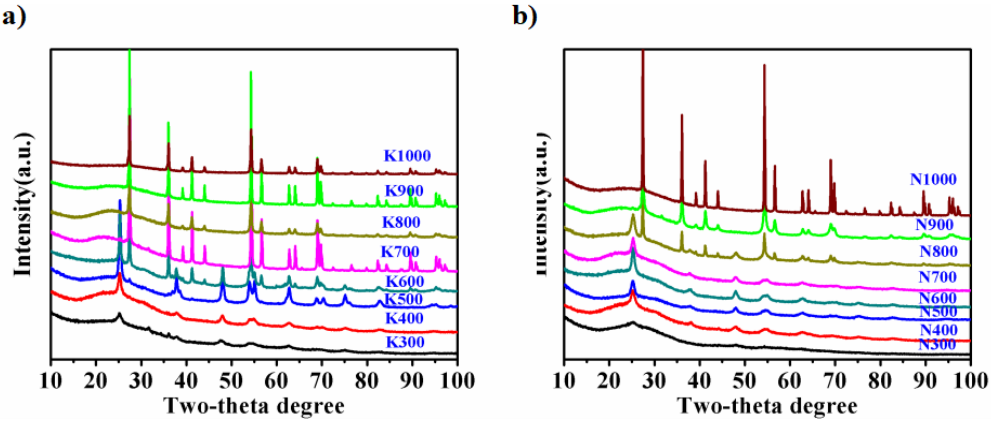

Figure 2. a) Diffractogrames DRX des matériaux composites obtenus à partir de $[Ti_2O(OAc)_2(HOAc)_2Cl_4]$ calciné à différentes températures [300 °C (K300), 400 °C (K400), 500 °C (K500), 600 °C (K600), 700 °C (K700), 800 °C (K800), 900 °C (K900), et 1000 °C (K1000)] dans l'air (22% de dioxygène et 78% de diazote); (b) Diffractogrames DRX des matériaux composites calcinés à différentes températures [300 °C (N300), 400 °C (N400), 500 °C (N500), 600 °C (N600), 700 °C (N700), 800 °C (N800), 900 °C (N900), et 1000 °C (N1000)] en présence uniquement de diazote.

La **Figure 3** présente la première courbe de charge et de décharge des matériaux composites obtenus dans la plage de tension de 0 à 3 V et une densité de courant de 50 mA/g. Les premières capacités spécifiques de décharge des matériaux K500, K600, K800 et K900 sont respectivement égales à 430,7 mAh/g, 181,6 mAh/g, 209,6 mAh/g et 35,9 mAh/g. Les premières capacités spécifiques de décharge des matériaux N500, N600, N800 et N900 sont respectivement égales à 942,6 mAh/g, 696,4 mAh/g, 515 mAh/g et 374,5 mAh/g.

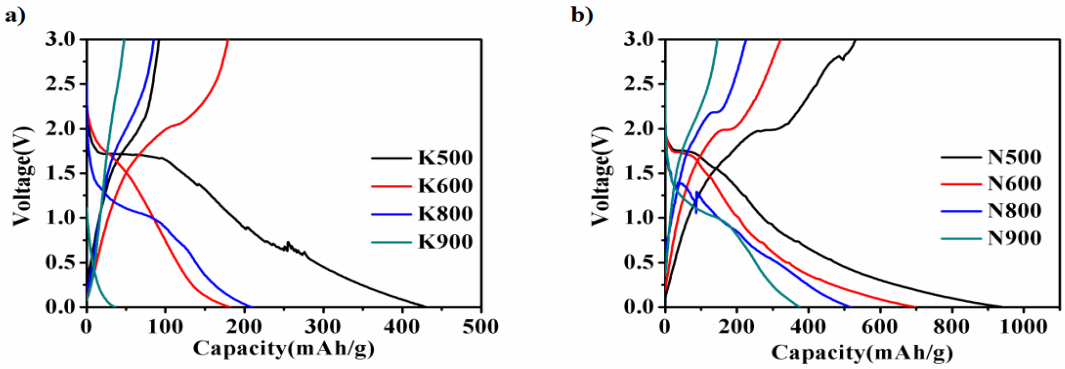

Figure 3. (a) Premières courbes de charge et de décharge des matériaux K500, K600, K800, K900 mesurées avec une densité de courant de 50 mA/g. (b) Premières courbes de charge et de décharge des matériaux N500, N600, N800, et N900 mesurées avec une densité de courant de 50 mA/g.

2.3. Préparation et propriétés des matériaux polymères hybrides préparés avec des monomères POT et des monomères dérivés du thiophène.

La diversité structurelle et les sites de coordination ajustables font que les monomères **POT** tels que $Ti_3O(TC)_2(iPrO)_8$, $Ti_4O(TC)_2(iPrO)_{10}$, et $Ti_6O_6(TA)_6(iPrO)_6$ peuvent être des blocs de construction de taille nanométrique pour la synthèse de nouveaux matériaux polymères hybrides conjugués. Ainsi, nous avons sélectionné et/ou synthétisé plusieurs monomères dérivés du thiophène pour préparer de nouveaux matériaux polymères hybrides tels que le 3,4-éthylènedioxythiophène (**EDOT**), le 3-(N-trifluoroacétamido) thiophène (**F-TH**), le tris[4-(3,4-l'éthylènedioxythiophène)phényl]amine (**TEPA**) ainsi que la porphyrine 5,15-ditolyl de zinc (**ZnT_2P**). De nouveaux films hybrides ont ensuite été préparés et déposés sur verre conducteur ITO par polymérisation électrochimique des monomères **EDOT**, **TEPA** ou **ZnT_2P** en présence de divers cluster POTs : ($Ti_6O_6(TA)_6(iPrO)_6$) (**POT-1**) ou ($Ti_4O(TC)_2(iPrO)_{10}$ (**POT-2**) (cf. **Figure 1**, TC = thiophène-3-carbonate, TA = thiophène-3-acétate).

Par exemple, comme présenté sur la **Figure 4**, l'électropolymérisation de $Ti_6O_6(TA)_6(iPrO)_6$ (**POT-1**) en présence du 3,4-éthylènedioxythiophène (**EDOT**) permet d'obtenir un film 3D nanoporeux et stable (**Poly-(EDOT-POT-1)**). La morphologie du copolymère hybride conjugué **Poly-(EDOT-POT-1)** est uniquement influencée par le potentiel d'électropolymérisation

appliqué. **Poly-(EDOT-POT-1)** est un matériau d'électrode prometteur adapté au transport d'ions rapide et présente des propriétés électrochromiques améliorées par rapport aux propriétés du polymère **PEDOT** (poly-(3,4-éthylènedioxythiophène)) seul (**Figure 5**). Il présente également une capacité 35% plus élevée (102,5 $F.g^{-1}$) par rapport au polymère parent, **PEDOT** (75,8 $F.g^{-1}$) mesuré à une densité de courant de 1 $A.g^{-1}$. Les propriétés sont confirmées par les mesures d'impédance.

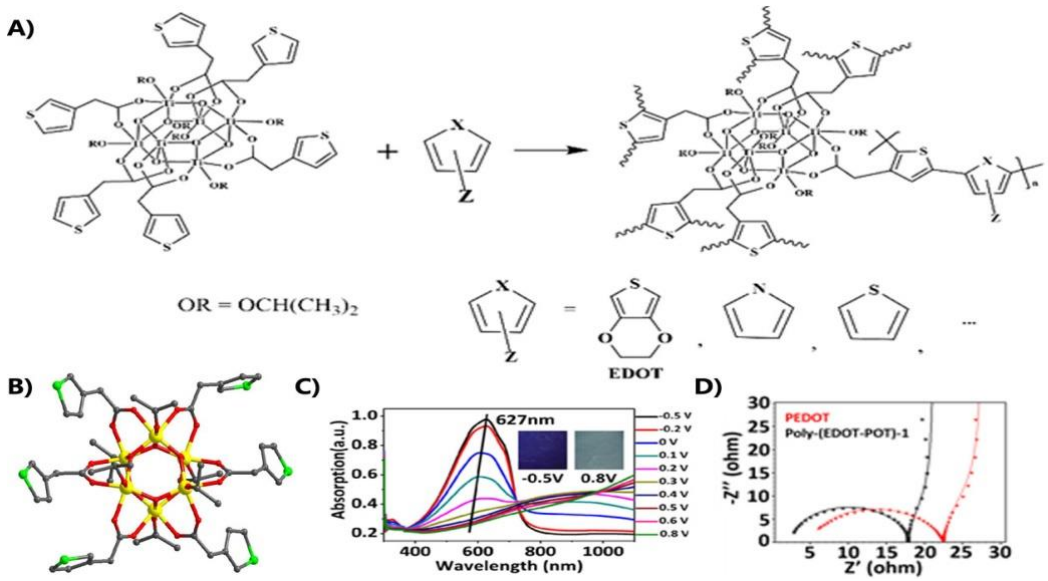

Figure 4. A) Stratégie de copolymérisation utilisée pour obtenir des matériaux hybrides conjugués à partir du cluster **POT-1** ; B) Structure RX à l'état solide du **POT-1** ($Ti_6O_6(TA)_6(iPrO)_6$, TA = thiophène-3-acétate). Les atomes H ont été omis pour plus de clarté (rouge = O, gris = C, vert = S, jaune = Ti) ; C) Spectres d'absorption UV-vis du polymère **Poly-(EDOT-POT-1)** à des tensions appliquées entre -0,8 V et 1,2 V dans une solution TBAH (0,1 M) / CH_2Cl_2 (les encarts sont les photographies des films polymères déposés sur électrode transparente du type ITO). D) Diagrammes de Nyquist (spectroscopie d'impédance électrochimique) des électrodes modifiées : **PEDOT** (courbe rouge) et **Poly-(EDOT-POT-1)** (courbe noire) mesurées dans une solution $LiClO_4$ 0,1 M + CH_3CN à -0,156 V et -0,110 V respectivement. Les symboles représentent les données expérimentales et les lignes pleines les courbes simulées.

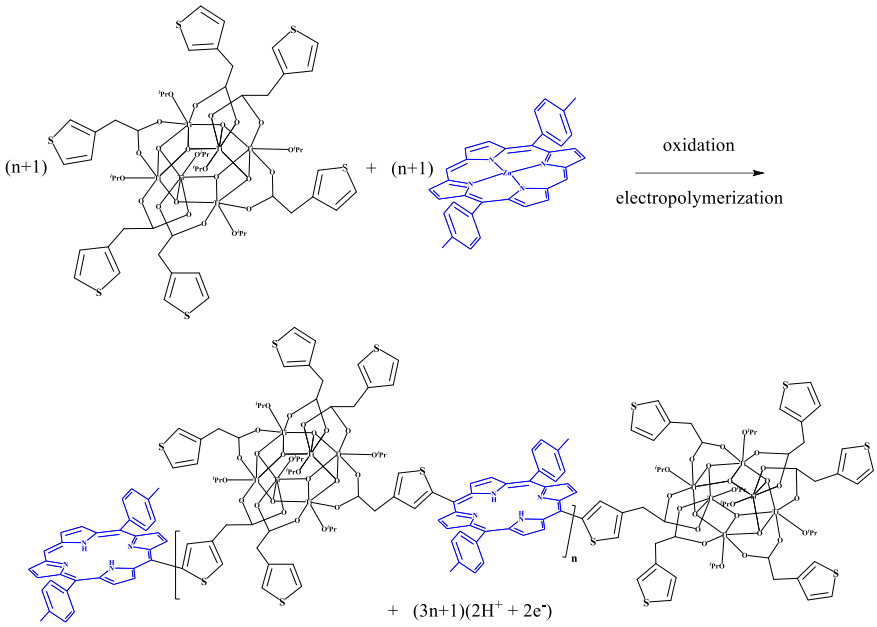

Schéma 1. Voie synthétique de nouveaux films de copolymères hybrides **Poly-(H_2T_2P-POT-1).**

Comme décrit sur le **Schéma 1**, de nouveaux films de copolymère hybride **Poly-(H_2T_2P-POT-1)** ont également été préparés par polymérisation électrochimique de la porphyrine monomère 5,15-(p-tolyl) porphyrine de zinc (**ZnT_2P**) en présence du cluster $Ti_6O_6(TA)_6(iPrO_6$ (**POT-1**) sur électrode transparente du type ITO.

La formation des films jaunes bruns correspondant au copolymère **Poly-(H_2T_2P-POT-1**) a été obtenue par électropolymérisation. Celle-ci a été réalisée sous atmosphère d'argon en milieux NBu_4PF_6 0,1 mol L^{-1} + CH_3CN / 1,2-$C_2H_4Cl_2$ (3/7) contenant 2,5 × 10^{-4} mol L^{-1} de **ZnT_2P** ainsi que 2,5 × 10^{-4} mol L^{-1} de **POT-1**. Des électrodes transparentes du type ITO, d'une surface de 1 cm^2, ont été utilisées comme électrode de travail. Après électropolymérisation, les électrodes de travail modifiées ont été systématiquement lavées avec CH_3CN afin d'éliminer les traces du sel de conductibilité NBu_4PF_6 et les monomères restant éventuellement sur les films électrodéposés. Comme le montre la **Figure 5**, l'emploi du cluster **POT-1** semble réagir avec le radical cation (**Zn$T_2P^{+\bullet}$**) électrogénérés lors des balayages voltamétriques itératifs [11-13].

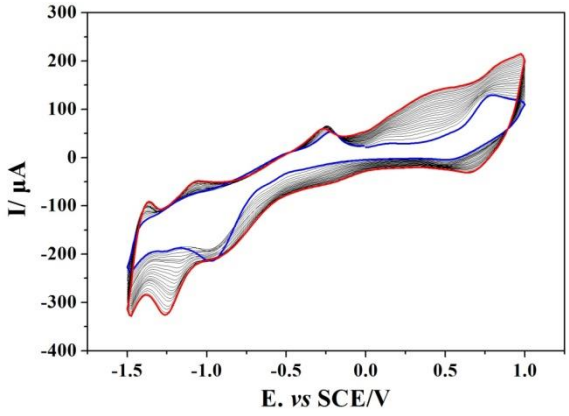

Figure 5. Voltammogrammes cycliques enregistrés au cours de 25 premiers balayages itératifs effectués entre -1,50 V et +1,00 V / ECS en milieu NBu_4PF_6 0,1 mol.L^{-1} + 1,2-$C_2H_4Cl_2$/CH_3CN (7/3) avec **ZnT_2P** (0,25 mmol.L^{-1}) en présence de cluster **POT-1** (0,25 mmol L^{-1}). Electrode de travail : ITO. S = 1 cm^2, v = 0,1 V s^{-1}. Courbe bleue : premier scan (n = 1). Courbe rouge : scan final (n = 25).

Comme le montre la **Figure 6**, les spectres UV-visible-NIR sur des électrodes ITO revêtues du copolymère ont été mesurés à différentes épaisseurs. On peut remarquer qu'au cours du processus d'électropolymérisation, la métalloporphyrine de zinc s'est démétallée et présente 4 bandes Q entre 500 nm et 680 nm au lieu de 2 initialement ce qui est typique de la présence de base libre **H_2T_2P** au sein du polymère que l'on pourrait nommer **Poly-(H_2T_2P-POT-1)**. L'intensité d'absorption du film, qui correspond à l'absorption des unités porphyrines, augmente linéairement avec le nombre de balayage itératif utilisé lors de l'électropolymérisation. Cela peut être expliqué par le mécanisme d'électropolymérisation libérant des ions H^+.

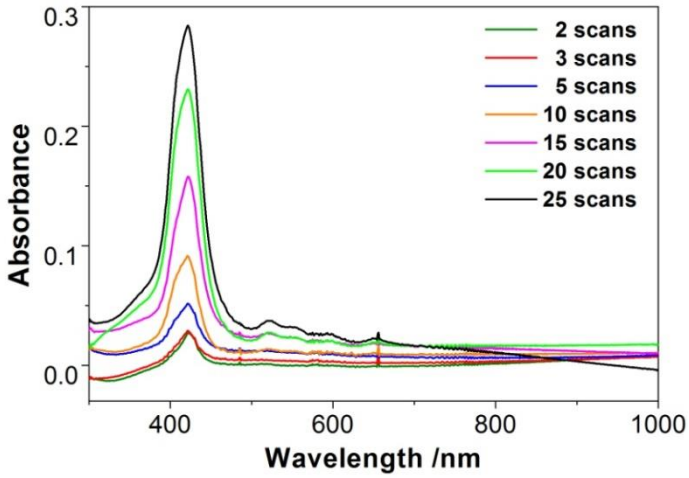

Figure 6. Spectres d'absorption UV-visible-NIR de **Poly- (H_2T_2P-POT-1)** sur ITO avec différents nombres de balayages itératifs entre -1,50 et +1,00 V *vs.* SCE (v = 100 mV.s^{-1}). Remarque : un seul côté de la plaque de verre est recouvert avec un film transparent conducteur du type ITO.

La **Figure 7** montre les courbes courant-potentiel typiques de films minces **Poly-(H_2T_2P-POT-1)** déposés sur électrodes ITO mesurée dans une solution aqueuse contenant un médiateur redox

reversible 5 mM I_2 / 0,5 M I^-. Le potentiel d'équilibre du couple redox I_3^-/ I^- en solution est pris comme potentiel de référence à 0 V dans les voltamogrammes cycliques. La courbe obtenue en l'absence d'illumination a été analysée dans un premier temps (courbe noire). Pour l'électrode ITO nue (sans présence du copolymère), presque aucun courant faradique n'est observé entre -0,3 et 0,3 V, révélant que les cinétiques d'oxydation de I^- et de réduction de I_3^- sur électrode ITO sont lentes, ce qui est connu dans la litérature [14]. Cependant, les courants d'oxydation I^- et de réduction I_3^- sont significativement augmentés sur les électrodes d'ITO modifiées par le copolymère **Poly-(H_2T_2P-POT-1)**. Pour l'oxydation I^-, un courant anodique vers 0,14 V est observé, mais des études complémentaires sont nécessaires pour expliquer pourquoi le courant d'oxydation passe par un maximum. La courbe courant-potentiel mesurée sous illumination avec de la lumière visible et en condition potentiodynamique est également représentée **Figure 7** (courbe rouge). La réponse du photocourant en mode potentiostatique à 0 V sous des cycles d'éclairage marche-arrêt est représentée **Figure 8**. Sous illumination dans le domaine du visible, le potentiel de circuit ouvert augmente d'environ 40 mV. Au-dessus de ce potentiel, le courant d'oxydation I^- devient prédominant du fait de la concentration élevée en ions I^- en solution, empêchant ainsi une nouvelle augmentation du photopotentiel. Pour les potentiels inférieurs à l'OCP, un photocourant négatif est observé. Le photocourant à 0 V du film mince **Poly-(H_2T_2P-POT-1)** atteint -45 µA.cm^{-2} (expérience potentiostatique) ou -90 µA.cm^{-2} (mesuré à partir des voltamétrie cyclique). Les résultats des tests de photoélectrochimie indiquent que les films obtenus présentent de bonnes propriétés électrochimiques et photoélectrochimiques.

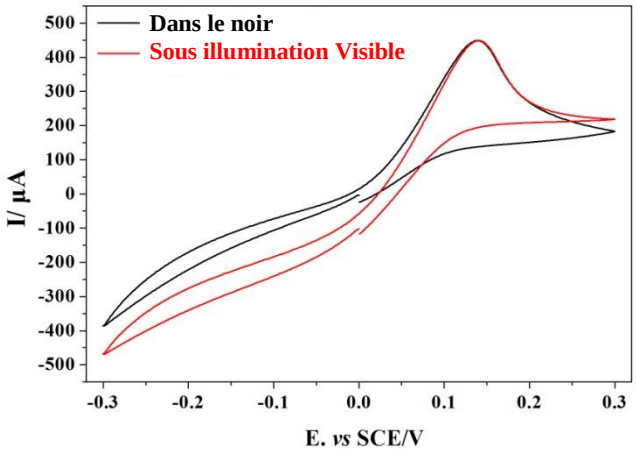

Figure 7. Courbes potentiel-courant des **poly-(H_2T_2P-POT-1)** films.

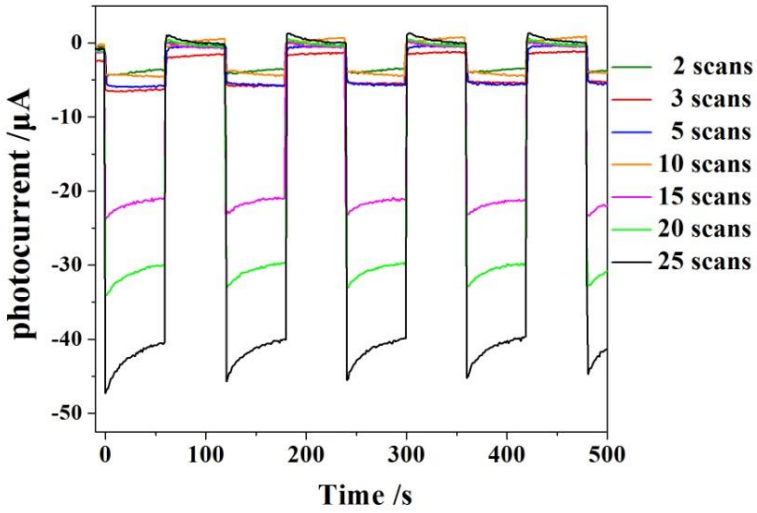

Figure 8. Réponses photoélectrochimiques des **poly-(H_2T_2P-POT-1)** films obtenus avec divers nombres de balayages itératifs.

2) Conclusion générale

En résumé, cette thèse a permis la conception et la synthèse de plusieurs nouveaux matériaux qui ont été préparés à partir de cluster **POT.** Les matériaux composites **TiO_2/C** peuvent être utilisés comme matériaux d'électrode pour batterie Li-ion et en qualité de supercondensateur en raison de leur excellente capacité de stockage d'énergie. Les matériaux composites **$CeTi_xO_y$/PEDOT** et **Poly-(EDOT-POT-1)** préparés ont une forte surface hydrophobe et présentent des propriétés électrochromes prometteuses. Ces matériaux peuvent être utilisés dans des dispositifs électrochromes tels que les supercondensateurs électrochromes.

Le film **Poly-(H_2T_2P-POT-1)** présente un bon comportement pour la génération de photocourant où le contrôle de l'épaisseur des films est d'une grande importance pour optimiser la génération de photocourant sous éclairage visible. L'efficacité de conversion globale η de la cellule scellée reste à étudier.

Nos travaux dans cette thèse ouvriront la voie à la fabrication de matériaux électrochromiques prometteurs avec d'excellentes performances intégrées et élargiront les applications des clusters polyoxotitanes.

2) Références

1. P. Yin, P. Wu, Z. Xiao, D. Li, E. Bitterlich, J. Zhang, P. Cheng, D. V. Vezenov, T. Liu, Y. Wei, *Angew. Chem. Int. Ed.* **2011**, *50*, 2521-2525.

2. F. Xiao, J. Hao, J. Zhang, C. Lv, P. Yin, L. Wang, Y. Wei, *J. Am. Chem. Soc.* **2010**, *132*, 5956-5957.

3. J. Hao; X. Yun, L. Wang, L. Ruhlmann, Y. Zhu, Q. Li, P. Yin, Y. Wei, H. Guo, *Angew. Chem. Int. Ed.* **2008**, *47*, 2626-2630.

4. Y. Lv, W. Du, Y. Ren, Z. Cai, Y. Kuai, C. Zhang, Z. Chen, D. S. Wright, *Inorg. Chem. Front.*, **2016**, *3*, 1119-1123.

5. G. Liu, X. Yang, A. Bonnefont, Y. Lv, J. Chen, W. Dan, Z. Chen, L. Ruhlmann, D. S. Wright, C. Zhang, *Chem. Commun.*, **2018**, *54*, 14132-14135.

6. Y. Lv, Z. Cai, D. Yan, C. Su, W. Li, W. Chen, Z. Ren, Y. Wei, M. Ouyang, C. Zhang, D. S. Wright, *RSC Adv.* **2016**, *6*, 57–60.

7. J. Liu, Z. Cai, Y. Lv, Y. Zhang, C. Su, M. Ouyang, C. Zhang, D. S. Wright, *J. Mater. Chem. A*, **2015**, *3*, 1837-1840.

8. Y. Lv, J. Cheng, P. D. Matthew, J. P. Holgado, J. Willkomm, M. Leskes, A. Steiner, D. Fenske, T. C. King, P. T. Wood, L. Gan, R. M. Lambert, D. S. Wright, *Dalton Trans.*, **2014**, *43(23)*, 8679-8689.

9. Y. Lv, J. Cheng, A. Steiner, L. Gan, D. S. Wright, *Angew. Chem. Int. Ed.*, **2014**, *31*, 476-482.

10. Y. Lv, J. Willkomm, A. Steiner, L. Gan, E. Reisner, D. S. Wright, *Chem. Sci.*, **2012**, *3*,2470-2473.

11. A. Giraudeau, L. Ruhlmann, L. El-Kahef, M. Gross, *J. Am. Chem. Soc.* **1996**, *118*, 2969-2679.

12. L. Ruhlmann, A. Schulz, A. Giraudeau, C. Messerschmidt, J.-H. Fuhrhop, *J. Am. Chem. Soc.*, **1999**, *121*, 6664-6667.

13. L. Ruhlmann, J. Hao, Z. Ping, A. Giraudeau, *J. Electroanal. Chem.* **2008**, *621*, 22-30.

14. M. Boudiaf, Y. Liang, R. Lamare, J. Weiss, A. Bonnefont, L. Ruhlmann, *Electrochim. Acta*, **2019**, *309*, 432-449.

LISTE DES COMMUNICATIONS :

Oral :

[1] L. Ruhlmann, A. Bonnefont, V. Badets, Y. Liang, Z. Huo, D. Zhang, **Y. Lv** "Hybrid polyoxometalate materials for photo(electro)chemical applications", *FMOCS VI (Frontiers in metaloxide cluster science)*, August 19-22, **2019**, *Corvallis*, Oregon, USA, Keynote, *[Conférence Internationale, **Keynote**]*

[2] Y. Liang, **Y. Lv**, V. Badets, A. Bonnefont, **L. Ruhlmann** "Electrosynthesis and photovoltaic properties of stable metallo-isoporphyrin/metalloporphyrin copolymer", *Journée Institut de Chimie UMR 7177*, October 28-29, **2019**, *Strasbourg*, France, *[Conférence Nationale]*

[3] Y. Liang, **Y. Lv**, V. Badets, A. Bonnefont, **L. Ruhlmann** "Electrosynthesis of stable metallo-isoporphyrin/metalloporphyrin copolymer", *GDR Mapyro, 2rd Mapyro Symposium*, November 14, **2019**, *Lyon*, France, *[Conférence Nationale]*

[4] Y. Liang, **Y. Lv**, V. Badets, A. Bonnefont, L. Ruhlmann "Electrosynthesis and photochemical properties of stable metallo-isoporphyrin copolymer", *Journée des doctorants en Chimie 2019*, December 3, **2019**, *Strasbourg*, France, *[Conférence Nationale]*

[5] L. Ruhlmann, Y. Liang, **Y. Lv**, V. Badets, A. Bonnefont " Photoelectrochemical properties of original hybrid organic – inorganic porphyrin – polyoxometalate copolymers: from flat to mesoporous ITO electrodes", *International Workshop on Electrochemistry of Electroactive Materials, WEEM-2019, June 16th - June 21st*, **2019**, *Borovets, Bulgaria [Conférence Internationale, Conférence invitée]*

Poster :

[1] Y. Liang **Y. Lv**, V. Badets, A. Bonnefont, L. Ruhlmann, "Stable isoporphyrin/porphyrin copolymer: mechanism of the electrochemical routes and photovoltaic properties", *International Workshop on Electrochemistry of Electroactive Materials, WEEM-2019, June 16th - June 21st*, **2019**, *Borovets, Bulgaria [Conférence Internationale]*

LISTE DES PUBLICATIONS (en rapport avec les travaux de thèse) :

1. "Conjugated hybrid films based on a new polyoxotitanate monomer",

G. Liu, X. Yang, A. Bonnefont, **Y. Lv***, J. Chen, W. Dan, Z. Chen, L. Ruhlmann*, D. S. Wright, C. Zhang*,

Chemical Communications, **2018**, *54, 14132-14135. Auteur correspondant.*

2. "A New Polyethylene Composite Material Based on Nano Silver Particles Loaded Graphene Oxide",

F. Zhang, K. Zhang, M. Zhou, C. Chen, Z. Cai, G. Wei, X. Jiang, C. Zhang, L. Ruhlmann, **Y. Lv***,

Journal Inorganic Materials, **2019**, *34(6), 633-640. Auteur correspondant.*

3. "Preparation and electrochemical properties of a new multifunctional inorganic/organic composite film",

J. Chen, P. Ma, C. Zhang, L. Ruhlmann, **Y. Lv***,

Journal Inorganic Materials, **2020**, *35(2), 217-223. Auteur correspondant.*

4. "Recycling Iron-Containing Sludges from the Electroflocculation of Printing and Dyeing Wastewater into Anode Materials for Lithium-Ion Batteries",

G. Liu, Y. Shen, P. Ma, S. Zhao, A. Bonnefont, **Y. Lv*** C. Wang, L. Ruhlmann,* C. Zhang*,

ChemSusChem; **2020**, *13, 3469– 3478. Auteur correspondant.*

5. "An Efficient Electrochromic Supercapacitor Based on Solution-Processable Nanoporous Poly{tris[4-(3,4-ethylenedioxythiophene)phenyl]amine}",

Y. Lv, X. Yang, W. Du, P. Ma, H. Wang, A. Bonnefont, D. S. Wright,* L. Ruhlmann,* C. Zhang*,

ChemSusChem; **2020**, *13, 3844– 3854.*

6. "Fluorinated Oleophilic Electrochromic Copolymer Based on 3-(N-Trifluoroacetamido) thiophene and 3,4-

Ethylenedioxythiophene (EDOT)",

H. Wang, Y. Shen, P. Ma, A. Bonnefont, **Y. Lv***, L. Ruhlmann,*H. Ni, W. Liu, C. Zhang*,

ChemElectroChem; **2020**, *7, 3038–3043. Auteur correspondant.*

List of Abbreviations

3D	**three-dimensional**
AFM	**Atomic Force Microscopy**
BINOL	**1,1'-bi-2-naphthol**
$BMIMBF_4$	**1-butyl-3-methylimidazolium tetrafluoroborate**
$BMIMTf_2N$	**bis[(trifluoromethyl)sulfonyl]imide**
CP	**Conjugated Polymers**
CE	**Coloration Efficiency**
CV	**Cyclic Voltammogram**
DCM	**dichloromethane**
DMF	**N,N-dimethylformamid**
DTA	**Differential Thermal Analysis**
EQCM	**Electrochemistry Quartz Crystal Microbalance**
EC	**Ethylene Carbonate**
EMC	**Ethyl Methyl Carbonate**
DMC	**dimethyl carbonate**
DTAB	**dodecyltrimethylammonium bromide**
ECDs	**electrochromic devices**
ECSCs	**electrochromic supercapacitors**
EDOT	**2,3-dihydrothieno-1,4-dioxin**
ESR	**Electron Spin Resonance**
EIS	**Electrochemical Impedance Spectroscopy**
F-TH	**3-(N-trifluoroacetamido)thiophene**
FTO	**Fluorine-doped Tin Oxide**
FT-IR	**Fourier Transform InfraRed**
HOMO	**Highest Occupied Molecular Orbital**

ITO	**Indium Tin Oxide**
ILs	**Ionic Liquids**
IR	**infrared**
LUMO	**Lowest Unoccupied Molecular Orbital**
L	**Ligand**
M	**Metal**
MOs	**Molecular Orbitals**
MS	**mass spectra**
NBu_4PF_6	**tetrabutylammonium hexafluorophosphate**
NMP	**1-Methyl-2-pyrrolidinone**
NMR	**nuclear magnetic resonance**
NIR	**near infrared**
NMR	**nuclear Magnetic Resonance**
PCH	**thiophene-3-carboxylic acid**
PEDOT	**poly(2,3-dihydrothieno-1,4-dioxin)**
PEC	**photo-electro-chemical**
PDIs	**polydispersity indices**
GPC	**Gel Permeation Chromatography**
P(F-TH)	**poly(3-(N-trifluoroacétamido) thiophène)**
P(F-TH:EDOT)	**poly(3-(N-trifluoroacétamido) thiophène-*co*-2,3-dihydrothieno-1,4-dioxin)**
Phen	**1,10-phenanthroline**
Poly-(EDOT-POT-1)	**poly(2,3-dihydrothieno-1,4-dioxin-*co*-POT-1)**
Poly-(ZnT_2P-POT-1)	**poly(zinc-5,15-ditolyl-porphyrin-*co*-POT-1)**
POM	**polyoxometalate**
POT	**polyoxotitanate**
PPy	**polypyrrole**
PTEPA	**poly(tris[4-(3,4-ethylenedioxythiophene)phenyl]amine)**
PTPA	**polytriphenylamine**

PVDF	**polyvinylidene fluoride**
SCE	**Saturated Calomel Electrode**
SEI	**Solid Electrolyte Interface**
SEM	**Scanning Electron Microscopy**
sXRD	**single-crystal X-Ray Diffraction**
TGA	**thermogravimetric analyses**
TBA	**tetrabutylammonium**
$TEABF_4$	**tetraethylammonium tetrafluoroborate**
TEPA	**tris[4-(3,4-ethylenedioxythiophene)phenyl]amine**
TA	**thiophene-3-acetic acid**
TC	**thiophene-3-carboxylic acid**
$TEAPF_6$	**tetraethylammonium hexafluorophosphate**
TBAP	**tetrabutylammonium perchlorate**
THF	**tetrahydrofuran**
TPA	**triphenylamine**
UV	**Ultra Violet**
Vis	**Visible**
XPS	**X-ray Photoelectron Spectroscopy**
XRD	**X-ray diffraction**
ZnT_2P	**zinc-5,15-ditolyl-porphyrin**

General introduction

Polyoxotitanates (**POTs**), which contain nano or subnano sized Ti_xO_y cores, can be precusors of various nanoscale TiO_2 materials. As one of the most prosperous classes of Polyoxometalates (**POMs**), **POTs** have been closely related to many environmental sciences and photo-activities that broadly impact in the aera of energy. Besides, **POTs** bridge the gap between molecules and nanoparticles or bulk titania materials, and exhibits special intrinsic properties. **POTs** have accurate structural information on the crystalline materials which can be acquired using an X-ray technique. Furthermore, many **POTs** stabilized by organic ligands are readily dissolved in organic solvents for recrystallization and post-functionalization, therefore **POTs** can also serve as the building blocks for the bottom-up assembly of a variety of novel functional materials.

On the other hand, conjugated polymers (**CPs**) have attracted widespread attention for a variety of applications in organic electronic devices including photovoltaic cells, organic light-emitting diodes, organic field effect transistors, chemical sensors, electrochromic devices, batteries and supercapacitors, etc. Nevertheless, the relatively poor stability of **CPs** is still a major obstacle to their applications. **POTs** can be employed as 'nano-blocks' for the formation of new organic-inorganic hybrid materials with **CPs**, these hybrid matrials usually have better stability and exhibit excellent characteristics.

Chapter I corresponds to the literature review of materials based on **POTs** and **POMs** as well as their potential application area. Thanks to the development of synthetic methods in the past two decades, a large amount of POTs with various nuclearities and diverse structural types have been obtained and classified. It has been reported that the **POTs** and metal ion doped **POTs** could be used as single-source precursors for TiO_2 and $M@TiO_2$ deposition. While the functional ligands modified **POTs**

exhibit more diverse properties which are either from the functional ligands themselves or synergistically as a result of the combination of the properties of the functional ligand with the Ti_xO_y core of **POTs**. Hence the applications of **POTs** span the areas of supramolecular chemistry, photocatalysis, photochromism, photoluminescence, asymmetric catalysis and gas adsorption. Materials based on **POTs** have exceptional future promise in efficient and environmentally-friendly technologies for energy conversion, storage as well as other applications.

Chapter II focused on the synthesis and structural determination of different **POTs**. **POT-1**, **POT-2**, **POT-3**, **POT-4** are functional ligands modified **POTs** while **POT-6**, **POT-8**, **POT-9**, **POT-10, POT-11** are metal doped **POTs**. The cost of synthesizing large amounts of **POT-5** is relatively low, thus **POT-5** was further studied the preparation and application of a series of C@TiO_2 materials through calcination of **POT-5**.

The object of chapter III is to form a series of C@TiO_2 composite materials. The C@TiO_2 material **N800** calcined in nitrogen flow at 800 ^oC exhibits excellent electrochemical performance, which is mainly attributed to the following aspects: First, the nanoporous structure of **N800** is beneficial to the transport of the electrolyte. Second, the porous structure of **N800** has a large specific surface area, which can increase the contact area between the electrolyte and the electrode. Third, the nanostructure can effectively shorten the transmission distance of lithium ions. Fourth, the carbon component in **N800** can increased the conductivity of this composites which ensures rapid charge-discharge, and good rate performance.

The aim of chapter IV is to develop new synthesis method for hybrid materials based on POT and CPs. CPs such as **P(F-TH)**, **P(F-TH:EDOT)**, **PTEPA** and **PEDOT** were prepared firstly (where **P(F-TH)** = poly(3-(N-trifluoroacétamido) thiophène), **P(F-**

TH:EDOT) = poly(3-(N-trifluoroacétamido) thiophène-co-2,3-dihydrothieno-1,4-dioxin), **PTEPA** = poly(tris[4-(3,4-ethylenedioxythiophene)phenyl]amine), and **PEDOT** = poly(2,3-dihydrothieno-1,4-dioxin)). These polymers exhibit significant electrochromic properties and have good electricity storage capacities. Furthermore, different **POTs** are incorporated into CPs and a series of inorganic/organic hybrid materials with improved electrochemical performances were obtained. Especially, **Poly-(EDOT-POT-1)** films have promising electrochromic properties and electricity storage capacities, this material can be used as electrode material in ECSC. **Poly-(ZnT$_2$P-POT-1**) films exhibit good photocurrent generation behavior, which worth further study.

In summary, this thesis reports design and synthesis of several new materials which were prepared based on **POTs**: **TiO$_2$/C** composite materials can be used as electrode materials for Li-ion battery and supercapacitor because of their excellent energy storage capacity. **CeTi$_x$O$_y$/PEDOT** composites and **Poly-(EDOT-POT-1)** have strong hydrophobic surface and exhibit promising electrochromic properties, these materials can be used in electrochromic devices such as electrochromic supercapacitor. **Poly-(ZnT$_2$P-POT-1)** films exhibit good photocurrent generation behaviour, and the control of the thickness of the **Poly-(ZnT$_2$P-POT-1)** films is of great importance to optimize the generation of photocurrent under visible illumination. As homogeneous hybrid materials, **POTs** grafting thiophene conjugate polymers are expected to solve or significantly decrease those problems caused by uneven dispersion and heterogeneity interfaces in conventional composite materials. Our work in this thesis will pave the way to fabricate promising electrochromic materials with excellent integrated performance and expand the applications of **POMs**.

Chapter 1

Introduction and literature review

1.1 World Energy Needs

In order to improve our daily life, worldwide scientists and engineers try our best to harness natural energy resources. After the first industrial revolution in the 18th century, massive coal resourses were exploited to produce energy, and the second industrial revolution since the 19th century introduced petroleum as fuel, fossil fuels have supplied major part of world's total world energy consumption at present. However, fossil fuel reserves are facing a rapid depletion due to rapid rise in energy consumption in last few decades; limitation of available fossil fuels is an important factor for global oil crises [1] and wars in Middle East [2]. Besides, extreme use of nonrenewable fossil fuels caused undesired effects on natural environment, uncontrolled emission of carbon dioxide (CO_2) and toxic gasses, responsible for global warming [3]. In 2015, the Paris Agreement concluded many years of negotiation and reset the aim of international climate policy to holding global warming to levels well below 2 °C and pursuing efforts to limit it to 1.5 °C [4], Fulfiling domestic energy requirements to sustain industrialisation without increasing fossil fuels demand is the critical challenge nowadays. Thus, there is an increasing demand for effient and environmental-friendly technologies and devices for energy conversion, storage as well as application. Functional materials play a vital role and have important scientific significance for researches and developments.

1.2 Photo-electrochemical Cell

As the world's population grows and new economies emerge, novel solutions are necessary to provide energy to communities across the globe, this is one of society's

basic needs. Solar energy is an inexhaustible, non-polluting and probably the most uniformly distributed energy source worldwide. In fact, "The amount of solar radiation striking the earth over a three-day period is equivalent to the energy stored in all fossil energy sources." Solar energy conversion and utilization is therefore one of the most important energy research topics recently [5].

Photo-electro-chemical (**PEC**) devices are used for the absorption of solar energy and its conversion to a usable form of chemical energy. As shown in **Figure 1**, **PEC** devices can convert abundant solar energy directly into stored electric energy or value-added chemicals (e.g., hydrogen, carbon products) which have great potential to eliminate the intermittency issue of the solar energy supply. Tremendous works have been doing to achieve boosted conversion efficiency of **PEC** devices [6].

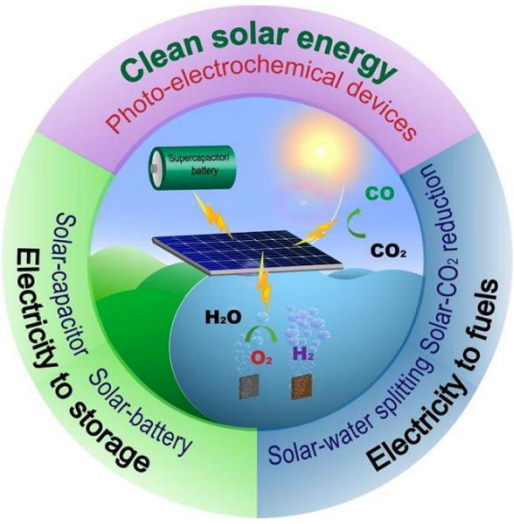

Figure 1. Schematic view of PEC devices. (Adapted from Ref. 6)

One of the most important portions in a good **PEC** device is the photoactive semiconductor electrode material, which absorbs radiations with photon energy (hυ) greater than their band gap energy (E_g). In 1972, Fujishima and Honda firstly reported using single crystal TiO_2 as a photo-anode materials of **PEC** devices for water splitting [7], since then, there has been a considerable progress in the research of **PEC** electrode materials. In 1978, Nozik provided an analytical account of the photo-

electro-chemical devices [8]. In 1984, Heller gave an excellent analysis of efficiencies of various photo-electro-chemical systems [9]. In 1990, Getoff [10] and Pleskov [11a] gave a detailed analysis of **PEC** afterward. Around **2015**, Gao's group [11b] demonstrates how **PEC** efficiency can be enhanced by optimizing the interface energetics and minimizing the reflectance of the surface. The stability of the photoelectrode was greatly enhanced by a thin TiO_2 protection layer. The use of scarce materials can be significantly reduced by using bottom-up grown nanowires. These improvements resulted in the highest photocathodic power-saved efficiency of 15.8% for single junction water reduction at that time [12]. In 2017, a new finding of cocatalyst-free and self-sensitized photocatalytic systems for splitting water into hydrogen by comparatively cost-effective Cu_2X_2-based **MOF**s have been presented for the first time. It was a semiconductive **MOF**s material [13], and in 2019, the photo/electrochemical applications of a variety of metal sulfides (MS_x)/TiO_2 heterojunctions were summarized, and the authors' perspective on future architectural design and electrode construction is given in [14].

1.3 Energy Storage devices

Electricity is a fundamental building block in our modern world; the surplus electricity has to always be generated to meet varying demand. The total installed power generation using renewable energy (including hydropower, wind, solar, biomass, geothermal energy and so on) systems reached 2588 GW by the end of 2019 [15], but many available renewable energy systems like solar and wind are less predictable and more time variant. The integration of renewable energy systems with conventional power system brings several new challenges due to their intermittent nature. Energy storage is considered handy system and has better potential to improve

the reliability of the power system. The integration with energy storage devices can reduce the complexities that arise due to the intermittent nature of renewable energy systems and could be used to reduce the power fluctuations. Both China and the United States are investing a considerable amount in adding energy storage devices and system to their electricity network [16].

1.3.1 Metal-ion batteries

Electrochemical batteries, which are one kind of the most efficient energy storage devices, have the advantages of facile storage and transport and high conversion efficiency. Metal-ion batteries (the metal ion could be Al^{3+}, Zn^{2+}, Ca^{2+}, Mg^{2+}, K^{+}, Na^{+}, Li^{+}, etc.) have attracted extensive interest due to their high energy density and become the most popular electrochemical energy storage devices in the past several decades. Metal-ion batteries have been widely used among the power system applications, their applied power reach to megawatts [17].

Usually, the electrode materials for metal-ion batteries are transition metal-based (e.g. Co, Ni, Mn, V, Ti, etc.) inorganic materials which have the advantages of good capacity and high energy density. However, inorganic electrode materials always have limitation about resource shortage and environmental pollution. Furthermore, during charge-discharge cycling of batteries, the extraction/intercalation of the ions from/into the inorganic electrode materials always leads to volume expansion, phase transition and even pulverization, resulting in capacity decay [18]. Organic polymers have also been studied as electrode materials for rechargeable metal-ion batteries about 40 years. There are a variety of organic polymer materials have been reported for metal-ion batteries [19]. Unlike inorganic materials, the volume expansion and structural variation of polymeric electrode materials are not severe due to their flexibility.

Conjugated polymers, especially the covalent organic frameworks with nanopores are remarkable electrode materials for metal-ion batteries. Conjugated polymers are superior in abundant surface areas, tunable chemical structures and nanopores that are even more remarkable for batteries with intercalation of large-sized ions. More importantly, these materials have the structural diversity and their electrochemical performance could be modified through facile molecular design. Therefore, the researches on these materials have become one of the most interesting areas for metal-ion batteries [20].

1.3.2 Supercapacitors

As another important kind of energy storage devices, supercapacitors have been widely studied in recent years due to their rapid charge and discharge rate, ultra-high power density and long cycle life. Mechanism of energy storage in supercapacitors could be considered as two phenomena: the first mechanism utilizes electrostatic accumulation of charge in electrical double layer and involves electrode materials with a well-developed surface area; thus, charge storage takes place at the electrode/electrolyte interface, the second one is based on reversible redox reactions occurring on electrode materials. Nowadays, supercapacitors have emerged as appealing alternatives to rechargeable energy storage devices in storage systems and renewable energy generation [21]. The research of electrode materials with stable structure, high electrochemical activity, large specific surface area and simple preparation process is the key problems for high performance supercapacitors.

Recently, various carbon materials with different porous morphology and physical properties have been studied as potential electrode materials in supercapacitors [22]. Much attention has also been focused also on conducting polymers such as

polypyrrole (**PPy**), polyaniline, polythiophene, and their derivatives [23]. What's more, transition metal-based compounds are re-attracting attentions since their charge storage mechanism of reversible cations intercalation/deintercalation processes, and can be used as anode for asymmetric lithium-ion supercapacitors with improved energy density [24].

1.4 Electrochromic devices and materials

Electrochromism is the phenomenon where the optical transmittance or absorbance of a material or device changes changes under an applied electric potential as effected either by an electron-transfer (redox) process or by a sufficient electrochemical potential. As illustrated in **Figure 2,** due to the optical switching behavior, electrochromic materials provide great opportunities for energy-saving and color-tuning applications, including architectural "smart windows", rear-view mirrors for cars, and display devices [25].

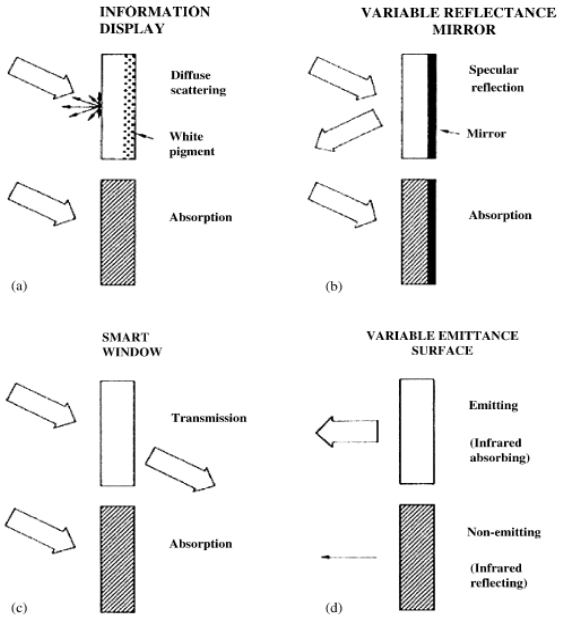

Figure 2. Principles of four different applications of electrochromic devices. Arrows indicate incoming and outgoing electromagnetic radiation; the thickness of the arrows signifies radiation intensity. (Adapted from Ref. 25)

Nowadays, commercial applications of electrochromic materials in devices include antiglare car mirrors, electrochromic sunglasses as well as smart windows for use in cars, aircraft, and buildings; electrochromic strips as battery state-of-charge indicators. Through adjust the interior sunlight, smart windows could lower the energy consumption and improve the indoor comfort. There are many proposed applications for electrochromic materials such as protective eyewear, reusable price labels, glare-reduction systems for offices, controllable aircraft canopies, camouflage materials, spacecraft thermal control, chameleonic fabrics, controllable light-reflective or light-transmissive display devices for optical information and storage and devices for frozen-food monitoring, optical iris for camera lens [26].

There have been reported a vast number of inorganic or organic materials exhibiting electrochromic properties, but only those materials with favorable electrochromic performance parameters are potentially useful since most of commercial applications require electrochromic materials with a high contrast ratio, coloration efficiency, write-erase efficiency and long cycle life [27]. Inorganic electrochromic materials have emerged at the forefront for real-world applications and potential commercialization recently. Many inorganic electrochromic materials exhibit wide range of working temperature, long-term durability and good chemical stability. However, most of these materials suffer from the shortcoming of poor switching speed which is due to the low electrical conductivity of the inorganic material, the slow ionic transporting efficiency and the high-volume expansion during cycling [28]. Organic electrochromic materials, which are characterized by their fast response and rich color palette, are widely investigated [29]. These classes of materials include organic molecules, polymers, and covalent organic frameworks. In comparison with the inorganic electrochromic counterparts, most of organic electrochromic materials

exhibit inferior thermal and chemical stabilities, which therefore limited their practical use. Nanostructured surface of materials provides numerous active sites and shortens the ion's diffusion paths [30]. Thus, as a means to further improve the switching speed, nanostructured electrochromic materials have been investigated in recent years. A nanostructured electrochromic material is expected to attain a rapid switching speed.

1.5 Materials based on polyoxometalates (POMs)

Metal oxides, which are the most dominant materials in the Earth's crust, have been shaping civilizational and technological developments for thousands of years. With the aim of discovering novel useful properties including electrocatalysis photocatalysis and electron storage that aid in solving urgent global challenges relating to clean energy production the demand and interest in the further exploitation of Earth's abundant metal oxides and their confinement to the nanoscale is greater and greater [31]. Polyoxometalates (**POMs**) are combinations between oxygen and early transition metals at their highest oxidation states through atomic-precision synthesis. POMs are molecular oxides which may also contain a variety of heteroatoms and often exhibit similar skeletal topologies of discrete nanoscale molecular formed during self-assembly processes [32]. One of the most significant properties of **POM**s is the ability to accept and release a specific number of electrons without decomposing or change in their structural arrangements, there are numerous applications of **POM**s in catalysis, medicine and materials science [33]. Currently, there has been a growing interest in diversifying the physicochemical properties of **POM**s by creating hybrid organic/inorganic **POM** architectures. These hybrid materials have been widely studied in the area of surfactants, catalysis, surface functionalization, light harvesting materials, eticular materials, non-linear optics, as

well as charge storing materials [34]. **POM**s are ideal candidates for the development of a new type of supramolecular chemistry based upon the building-block ideas, they are set to become a paradigm for those working in nanoscale science.

1.6 Materials based on polyoxotitanates (POTs)

TiO_2 based materials have drawn tremendous attention as highly stable and environmentally benign materials with a range of applications spanning from the paint pigment to semiconductors for sensors, energy storage and photonic devices. In particular, there is a growing interest on the application of TiO_2 for solar energy harvesting. As widely used semiconductors, solid-state TiO_2 with various nano-structural forms have been thoroughly documented in the literature [35]. However, mainly owing to the inherent difficulties in exploring dynamic processes at the TiO_2 surface where chemical reactions occur (e.g., pollutant degradation, water splitting), detailed understanding of the TiO_2 surface chemistry at the atomic level is still lacking [35-39]. Furthermore, because of the insolubility of most TiO_2 based materials, studies using solution-based analytical techniques are very hard.

Using recently developed synthetic approaches, the successful synthesis of atomically well-defined polyoxotitanates (**POTs**) allowed chemists and material scientist to gain new insights into molecular activation using TiO_2. To date, as one of the most prosperous classes of **POM**s, **POT**s have been closely related to many photo-activities that broadly impact in the aera of energy and environmental sciences [40,41]. Besides, **POT**s bridge the gap between molecules and nanoparticles or bulk titania materials, and exhibits special intrinsic properties. Compared to TiO_2 nanoparticles, **POTs** have at least two advantages. Firstly, accurate structural information on these crystalline materials can be acquired using an X-ray technique, which provides basic but precise structural data for theoretical calculations and mechanism explanation. Secondly, **POT**s stabilized by

organic ligands are readily dissolved in organic solvents for recrystallization and post-functionalization, and **POT**s serve as the building blocks for the bottom-up assembly of a variety of novel functional materials, too [42]. Thus, these molecular materials with the same composition, size and shape can greatly overcome the imprecise and inhomogeneous characteristics of TiO_2 nanoparticle materials.

1.6.1 Synthetic strategies of POTs

The synthetic approaches of **POT**s have been largely developed from traditional strict inert condition synthesis to solvothermal or ionothermal reactions, and even water phase synthesis in the past few years [43-46]. Diverse synthetic methods open windows for the preparation of novel **POT**s with designed molecular structures and the engineering of their properties. So far, more than five hundred **POT**s' structures have been determined and documented. As shown in **Figure 3**, the nuclearity of **POT**s keeps growing from Ti_3 to Ti_{52} [47-50]. In addition, diverse **POT** building blocks were successfully incorporated for the construction of extended frameworks, such as COK-69, MIL-91, MIL-125, MIL-125-NH_2, MOF-901, MOF-902, NTU-9, PCN-22 and Ti-MIL-101 [51-53].

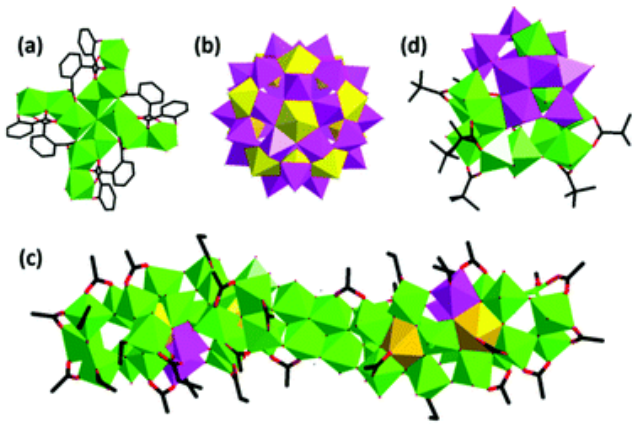

Figure 3. Polyhedral views of recently reported high-nuclearity POTs: (a) $[Ti_{13}O_{10}$-(o-BDC)$_4$(SAL)$_4$(O^iPr)$_{16}$], (b) Ti_{42} of TOF-1, (c) Ti_{52} of COM-3, and (d) [I@Ti_{22}(μ-O)$_{11}$(μ_3-O)20(μ_1-O^iPr)$_{16}$(μ_2-O^iPr)$_2$(^{t}BuCOO)$_9$(OH_2)H_3] (I_3)·HO^iPr. Alkoxide ligands are omitted for clarity. Atomic code: red, O; black, C. Polyhedral colour code: pink, TiO_5; green, TiO_6; yellow, TiO_7. (Adapted from Ref. 50)

Most of reported **POM**s are polyanions, and could be synthesized in aqueous solution. The metal atoms of these **POM**s are transition metals such as Mo, W, V, Nb, Ta in their high oxidation states. However, the poor degree of control of crystallization in a common water solvent has hampered the development of **POT**s, since Ti(IV) ions are easy to spontaneous hydrolysis in water which lead to an uncontrolled precipitation of TiO_2. Recently, diverse synthetic methods have been developed to facilitate the acquisition of **POTs** attributed to the worldwide research efforts.

Schubert's group [54, 55], Wright's group [45] and other forerunner groups developed a synthetic method where **POT**s were synthesized under strict inert conditions using easy hydrolysis of $Ti(OR)_4$ as starting material, and a dry, O_2-free atmosphere was used throughout all of the syntheses. Besides, solvothermal technique has also been proved to be a useful method in making crystalline **POT**s [56]. Compared to room temperature reactions, the high temperature and pressure can accelerate the solubility of the starting material, more components can be therefore employed into the reaction system, which enriches structural diversity and functional extension [57,58]. In addition, the reaction cycle is largely reduced from several weeks in room temperature synthesis to several days in solvothermal synthesis. Reaction parameters in solvothermal synthesis could be controlled easily by setting the oven at different temperatures, required times as well as the warming up and cooling down rate.

$Ti(OR)_4$ in combination with HO-R solvents are the most prevalent titanium precursors and have been extensively used to obtain **POT**s. Besides $Ti(OR)_4$, there are other titanium salts like $TiCl_4$ and $TiOSO_4$, which can readily dissolve in water, forming highly acidic aqueous solution to prevent hydrolysis and can be used in the water phase reaction for the synthesis of **POT**s. For example, a series of **POT**s synthesized in aqueous solution have been reported by Wang's group [59-61].

Compare to conventional solvents, ionic liquids usually act as both solvent and template for solvent-free synthesis which can reduce environmental contamination and potentially be more convenient than solvent-based synthesis. Recently, ionothermal synthesis has been extensively employed in the synthesis of inorganic zeolites and hybrid metal organic frameworks [62,63]. In 2017, a deep eutectic solvent synthesis approach has been successfully employed in the isolation of **POT**s [64]. The anions in the deep eutectic solvents played an important role in the formation of the **POT** molecules. Although the ionothermal synthesis of **POT**s is still in its early stages, it is one of the most promising and environmental friendly synthetic methods in light of the variety of ionic liquids and deep eutectic solvents.

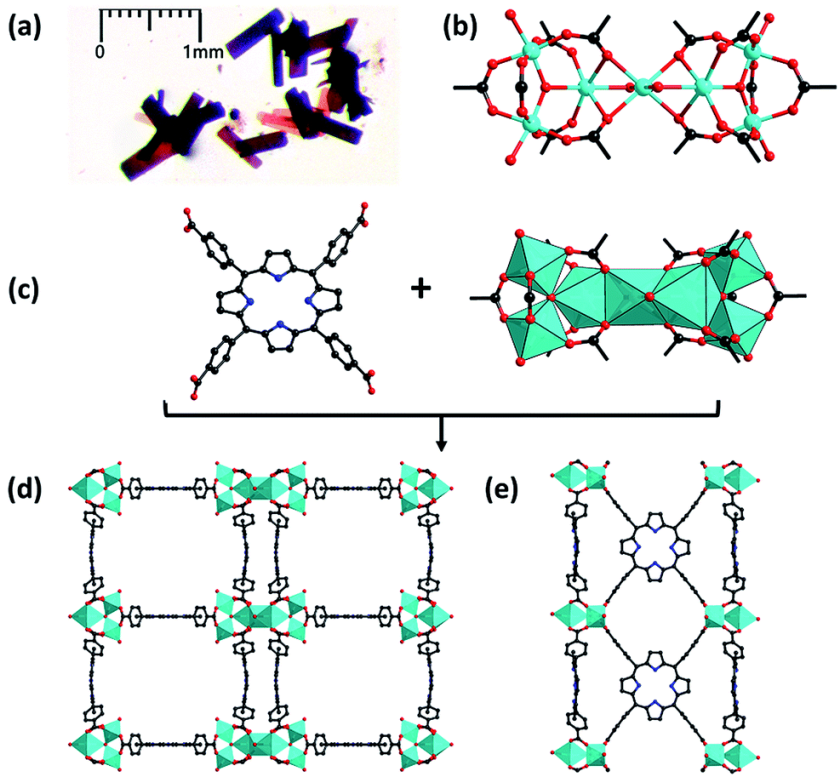

Figure 4. (a) Microscope image of PCN-22 crystals; (b) structure of the Ti_7O_6 cluster (only O atoms of DEF molecules are shown for clarity); (c) representation of the tetratopic TCPP linker (left) and 12-connected Ti_7O_6 cluster (right); (d) views of the structure of PCN-22 along a-axis and (e) b-axis. Color scheme: red O; black C; blue N; and cyan Ti. H atoms are omitted for clarity. (Adapted from Ref. 67)

Apart from one-pot reactions, two-step synthesis or stepwise method with a higher level of controllability was developed. Under these circumstances, the crystals of **POTs** are themselves used as the Ti source and precursors [65,66]. Furthermore, this stepwise approach can be used to obtain extended cluster based frameworks. As shown in **Figure 4**, Zhou's group has used a photocatalytic **POT**, $Ti_6O_6(O^iPr)_6(ABZ)_6$ (ABZ = 4-aminobenzoate) as a precursor to a 3D framework combining the **POT** with photosensitizing porphyrinic linkers [67].

1.6.2 Structure of POTs

Development and improvement of synthetic methods contribute greatly to the structural diversity of **POT**s. In an important review reported by Sanchez's group, they systematically classified structures into three types according to their bridging ligands [40]. Coppens' group summarized the high-nuclearity (>Ti_{10}) **POT**s into seven detailed basic structure types [41] while Zhang's group have introduced the up-to-date progress of POTs from low to high nuclearity [50].

Modification with functional ligands is an important method to additional structural diversity of **POT**s. Bandgap measurements and bandgap calculations have clearly illustrated that this method will adjust the chemical reactivity of **POT**s [41]. Similar with dye-sensitized TiO_2, the optical response of **POT**s can be largely extended to visible region when **POT**s are combined with photosensitizers and form a crystalline-integrated dye-sensitized photoactive structure. In 2012, Coppens' group reported the interfacial electron transfer into p-nitrophenyl acetylacetone functionalized **POT**s of Ti_{17}, which is a pioneering work for a sensitized semiconductor nanoparticle with precisely defined structure of the interface as well as molecular adsorption mode [68]. In 2014, Dai's group obtained a **POT** containing 9-anthracenecarboxylate antennae which exhibiting good

photocurrent transfer property and fluorescent property [69]. Marom's group reported catechol-functionalized **POTs** with different sizes. Owing to penetration of the highest occupied catechol levels into the band gap of the Ti_xO_y cores, all of these **POTs** show a deep-red colour [70]. As shown in **Figure 5**, Zhang's group [71] has used a robust phosphonate-stabilized **POT** as a platform to investigate the bandgap modulation and engineering of **POTs**. In their work, the applied PTC had a similar cluster core to $[Ti_6O_4(OiPr)_{10}(O_3PR)_2]^{2+}$, while a variety of O-donor ligands, including sulfonates, phosphonates, and carboxylates have been introduced as the functional organic species without changing the $\{Ti_6\}$ core. As confirmed by absorption spectra analysis, the increasing electron-withdrawing effect of the organic species allowed the gradual reduction of the bandgaps of **POTs** [71].

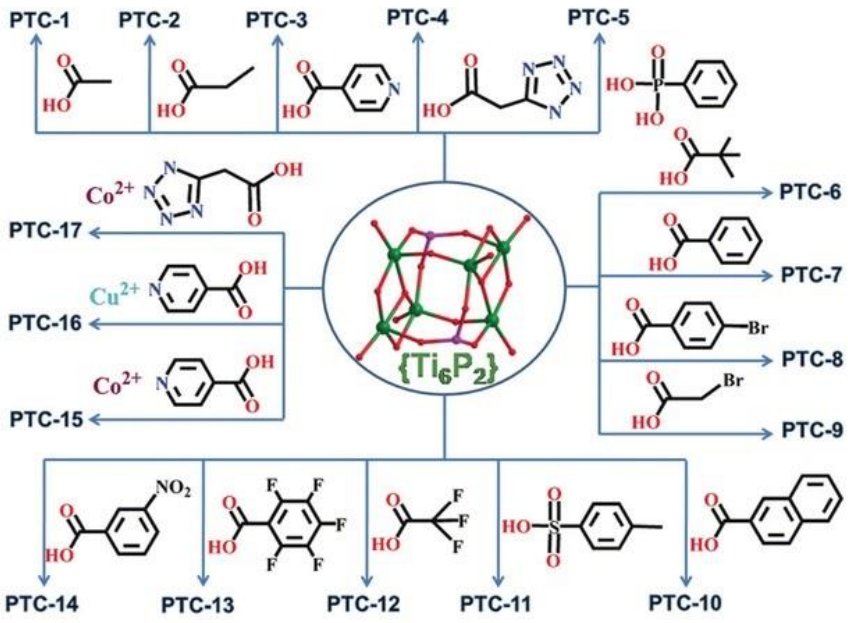

Figure 5. Illustration of the ligand modification of phosphonate-stabilized $[Ti_6O_4(O^iPr)_{10}(O_3PR)_2]^{2+}$. (Adapted from Ref. 71)

Metal and non-metal elements doping has proven to be another effective method for adjusting structures and properties of **POTs**. A range of metal ions (including alkaline/alkaline earth metals, transition metals, lanthanide ions and so on) and non-metal

elements (such as N, P, S) have been successfully incorporated into **POTs**. Compared to none doped **POTs** and pure TiO_2 nanoparticles, the bandgaps of doped **POTs** were narrowed by introducing additional energy levels. Interstitial **POTs** doping involves a wide range of monovalent alkali metals, divalent transition metals as well as trivalent lanthanide metals. According to the connectivity and distance between the Ti_xO_y core and the doped metals, metal-doped **POTs** can be divided into two types. In one type, doped metals are directly bonded to the Ti_xO_y core through bridging-O atoms [72]. In another type, the **POTs** are functionalized with a large polymetallic species to form intercluster complexes, where the two components are separated. Coppens' group carried out the analysis of a series of homo-disperse transition metal doped **POTs** with the molecular formula $Ti_{11}(MX)O_{14}(O^iPr)_{17}$ (M = Mn, Fe or Co; X = Cl, Br or I) to reveal how substitutional doping affects light absorption. They found that all doped **POTs** show red-shifted absorption wavelengths compared with the non-substituted Ti_{12} **POT**. In addition, light absorption varies significantly with the variation of the transition metal dopant [73]. Wang's group further studied the dopant effects of this analogue series $Ti_{11}O_{14}(O^iPr)_{17}(ML)$ (M = Mg, Ca, Zn, Cd, Co, or Ni; L = Cl, Br, I, or NO_3). Through UV-Vis absorption spectra analysis, they found that Co and Ni doping could reduce the **POTs** bandgaps and enhance the absorption of solar light, whereas for Mg, Ca, Zn, and Cd doping only varied slightly the bandgap compared to non-substituted Ti_{12} **POT** [74]. In 2017, Liu's group reported an indium-doped **POT** of $[Ti_{12}In_6O_{18}(OOCC_6H_5)_{30}]$ with ultrahigh stability in both acid and base aqueous solutions. This **POT** not only exhibits a visible-light-driven photocatalytic activity for H_2 evolution in an aqueous system without any cocatalyst but also can produce pronounced photocurrent and reactive oxygen species for the degradation of pollutants under visible irradiation [75]. It is notable that an isostructural chromium-doped **POT** of $[Ti_{12}Cr_6O_{18}(OOCC_6H_5)_{30}]$ also showed a high H_2 evolution efficiency under full solar spectrum light [76]. In 2013, Coppens' group reported a manganese-

doped **POT** of $Ti_{14}MnO_{14}(OH)_2(OEt)_{28}$ which is a bit smaller and similar to the **POT** of $Ti_{17}O_{24}(O^iPr)_{20}$. With the substitution of the central tetrahedral by a Mn(II) ion, this **POT** lacks a pair of 5-fold coordinated Ti atoms. Optical diffuse-reflection spectra measurements showed that the bandgap of this doped **POT** red-shifted 0.55 eV compared to that of commercial anatase, which was also smaller than that of the undoped **POT** of $Ti_{17}O_{24}(O^iPr)_{20}$ [77]. In 2014, Wright's group [56] further extended the transition metal to Fe (II) and Ga (III) in $[(M)Ti_{14}(OEt)_{28}O_{14}(OH)_n]$ [M = Mn (II), Fe(II), n = 2; M = Ga (III), n = 1].

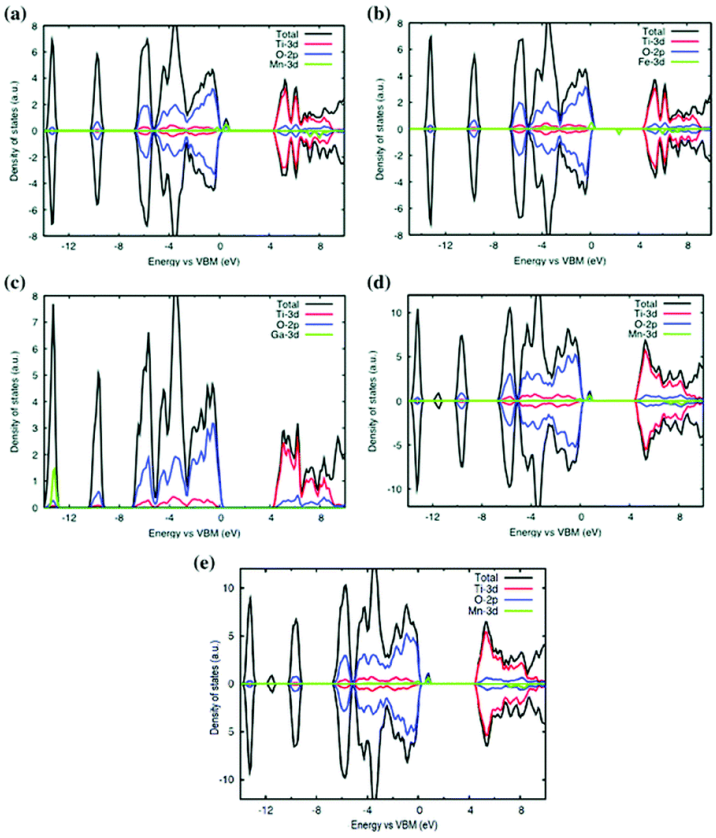

Figure 6. B3LYP functional method calculated projected density of states of (a) $[MnTi_{14}(OEt)_{28}O_{14}(OH)_2]$, (b) $[FeTi_{14}(OEt)_{28}O_{14}(OH)_2]$, (c) $[GaTi_{14}(OEt)_{28}O_{14}(OH)]$, (d) $[Ti_{28}MnKO_{37}(OH)(OEt)_{40}]$ and (e) $[Ti_{27}MnKO_{35}(OH)_2(OEt)_{39}]$. (Adapted from Ref. 56)

As shown in **Figure 6**, it has been concluded that the bandgaps highly depended on the attributes of the doping metals. Mn (II) and Fe (II) have partially occupied 3d orbitals which mix with valence band of the Ti_xO_y cores, producing energy levels near

valence band and leading to a small reduction in the bandgaps. But in Ga (III) doped **POT** of $GaTi_{14}(OEt)_{28}O_{14}(OH)_n$ the full-shell d^{10} configuration of Ga (III) has a much lower energy level hardly affecting the bandgap since it does not mix with the valence band.

1.6.3 Properties and applications of POTs

POTs can be used as single-source precursors for various titania materials. As shown in **Figure 7**, the presence of hydrolysable organic surface groups in **POT** cages of the type $[Ti_xO_y(OR)_z]$ or **M-POT** cages $[Ti_xO_y(OR)_zM_nX_m]$ (M = a metal ion, X = an anion such as halide) introduces the prospect of the application of **POTs** as single-source precursors for the deposition of a series of titania materials [78, 79]. However, hydrolysis of the ligand-functionalised **POTs** of the type $[Ti_xO_y(OR)_z(L)_m]$ (L = functional ligand) may be hindered by the presence of more robust ligands. In several cases, ligand-functionalised **POTs** often survive intact even in aqueous solutions. It may require special treatment (e.g. heating, autoclaving, addition of specific nucleation tuners…) for degradation ligand-functionalised **POTs** into titania materials [80-82].

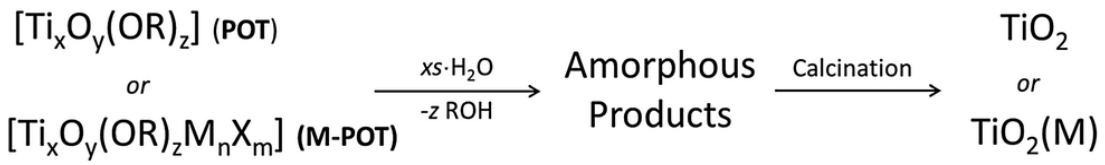

Figure 7. Reaction scheme of **POT** cages $[Ti_xO_y(OR)_z]$ or M-POT cages $[Ti_xO_y(OR)_zM_nX_m]$ upon hydrolysis and further calcination, forming TiO_2 or metal-doped TiO_2 [M@TiO_2]. The amorphous products initially formed probably consist of TiO_2 mixed with organic residues. (Adapted from Ref. 42)

Materials generated by **POTs** from hydrolysis under various conditions is usually amorphous titania. Upon calcinating at 400 °C, amorphous titania will be converted to crystalline anatase and further to rutile around 500 °C [83]. Furthermore, the ligand-

functionalised **POTs** under these circumstances can allow the conversion to titania to follow a different reaction route. For example, the tetranuclear cage [Ti_4(μ4-O)(μ-furfuryloxo)$_{14}$] can convert to titania materials via cationic polymerization using trifluoromethanesulfonic anhydride as the initiator [84]. Phase purity of converted titania materials can be fine-tuned through altering treatment conditions. Solely anatase phase of TiO_2 can be obtain via pretreatment with excess distilled water at 100 °C before calcination at 400 °C produces, while mixture materials of anatase and rutile phases could be prepared through directly calcinating at 400 °C.

What's more, organic ligands not only act as sources of detrimental carbon impurities for titania crystallization, but also can be employed to produce novel hybrid titania materials. Self-assembled TiO_2@C nanostructured composites have been produced simply via calcinating the **POTs** in nitrogen atmosphere [46,85]. As shown in **Figure 8**, through varying the type of **POTs** and the reaction conditions, the morphologies of the formed composites can be fine-tuned.

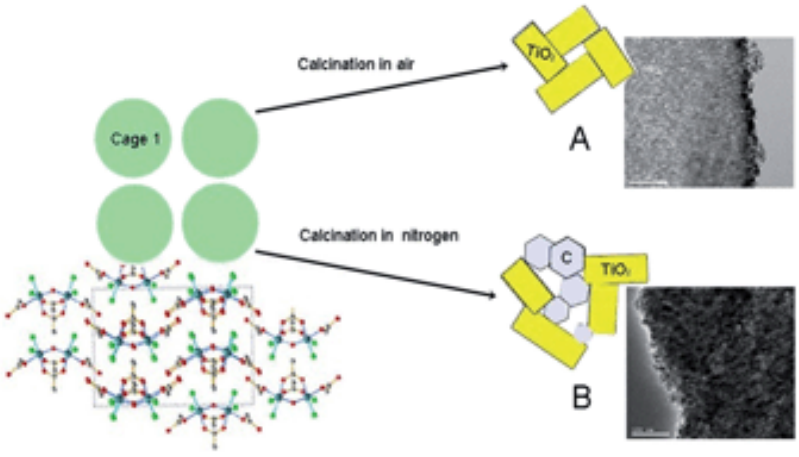

Figure 8. Hypothesis of the mechanisms from **POT** (cage 1) to TiO_2@C composites materials A and B. (Adapted from Ref. 85)

POTs can also be used as nano-building blocks for hybrid materials construction. Inorganic–organic hybrid materials combine the inorganic and organic components on

the molecular scale to achieve a synergetic marriage of properties inherent to each constituent [86]. In synthesizing hybrid materials, the nano-building block based method is particularly attractive and **POTs** represent an important family of nano-building blocks [87,88]. Rozes and Sanchez have thoroughly reviewed the 'Lego-Like' construction of hybrid materials based on **POTs** as well as their syntheses, structures and nano-building blocks applications [40]. As shown in **Figure 9**, the construction of POT-based hybrid materials is built upon the possibility of modifying these preformed **POTs** with polymerisable functional ligands, through which the polymerisable **POTs** can be inter-connected through ligand-induced aggregation, crosslinking, and metal–organic-framework formation. Substituting the more labile alkoxide groups into functional ligands, especially multidentate ligands can readily stabilize **POTs** against hydrolysis. Such substitution is regioselective and can be carried out in a controlled manner, paving the way for the broad use of **POTs** in hybrid materials construction [89, 90].

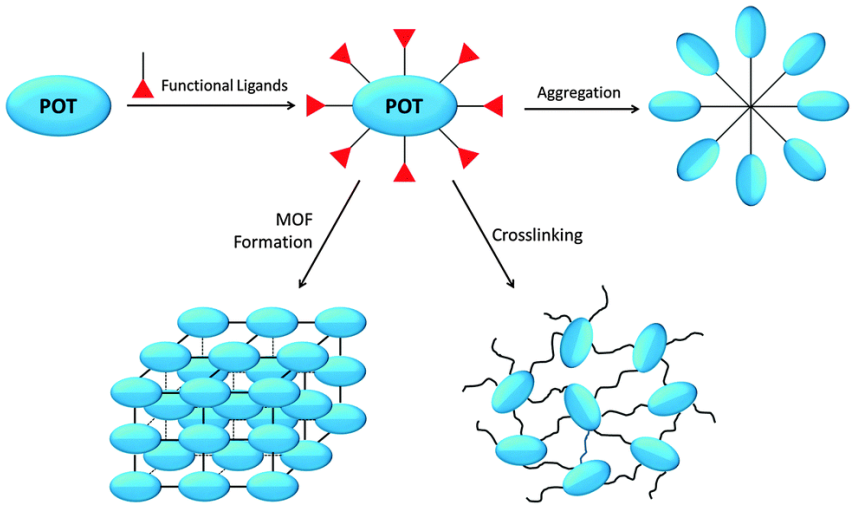

Figure 9. Schematic illustration of the construction of inorganic–organic hybrid materials from **POTs**. (Adapted from Ref. 42)

For instance, using the alkyne–azide click reaction, the outward-pointing alkyne groups in the **POT** of $[Ti_6O_4(OPr)_8(OOC(CH_2)_2CCH)_8]$ can be employed as

molecular ‘docks’ in reaction with azide groups to produce **POT**-based inorganic-organic hybrids [91].

Besides, the concept of nano building blok can be extended to the interaction of **POTs** with macro-surfaces. As shown in **Figure 10**, the classic **POT** of $[Ti_{16}O_{16}(OEt)_{32}]$ was modified using the thiol–ether linker $[HO(CH_2)_4SCH_3]$. The resulting **POT** of $[Ti_{16}O_{16}(OEt)_{24}\{O(CH_2)_4SCH_3\}_8]$ was further covalently tethered onto a gold surface using five out of the eight thiol anchors in the **POT** [92]. Interestingly, the parent **POT** $[Ti_{16}O_{16}(OEt)_{32}]$ undergoes extensive decomposition on the surface of gold. The stability of the **POT** of $[Ti_{16}O_{16}(OEt)_{24}\{O(CH_2)_4SCH_3\}_8]$ revealed the importance of the soft thiol-modification for enhancing molecular stability and effective tethering onto the gold surface. Such surface tethering techniques could have broad applications in surface-based technologies such as heterocatalysis, sensors, and so on.

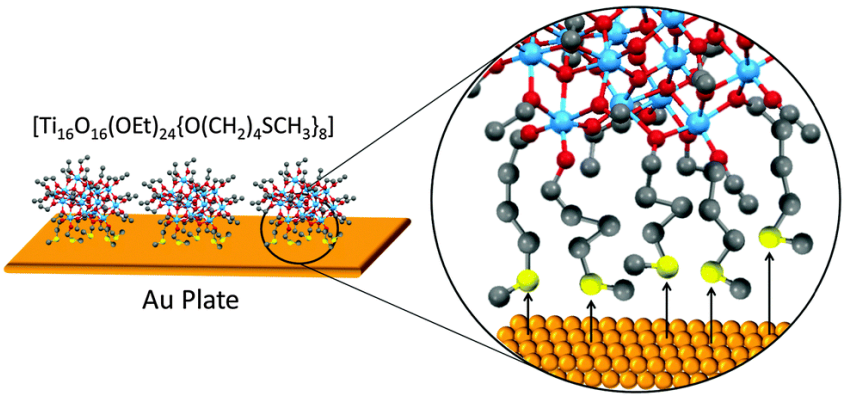

Figure 10. Schematic of the possible tethering mode **POT** of $[Ti_{16}O_{16}(OEt)_{24}\{O(CH_2)_4SCH_3\}_8]$ onto an Au surface. Blue = Ti, red = O, grey = C, yellow = S, orange = Au. The Au–S interactions are indicated by black arrows. (Adapted from Ref. 92)

POT based material can be used as photocatalysts [42]. The principle mechanism by which **POTs** mediate photocatalysis involves the photo-induced electron excitation of the Ti_xO_y core from the valence band [predominantly O(p)] to the conduction band [mainly Ti(d)]. After that, electrons and holes generated migrate to the surface

of **POT** based materials where redox reactions occur. Usually, **HOMO–LUMO** gaps or band gaps of unmodified **POTs** and **POT** based materials are in the range of 3.5–4.0 eV, which means that electronic excitation from the valence band to conduction band requires ultraviolet photons with wavelength less than ca. 350 nm. Doping **POT**, especially metal doping **POT**, has proved to be effective in narrowing the band gaps via introducing additional energy levels within the band gap of the Ti_xO_y core. As shown in **Figure 11**, functional ligand modification can be another important method for enhancing light absorption of **POTs** since functional ligands may act as photo-sensitizers that can harvest long wavelength photons and then transfered these photoexcited electrons to the Ti_xO_y core of **POT** [71,93]. It is worth mentioning that isolated ligands not necessarily absorb at the same energy as the ligand modificated **POT**, because the ligand **HOMO–LUMO** can be mixed with the energy bands of the Ti_xO_y core upon bonding with **POTs**, which gives rise to a much narrower gap [94].

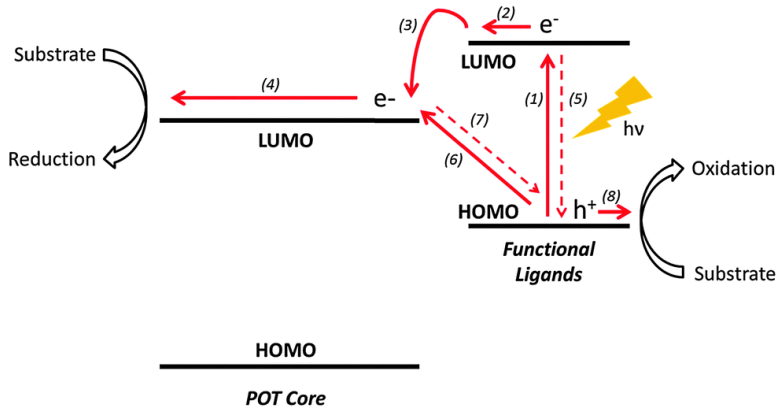

Figure 11. The mechanism of photocatalytic reactions mediated by ligand modificated POTs: (1) excitation of a functional ligand, (2) and (3) electron transfer from the excited functional ligand to the POT core, (4) electron transfer to the photocatalytic reaction substrate, (5) electron–hole recombination, (6) ligand-to-metal charge transfer, (7) electron–hole recombination, (8) hole transfer to the photocatalytic reaction substrate. (Adapted from Ref. 42)

Depositing **POTs** onto transparent conducting substrates such as fluorine-doped tin oxide (**FTO**) and indium tin oxide (**ITO**) and measuring the generated photocurrent upon light irradiation with or without applied voltages is a convenient way to study the photo-responses of **POTs** and **POT** based materials. But as smaller **HOMO–LUMO** separation has to be balanced against the rate of hole–electron recombination, it can be noted that the photocurrent response is not equivalent to photocatalytic activity. Thus, the optimum characteristics for high photocatalytic activity generally include a reasonably small **HOMO–LUMO** gap and a slow recombination rate. Visible light absorption can be combined with the potential for hole–electron migration to the surface of the **POTs** or **POT** based materials, where reactions with substrates can occur. As shown in **Figure 12**, Dai's group successfully obtained two loosely-packed **POTs**, $[Ti_{13}O_{10}(o\text{-}BDC)_4(SAL)_4(O^iPr)_{16}]$ (5) (**Figure 12a**) and $[Ti_{13}O_{10}(o\text{-}BDC)_4(SAL\text{-}Cl)_4(O^iPr)_{16}]$ (6), and the corresponding photoelectrodes by spin-coating of these cages [95].

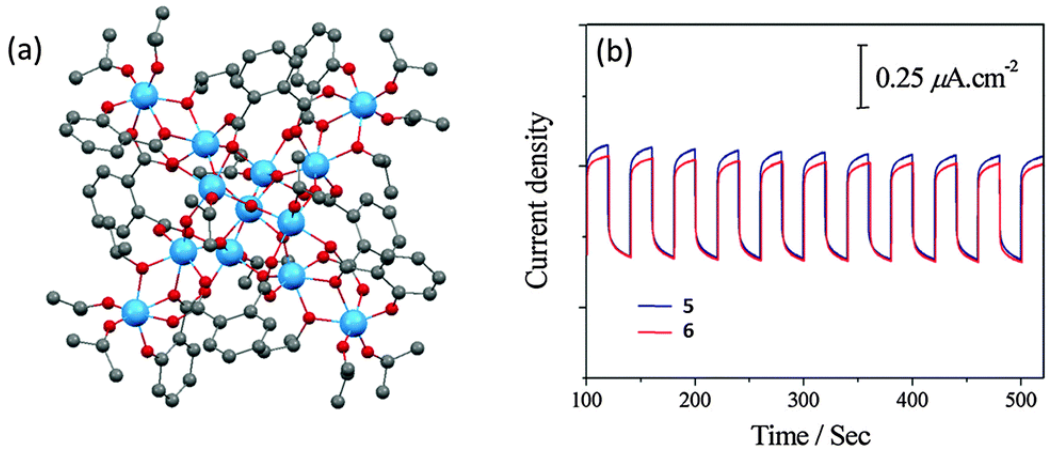

Figure 12. (a) **POT** molecular structure of $[Ti_{13}O_{10}(o\text{-}BDC)_4(SAL)_4(O^iPr)_{16}]$, blue = Ti, red = O, grey = C, hydrogen atoms are omitted for clarity. 6 is isostructural with 5, except that the –OH ortho hydrogen atoms are substituted by chlorine in four out of the six salicylate ligands; (b) photocurrent responses of the films of 5 and 6 on ITO upon cycling the irradiation. (Adapted from Ref. 95)

IR spectra analysis verified that the structures of **POTs** are retained on the electrode

substrate, and a significant photocurrent was observed, confirming the photo-response of these **POTs** (**Figure 12b**). Both **POTs** show band gaps of ca. 2.5 eV that have been extended significantly into the visible region, although the utilized ligands themselves are transparent to visible light. Unfortunately, due to the non-conducting nature of the organic components, the magnitude of the photocurrent in both **POTs** is relatively small and the shape of the photocurrent plot is not an ideal square wave. A similar photocurrent response has been observed in 9-anthracenecarboxylic acid and catechol modified POTs, too [69]. Owing to the catechol HOMO energy level mixing with Ti_xO_y core of **POTs**, the colour of $[Ti_6O_4(O^iPr)_6(cat)_4(9\text{-}AC)_2]$ are deep red with a band gap of ca. 2.05 eV, but the photocurrent is far lower than that of yellow **POT** of $[Ti_6O_6(O^iPr)_6(9\text{-}AC)_6]$, which only has 9-AC as functional ligands and exhibits a band gap of ca. 2.72 eV. These phenomena emphasis that efficient light absorption does not always lead to a good photoelectrochemical response. Metal complexes containing 1,10-phenanthroline (**Phen**), which give rise to low band-gap materials or low **HOMO–LUMO** gap molecular complexes, are one of the most important families of photosensitive dyes. So far, **POTs** containing Phen as functional ligands are still rare. Dai's group reported two Phen-modified **POTs** $[Ti_{17}O_{28}(O^iPr)_{16}(CoPhen)_2]$ and $[Ti_{17}O_{28}(O^iPr)_{16}(HO^iPr)_2(CdPhen)_2]$ [96]. Coppens' group reported an Fe analogue, $[Ti_{17}O_{28}(O^iPr)_{16}(FePhen)_2]$ [97]. In 2015, Wright's group reported Phen-modified Mn doped **POT** of $[Ti_{18}MnO_{30}(OEt)_{20}(MnPhen)_3]$ [98], which exhibits different structural features. In this **POT**, the three Phen ligands are coordinated to the three Mn(II) centres to give a core structure with approximate C_{3v} symmetry, but the fourth Mn(II) ion is tetra-coordinated by four oxo-O atoms and embedded in the core of **POT**. In these Phen modified **POTs**, it is difficult to investigate the physical effect of Phen coordination on Ti_xO_y cores due to the lack of direct bonding between Phen and Ti atoms. The photocurrent from these Phen modified **POTs** is transition-metal specific.

Significant photocurrent can be observed in the Co- and Fe-doped **POTs**, but only much weaker photocurrent can be observed in the related Cd-doped POT, and completely no photocurrent can be observed in the Mn-doped **POT**. Raman, IR and EDX data of the hydrolytic deposited films of **POT** on an ITO substrate in the presence of ambient air show that this is [CoPhen]-decorated titania. The larger photocurrent of Co- and Fe-doped **POTs** compared with Cd- and Mn- doped **POT** is probably because of the greater redox activity of the transition metal ions. For example, $[Co(Phen)_3]^{3+/2+}$ cations are a widely recognized photosensitizer with the reversible photoelectrochemical redox couple Co^{3+}/Co^{2+}, the excited [Co(Phen)] fragment in Co-doped **POT** could transfer electrons to the conduction band of the Ti_xO_y core of **POT** under irradiation [99]. Another important aspect of these **POTs** based materials is their morphologies. Generally, hollow-structured TiO_2 with a high surface area, low density and high loading capacity can be used to improve the photon-to-energy conversion efficiency in solar cells and water splitting. The fabrication of hollow nano-structured materials, such as hollow spheres without using a template or surfactant, is still a challenge, owing to the insolubility of titania and fast hydrolysis of titanate alkoxides or salts. As shown in **Figure 13**, self-assembled microspheres or doughnut-like structures can be obtained easily by solution deposition using the **POTs** as a precursor [96]. Possible mechanism of formation may be that the deposited **POT** molecules quickly self-aggregates upon evaporation of the solvent to form solvated spheres. The size of spheres is dependent on the solution concentration and evaporation rate. Shell of titania forms on the surface of the solvated spheres as a result of atmospheric moisture. Hollow spheres emerge with continuous hydrolysis and release of the inner solvent.

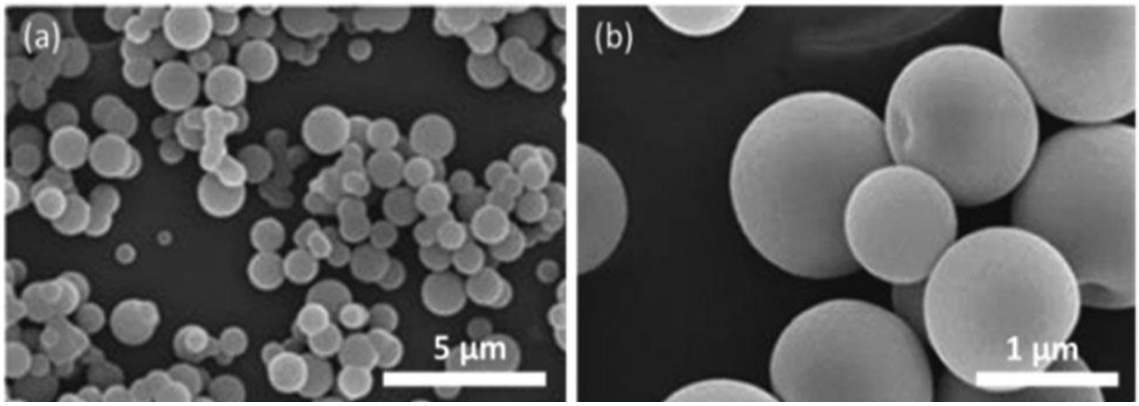

Figure 13. SEM images of the deposited films from: (a) and (b) $[Ti_{17}O_{28}(O^iPr)_{16}(CoPhen)_2]$ (Adapted from Ref. 96)

POTs have been investigated in photocatalytic hydrogen evolution and organic pollutant photodegradation. Zhao's group synthesized three carboxylate-modified hexanuclear **POTs** of the type $[Ti_6O_4(OR)_8(OOCR')_8]$ containing isostructural Ti_6O_4 cores [100]. Suspensions consisting of these **POTs,** water and methanol produced gaseous hydrogen under UV irradiation. Identical XRD patterns before and after reaction confirm that the **POT**'s structure is stable in aqueous conditions, which imply that the photocatalytic activity originates from the **POTs** rather than any of potential hydrolysis products. In 2012, Dai's group reported photodegradation of organic pollutants by **POTs** using white light irradiation in the presence of a UV filter (> 420 nm) in an aqueous dispersion of microcrystals of $[Ti_6O_3(o\text{-}BDC)_2(O^iPr)_{14}]$. In their study, more than 90% decay of methyl orange was observed after irradiation for 100 minute [101].

Photochromic behaviour has been also observed in several **POTs**. As shown in **Figure 14**, under UV-Vis irradiation, the colourless transparent crystals of $[Ti_6O_4(o\text{-}BDC)_2(o\text{-}BDC\text{-}^iPr)_2(O^iPr)_{10}]$ became purple-grey [100]. This colour change was attributed to the formation of photo-induced Ti (III) ions, which was comfirmed by ESR spectroscopy. Single crystal X-ray diffraction result exhibits that no structural change was detected after irradiation, which indicated that the photochemical reaction

only occurs on the surface of **POT**. Back-oxidation of Ti(III) ions to Ti (IV) can be achieved easily by exposing the coloured crystals to oxygen gas. Although it is still elusive about the detailed reaction behind this photochromic behaviour, but it seems that the overall **POT** structure is crucial since other **POTs** (e.g. a **POT** frame work $[Ti_8O_8(OH)_4(1,4\text{-BDC})_6]$) rarely show photochromism under identical conditions [102]. This photochromic phenomenon not only can be used for the rational design of optical devices, but is also underpins photocatalytic activities (such as the ability to oxidize alcohols to aldehydes) for **POT** based materials.

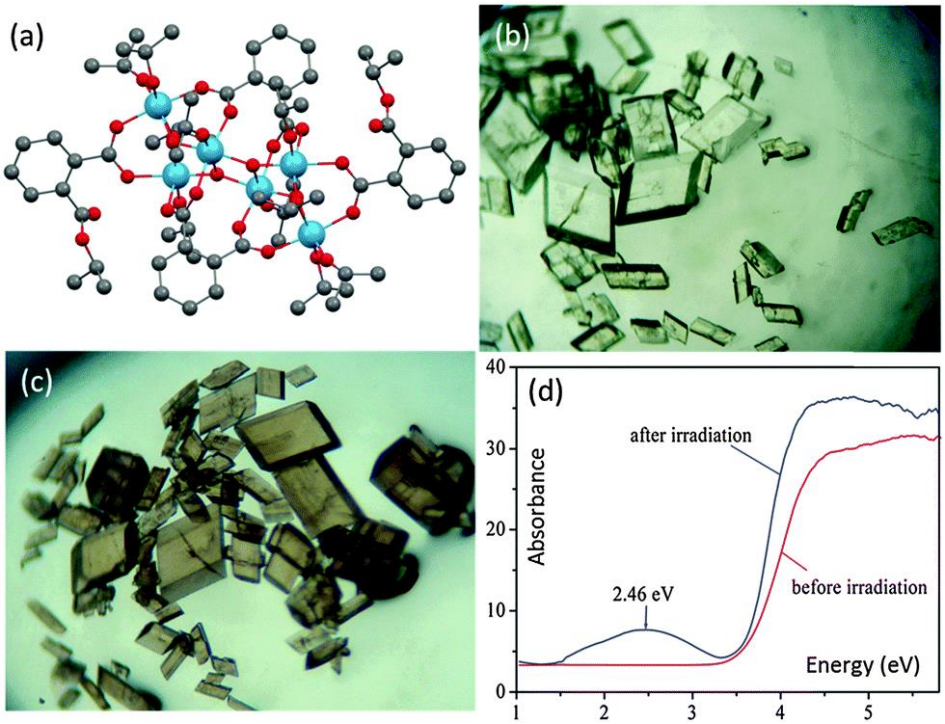

Figure 14. (a) Solid-state structure of $[Ti_6O_4(o\text{-BDC})_2(o\text{-BDC-}^iPr)_2(O^iPr)_{10}]$, blue = Ti, red = O, grey = C, hydrogen atoms are omitted for clarity; optical microscope images of crystalline blocks of $[Ti_6O_4(o\text{-BDC})_2(o\text{-BDC-}^iPr)_2(O^iPr)_{10}]$ before (b) and after (c) irradiation; (d) UV-Vis spectra of an analogous photochromic L-POT $[Ti_6O_3(o\text{-BDC})_2(O^iPr)_{14}]$ before and after irradiation. (Adapted from Ref. 100)

Many **POT** based materials have photoluminescence phenomenon. Photoluminescence of **POTs** mainly arises from the peripheral functional ligands rather than the Ti_xO_y core. Besides, some lanthanide doped **POTs** also have

photoluminescence [103].

Catalysts based on **POTs** have been applied to a number of enantioselective carbon–carbon bond-forming reactions (e.g. oxidation of thilanisole, carbonyl–ene reactions, cyanosilylation of aldehydes, nitro-aldol reactions, asymmetric allylation of aldehydes/ketones and asymmetric sulphide oxidation as well as Diels–Alder cycloaddition), especially those **POTs** coordinated with 1,1'-bi-2-naphthol (BINOL) and their derivatives [104,105]. Even though catalytically-active species may present in a small amount, the **Ti–BINOL** catalysed reactions could undergo a ligand-accelerated catalysis process which involves *in situ* selection of the active species from thermodynamically accessible complexes [106]. Thus, it is hard to identify and isolate the actual catalytically-active species, structural information on the real catalysts in this area is very lacking so far. For instance, as a well-known mononuclear complex, [Ti(BINOLato)(O^iPr)$_2$] is can be the pre-catalyst for many reactions, but [Ti(BINOLato)(O^iPr)$_2$] itself is not the active species [107]. Compared to the large amount of reports investigating the catalytic performance of Ti–BINOL catalysts, there are only a few reports involving structurally-characterised of these catalysts [108-113]. As shown in **Figure 15**, the tetranuclear **POTs** [Ti$_4$(μ_3-OH)$_4$(μ-R-BINOLato)$_6$] and [Ti$_4$(μ_3-OH)$_4$(μ-S-BINOLato)$_6$] are of particular interest (**Figure 15a**) among the catalysts with known structures. Because they are extremely stable, even in strongly acidic or basic conditions under reflux. All six BINOLato ligands within [Ti$_4$(μ_3-OH)$_4$(μ-R-BINOLato)$_6$] and [Ti$_4$(μ_3-OH)$_4$(μ-S-BINOLato)$_6$] have the same stereochemistry, either R or S, bonding with the distorted cubic core of **POTs** via Ti–O bonds. Mahrwald and and Schetter have found that the **POT** of [Ti$_4$(μ_3-OH)$_4$(μ-S-BINOLato)$_6$] is an effective catalyst in the catalysis of aldol addition at the more steric α-encumbered side of unsymmetrical ketones with high regioselectivity [110]. Only loading of 0.2 mol% catalyst are enough to afford complete conversion

without forming a significant amount of byproducts. Furthermore, the **POTs** of $[Ti_4(\mu_3\text{-}OH)_4(7,7'\text{-di-R-(R)-BINOLato})_6]$ have been found to catalyse {2+3} cycloaddition reactions, introduction of the sterical substituent leading to an increase in enantioselectivity for the exo-product [113].

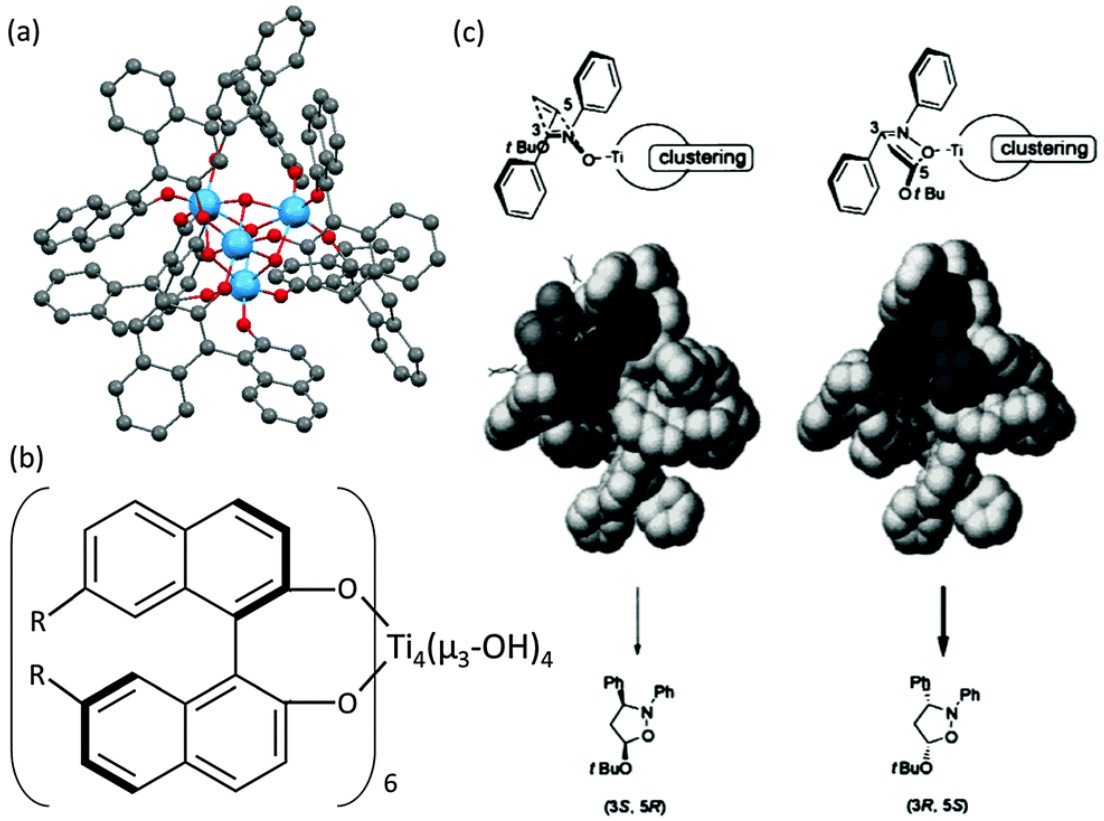

Figure 15. (a) Molecular structure of the tetranuclear $[Ti_4(\mu_3\text{-}OH)_4(R\text{-BINOLato})_6]$, the *S*-BINOL enantiomer structure has a similar configuration (not shown); (b) molecular representation of 7,7′-substituted $[Ti_4(\mu_3\text{-}OH)_4(7,7'\text{-di-}R\text{-BINOLato})_6]$ cage; (c) illustration of the steric reason for the favorable production of (3*R*,5*S*) over (3*S*,5*R*) products. (Adapted from Ref. 110)

There is no intermolecular covalent or coordination bonds in **POTs**' crystalline blocks which would form extended network structures like **MOFs**. **POTs** possess clear advantages as potential gas adsorbents over many other materials. Firstly, unlike most **MOFs**, **POTs** do not lose sorption properties upon amorphization, therefore **POTs** can be utilized under a wide range of conditions, Secondly, **POTs** are soluble and

therefore can readily be modified or processed into other forms using solid or solution techniques, Thirdly, the facile synthesis and vast structural diversity of **POTs** are nearly comparable to those of **MOFs** [114]. It has been reported that several **POTs** are good candidates for gas adsorping [115, 116a].

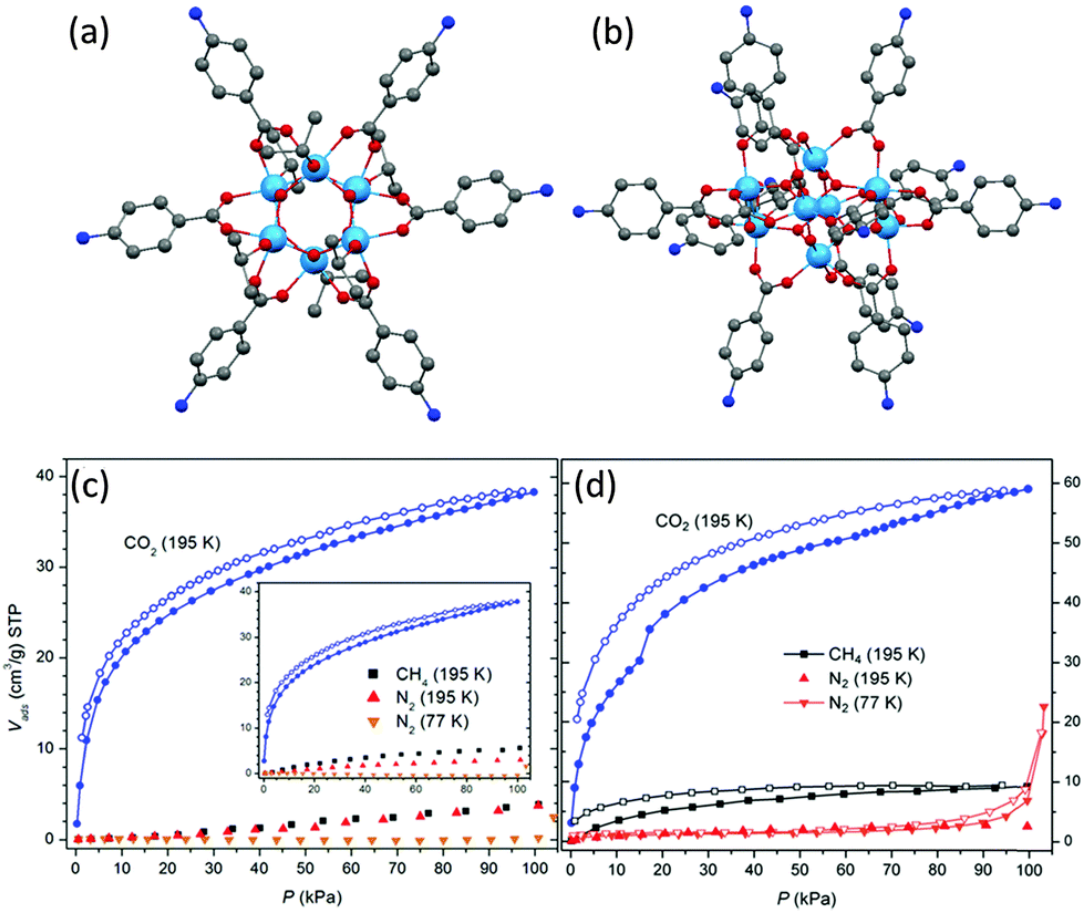

Figure 16. POTs' structures of (a) $[Ti_6O_6(abz)_6(O^iPr)_6]$ and (b) $[Ti_8O_{10}(abz)_{12}]$ (abz = aminobenzoate), blue = Ti, red = O, blue = N, grey = C, hydrogen atoms are omitted for clarity. Gas-sorption isotherms measured for compound (c) $[Ti_6O_6(abz)_6(O^iPr)_6]$ and (d) $[Ti_8O_{10}(abz)_{12}]$; inset of (c) is the isotherms of $[Ti_6O_6(abz)_6(O^iPr)_6]$ with complete crystalline disruption; filled and open symbols denote adsorption and desorption, respectively. (Adapted from Ref. 116)

As shown in **Figure 16**, it is demonstrated that neither $[Ti_6O_6(abz)_6(O^iPr)_6]$ (abz = aminobenzoate) nor $[Ti_8O_{10}(abz)_{12}]$ has any N_2 or CH_4 adsorption properties, interestingly these two **POTs** exhibit significant uptake of CO_2 at 195 K, which is

possibly due to the small kinetic diameter of CO_2 (*c*a 3.3 Å). Besides the polar nature of the C=O bond facilitates interaction with the polar regions of the solids. After complete amorphitization of the crystallinity of $[Ti_6O_6(abz)_6(O^iPr)_6]$, the CO_2 adsorption capability of this **POT** is still retained. The phenomenon shows that it is irrelevant whether the sample of **POT** is crystalline or not and the selective and reversible adsorption of gaseous CO_2 by **POT** molecule.

1.7 Hybrid materials based on Conjugated polymer (CPs) and POMs

CPs are organic macromolecules which can be characterized by a backbone chain of alternating single- and double- bonds. The overlapping p-orbitals of **CPs** usually create a system of delocalised π-electrons, resulting in useful optical and electronic properties.

CPs have attracted widespread attention for a variety of applications in organic electronic devices such as electrochromic devices, photovoltaic cells, organic light-emitting diodes, organic field effect transistors, chemical sensors, batteries and supercapacitors and so on. Nevertheless, the relatively poor stability of **CPs** is still a major obstacle to their applications.

The development of **POM**s grafted **CPs** materials, in which **POMs** are firmly anchored to the **CPs** matrix through covalent bonds, are expected to fundamentally solve the uneven dispersion of the components faced by composite materials and these hybrid matrials usually have better stability and exhibit excellent characteristics. Peng's Group [116b] copolymerized the modified hexanuclear molybdenum oxide cluster with thiophene monomers to synthesize a polymer containing molybdenum oxide cluster $[Mo_6O_{17}(NArI)_2]$ with high photoelectric conversion efficiency. Abe's group [116c] modified the thiophene derivative 4-(2,2'-dithiophene) pyridine on the surface of the trinuclear ruthenium oxygen cluster, and prepared the ruthenium-containing

electrochromic polymer film. However, the synthesis method of this type of main chain block polymer material is more complicated, and because the conjugated main chain is interrupted by polymetallic oxygen clusters, the conduction of electrons is affected. In the case of the **POTs**, it can be employed as 'nano-blocks' for the formation of new organic-inorganic hybrid materials with **CPs.**

In summary, thanks to the development of synthetic methods in the past two decades, a large amount of **POTs** with various nuclearities and diverse structural types have been obtained and classified. It has been reported that the **POTs** and M doped **POTs** could be used as single-source precursors for **TiO_2** and **M@TiO_2** deposition. While the functional ligands modified **POTs** exhibit more diverse properties which are either from the functional ligands themselves or synergistically as a result of the combination of the properties of the functional ligand with the Ti_xO_y core of **POTs**. Hence the applications of **POTs** (especially ligands modified **POTs**) span the areas of supramolecular chemistry, photocatalysis, photochromism, photoluminescence, asymmetric catalysis and gas adsorption. **POTs** and materials based on **POTs** have exceptional future promise in a number of technological fields.

Chapter 2

Synthesis and Structures of POTs

2.1 Introduction

POTs containing well-defined ratios of Ti atoms to the dopant metals or organic ligands are very interesting since these **POTs** are potential single source precursors to useful materials such as metal-doped TiO_2 with structurally well-defined models for metal-mediated photocatalysis. In this chapter, experimental details for the synthesis of several new **POTs** are summarized. The structure of these **POTs** are determined by single crystal X-ray diffraction, which are also presented.

2.2 Results and Discussion

2.2.1 Chemicals and Instrumentation

All chemicals used in this work were commercially available and used as received without further purification, unless specified. The growth process for the synthesis of **POT-6**, **POT-7**, **POT-8**, **POT-9**, **POT-10**, **POT-11** is using solvothermal method. Solvothermal synthesis is a commonly used method for preparation of different types of materials based on solution reaction-based approach. Compared to other synthesis method for **POTs**, there are obvious advantages such as the compositions of synthesized **POTs** can be well controlled, the simplicity and easy variation of process parameters. In general, solvothermal method involves crystallizing a substance at a high temperature and high vapor pressure using an organic solution. The processes of solvothermal reactions are carried out in autoclaves under controlled temperature and pressure, which allows the temperature of reactions above the boiling point of organic solution. As shown in **Figure 17**, autoclaves for solvothermal reactions are hermitically sealed steel vessels with Teflon inner cylinder which could withstand high temperatures and

pressures for long durations. The chemically inert cylinder must not take part in the solvothermal process.

Crystal data were collected on a Bruker D8 VENTURE diffractometer using Mo(Kα) radiation (λ = 0.71073 Å). The structures were solved by Direct Methods and refined by full-matrix least squares on F^2 [117]. Infrared (**IR**) spectra were adopted using a Nicolet 6700 spectrometer (Thermo Fisher Nicolet, USA) with KBr pellets. Powder X-ray diffraction (**pXRD**) experiments were performed using a X'Pert Pro diffractometer with Cu-Kα radiation (λ= 1.5418Å) operating at 40 kV and 40 mA and the scanning angle ranged from 5° to 50° of 2θ. Proton (^{1}H) nuclear magnetic resonance (**NMR**) spectra were measured in chloroform-d ($CDCl_3$) using Bruker AVANCE III 500 MHz spectrometers. ESI-MS was carried out on ThermoFisher LCQ^{TM} Deca XP plus. UV-vis spectra were obtained using a UV-1800 spectrophotometer (SHIMADZU), and visible and NIR transmission spectra was performed in 0.1 mol/L $TBAPF_6$/DCM solution. Thermogravimetric (**TG**) analyses were performed on a Mettler Toledo TGA/DSC 1 under nitrogen atmosphere.

The crystals of **POT-1**, **POT-2**, and **POT-3** was firstly obtained by one of my author coworkers: Dr. Gang Liu in Prof. Cheng Zhang's Lab of Zhejiang University of Technology; the crystals of **POT-4** was firstly obtained by my anthor coworkers: Mr. Xing Yang in Prof. Cheng Zhang's Lab of Zhejiang University of Technology; **POT-5, POT-6**, **POT-7**, **POT-8**, **POT-9**, **POT-10**, **POT-11** were strucutally determined in Univeristy of Cambridge with the help of Prof. Dominic S. Wright.

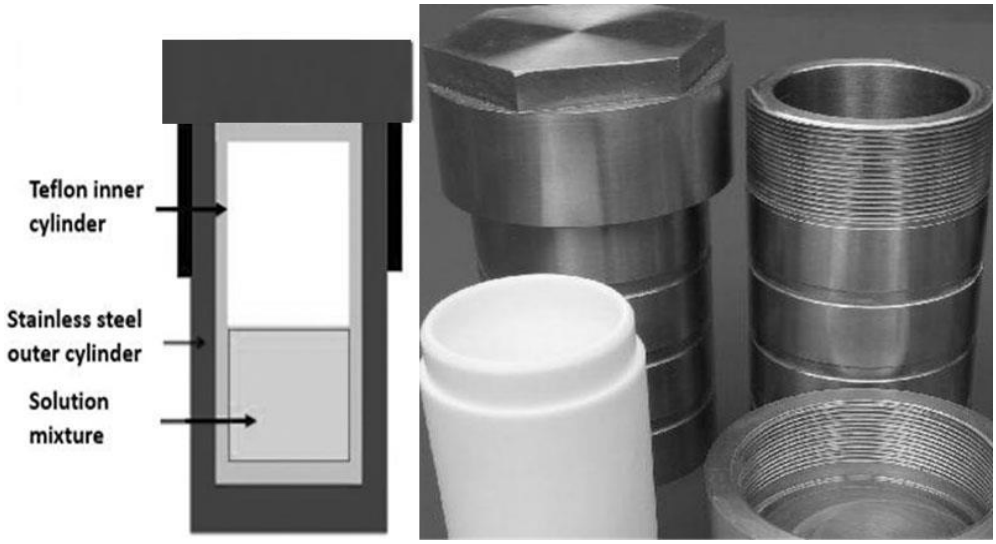

Figure 17. A schematic description and a photographic view of the autoclave used in the present study for solvothermal synthesis for POTs.

2.2.2 Synthesis and Characterisation of $[Ti_6O_6(O^iPr)_6(TA)_6]$ (POT-1).

Titanium isopropoxide (1 ml, 4.8 mmol), Thiophene-3-acetic acid (**TAH**) (0.5g, 3.45mmol) and isopropyl alcohol (4.5ml) were mixed in a glass bottle and heated at 60^{o}C for 5 days. Some transparent strip crystals of $Ti_6O_6(O^iPr)_6(TA)_6$ (**POT-1**), yield 0.25g (29 % with respect to Ti supplied), was obtained. **IR** (800-4000 cm^{-1}), ν/ cm^{-1} = 716.4(vs), 831.3(m), 854.2(m), 1159.0(s), 1112.4(vs), 1160.3(m), 1243.3(m), 1283.2(m), 1293.5(m), 1332.4(m), 1361.9(w), 1378.3(vs), 1395.7(vs), 1436.8(vs), 1461.3(s), 1545.2(vs), 1602.4(s), 2618.1(vw), 2869.8(m), 2931.2(m), 2970.7 (s), 3106.1(m).

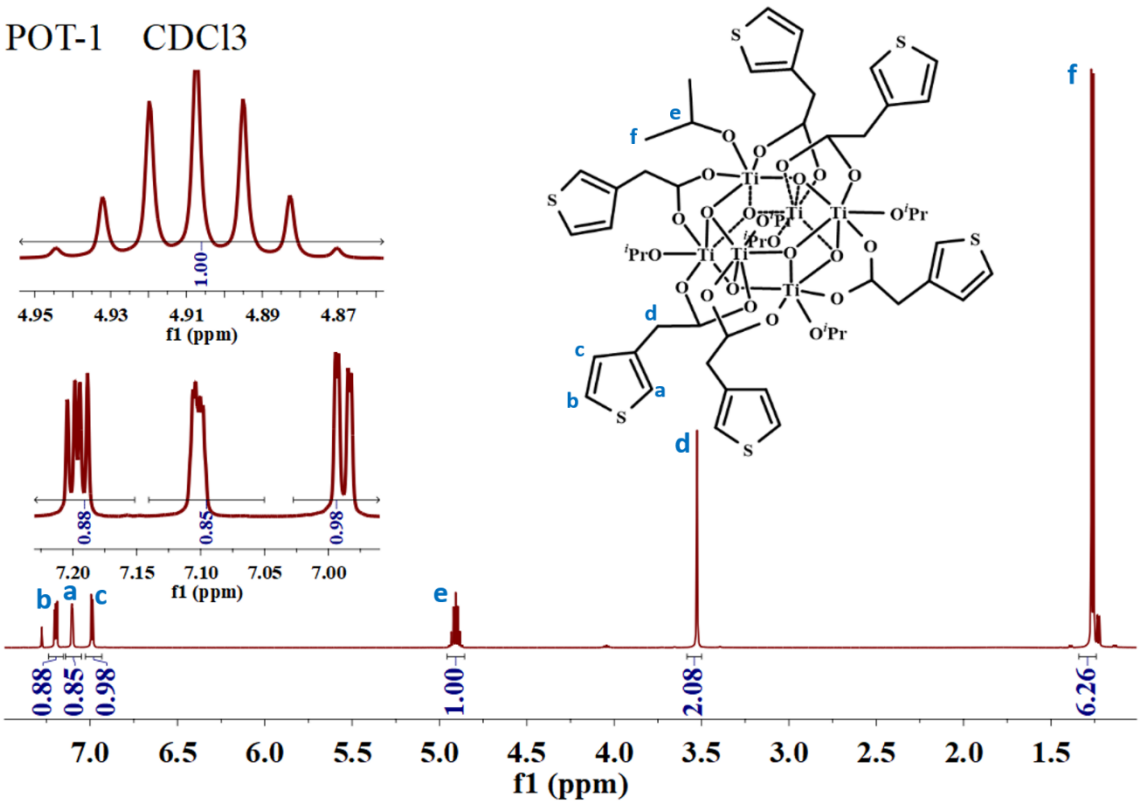

Figure 18. The ^{1}H NMR of **POT-1** in $CDCl_3$.

Crystals of **POT-1** are stable in air and soluble in various organic solvents like toluene, tetrahydrofuran, chloroform and dichloromethane (**DCM**). As shown in **Figure 18**, the room-temperature ^{1}H NMR spectrum of **POT-1** in $CDCl_3$ shows that the ratio of the **TA** to ^{i}PrO ligands in **POT-1** is 1:1, the same as in the solid-state structure. The fact that the ^{1}H NMR spectrum of **POT-1** does not change with concentration suggests that the structure remains the same in $CDCl_3$ as in the solid state. The high-resolution +ve ion electrospray mass spectrum (**Figure 19**) shows a signal at m/z = 1584.972 for $[M+H]^+$ (calc. 1584.973), with the correct isotopic distribution pattern, together with peaks for $[M+Na]^+$ and $[M+K]^+$. As shown in **Figure 20**, the bulk purity of crystalline **POT-1** is confirmed by the powder X-ray diffraction (**pXRD**) spectrum which is identical to the pattern derived from its **sXRD** data. TG and differential thermal analysis (DTA) show that **POT-1** is not thermally decomposed at temperatures lower than 150^{o}C (**Figure 21a**). As shown in **Figure 21b**, comparable with reported **POT**

cages, the band gap determined from the solution-state UV visible spectrum of **POT-1** is ca. 3.79 eV. These above characterization work was mainly completed by my co-worker Dr. Liu Gang in 2018.

(a)

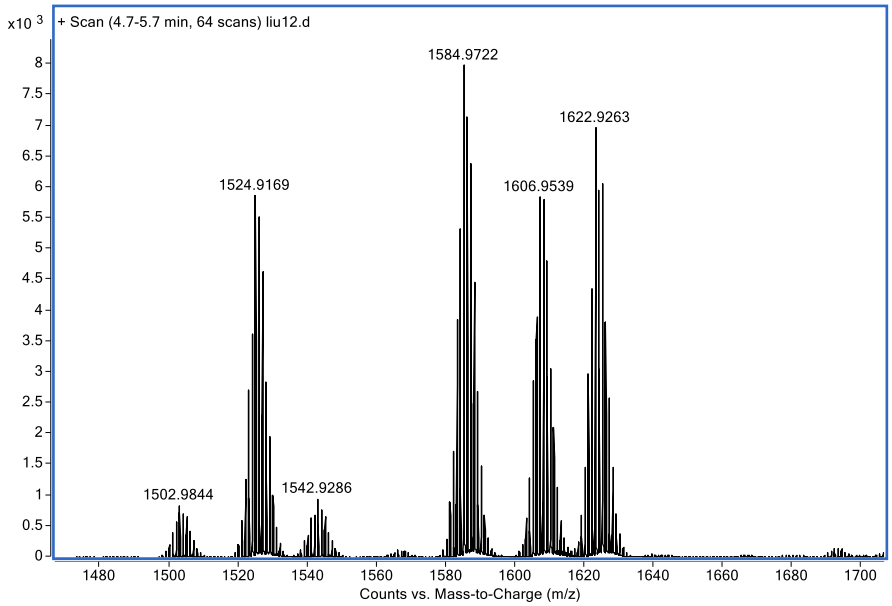

(b)

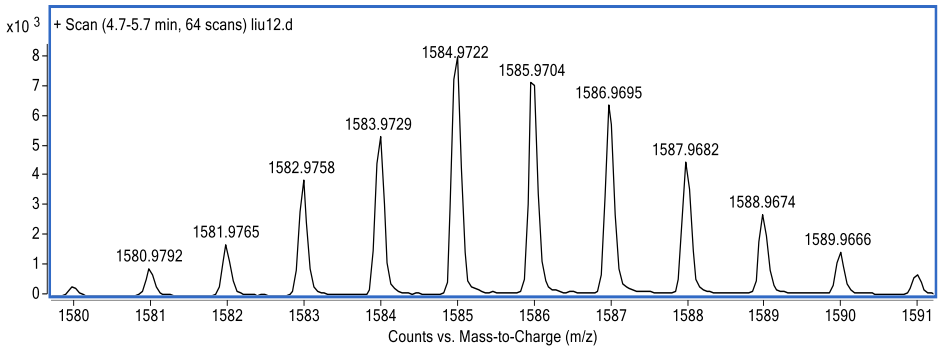

(c)

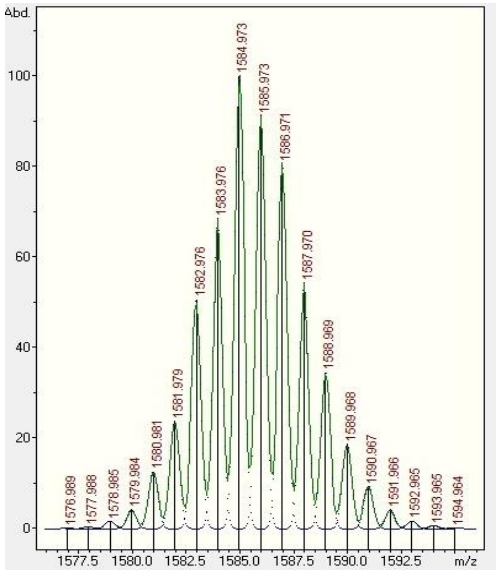

(d)

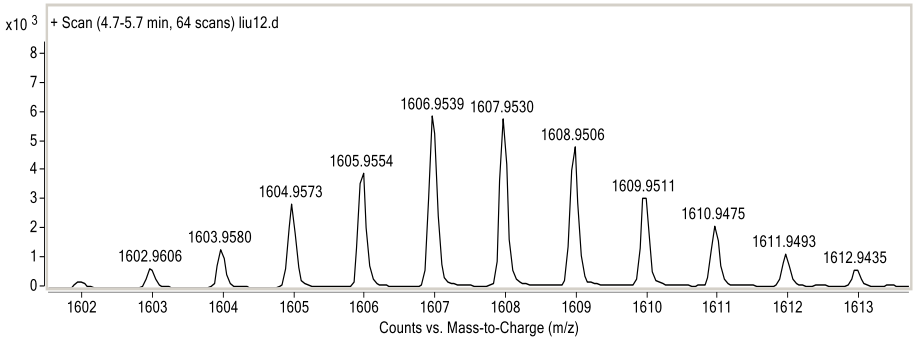

(e)

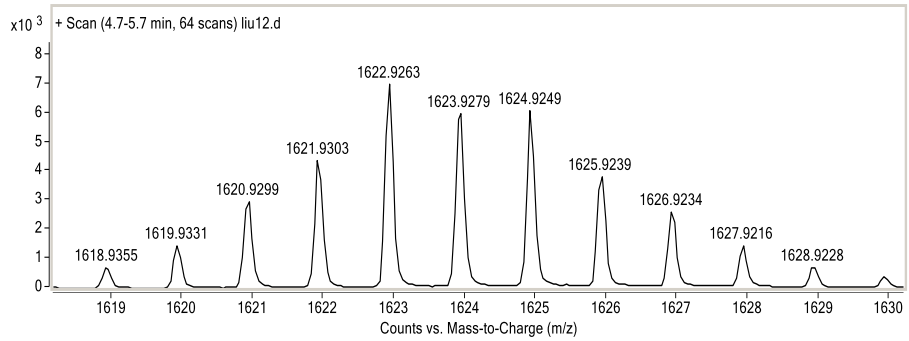

Figure 19. (a) ESI-MS spectrum of **POT-1** in $CDCl_3$ solution. The sample were dissolved and kept in $CDCl_3$ before MS analysis, which was diluted by ACN and immediately before injected into the MS instrument; (b) Zoomed image of the spectrum peaks around 1584.9; (c) Simulation of the pattern for $[M+H]^+$; (d) Zoomed image of the spectrum peaks around 1606.9 for $[M+Na]^+$; (e) Zoom of the spectrum peaks around 1622.9 for $[M+K]^+$.

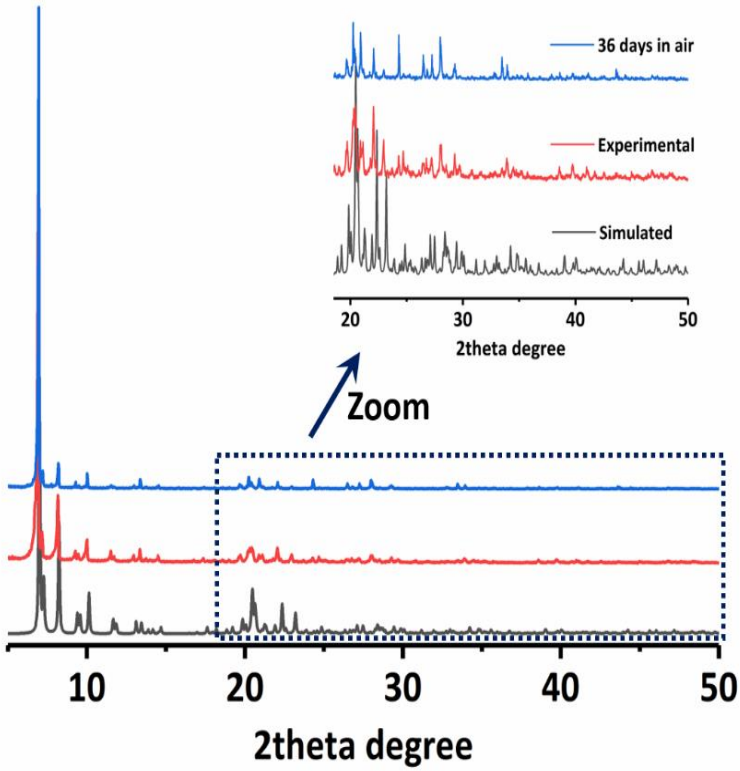

Figure 20. X-ray Powder Diffraction (pXRD) of **POT-1**.

(a)

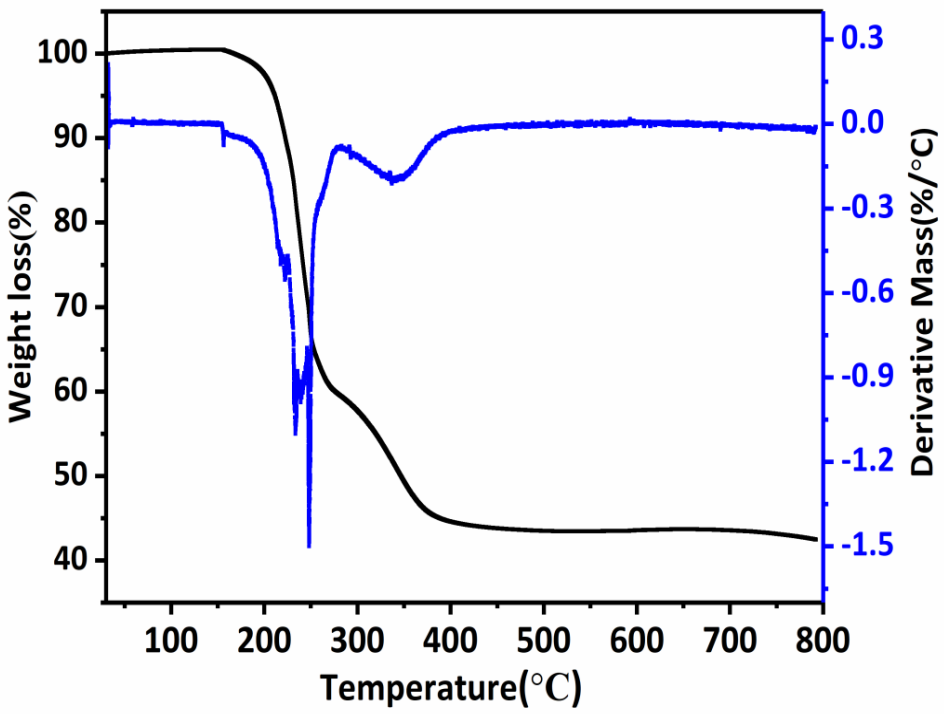

(b)

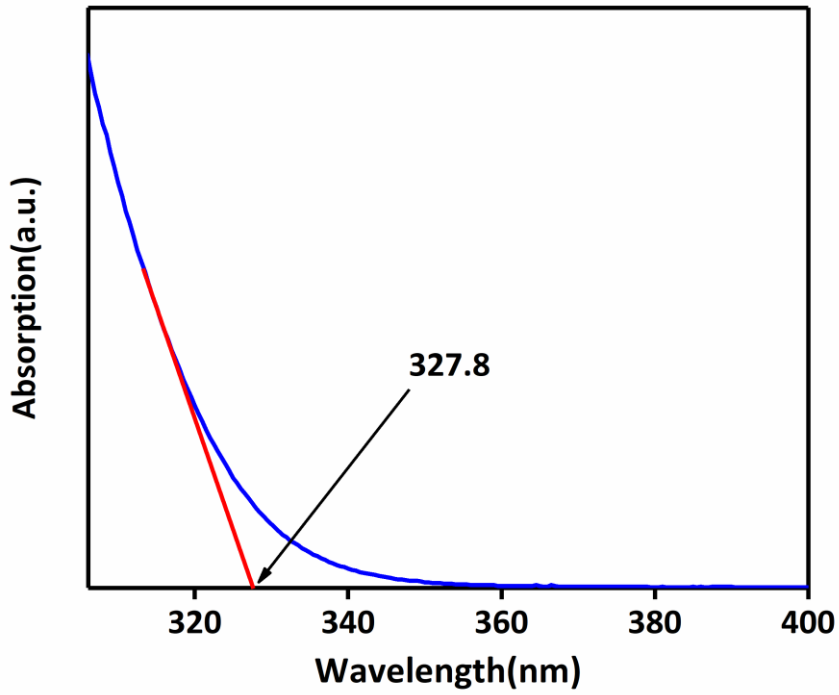

Figure 21. (a) The TGA (black) and DTA (blue) curve of **POT-1**, (b) The UV-vis spectrum of 0.01g/mL **POT-1** in CH_2Cl_2.

As shown in **Figure 22**, A single-crystal X-ray diffraction (**sXRD**) analysis shows that it has a hexameric 'stack' arrangement, containing a Ti_6O_6 core. Each of the chemically-equivalent Ti(IV) centres has a six-coordinate, octahedral geometry, being bonded to three μ_3-O oxo-atom within the core, two O atoms from two **TA** ligands (**TA** = thiophene-3-acetic acid) and one isopropoxide-O atom. The peripheral "thiophene tentacles" face outwards from the core. The **sXRD** data and refinement of **POT-1** are summarized and shown in **Table 1**. Selected bond lengths (Å) and angles (°) are shown in **Table S1**. **POT-1** is the first structurally determined **POT** cage in which the assembly is achieved exclusively by incorporation of polymerizable **TA** ligand into a Ti_xO_y core.

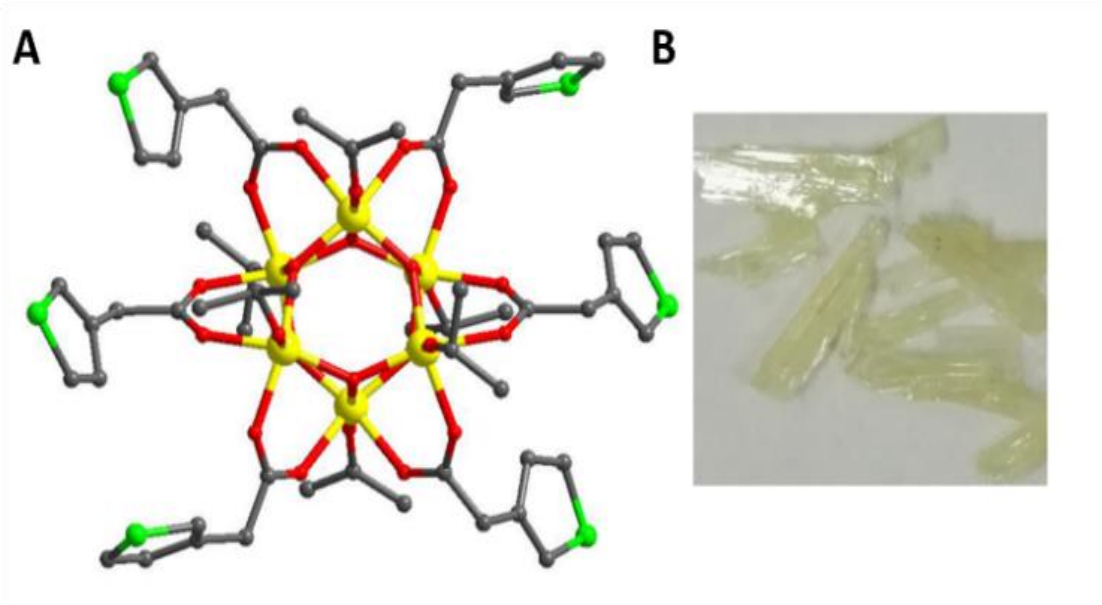

Figure 22. (A) Solid-state structure of **POT-1**, H-atoms have been omitted for clarity (red = O, gray = C, green = S, yellow = Ti); (B) Photographic image of crystals of **POT-1**.

Table 1. Details of the structure solution and refinement of **POT-1**

Compound	**POT-1**
Chemical formula	**$C_{54}H_{72}S_6O_{24}Ti_6$**
FW	1584.9
Crystal system	Triclinic
Space group	*P-1*
a (Å)	10.2226(7)
b (Å)	13.5319(9)
c (Å)	13.5794(9)
α(°)	105.493(2)
β (°)	99.264(2)
γ(°)	107.574(2)
V (Å^3)	1664.9(2)
Z	1
Calculated Density (Mg/m^3)	1.579
Absorption coefficient(mm^{-1})	0.949
reflections collected	35237
independent reflections (R_{int})	7666 (0.0202)
*R*1, *wR*2 [$I>2\sigma(I)$]	0.0331, 0.0811
*R*1, *wR*2 (all data)	0.0381, 0.0841

2.2.3 Synthesis and Characterisation of $[Ti_3O_5(O^iPr)_8(TC)_2]$ (POT-2).

Titanium isopropoxide (1 ml, 4.8 mmol), thiophene-3-carboxylic acid (**TCH**) (0.13 g, 1.0 mmol) and isopropyl alcohol (4.5ml) were mixed in a glass bottle and heated at 80^{o}C for 2 days, colorless crystals of $Ti_3O_5(O^iPr)_8(TC)_2$ (**POT-2**) were obtained by cooling to room temperature, yield 0.20g (21 % with respect to Ti supplied). The infrared spectrum of **POT-2** is shown in **Figure 23**.

As shown in **Figure 24**, **sXRD** analysis shows that **POT-2** contains a Ti_3O core. A Ti(IV) centre have a six-coordinate, octahedral geometry, being bonded to a μ_3-O oxo-atom within the core, two O atoms from two **TC** ligands (**TC** = thiophene-3-carboxilic acid) and three isopropoxide-O atoms, another six-coordinate Ti(IV) centre also displays octahedral geometry, being bonded to a μ_3-O oxo-atom within the core, a O atoms from one **TC** ligand and four isopropoxide-O atoms, the rest five-coordinate Ti(IV) centre displays triangular bipyramid geometry, being bonded to a μ_3-O oxo-atom within the core, a O atoms from one **TC** ligand and three isopropoxide-O atoms. The **sXRD** data and refinement of **POT-2** are summarized and shown in **Table 2**. Selected bond lengths (Å) and angles (^{o}) of **POT-2** are shown in **Table S2**.

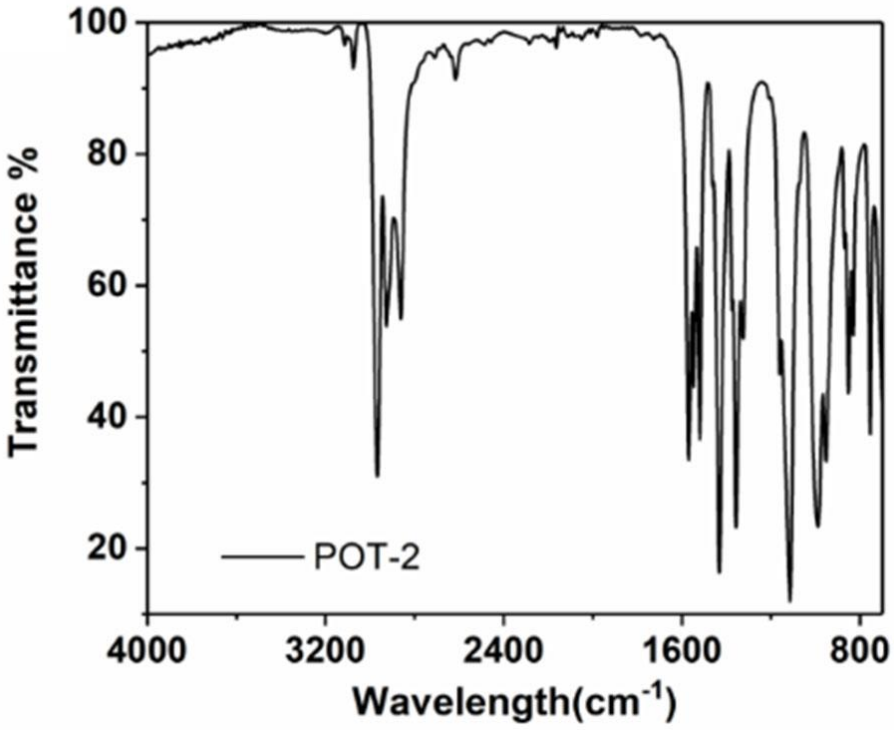

Figure 23. Infrared spectrum of monomer **POT-2.**

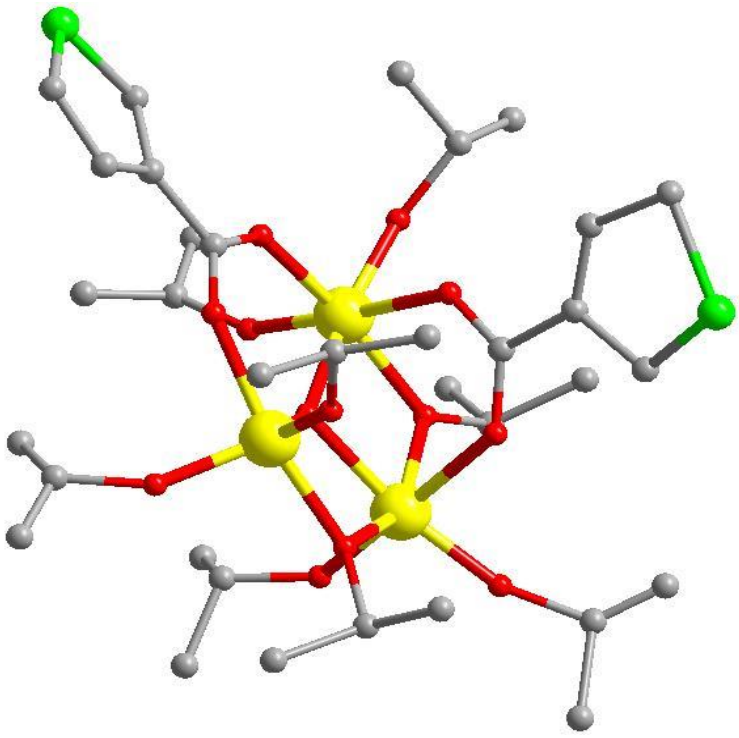

Figure 24. Solid-state structure of **POT-2**, H-atoms have been omitted for clarity (red = O, gray = C, green = S, yellow = Ti).

Table 2. Details of the structure solution and refinement of **POT-2**

Compound	**POT-2**
Chemical formula	$C_{34}H_{62}O_{13}S_2Ti_3$
FW	886.60
Crystal system	Monoclinic
Space group	$P2_1/n$
a (Å)	12.5531 (8)
b (Å)	17.3566 (9)
c (Å)	20.9572 (12)
β (°)	93.091 (2)
V (Å^3)	4559.5 (5)
Z	4
Calculated Density (mg/m^3)	1.283
Absorption coefficient(mm^{-1})	0.66
reflections collected	20826
independent reflections (R_{int})	4183 (0.060)
*R*1, *wR*2 [$I>2\sigma(I)$]	0.0911, 0.228
*R*1, *wR*2 (all data)	0.142, 0.254

2.2.4 Synthesis and Characterisation of $[Ti_3O_5(O^iPr)_8(PC)_2]$ (POT-3).

Titanium isopropoxide (1 ml, 4.8 mmol), Pyrrole-3-carboxylic acid (**PCH**) (0.12 g, 1.0 mmol) and isopropyl alcohol (4.5 ml) were mixed in a glass bottle and heated at 80^{o}C for 2 days, colorless crystals of $Ti_3O_5(O^iPr)_8(PC)_2$ (**POT-3**) were obtained by cooling to room temperature, yield 0.25g (30 % with respect to Ti supplied). The infrared spectrum of **POT-3** is shown in **Figure 25**.

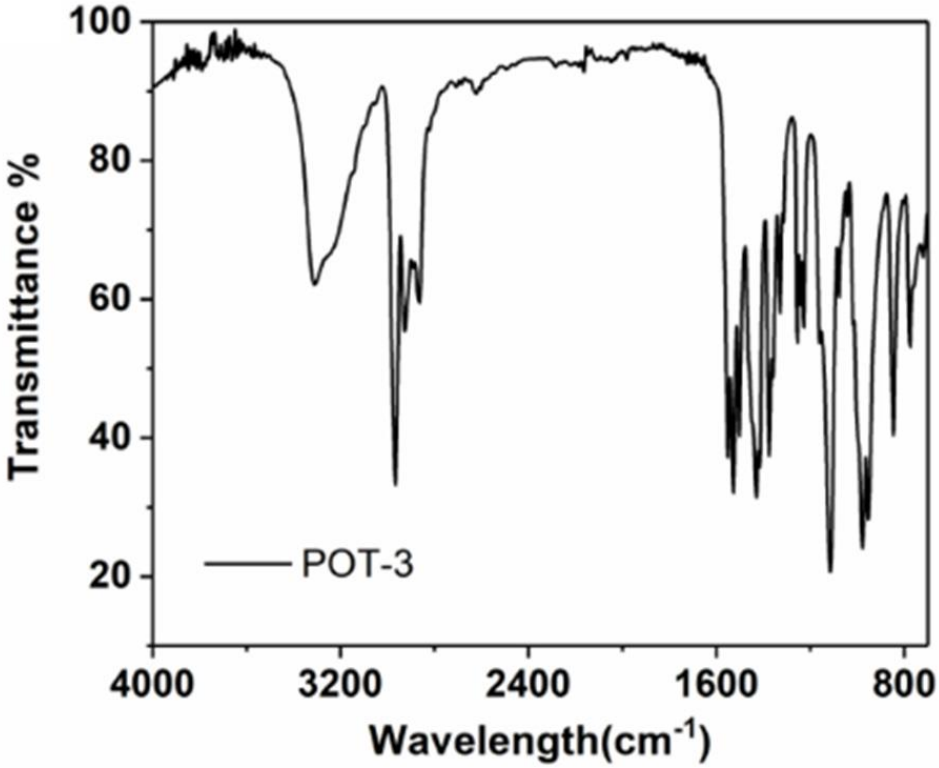

Figure 25. Infrared spectrum of monomer **POT-3**.

As shown in **Figure 26**, sXRD analysis shows that **POT-3** is the isostructure of **POT-2**, which also contains a Ti_3O core. A Ti(IV) centre have a six-coordinate, octahedral geometry, being bonded to a μ_3-O oxo-atom within the core, two O atoms from two **PC** ligands and three isopropoxide-O atoms, another six-coordinate Ti(IV) centre also displays octahedral geometry, being bonded to a μ_3-O oxo-atom within the core, a O atom from one **PC** ligand and four isopropoxide-O atoms, the rest five-coordinate Ti(IV) centre displays triangular bipyramid geometry, being bonded to a μ_3-O oxo-atom within the core, a O atom from one **PC** ligand and three isopropoxide-O atoms. The sXRD data and refinement of **POT-3** are summarized and shown in **Table 3**. Selected bond lengths (Å) and angles (°) of **POT-3** are shown in **Table S3**.

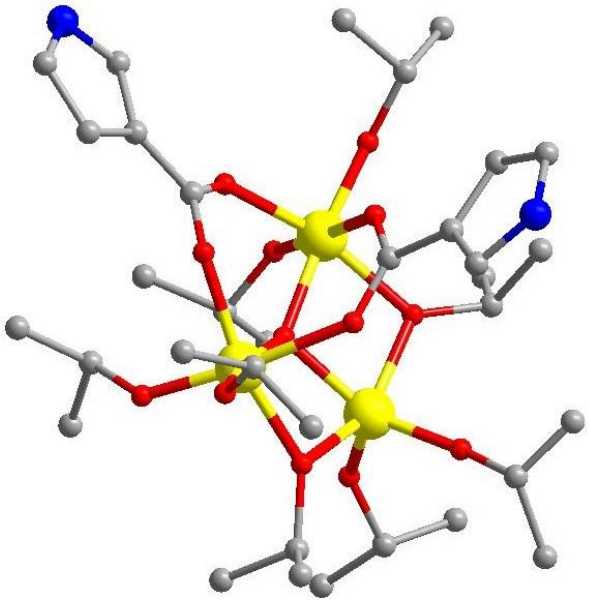

Figure 26. Solid-state structure of **POT-3**, H-atoms have been omitted for clarity (red = O, gray = C, blue = N, yellow = Ti).

Table 3. Details of the structure solution and refinement of **POT-3**.

Compound	**POT-3**
Chemical formula	$C_{34}H_{64}N_2O_{13}Ti_3$
FW	852.55
Crystal system	Monoclinic
Space group	$P2_1/n$
a (Å)	12.181 (2)
b (Å)	25.106 (5)
c (Å)	14.301 (3)
β (°)	91.95 (3)
V (Å^3)	4370.9 (15)
Z	4
Calculated Density (Mg/m^3)	1.293
Absorption coefficient(mm^{-1})	0.59
reflections collected	5010
independent reflections (R_{int})	6824 (0.047)
*R*1, *wR*2 [$I>2\sigma(I)$]	0.0453, 0.142
*R*1, *wR*2 (all data)	0.0626, 0.156

2.2.5 Synthesis and Characterisation of $[Ti_4O_6(O^iPr)_{10}(TC)_2]$ (POT-4).

Titanium isopropoxide (1 ml, 4.8 mmol), Thiophene-3-carboxylic acid (**TCH**) (0.13 g, 1.0 mmol), cobalt bromide hexahydrate 0.176 g (0.54 mmol) and anhydrous acetonitrile (6.0 ml) were mixed in a glass bottle and heated at 80°C for 3 days, colourless crystals of $Ti_4O_6(O^iPr)_{10}(TC)_2$ (**POT-4**) were obtained by cooling to room temperature, yield 0.23g (22 % with respect to Ti supplied). As shown in **Figure 27**, sXRD analysis shows that **POT-4** contains a Ti_4O_2 core with 4 Ti(IV) centers, a μ_4-O oxo-atom and a μ_2-O oxo-atom. Each Ti(IV) centre have a six-coordinate, octahedral geometry. The sXRD data and refinement of **POT-4** are summarized and shown in **Table 4**. Selected bond lengths (Å) and angles (°) of **POT-4** are shown in **Table S4**.

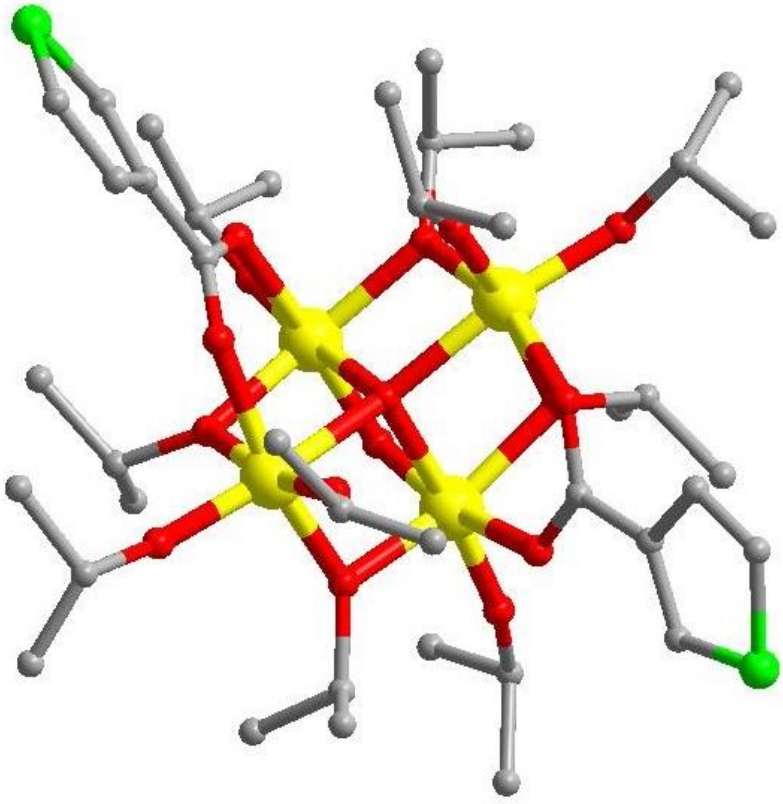

Figure 27. Solid-state structure of **POT-4**, H-atoms have been omitted for clarity (red = O, gray = C, green = S, yellow = Ti).

Table 4**.** Details of the structure solution and refinement of **POT-4**.

Compound	**POT-4**
Chemical formula	$C_{40}H_{76}O_{16}S_2Ti_4$
FW	1068.72
Crystal system	Orthorhombic
Space group	$P2_12_12_1$
a (Å)	12.424(4)
b (Å)	14.785(2)
c (Å)	28.947(2)
V (Å^3)	5317.3(7)
Z	4
Calculated Density (Mg/m^3)	1.335
Absorption coefficient(mm^{-1})	0.717
reflections collected	53508
independent reflections (R_{int})	12195 (0.0463)
*R*1, *wR*2 [$I>2\sigma(I)$]	0.0413,0.0723
*R*1, *wR*2 (all data)	0.0580,0.0777

2.2.6 Synthesis and Characterisation of $[Ti_2O(OAc)_2(HOAc)_2Cl_4]$ (POT-5).

10.0 ml Titanium tetrachloride (91.0 mmol), 20 ml glacial acetic acid (HOAc), 20.0ml dry toluene were mixed together and stirred under nitrogen at 35 °C for 30 minutes, cooling at 1°C per hour to room temperature gave colorless crystals of $[Ti_2O(OAc)_2(HOAc)_2Cl_4]$ (**POT-5**), yield 8.73g (39 % with respect to Ti supplied). IR data (KBr, cm^{-1}) for **POT-5**: 3270s, 2930w, 1636m, 1587m, 1503s, 1489s, 1313w, 1275m, 1147s, 1112s, 1089s, 941w, 825w, 754m, 698m, 626m, 525m.

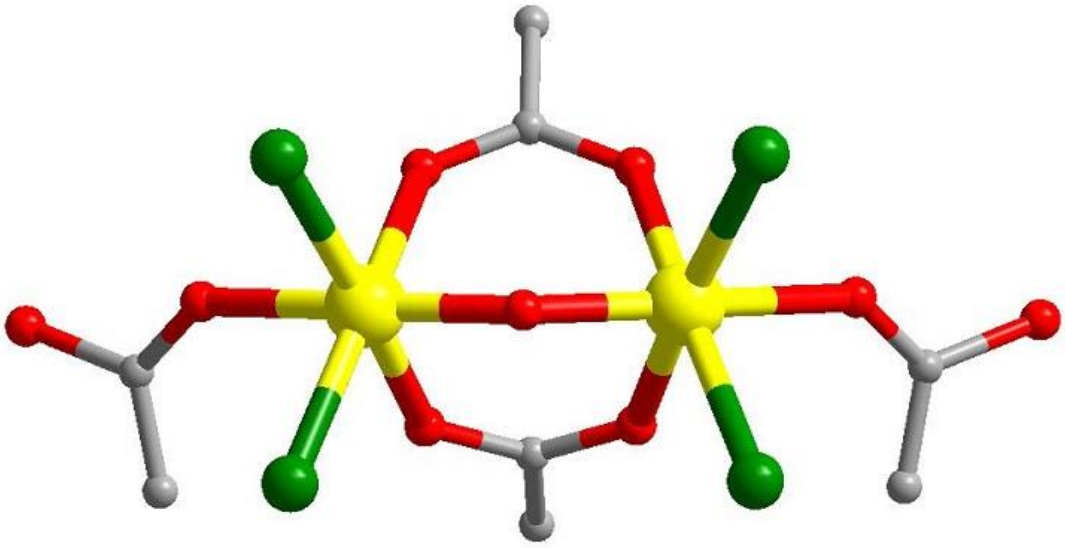

Figure 28. Solid-state structures of **POT-5**. H-atoms (which could not be located from X-ray data) have been omitted for clarity (red = O, gray = C, green = Cl, yellow = Ti).

As shown in **Figure 28**, sXRD analysis shows that **POT-5** contains a Ti_2O core, two Ti(IV) centers are associated by two bridging acetate ligands and a m-O atom. The six-coordinated octahedral geometry of each of the symmetry-related Ti(IV) centers is completed by two terminal chloride ligands and by bonding to the O-atom of an acetate ligand. Details of the structure solutions and refinements of **POT-5** are listed in **Table 5,** selected bond lengths (Å) and angles (º) of **POT-5** are shown in **Table S5**.

Because the cost of synthesizing large amounts of **POT-5** is relatively low, we further studied the preparation and application of a series of TiO_2@C materials through calcination of **POT-5**.

Table 5 Details of the structure solution and refinement of **POT-5**.

Compound	**POT-5**
Chemical formula	**$C_8H_{14}Cl_4O_9Ti_2$**
FW	491.79
Crystal system	Orthorhombic
Space group	*Pnma*
Unit cell dimensions	
a (Å)	12.6154(9)
b (Å)	18.5017(14)
c (Å)	7.6960(5)
V (Å^3)	1796.3(2)
Z	4
ρ_{calc} (Mg/m^3)	1.818
μ (Mo-Kα) (mm^{-1})	1.520
reflections collected	17798
independent reflections (R_{int})	1907 (0.0423)
*R*1, *wR*2 [$I>2\sigma(I)$]	0.0435, 0.1096
*R*1, *wR*2 (all data)	0.0492, 0.1132

2.2.7 Synthesis and Characterisation of [$Ti_2(OEt)_9InI_2$] (POT-6).

Titanium(IV) ethoxide (2.0 ml, 8.8 mmol), indium iodide anhydrous (0.495 g, 1 mmol) and absolute ethanol (5 ml) was placed in an autoclave under nitrogen and the mixture heated to 150 ºC for 3 days. Colourless crystals of [$Ti_2(OEt)_9InI_2$] (**POT-6**) were obtained by cooling to room temperature.

Structure solutions and refinements details of **POT-6** are listed in **Table 6,** selected bond lengths (Å) and angles (º) of **POT-6** are shown in **Table S6**. As shown in **Figure 29**, sXRD analysis shows that **POT-6** contains a Ti_2InO_5 core, each of Ti(IV) centre is bonded with four bridging ethoxide ligands and two terminal ethoxide ligands to form a six-coordinated octahedral geometry, the In(III) centre is connected with four bridging ethoxide ligands and two terminal iodide ligands and formed a six-coordinated

octahedral geometry, too.

Till now, we have only obtained a few amount of **POT-6**, so that more studies of **POT-6** haven't been done yet.

Table 6. Details of the structure solution and refinement of **POT-6**.

Compound	**POT-6**
Chemical formula	$\mathbf{C_{18}H_{45}I_2InO_9Ti_2}$
FW	869.96
Crystal system	Triclinic
Space group	*P-1*
a (Å)	10.661(5)
b (Å)	11.329(2)
c (Å)	15.041(3)
α (°)	94.671(6)
β (°)	96.478(6)
γ (°)	116.08(3)
V (Å^3)	1603.6(6)
Z	2
Calculated Density (Mg/m^3)	1.802
Absorption coefficient(mm^{-1})	3.16
reflections collected	12832
independent reflections (R_{int})	5094 (0.0470)
$R1$, $wR2$ [$I>2\sigma(I)$]	0.0980, 0.2462
$R1$, $wR2$ (all data)	0.1103, 0.2509

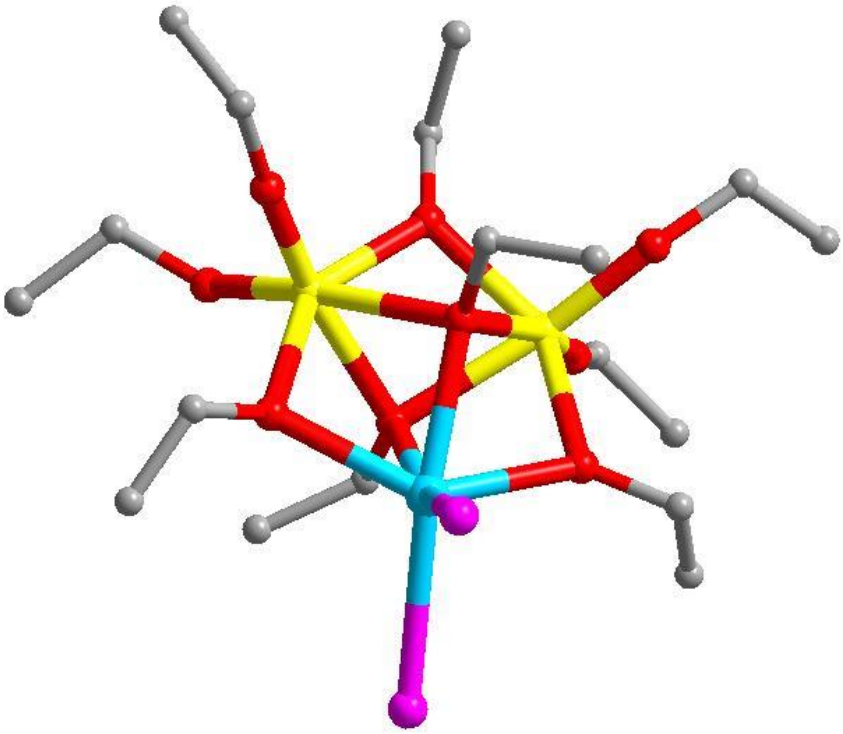

Figure 29. Solid-state structures of **POT-6**. H-atoms (which could not be located from X-ray data) have been omitted for clarity (red = O, gray = C, pink = I, blue = In, yellow = Ti).

2.2.8 Synthesis and Characterisation of [$Ti_3O(O^iPr)_9Cl$] (POT-7).

Titanium isopropoxide (2 ml, 9.54 mmol), tungsten(VI) chloride anhydrous (0.397 g, 1mmol) and isopropanol anhydrous (7 ml) was placed in an autoclave under nitrogen and the mixture heated to 150 ^oC for 3 days. Colourless crystals of [$Ti_3O(O^iPr)_9Cl$] (**POT-7**) were obtained by cooling to room temperature.

As shown in **Figure 30**, sXRD analysis shows that **POT-7** contains a Ti_3O_4Cl core, each of Ti(IV) centre is six-coordinated octahedral geometry, being bonded with a μ_3-O oxo-atom and a μ_3-Cl atom within the core, two bridging isopropoxide ligands and two terminal isopropoxide ligands. Interestingly, there is a μ_3-Cl atom in the core of **POT-7**, which is very rare. Structure solutions and refinements details of **POT-7** are listed in **Table 7,** selected bond lengths (Å) and angles (^{o}) of **POT-7** are shown in **Table S7**.

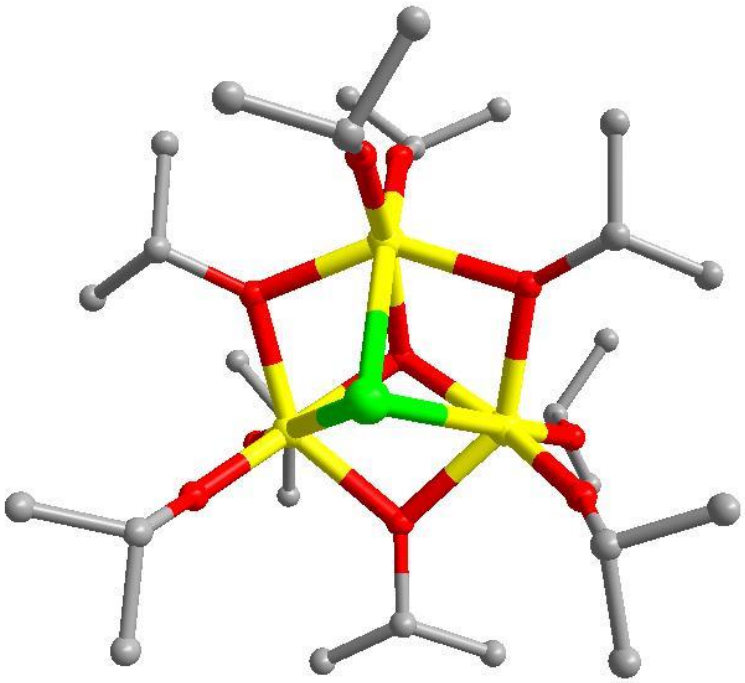

Figure 30. Solid-state structures of **POT-7**. H-atoms (which could not be located from X-ray data) have been omitted for clarity (red = O, gray = C, green = Cl, yellow = Ti).

Table 7 Details of the structure solution and refinement of **POT-7**

Compound	**POT-7**
Chemical formula	**$C_{27}H_{63}ClO_{10}Ti_3$**
FW	726.92
Crystal system	Tetragonal
Space group	$P4_32_12$
a (Å)	12.6345(10)
b (Å)	12.6345(10)
c (Å)	50.131(6)
V (Å^3)	8002.5(13)
Z	8
Calculated Density (Mg/m^3)	1.207
Absorption coefficient(mm^{-1})	0.693
reflections collected	90598
independent reflections (R_{int})	3799 (0.0943)
*R*1, *wR*2 [$I>2\sigma(I)$]	0.0669, 0.1907
*R*1, *wR*2 (all data)	0.0786, 0.2060

2.2.9 Synthesis and Structure of [$Ti_3O(CO_3{}^iPr)(O^iPr)_{10}CoBr$] (POT-8).

Titanium isopropoxide (2 ml, 9.54 mmol), cobalt bromide anhydrous (0.25g, 1.14 mmol) and isopropanol anhydrous (5 ml) was placed in an autoclave under nitrogen and the mixture heated to 150 ^oC for 3 days, the obtained blue solution were futher placed in -15^oC, violet crystals of [$Ti_3O(CO_3{}^iPr)(O^iPr)_{10}CoBr$] (**POT-8**) were obtained in two weeks.

As shown in **Figure 31**, sXRD analysis shows that **POT-8** contains a Ti_3CoO_6 core, containing two six-coordinated Ti(IV) centres, one five-coordinated Ti(IV) centre and one five-coordinated Co(II) centre. Each six-coordinated Ti(IV) centre exhibits octahedral geometry, being bonded with a μ_4-O oxo-atom, three bridging isopropoxide ligands and a terminal isopropoxide ligands, a O atom from isopropyl carbonate ($CO_3{}^iPr$) ligand. The five-coordinated Ti(IV) centres shows distorted trigonal bipyramidal geometry, being bonded with a μ_4-O oxo-atom, two bridging isopropoxide ligands and two terminal isopropoxide ligands, The five-coordinated Co(II) centre also shows distorted trigonal bipyramidal geometry, being bonded with a μ_4-O oxo-atom, three bridging isopropoxide ligands and a terminal bromide ligand. Interestingly, the isopropyl carbonate ($CO_3{}^iPr$) ligand is not belong to starting chemical but probably derived from in situ oxidation of isopropanol during slovothermal synthesis of **POT-8**.

Structure solutions and refinements details of **POT-8** are listed in **Table 8**, selected bond lengths (Å) and angles (^{o}) of **POT-8** are shown in **Table S8**.

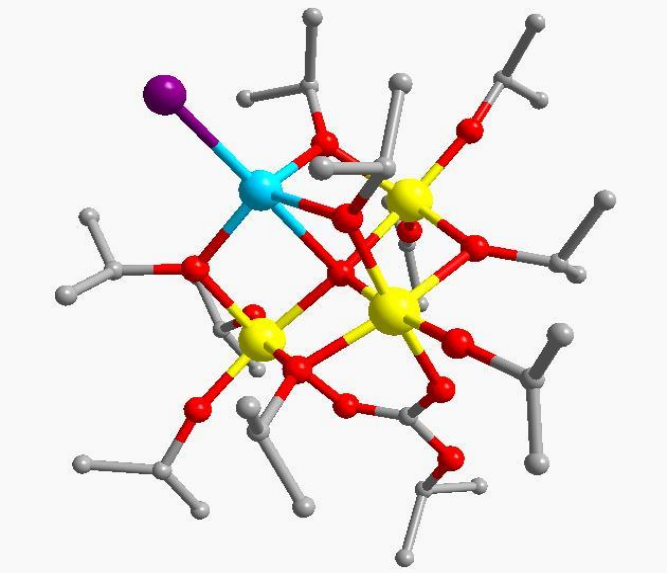

Figure 31. Solid-state structures of **POT-8**. H-atoms (which could not be located from X-ray data) have been omitted for clarity (red = O, gray = C, blue = Co, violet = Br, yellow = Ti).

Table 8. Details of the structure solution and refinement of **POT-8**.

Compound	**POT-8**
Chemical formula	**$C_{34}H_{77}BrCoO_{14}Ti_3$**
FW	992.50
Crystal system	Monoclinic
Space group	$P2_1/c$
a (Å)	11.127(6)
b (Å)	19.130(2)
c (Å)	24.610(6)
β (°)	107.424(4)
V (Å^3)	4998.4(8)
Z	4
Calculated Density (Mg/m^3)	1.319
Absorption coefficient(mm^{-1})	1.639
reflections collected	79293
independent reflections (R_{int})	7276 (0.1455)
*R*1, *wR*2 [$I>2\sigma(I)$]	0.0562, 0.1275
*R*1, *wR*2 (all data)	0.0954, 0.1488

2.2.10 Synthesis and Structure of $[Ti_4O_2(O^iPr)_{14}CeCl_2]$ (POT-9).

Titanium isopropoxide (2 ml, 9.54 mmol), cerium chloride anhydrous (0.246g, 1.0 mmol) and isopropanol anhydrous (7 ml) was placed in an autoclave under nitrogen and the mixture heated to 150 ^oC for 3 days, the obtained orange solution was futher placed in room temperature, violet crystals of $[Ti_4O_2(O^iPr)_{14}CeCl_2]$ (**POT-9**) were obtained by cooling in three weeks. Yield 0.58g 27%.

As shown in **Figure 32**, sXRD analysis shows that **POT-9** contains a $Ti_4O_6CeCl_2$ core, containing four six-coordinated Ti(IV) centres and a eight-coordinated Ce(III) centre. Each six-coordinated Ti(IV) centre exhibits octahedral geometry, being bonded with a μ_3-O oxo-atom, three bridging isopropoxide ligands, a terminal isopropoxide ligands and a μ_3-O chloride ligand. The eight-coordinated Ce(III) centre exhibits dodecahedron geometry, being bonded with two μ_4-O oxo-atom, two μ_3-O chloride ligands, and four bridging isopropoxide ligands. Structure solutions and refinements details of **POT-9** are listed in **Table 9**, selected bond lengths (Å) and angles (^{o}) of **POT-9** are shown in **Table S9**.

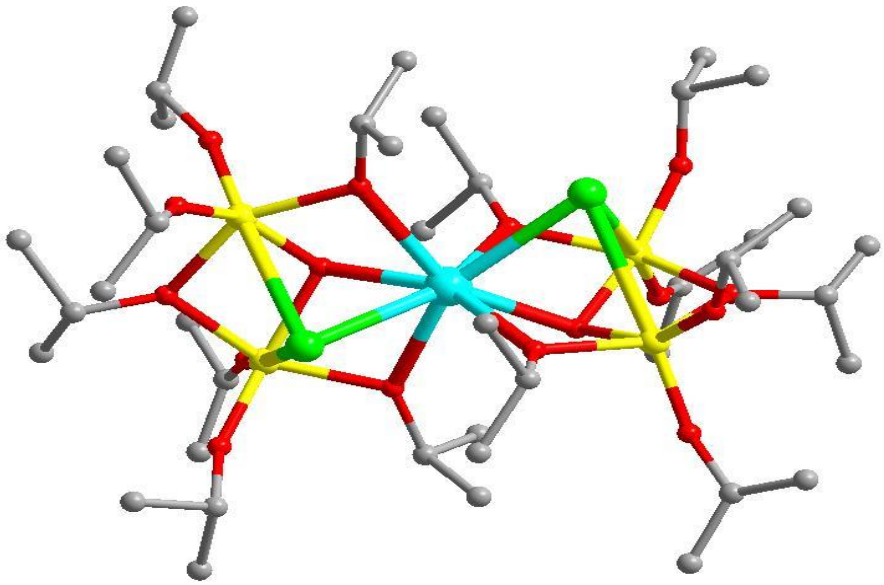

Figure 32. Solid-state structures of **POT-9**. H-atoms (which could not be located from X-ray data) have been omitted for clarity (red = O, gray = C, blue = Ce, green = Cl, yellow = Ti).

Table 9. Details of the structure solution and refinement of **POT-9**.

Compound	**POT-9**
Chemical formula	**$C_{42}H_{98}CeCl_2O_{16}Ti_4$**
FW	1261.82
Crystal system	Monoclinic
Space group	$P2_1/c$
a (Å)	12.822(2)
b (Å)	15.481(4)
c (Å)	32.339(3)
β (°)	92.822(3)
V (Å^3)	6411.2(10)
Z	4
Calculated Density (Mg/m^3)	1.307
Absorption coefficient(mm^{-1})	1.308
reflections collected	56703
independent reflections (R_{int})	11236 (0.0758)
*R*1, *wR*2 [$I>2\sigma(I)$]	0.0612, 0.1522
*R*1, *wR*2 (all data)	0.0854, 0.1737

2.2.11 Synthesis and Structure of $[Ti_{22}O_{28}(C_2O_4)(O^iPr)_{34}Cu]$ (POT-10).

Titanium isopropoxide (2.0 ml, 9.54 mmol), cuprous iodide anhydrous (0.19g, 1.0 mmol) and isopropanol anhydrous (5.0 ml) tetrahydrofuran anhydrous (5.0 ml) were placed in an autoclave under nitrogen and the mixture heated to 150 °C for 5 days, the obtained green solution were futher placed in room temperature, green crystals of $[Ti_{22}O_{28}(C_2O_4)(O^iPr)_{34}Cu]$ (**POT-10**) were obtained by cooling in four weeks. Yield: only trace amount.

As shown in **Figure 33**, sXRD analysis shows that **POT-10** contains two $Ti_{11}CuO_{16}$ core, containing eleven Ti(IV) centres and a Cu(II) centre. The Cu(II) centre is four-coordinated to assume a plane quadrilateral geometry being bonded with two μ_3-O oxo-

atoms, and two O atoms in oxalate anion (C_2O_4), the oxalate anion bridged two $Ti_{11}CuO_{16}$ core. So far, reported crystal structures about Cu(II) doped **POTs** is very rare. What's more, it is notable that the bridging oxalate anion in **POT-10** is derived form isopropanol through the in situ oxidation reaction during solvothermal process. Structure solutions and refinements details of **POT-10** are listed in **Table 10,** selected bond lengths (Å) and angles (°) of **POT-10** are shown in **Table S10**.

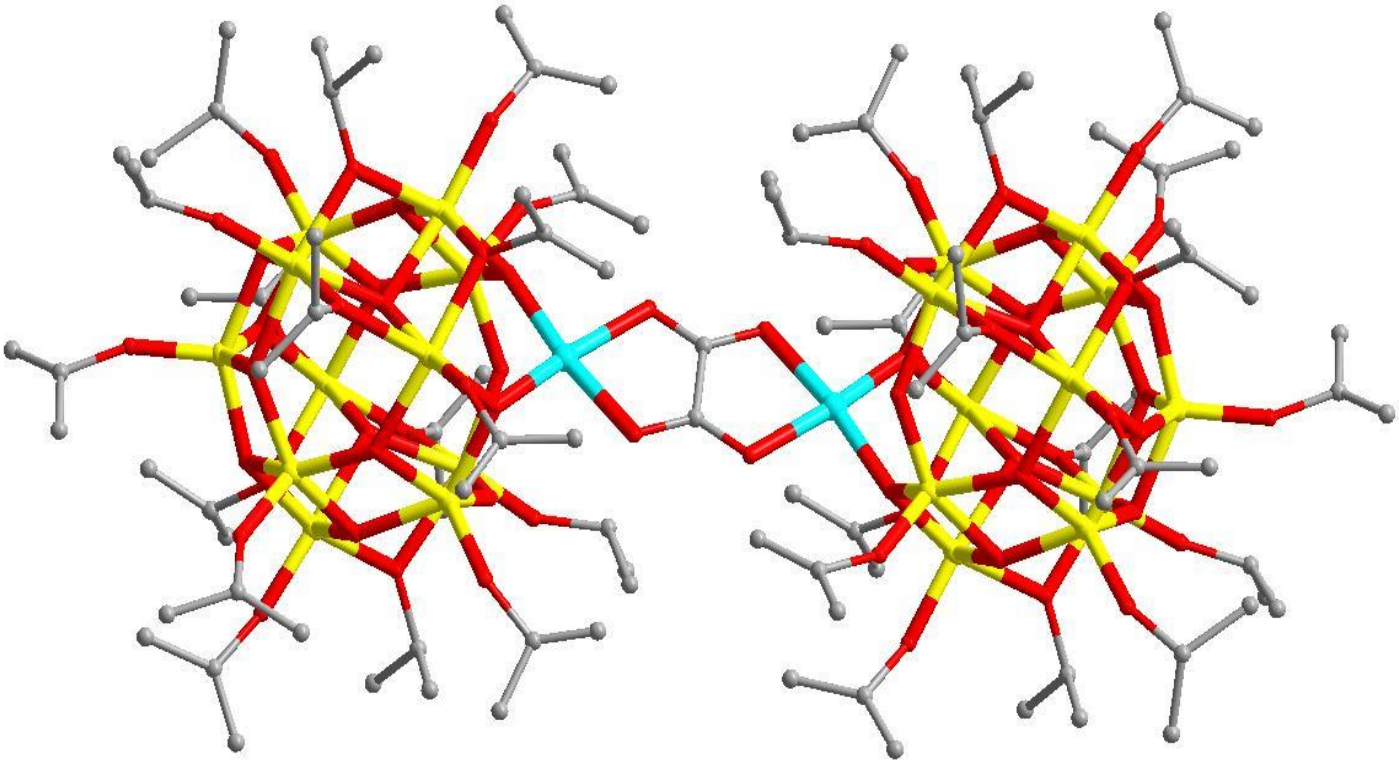

Figure 33. Solid-state structures of **POT-10**. H-atoms (which could not be located from X-ray data) have been omitted for clarity (red = O, gray = C, blue = Cu, yellow = Ti).

Table 10. Details of the structure solution and refinement of **POT-10**.

Compound	**POT-10**
Chemical formula	$\mathbf{C_{104}H_{238}Cu_2O_{66}Ti_{22}}$
FW	3725.81
Crystal system	Triclinic
Space group	*P-1*
a (Å)	14.6523 (9)
b (Å)	15.1144 (14)
c (Å)	24.459 (5)
α (°)	74.189 (14)
β (°)	76.906 (11)
γ (°)	66.230 (7)
V (Å^3)	4727.6 (12)
Z	1
Calculated Density (Mg/m^3)	1.309
Absorption coefficient(mm^{-1})	1.159
reflections collected	45351
independent reflections (R_{int})	16615 (0.0450)
$R1$, $wR2$ [$I>2\sigma(I)$]	0.0717, 0.2049
$R1$, $wR2$ (all data)	0.1092, 0.2241

2.2.12 Synthesis and Structure of $[Ti_{12}O_{16}(O^iPr)_{16}][Ti_{12}O_{15}(O^iPr)_{17}]^+[(ICo)_6Ti_{15}O_{24}(O^iPr)_{18}(I)]^-$ (POT-11).

Titanium isopropoxide (2.0 ml, 9.54 mmol), cobalt (II) iodide dihydrate (0.313g, 1.0 mmol) and isopropanol anhydrous (5 mL) were placed in an autoclave under nitrogen at 150 °C for 3 days, the obtained green solution were futher placed in room temperature, blue-green needle shaped crystals of $[Ti_{12}O_{16}(O^iPr)_{16}][Ti_{12}O_{15}(O^iPr)_{17}]^+[(ICo)_6Ti_{15}O_{24}(O^iPr)_{18}(I)]^-$ (**POT-11**) were selected in the mixture of crystals of POTs by cooling in four weeks. Yield 0.063g, 3%.

As shown in **Figure 34**, the single-crystal X-ray study of the structure of **POT-11** exists as an ion-separated arrangement in the solid state, $[Ti_{12}O_{16}(O^iPr)_{16}][Ti_{12}O_{15}(O^iPr)_{17}]^+[(ICo)_6Ti_{15}O_{24}(O^iPr)_{18}(I)]^-$. The $[Ti_{12}O_{15}(O^iPr)_{17}]^+$

cation of **POT-11** is closely related structurally to the previously reported neutral **POT** $[Ti_{12}O_{16}(O^iPr)_{16}]$ [118], only with one of the two μ_2-O atoms in this cage being replaced by an isopropoxide group (resulting in a net +1 charge).

More interesting is the anionic $[(ICo)_6Ti_{15}O_{24}(O^iPr)_{18}(I)]^-$ host–guest assembly of **POT-11**. This is composed of a neutral nearly D_3-symmetric heterometallic $Co_6Ti_{15}O_{42}$ cage in which the six tetrahedral Co^{II} ions are coordinated at its periphery within dimeric subunits. The $Ti_{15}O_{24}$ core of the anion forms an approximately spherical shell with an internal diameter of *ca.*8 Å, in which each of the Ti centres bonded to four equatorial oxo-atoms of the shell and an axial isopropoxide group and have chemically similar square-based pyramidal geometries. The remarkable feature of the anion is the apparent weakness of the bonding of the encapsulated iodide ion to the internal shell surface. Structure solutions and refinements details of **POT-11** are listed in **Table 11,** selected bond lengths (Å) and angles (°) of **POT-11** are shown in **Table S11**.

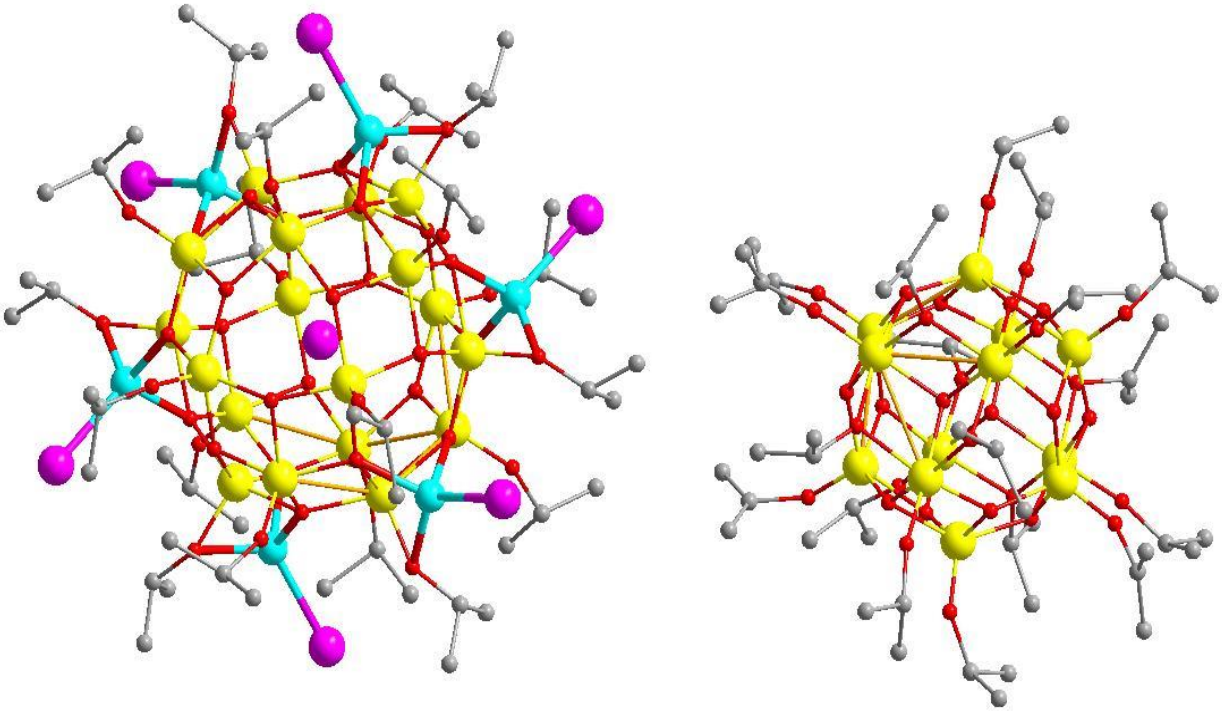

Figure 34. Solid-state structures of **POT-11**. H-atoms (which could not be located from X-ray data) have been omitted for clarity (red = O, gray = C, blue = Co, pink = I, yellow = Ti).

Table 11**.** Details of the structure solution and refinement of **POT-11**.

Compound	**POT-11**
Chemical formula	**$C_{153}H_{357}Co_6I_7O_{106}Ti_{39}$**
FW	7002.14
Crystal system	Trigonal
Space group	*P3₁m*
a (Å)	24.193(3)
b (Å)	24.193(3)
c (Å)	15.185(2)
α (°)	90.00
β (°)	90.00
γ (°)	120.00
V (Å^3)	7697.1(17)
Z	1
Calculated Density (Mg/m^3)	1.539
Absorption coefficient(mm^{-1})	2.03
reflections collected	145905
independent reflections (R_{int})	4912 (0.1017)
*R*1, *wR*2 [$I>2\sigma(I)$]	0.1358, 0.1671
*R*1, *wR*2 (all data)	0.3327, 0.3486

2.2.13 Synthesis of [Ti_8O_7(HOEt)$(OEt)_{21}$Ce] (POT-12)

The crystals of [Ti_8O_7(HOEt)$(OEt)_{21}$Ce] (**POT-12**) were obtained through the slovothermal reaction of the mixture containing tetraethyl titanate (3.5 mL, 15.4 mmol), anhydrous cerium chloride (0.246g, 1 mmol) and anhydrous ethanol (7 mL) into the autoclave. the mixture heated to 150 °C for 2 days gave a light yellow solution, and orange crystals of **POT-12** were obtained from the yellow solution through slowly evaporate the solvent at room temperature. The synthesis and structure of **POT-12** were reported in 2013 [116d]. Herein, we used **POT-12** as a precursor to prepare new hybrid material.

2.3 Conclusions

In summary, twelve different POTs with different formula and structure have been successfully synthesized and structural determined. In these POTs, there are functional ligands modified POTs like **POT-1**, **POT-2**, **POT-3**, **POT-4** and metal doped POTs like **POT-6**, **POT-8**, **POT-9**, **POT-10, POT-11,** which obtained via different synthesis method. The cost of synthesizing large amounts of **POT-5** is relatively low, thus we further studied the preparation and application of a serious of TiO_2@C materials through calcination of **POT-5**.

Chapter 3

New C@TiO_2 composite materials derived from POTs

3.1 Introduction

TiO_2 based materials, which have been widely used in photocatalysis, sensors, solar cells, lithium-ion batteries and other fields, are important candidates for anode materials of lithium-ion battery. These materials have many advantages, such as has easy-to-obtain, long charge-discharge cycle life, environmental friendly and small volume changes during charging and discharging process [119-123]. Compared with carbon materials, TiO_2 has a high charge and discharge platform (~1.5 V) which can avoid the generation of SEI (Solid Electrolyte Interface) film and lithium dendrites [124,125], but its disadvantages (e.g. wide band gap, poor conductivity, low specific capacity and so on) limit its commercialization in electrode materials of battery [126,127].

Through introducing nanoporous into TiO_2, the transmission of electrons and lithium ions can be effectively improved [128-133]. In addition, another effective modification method is to combine TiO_2 with highly conductive materials and fabricate composites. For instance, the conductivity of titanium dioxide can be significantly improved after combination with carbon-based materials, and their rate performance will be further improved [134-138].

In this chapter, we use **POT-5** ($[Ti_2O(OAc)_2(HOAc)_2Cl_4]$) as precursor to obtain porous C@TiO_2 materials through calcination in different atmospheres. These new materials are further used as anode material for lithium ion battery, their electrochemical performance is studied as well.

3.2 Results and Discussion

3.2.1 Chemicals and Instrumentation

All chemicals used were commercially available and used as received without further purification, unless specified. Powder XRD data was obtained by D/MAX-3C X-ray diffractometer from Rigaku Co., Ltd, using a Cu Kα radiation source (λ = 0.1541865 nm) with 2θ from 10˚ to 80˚. Fourier transform infrared (FT-IR) spectra were obtained by Thermo Fisher's Nicolet 6700 spectrometer, Scanning Electron Microscope (SEM) data were obtained by the FEI Nova Nano 450. The isothermal curves and pore size distribution were measured by the JW-BK122F type specific surface area and pore size analyzer. Particle size distributions were tested via dynamic light scattering nanometer particle size analyzer (Brookhaven Instruments Corporation).

3.2.2 Preparation of C@TiO_2

The crystals of **POT-5** were put into a tube furnace, then calcined in an air flow for 5 hours at 300 ºC, 400 ºC, 500 ºC, 600 ºC, 700 ºC, 800 ºC, 900 ºC or 1000 ºC, respectively. Nanoporous C@TiO_2 named **K300**, **K400**, **K500**, **K600**, **K700**, **K800**, **K900**, **K1000** were obtained. Calcination of the crystals of **POT-5** in a nitrogen flow for 5 hours at 300 ºC, 400 ºC, 500 ºC, 600 ºC, 700 ºC, 800 ºC, 900 ºC or 1000 ºC, respectively were also conducted giving nanoporous C@TiO_2 named **N300**, **N400**, **N500**, **N600**, **N700**, **N800**, **N900**, **N1000**.

3.2.3 Preparation and analysis of lithium-ion battery

The composite materials of C@TiO_2 were used as the anode materials for lithium-ion battery. The mixture of C@TiO_2, acetylene black and polyvinylidene fluoride (**PVDF**) with the mass ratio of 8 : 1 : 1 was stirred until it becomes a slurry with an appropriate amount of 1-methyl-2-pyrrolidinone (**NMP**), then the resulting slurry was poured on

the pure copper foil, using a spatula to scrape it on the copper foil evenly into a 90 μm thick film, and then baked in a vacuum drying oven at 60 ºC for 12 hours. The dried copper foil was used as the anode, the lithium metal sheet was used as the counter electrode, and Celgard 2400 film was used as the separator. $LiPF_6$ dissolved in ethylene carbonate/ethyl methyl carbonate/dimethyl carbonate (EC/EMC/DMC) with a volume ratio of 1:1:1 were used as the electrolyte. Finally, the CR2023 button batteries were assembled in a glove box filled with argon.

Assembled CR2023 button batteries were placed at room temperature for 24 hours, and the galvanostatic charge-discharge test was performed on the LANHE CT2001A battery test system at a voltage range from 0 to 3 V with different current densities. CHI660E (Shanghai, Chenhua) electrochemical workstation were used for cyclic voltammetry (CV) test (from 0 to 3 V, scan rate 0.5 mV/s) and for Electrochemical Impedance Spectroscopy (EIS) test (from 100 kHz to 0.01 Hz) of the battery.

3.2.4 Morphology characterization and analysis

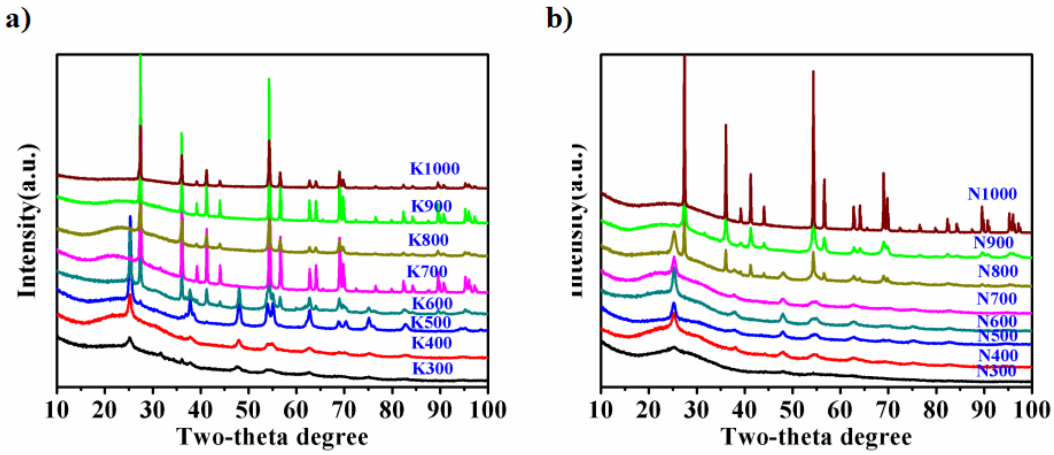

Figure 35. (a) XRD patterns about C@TiO_2 materials of **K300**, **K400**, **K500**, **K600**, **K700**, **K800**, **K900**, **K1000**, (b) XRD patterns about C@TiO_2 materials of **N300**, **N400**, **N500**, **N600**, **N700**, **N800**, **N900**, **N1000**.

Figure 35 displays the XRD patterns of a series of prepared C@TiO_2 materials. As

shown in **Figure 35a**, the XRD patterns of **K300**, **K400**, **K500** exhibit peaks around $2\theta = 25.5^{o}$ corresponding to (101) crystal plane of anatase TiO_2. The intensity of these peaks around $2\theta = 25.5^{o}$ are increased from the XRD patterns of **K300** to that of **K500**, beside, there is a weak peak at $2\theta = 26.7^{o}$ in the the **XRD** patterns of **K500**. This phenomenon confirms that there is amorphous phase in the materials of **K300**, **K400**, **K500,** but one main component of these materials is anatase TiO_2. However, for the calcination temperature up to 700 ^{o}C, the characteristic peaks in XRD patterns of **K700, K800, K900, K1000** are around $2\theta = 27.6^{o}$ corresponding to (110) crystal plane of rutile TiO_2, which show that their main component are rutile TiO_2. Interestingly, in the XRD patterns of **K600**, there are not only significant peak at $2\theta = 25.5^{o}$ but also strong peak at $2\theta = 27.6^{o}$. This phenomenon indicates that anatase and rutile TiO_2 are coexisting in **K600,** after calcination of **POT-5** at 600 ^{o}C. It can be inferred that when calcination temperature of **POT-5** is increased, the anatase TiO_2 component of the resulting materials is transformed to rutile TiO_2 step by step. As shown in **Figure 35b**, all the XRD patterns of **N300**, **N400**, **N500, N600, N700** exhibit peaks around $2\theta = 25.5^{o}$ corresponding to (101) crystal plane of anatase TiO_2. But the intensity of anatase signal is very weak in the XRD patterns of **N300**, and get stronger in that of **N400** to **N700**, which indicated that when calcination temprature rises from 300 ^{o}C to 700^{o}C, more amorphous phase TiO_2 component can transform to anatase component in the resulting materials. In the XRD patterns of **N800**, there are peaks at both $2\theta = 25.5^{o}$ and $2\theta = 27.6^{o}$, suggesting the coexistence of anatase and rutile components in **N800.** In the **XRD** patterns of **N900** and **N1000**, there are strong characteristic peaks of rutile, suggesting rutile TiO_2 is the main component in these two materials. These results show that compared to the calcination in air a higher calcination temperature is needed in inert nitrogen for transforming anatase component into rutile phase, which is probably because of the presence of considerable amount of carbon component that

affects the phase transformation.

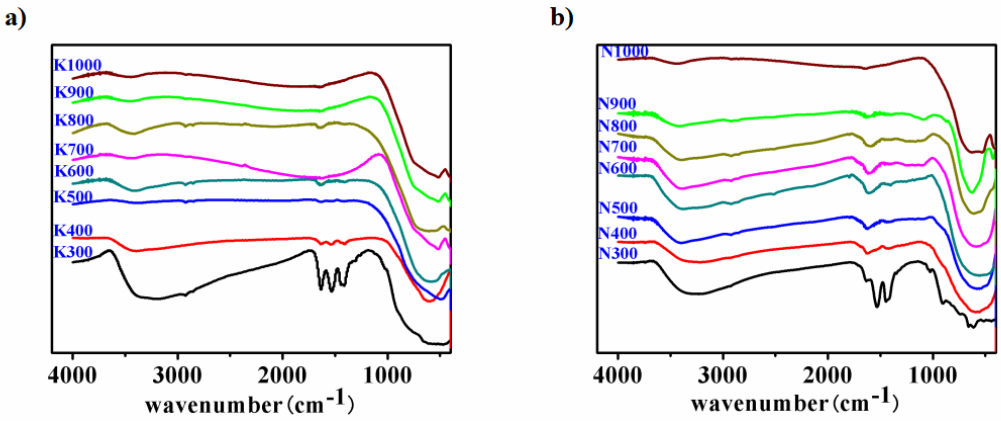

Figure 36. (a) IR curves about C@TiO_2 materials of **K300**, **K400**, **K500**, **K600**, **K700**, **K800**, **K900**, **K1000**, (b) IR curves about C@TiO_2 materials of **N300**, **N400**, **N500**, **N600**, **N700**, **N800**, **N900**, **N1000.**

Figure 36 displays the IR spectra of these prepared C@TiO_2 materials. All the spectra exhibit board absorption bands in the wavelength range of 400-800 cm^{-1} corresponding to the Ti-O bond. As shown in **Figure 36a**, the IR spectrum of **K300** has a broad absorption band around the wavelength of 3200 cm^{-1}, which may correspond to stretching vibration of hydroxyl group. Besides, there are absorption peaks around wavelengths of 1636.1 cm^{-1}, 1533.4 cm^{-1}, and 1411.8 cm^{-1}, which may correspond to symmetric (s) and asymmetric (as) stretching bands of carboxyl group. These results suggest that there is considerable amount of active components that have not been destroyed in **K300**. However, we can not find similar significant peaks in the IR spectra of **K500**, **K600**, **K700**, **K800**, **K900**, **K1000**, indicating most of active components were destroyed as the calcination temperature increases. As shown in **Figure 36b**, the IR spectrum of **N300** is similar with that of **K300**, suggesting considerable amount of organic compounds. But there are weak bands around the wavelength of 3200 cm^{-1} and 1500 cm^{-1} in the IR spectra of **N400**, **N500**, **N600**, **N700**, **N800**, which suggest the existence of active group like hydroxyl group and carboxyl group respectively. Both hydroxyl group and carboxyl group exhibit electrochemical

activity and can be found in active carbon usually.

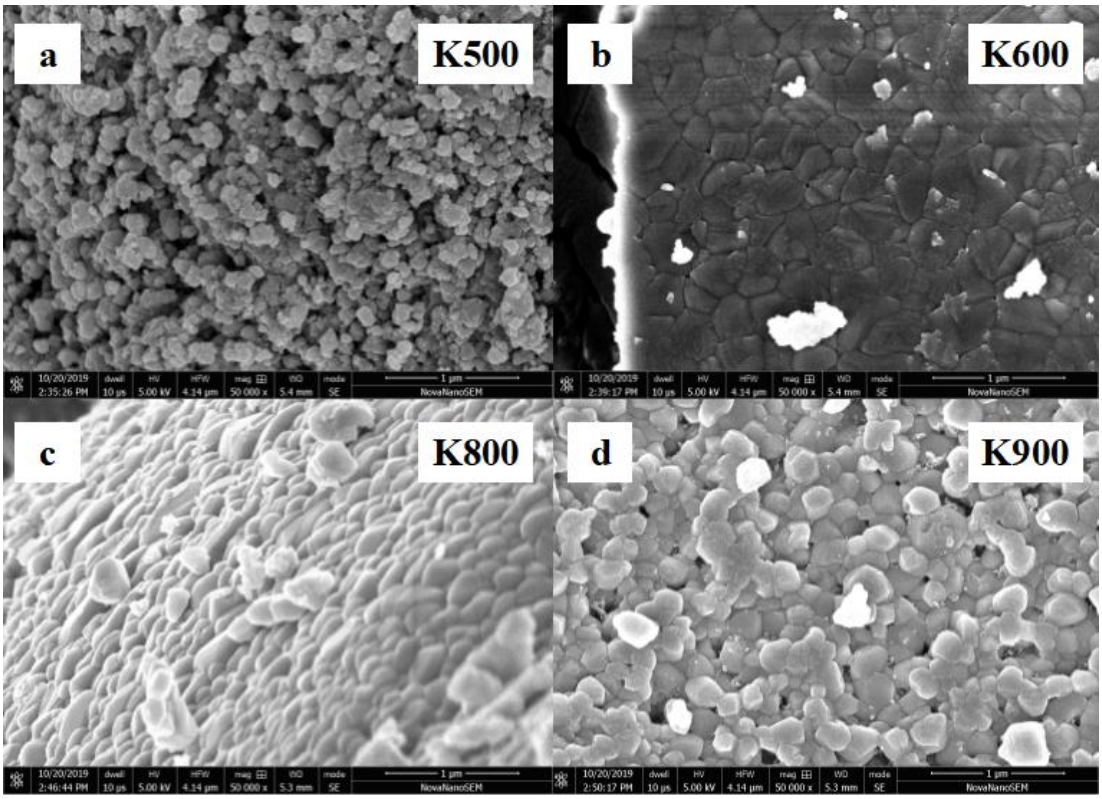

Figure 37. SEM images of (a) **K500**, (b) **K600**, (c) **K800**, (d) **K900**.

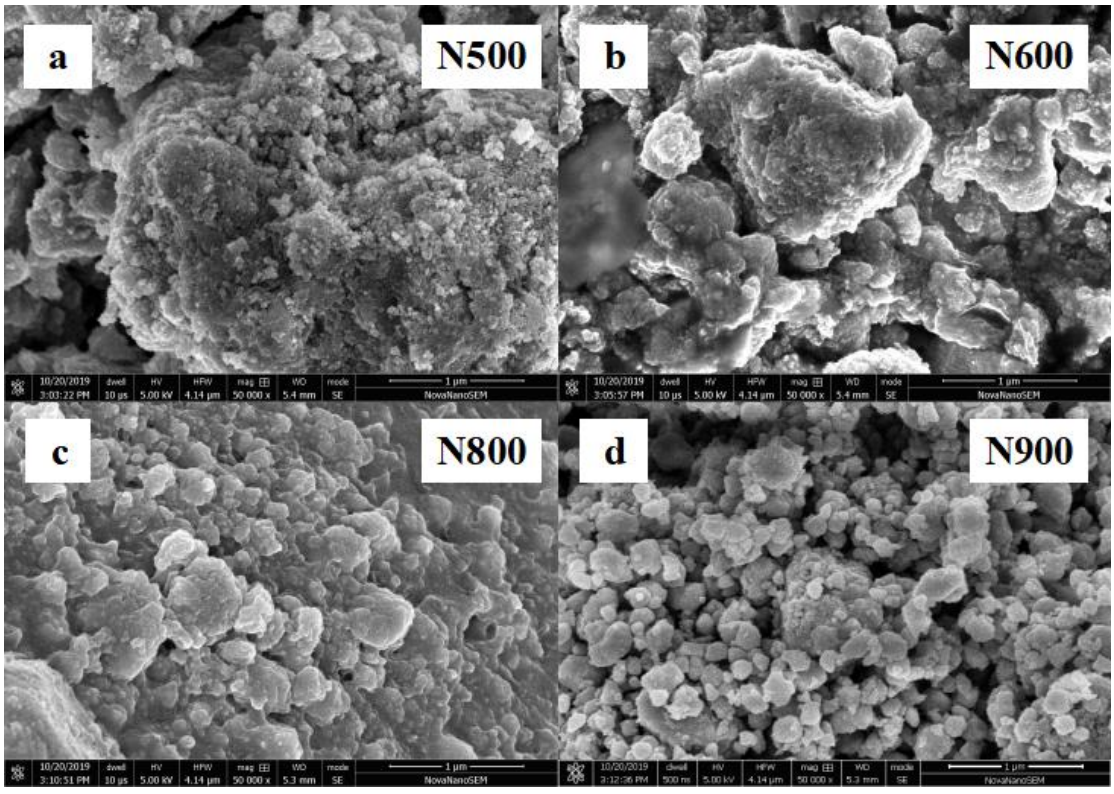

Figure 38. SEM images of (a) **N500**, (b) **N600**, (c) **N800**, (d) **N900**.

The SEM images of **K500**, **K600**, **K800**, and **K900** are shown in **Figure 37**. These materials are composed of small irregular particles. It can be found that the **K600**, **K800**, and **K900** particles are much tightly packed than that of **K500**. **Figure 38** shows the SEM images of **N500**, **N600**, **N800**, and **N900.** The materials' particles are stacked on top of each other, and there are a large number of fissures between the particles, which can be beneficial for the moving of ions.

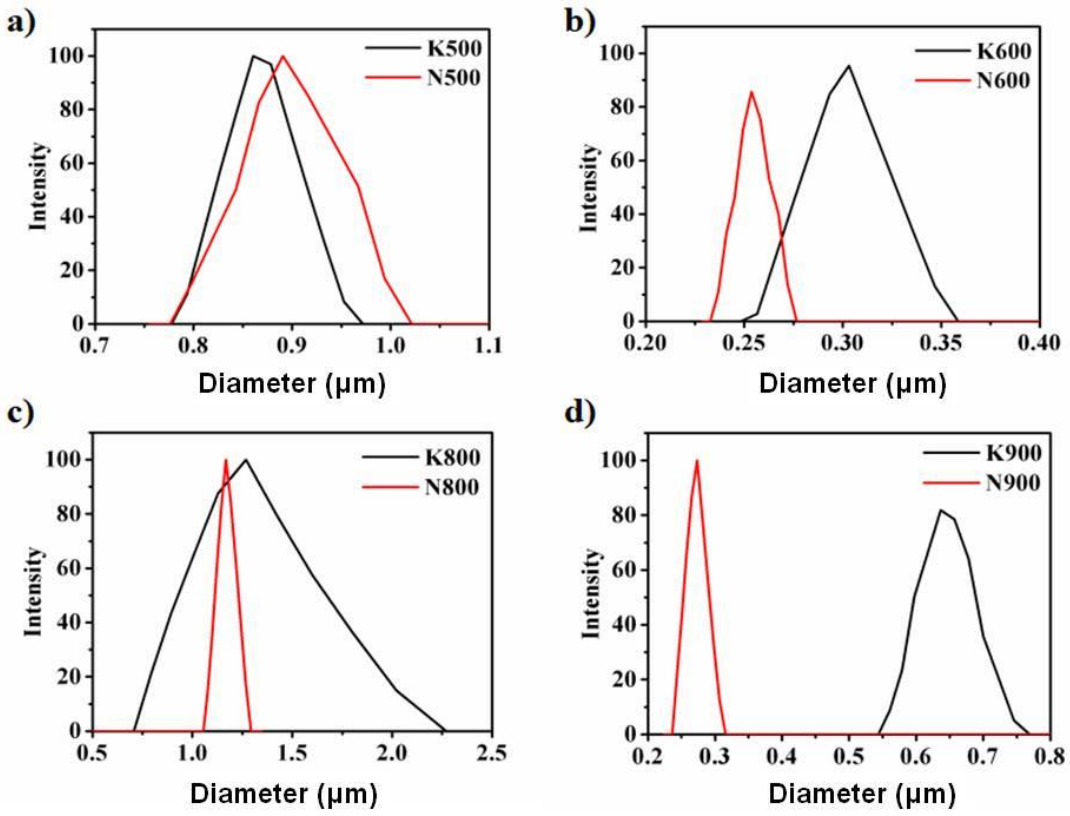

Figure 39. particle size distribution curve of (a) **K500** and **N500**, (b) **K600** and **N600**, (c) **K800** and **N800**, (d) **K900** and **N900**.

As shown in **Figure 39**, the average particle size of **N500** is with a bit larger than that of **K500**, but the particle sizes of **N600**, **N800**, and **N900** are significantly smaller than that of **K600**, **K800**, and **K900**, indicating that the presence of carbon can inhibit the growth of crystals, resulting in a smaller particle size. As the calcination temperature

rises, the porosity decreases and the crystal size increases.

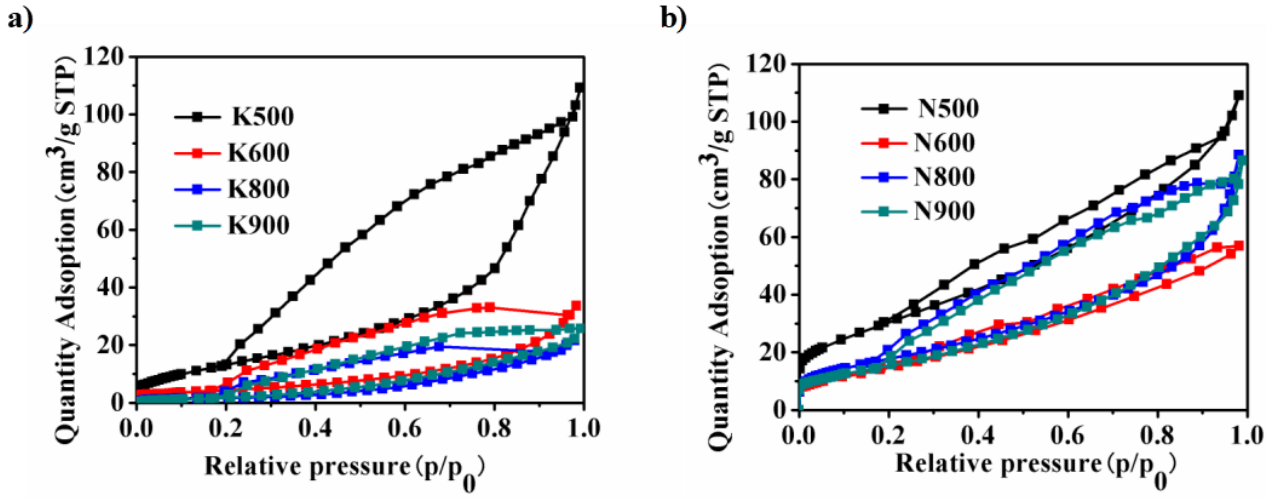

Figure 40. Nitrogen adsorption and desorption isotherms about (a) **K500**, **K600**, **K800**, **K900** and (b) **N500**, **N600**, **N800**, **N900**.

The nitrogen adsorption-desorption curves of **K500**, **K600**, **K800**, **K900**, **N500**, **N600**, **N800** and **N900** are shown in **Figure 40**. It can be seen that all the curves belong to type IV isotherms, with a relative pressure of 0.2-1 hysteresis loop, which means that all these materials contain mesoporous and microporous domains.

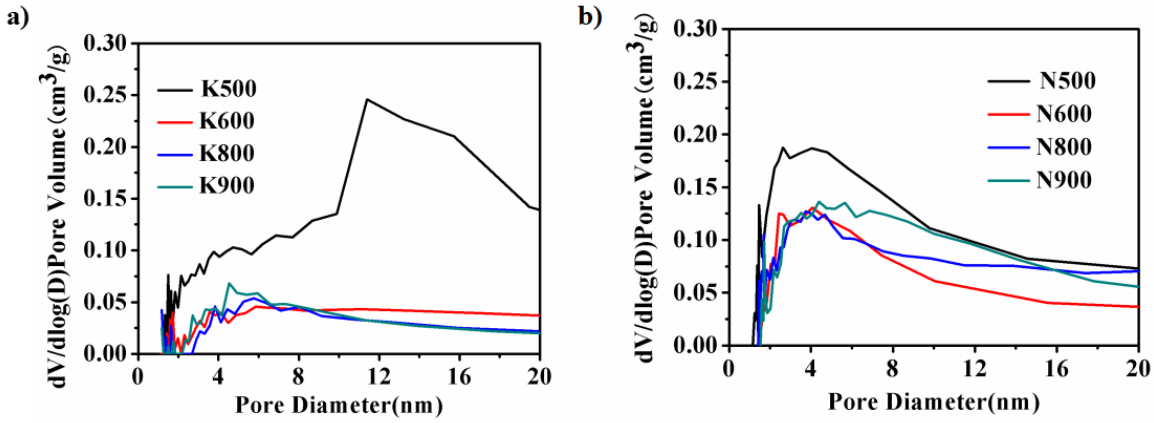

Figure 41. Pore size distribution curves of (a) **K500**, **K600**, **K800**, **K900** and (b) **N500**, **N600**, **N800**, **N900**.

Figure 41 shows the pore size distribution of the products **K500**, **K600**, **K800**, **K900**, **N500**, **N600**, **N800** and **N900**. The pore size distribution of all these materials are mainly concentrated in the mesopore range. The specific surface area, pore volume and average pore diameter of these materials are listed in **Table 12**. With the increase of the calcination temperature, the specific surface area and pore volume of the C@TiO_2 materials are decreasing because of the phase transformation from anatase to rutile, while the average pore diameter does not change much, which is due to the decomposition of the organic ligands. The specific surface areas of **N500**, **N600**, **N800** and **N900** are 98.914 m^2g^{-1}, 46.518 m^2g^{-1}, 66.356 m^2g^{-1}, 54.036 m^2g^{-1}, which are significantly higher than that of C@TiO_2 composites (**K500**, **K600**, **K800** and **K900**) calcined in air atmosphere at the same temperature. The carbon component inhibits the growth of crystals and can increase the specific surface area of the C@TiO_2 composites.

Table 12 Specific surface area and pore parameters of **K500**, **K600**, **K800**, **K900**, **N500**, **N600**, **N800**, **N900**.

sample	S_{BET}(m^2/g)	V_{me}（cm^3/g）	D_A (nm)
K500	46.129	0.194	7.764
K600	15.252	0.059	7.944
K800	5.820	0.041	7.732
K900	5.920	0.050	7.280
N500	98.914	0.194	4.724
N600	46.518	0.106	4.611
N800	66.356	0.156	6.088
N900	54.036	0.153	6.440

S_{BET}： specific surface area.
V_{me}: mesopore volume calculated by *BJH* method.
D_A: average pore size calculated by *BJH* method.

3.2.5 Electrochemical properties

To study the redox potential of the materials and the mechanism of lithium ion insertion/extraction and its electrochemical reaction, cyclic voltammetry (CV) analysis was first used for scanning the lithium battery at a constant sweep rate within a specified voltage range.

CV curves of a series of C@TiO_2 composites based lithium-ion batteries with a potential scan rate of 0.5 mV/s and voltage range from 0 to 3 V are shown in **Figure 42.** All of these C@TiO_2 composite materials have a pair of redox peaks around 2.10 V and 1.68 V, corresponding to the reversible process of lithium extraction/intercalation in the material.

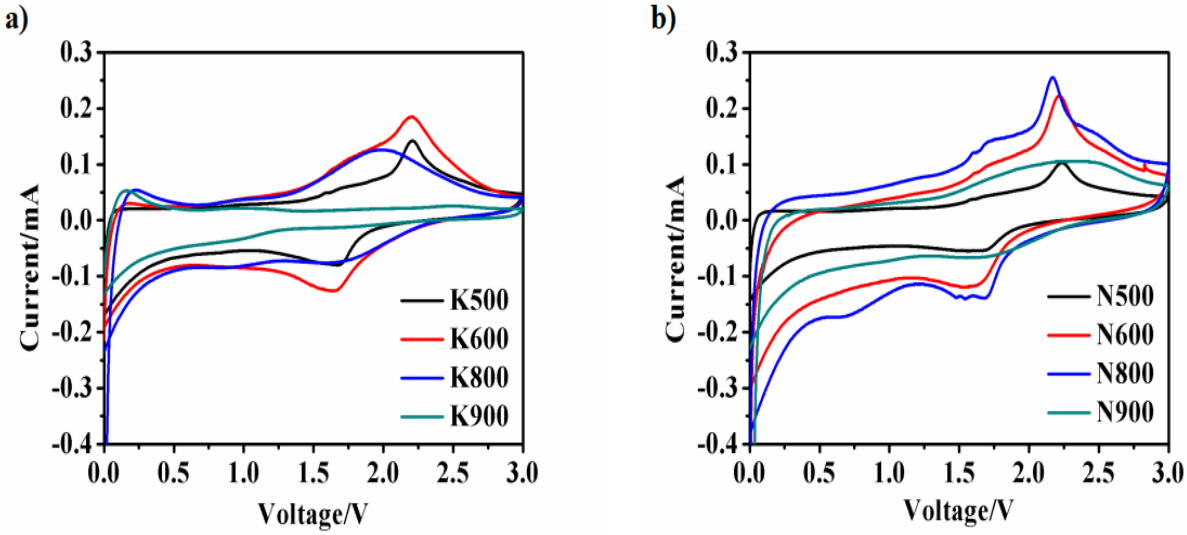

Figure 42. CV curves of (a) **K500**, **K600**, **K800**, **K900**, (b) **N500**, **N600**, **N800**, **N900.**

Figure 43 shows first cycle of galvanostatic charge-discharge curves about these C@TiO_2 composites with current density of 50 mA/g and the voltage range of 0-3 V. All of these materials have charging and discharge platforms between 1.68 V and 2.10 V, which are consistent with their CV results. As shown in **Figure 43a**, the first discharge specific capacities of materials **K500**, **K600**, **K800** and **K900** are 430.7 mAh/g, 181.6 mAh/g, 209.6 mAh/g and 35.9 mAh/g, respectively. As shown in

Figure 43b, the first discharge specific capacities of materials **N500**, **N600**, **N800** and **N900** are 942.6 mAh/g, 696.4 mAh/g, 515 mAh/g and 374.5 mAh/g respectively. The irreversible capacity of all materials during the first charge and discharge process is relatively large.

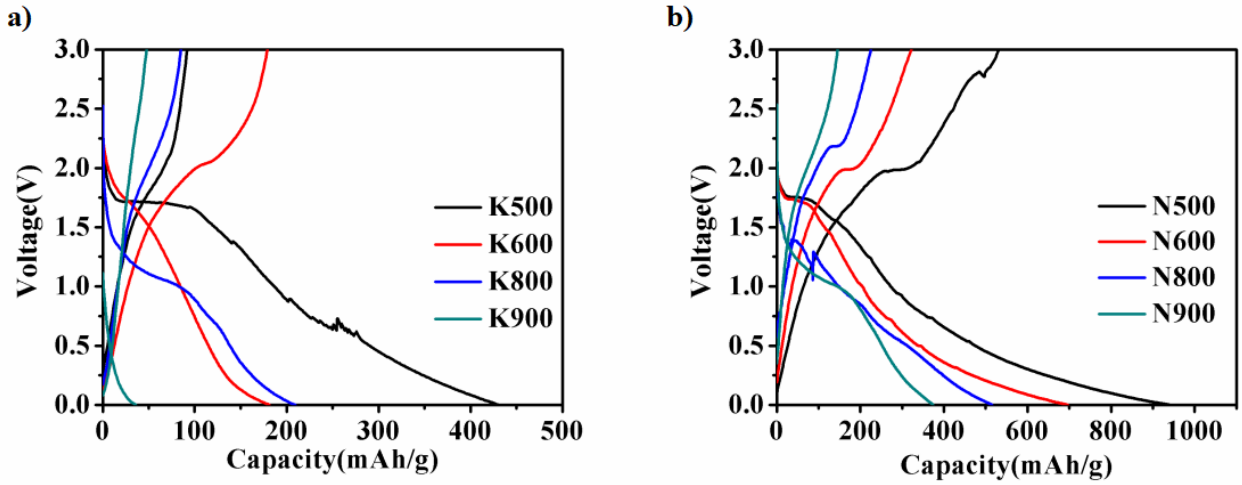

Figure 43. first cycle of galvanostatic charge-discharge curves at current density of 50 mA/g about (a) **K500**, **K600**, **K800**, **K900**, (b) **N500**, **N600**, **N800**, **N900**.

Figure 44a and **Figure 44b** show the rate performance of a series of C@TiO_2 composites as anode materials. As shown in **Figure 44a**, the materials calcined in air (**K500**, **K600**, **K800**, **K900**) show good rate performance. Their discharge specific capacity decreases regularly as the current density increases from 50 mA/g to 250 mA/g. But the reduction is relatively small, when the current density is restored to 50 mA/g, the specific discharge capacity of the material can also be restored to the initial value. The specific discharge capacity remains stable at the same current density, which is mainly due to the mesoporous structure of the C@TiO_2 composites. As shown in **Figure 44b**, the materials calcined in nitrogen (**N500, N600, N800, N900**) also have excellent properties. **N500, N600, N800, N900** have higher discharge capacity than **K500, K600, K800, K900**. Cycling stabilities of these materials are shown in **Figure 44c** and **Figure 44d**. At a current density of 50 mA/g, the initial specific capacities of **K500**, **K600**, **K800**, **K900** are 365.9 mAh/g, 291.5 mAh/g,

250.3 mAh/g, 86.9 mAh/g, respectively. While after 100 cycles, their specific capacities drop to 20.8 mAh/g (**K500**), 113.1 mAh/g (**K600**), 95.4 mAh/g (**K800**), 39.9 mAh/g (**K900**), the capacity retention rates are 5.7%, 38.8%, 38.1%, and 45.9%. The initial specific capacities of **N500**, **N600**, **N800**, **N900** are 629.3 mAh/g, 345.1 mAh/g, 446.7 mAh/g, 90.2 mAh/g respectively. After 100 cycles, the capacity is 295.6 mAh/g (**N500**), 192 mAh/g (**N600**), 340.4 mAh/g (**N800**), and 76 mAh/g (**N900**), while the capacity retention rate is 47%, 55.6%, 76.2%, 84.3%. The C@TiO_2 composite material **N800** has the best performance.

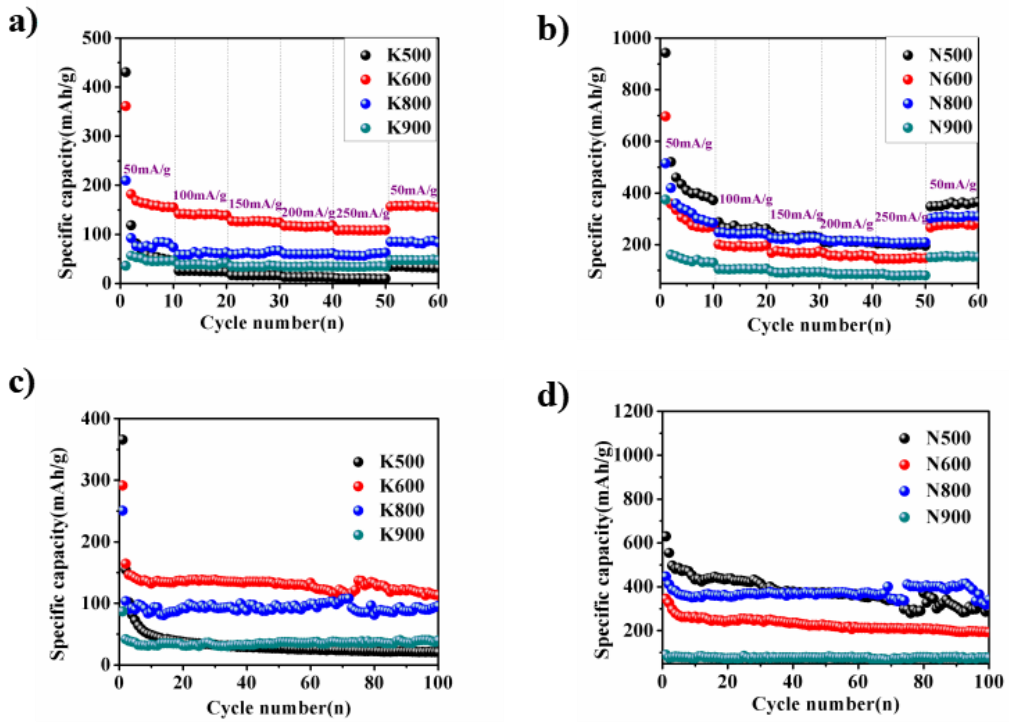

Figure 44. Rate capability diagrams of (a) **K500**, **K600**, **K800**, **K900** and **(b) N500**, **N600**, **N800**, **N900** at different current densities**,** cycling stability of (c) **K500**, **K600**, **K800**, **K900** and (d) **N500**, **N600**, **N800**, **N900**.

Nyquist plots of these C@TiO_2 composites (**K500**, **K600**, **K800**, **K900**, **N500**, **N600**, **N800**, **N900**) are shown in **Figure 45**. Each of these plot exhibit an arc in the high-frequency region and an oblique straight line in the low-frequency region. The semi-circle in the high frequency region represents charge transfer impedance of the

electrolyte and the electrode interface, while the straight line in the low frequency region related to the diffusion impedance of lithium ions in the electrode. As shown in **Figure 45a**, the charge transfer resistance of the electrode materials (**K500**, **K600**, **K800**, **K900**) was decreased as the calcination temperature rise from 500°C to 900°C. As shown in **Figure 45b**, the low frequency region of the Nyquist plots of **N500**, **N600**, **N800**, **N900** are nearly the same, indicating that the diffusion resistance of lithium ions on the electrode is similar. The charge transfer resistance of **N500**, **N600**, **N800**, **N900** is obviously smaller than that of **K500**, **K600**, **K800**, **K900**.

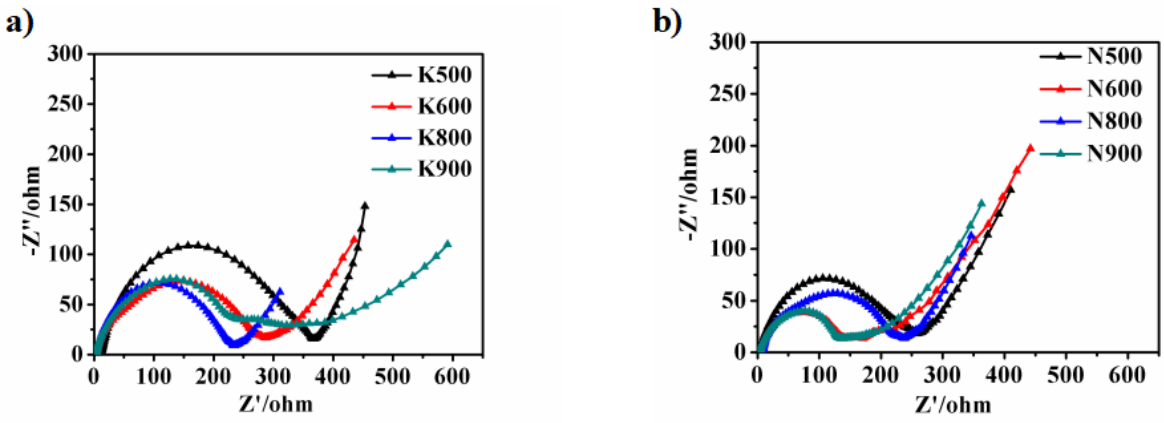

Figure 45. Nyquist plots of (a) **K500**, **K600**, **K800**, **K900** and (b) **N500**, **N600**, **N800**, **N900**.

3.3 Conclusions

In summary, the C@TiO_2 composite materials calcined in nitrogen flow **N800** exhibits excellent electrochemical performance, which is mainly attributed to the following aspects: First, the nanoporous structure of **N800** is beneficial to the electrolyte. Second, the porous structure of **N800** has a large specific surface area, which can increase the contact area between the electrolyte and the electrode. Third, the nanostructure can effectively shorten the transmission distance of lithium ions. Fourth, the carbon component in **N800** can increase the conductivity of this composites which ensures rapid charge-discharge, and good rate performance.

Chapter 4

Hybrid materials based on POTs and conjugated polymers

4.1 Introduction

The electrochromic devices (ECDs) such as electrochromic smart windows, which can efficiently adjust light transmission through reversible color and transparency changes under an external voltage, and supercapacitors (SCs), which are advanced electrochemical energy storage devices characterised for their high power density and short charging times, have similar working mechanisms and device structures. As a result, there is the interesting prospect of the integrating energy storage and electrochromic functions into one device. As a promising smart device, such electrochromic supercapacitors (ECSCs) have attracted considerable interest over the past decade [139-144]. In comparison with traditional ECDs, ECSCs not only have the function of energy storage, but also can act simultaneously as a smart energy monitor, indicating the state of energy storage capacity through color changes. In addition, ECSCs are also expected to overcome problems concerning external power sources and the limited range of application of conventional ECDs. Good electrode materials are one of the key problems for the development of ECSCs. In general, bare materials or inorganic materials have many defects. The use of organic-inorganic hybrid materials has gradually become our focus.

Conjugated polymers have been widely viewed as an attractive option for electrode materials due to their adjustable band gaps, large theoretical specific capacitances, good electrical conductivity, high elemental abundance, light weight, and tunable mechanical flexibility. On the other hand, there has been considerable interest in **POTs**, which possess well-defined inorganic Ti_xO_y cores surrounded by organic ligands. Recently, **POTs** have proved to be particular effective precursors for

formation of various titania composites, with controlled composition and morphology. **POTs** can also be employed as 'nano-blocks' for the formation of new organic-inorganic hybrid materials. For example, the introduction of styrenic groups allows copolymerization of the **POT** building block $Ti_{16}O_{16}(OEt)_{32-x}(OPhCH=CH2)_x$ with styrene to form hybrid three-dimensional network materials in which the titania nano-fillers are covalently linked to a non-conjugated organic polymer.

In addition, particularly pertinent to the studies presented here, are conjugated thiophene-polyoxomolybdate polymers which have been used in photovoltaic cells [145,146]. However, the synthesis of these materials requires a three-component chemical coupling procedure.

In this chapter, we designed and synthesized a series of conjugated polymers, and further combined conjugated polymers and **POTs** to obtain novel organic-inorganic hybrid materials using different methods. The electrochemical properties and photo electrochemical properties of these novel materials are studied.

4.2 Results and Discussion

4.2.1 Chemical and Instrumentation

All reagent grade chemicals were purchased from The Aldrich or Aladdin Reagent (Shanghai) companies. Ltd., and were used without further purification. Indium tin oxide (ITO)-coated glass (sheet resistance $R_s \leq 10\ \Omega$) was purchased from Guluo Glass Technology Co. Ltd. It was ultrasonically washed in deionized water, ethanol, acetone, toluene and (finally) ethanol solutions. Proton (^1H) nuclear magnetic resonance (NMR) spectra were recorded with a Bruker Avance III instrument (Bruker, Switzerland) at 500 MHz. Fourier transform infrared (FT-IR) spectra were obtained using a Nicolet 6700 spectrometer (Thermo Fisher Nicolet, USA). Extracted ion chromatogram and mass spectra (MS) were explored using a ABSCIEX HPLC-TripleTOF 5600 Mass Spectrometer. Elemental analysis was obtained using a Perkin-

Elmer 4200 elemental analyzer. Powder X-ray diffraction (pXRD) experiments were performed using a X'Pert Pro diffractometer with Cu-Kα radiation (λ= 1.5418 Å) operating at 40 kV and 40 mA and a scanning angle ranging from 5° to 50° of 2θ. Average molecular weight and polydispersity indices (PDIs) were measured through gel permeation chromatography (GPC) using a Waters Breeze 2 HPLC system. Scanning electron microscopy (SEM) images were collected using a field emission scanning electron microscope (Zeiss Gemini 300). Measurements of surface area and pore size were carried out using an ASAP 2460 surface area and porosimetry auto analyzer (Micromeritics, USA). Ultraviolet-visible (UV-vis) and near infrared (NIR) spectra were obtained using a UV-1800 spectrophotometer (Shimadzu, Japan).

4.2.2 Synthesis of organic monomers

4.2.2.1 Synthesis of 3-(N-trifluoroacetamido)thiophene (**F-TH**)

3-Aminothiophene oxalate (1.89 g, 0.01 mol) was dissolved in dichloromethane (40 ml), then triethylamine (2.53 g, 0.025 mol) was added. After the mixture solution was stirred and cooled to 0^{o}C in an ice water bath, trifluoroacetic anhydride (2.52 g, 0.012 mol) was added dropwise slowly and reacted at room temperature for 2 hours. At the end of the reaction, saturated $NaHCO_3$ solution was added until no bubbles formed. The reaction mixture was extracted with ethyl acetate three times, and the organic phase was combined. The organic phase was washed three times with saturated NaCl solution, dried by anhydrous Na_2SO_4, filtered, and evaporated. The crude product was further purified by column chromatography with dichloromethane/petroleum ether (4:1, by volume) to obtain white powder of **F-TH**. Anal. calcd for $C_6H_4NOF_3S$: C: H: N: S= 36.93: 2.07: 7.18: 16.43; found: C: H: N: S = 36.90: 2.00: 7.20: 16.50. ^{1}H NMR ($CDCl_3$, 25^{o}C TMS, δ): 8.16 (s, 1H), 7.71 (dd, *J*=3.2, 1.4Hz, 1H), 7.35 (dd, *J* = 5.4, 3.2Hz, 1H), 7.11 (dd, *J* = 5.2, 1.5Hz, 1H). MS (mass *m/z*): 195 [M^+]. FT-IR: 3284 cm^{-}

[1], 3159 cm^{-1}, 3124 cm^{-1}, 1701 cm^{-1}, 1595 cm^{-1},1387 cm^{-1}, 1193 cm^{-1}, 1152 cm^{-1}, 964 cm^{-1}, 837 cm^{-1}, 778 cm^{-1}.

The molecular structure of **F-TH** in solid state was determined via single crystal X-ray diffraction analysis. Colorless single crystals of **F-TH** suitable for sXRD analysis were grown via recrystallization and processed in CH_2Cl_2/CH_3CN (1:1, by volume) solution at room temperature. **F-TH** crystallizes in the orthorhombic non-centrally symmetric *Pca*2_1 space group with three similar molecules in one asymmetric unit, orientational disorder of the thienyl rings and F atoms are observed. A summary of the crystal data, collection parameters and refinement is given in **Table 13**, selected bond lengths (Å) and angles (°) are shown in **Table 14**.

Table 13. Details of the structure solution and refinement of **F-TH.**

Compound	F-TH
Chemical formula	$C_6H_4NOF_3S$
FW	195.16
Crystal system	Orthorhombic
Space group	*Pca*2_1
a (Å)	14.4988(10)
b (Å)	16.5844(9)
c (Å)	9.9542(5)
V (Å^3)	2393.5(2)
Z	12
Calculated density (Mg/m^3)	1.62464
Absorption coefficient(mm^{-1})	0.406
reflections collected	5010
independent reflections (R_{int})	2816 (0.017)
*R*1, *wR*2 [*I*>2σ(*I*)]	0.087, 0.261
*R*1, *wR*2 (all data)	0.107, 0.296

Table 14. Selected bond lengths (Å) and angles (°) of **F-TH**

Bond	Distance	Bond	Distance
C3_1—N1_1	1.429(10)	C6_2—F3_2	1.288(8)
C6_1—F3_1	1.308(9)	C6_2—F1_2	1.320(8)
C6_1—F2_1	1.330(9)	C6_2—F2_2	1.349(8)
C6_1—F1_1	1.338(9)	C3_3—N1_3	1.430(11)
N1_1—C5_1	1.297(12)	C6_3—F3_3	1.304(8)
C5_1—O1_1	1.211(13)	C6_3—F1_3	1.315(9)
C3_2—N1_2	1.422(10)	C6_3—F2_3	1.360(8)
N1_2—C5_2	1.276(13)	N1_3—C5_3	1.277(12)
C5_2—O1_2	1.237(14)	C5_3—O1_3	1.221(12
Atoms	Angles	Atoms	Angles
F3_1—C6_1—F2_1	117.8(12)	F1_2—C6_2—F2_2	95.5(11)
F3_1—C6_1—F1_1	111.7(11)	F1_3—C6_3—F2_3	100.7(11)
F2_1—C6_1—F1_1	100.3(12)	F3_3—C6_3—F1_3	115.5(12)
F3_2—C6_2—F1_2	109.6(11)	F3_3—C6_3—F2_3	110.8(10)
F3_2—C6_2—F2_2	119.3(11)		

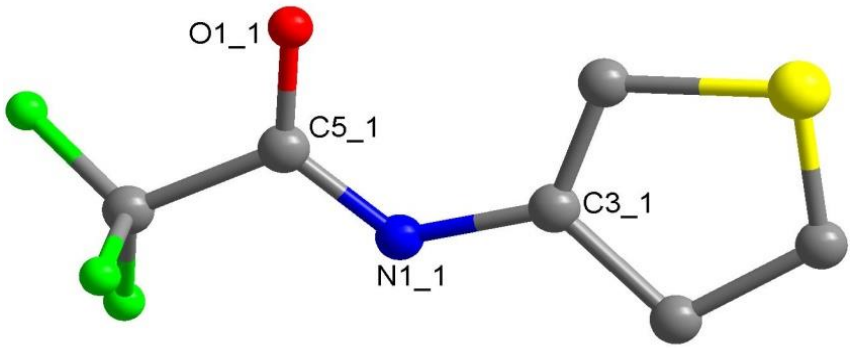

Figure 46. Molecular structure of **F-TH** with partial atom numbering scheme, H-atoms have been omitted for clarity (red = O, blue = N, gray = C, green = F, yellow = S), only one of the three independent molecules in the unit cell is shown.

As depicted in **Figure 46**, the structure of a **F-TH** molecule contains one S atom belonging to 3-thienyl ring, one N atom and one O atom belonging to an amide group, and three F atoms belonging to a CF_3 group. All the C—F bond lengths (1.29~1.36 Å) approach the standard value for a C(sp^2)—F single bond, and the C—O bonds

(1.21~1.24 Å) display double bond character, while the two type of C—N bond lengths are significantly different (**Table 15**), the C3_1—N1_1 (1.429(10) Å) bond exhibits single bond character but the C5_1—N1_1 (1.297(12) Å) bond length do not differ significantly from the $C(sp^2)==N(sp^2)$ standard value of 1.29 Å [147], indicating the partial double-bond feature of the amide bonds. As shown in **Figure 47**, there are amide-amide intermolecular hydrogen bonds connecting adjacent molecules to form one-dimensional chains lying parallel to the c axis, which further extend into a 3D supramolecular structure through Van der Waals interactions.

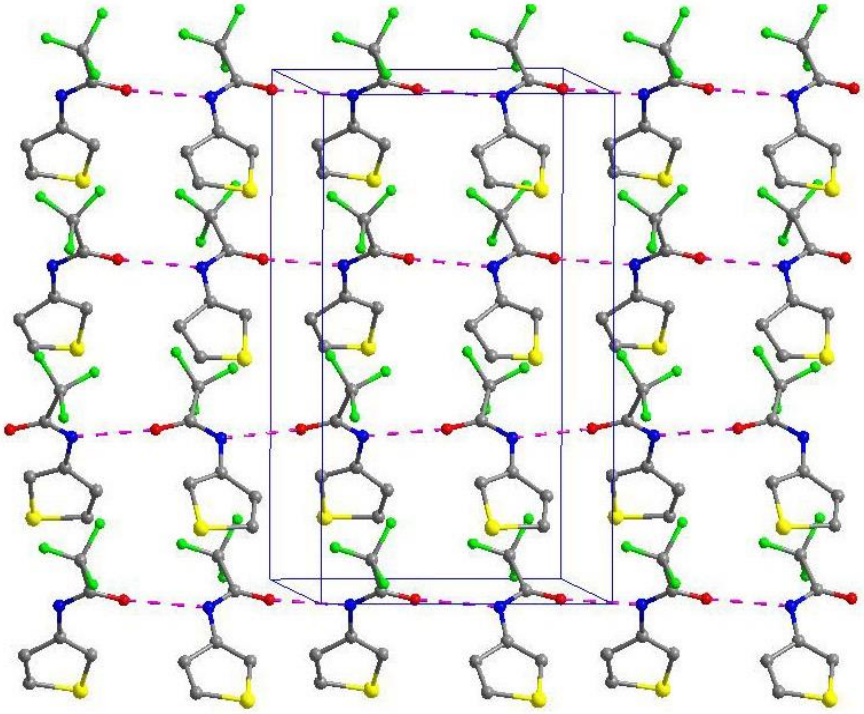

Figure 47. Molecular structure of **F-TH** with partial atom numbering scheme, H-atoms have been omitted for clarity (red = O, blue = N, gray = C, green = F, yellow = S), only one of the three independent molecules in the unit cell is shown.

Table 15 Hydrogen-bonding geometry (Å^{o}) of **F-TH**.

D—H•••A	D—H	H•••A	D•••A	D—H•••A
N1_1—H1B••• O1_1^{i}	0.860	2.068	2.875	156.13
N1_2—H1B••• O1_2^{ii}	0.860	2.065	2.877	157.19
N1_3—H1A••• O1_3^{iii}	0.860	2.081	2.878	153.83

Symmetry codes: (i) -x+1/2, y, z+1/2; (ii) -x-1/2, y, z-1/2; (iii) -x-1/2, y, z+1/2.

The distributions of the highest occupied molecular orbitals (HOMO) and the lowest unoccupied molecular orbitals (LUMO) computed at the B3LYP/6-311+G (d, p) level for the molecules of **F-TH**, thiophene and 3,4-ethylenedioxythiophene **(EDOT)** are illustrated in **Figure 48**. Calculation results indicate that the **F-TH** molecule has 49 occupied molecular orbitals (MOs), much more complicated in comparison with that of thiophene (22 occupied MOs) and **EDOT** (37 occupied MOs). The DFT calculations results of the HOMO level, LUMO level and HOMO-LUMO energy gap (E_g) of **F-TH** and **EDOT** are presented in **Table 16**. In these molecules, both the HOMOs and LUMOs are mostly π-antibonding type orbitals, **F-TH** has lower HOMO and LUMO levels than that of thiophene and **EDOT**. HOMO-LUMO energy separation has been used as a simple indicator of kinetic stability [148,149], the calculated E_g of **F-TH** is 5.98 eV, which is a bit smaller than E_g of thiophene (5.99 eV), and is larger than E_g of **EDOT** (5.61 eV) owing to strong electron-withdrawing ability of CF_3 group. These calculation results imply that **F-TH** may exhibit lower kinetic stability and higher chemical reactivity compared with **EDOT**.

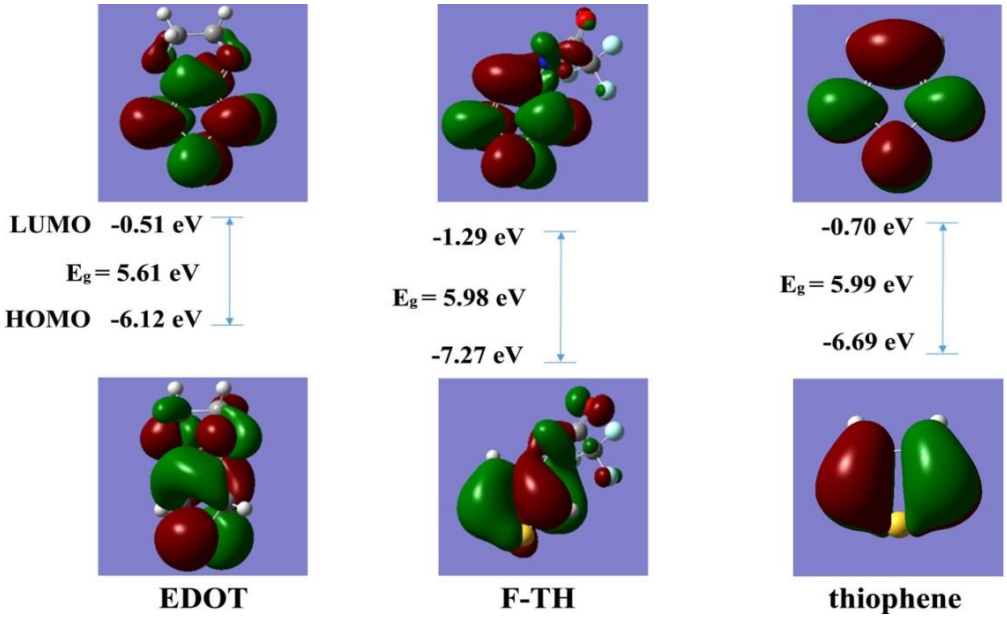

Figure 48. Molecular orbital surfaces and energies for the HOMO and LUMO of **EDOT**, **F-TH** and thiophene.

Table 16. DFT calculation Data of **F-TH**, thiophene and **EDOT**

Monomer	HOMO/eV	LUMO/eV	E_g/eV
F-TH	-7.27	-1.29	5.98
Thiophene	-6.69	-0.70	5.99
EDOT	-6.12	-0.51	5.61

4.2.2.2 Synthesis of tris[4-(3,4-ethylenedioxythiophene)phenyl]amine (**TEPA**)

As shown in **Figure 49**, the **TEPA** (tris[4-(3,4-ethylenedioxythiophene)phenyl]amine) monomer was obtained via a four-step synthetic route using **EDOT** and triphenylamine **TPA** (triphenylamine**)** as the starting materials in an overall yield of 55%.

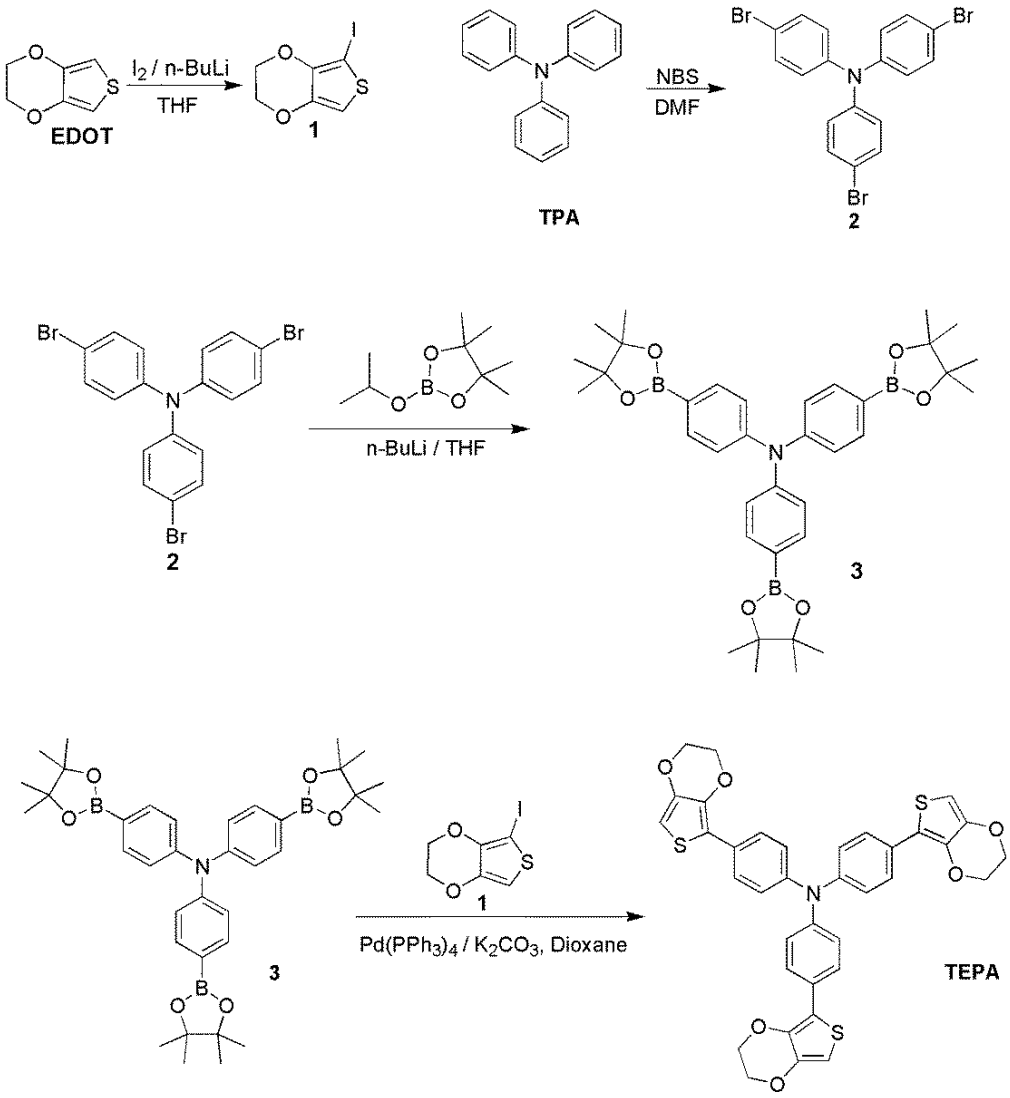

Figure 49. The new synthetic route for the **TEPA** monomer.

In detail, **TEPA** was obtained via a four-step synthetic route:

Step 1: synthesis of 2-iodo-3,4-(ethylenedioxy)thiophene (**1**).

A hexane solution of n-BuLi (16.1 mL, 2.4 M, 38.7 mmol) was added drop-wise to a solution of **EDOT** (5 g, 35.2 mmol) in tetrahydrofuran (THF, 50 mL) at –78 °C. The mixture was stirred for one hour at this temperature, then iodine (8.9 g, 35.2 mmol) in THF (50 mL) was slowly added to the solution, whereupon the red color slowly disappeared. After one hour of stirring at room temperature, water was added and the mixture was extracted with diethyl ether (3×100 mL). The combined organic layers were washed with aqueous Na_2SO_3, saturated $NaHCO_3$ solution, water and brine (100

mL each). The organic phase was dried over $MgSO_4$. After filtration and removing the solvent under vacuum, the white powder **1** was purified by recrystallization from ether (8.0 g, yield 84%).

Step 2: synthesis of 4,4',4''-Tribromotriphenylamine (**2**).

A solution of N-bromosuccinimide (NBS, 25 g,100 mmol) in N,N-dimethylformamide (DMF, 100 mL) was added drop-wise to a solution of **TPA** (10.0 g, 40.8 mmol) in DMF (100 mL) in a three-necked flask at 0 °C. The mixture was warmed to room temperature, stirred for an additional 12 hours, and then poured into excess water and extracted with CH_2Cl_2. The combined extracts were washed with brine and dried over $MgSO_4$ and then the solvent was evaporated under vacuum, the crude product of **2** (50 g, yield 100%) was obtained and used in the next step without purification.

Step 3: synthesis of Tris[4-(4,4,5,5-tetramethyl-1,3,2-dioxaborolan-2-yl) phenylamine (**3**).

n-BuLi (2.5 M in hexane, 85 mL, 205.4 mmol) was added dropwise to a solution of **2** (30 g, 62.2 mmol) in anhydrous THF (300 mL) at -78 °C under N_2 and the mixture was stirred for 2 hours. 2-Isopropoxy-4,4,5,5-tetramethyl-1,3,2- dioxaborolane (40.5 g, 217.7 mmol) was added in one portion to the mixture, which was then warmed to room temperature and stirred overnight. The solvent was evaporated under reduced pressure, the crude product was dissolved in CH_2Cl_2 (500 mL) and washed with water (3×200 mL). The organic phase was dried over $MgSO_4$, and the product of **3** was precipitated by reduction of the volume of the solvent to ca. 50 mL as a white solid (36.0 g, yield 64%).

Step 4: synthesis of **TEPA**.

A mixture of **1** (1.5 g, 5.6 mmol), **3** (0.9 g, 1.4 mmol) and K_2CO_3 (1.9 g, 14 mmol) was suspended in 30 mL of dioxane in a Schlenk flask. The air was removed by

evacuation and back-filling with argon. $Pd(PPh_3)_4$ (82 mg, 0.07 mmol) was added and the reaction mixture was degassed for 10 min with an argon flow. The mixture was then stirred under reflux for 24 h. The solvent was evaporated under vacuum and the residue was partitioned between CH_2Cl_2 and water, the organic phase was washed with brine and dried over $MgSO_4$ and then the solvent was evaporated under vacuum. The residue was purified chromatographically (SiO_2, PE: CH_2Cl_2=2:1) giving a yellow solid product of **TEPA** (0.80 g, yield 86%).

Samples obtained after chromatography were shown to be analytically pure by elemental analysis (calcd for **TEPA** ($C_{36}H_{27}NO_6S_3$): C: H: N: S= 65.0: 4.1: 2.1: 14.4; found: C: H: N: S = 65.0: 4.1: 2.1: 14.4). 1H NMR and FT-IR spectra of the obtained **TEPA** samples are similar to the reported spectra31 and are shown in **Figure 50** and **Figure 51**. The +ve ion electrospray MS (**Figure 52**) shows a peak at m/z = 666.1085 for $[M+H]^+$, which is very close to theoretical calculated value (666.1073).

In 2007, M. Chahma et al. reported the synthesis of **TEPA** through a Stille coupling reaction between tris[4-bromophenyl]amine and 2-tributylstannyl-3,4-ethylenedioxythiophene [150]. However, because of the toxicity of organotin reagents and the difficulties in separating organotin by-products from target products, this synthetic pathway his problematic in large-scale synthesis. As shown in **Scheme 1**, we obtained a light yellow powder of **TEPA** via a Suzuki-Miyaura cross-coupling reaction between tris[4-(4,4,5,5-tetramethyl-1,3,2-dioxaborolan-2-yl) phenylamine and 2-iodo-3,4-(ethylenedioxy)thiophene, the overall yield of **TEPA** through this four step synthetic route can be reached 55%. Compared with the previous route, our new route is greener and uses environmentally benign reagents. It will therefore be more suitable for industrial production.

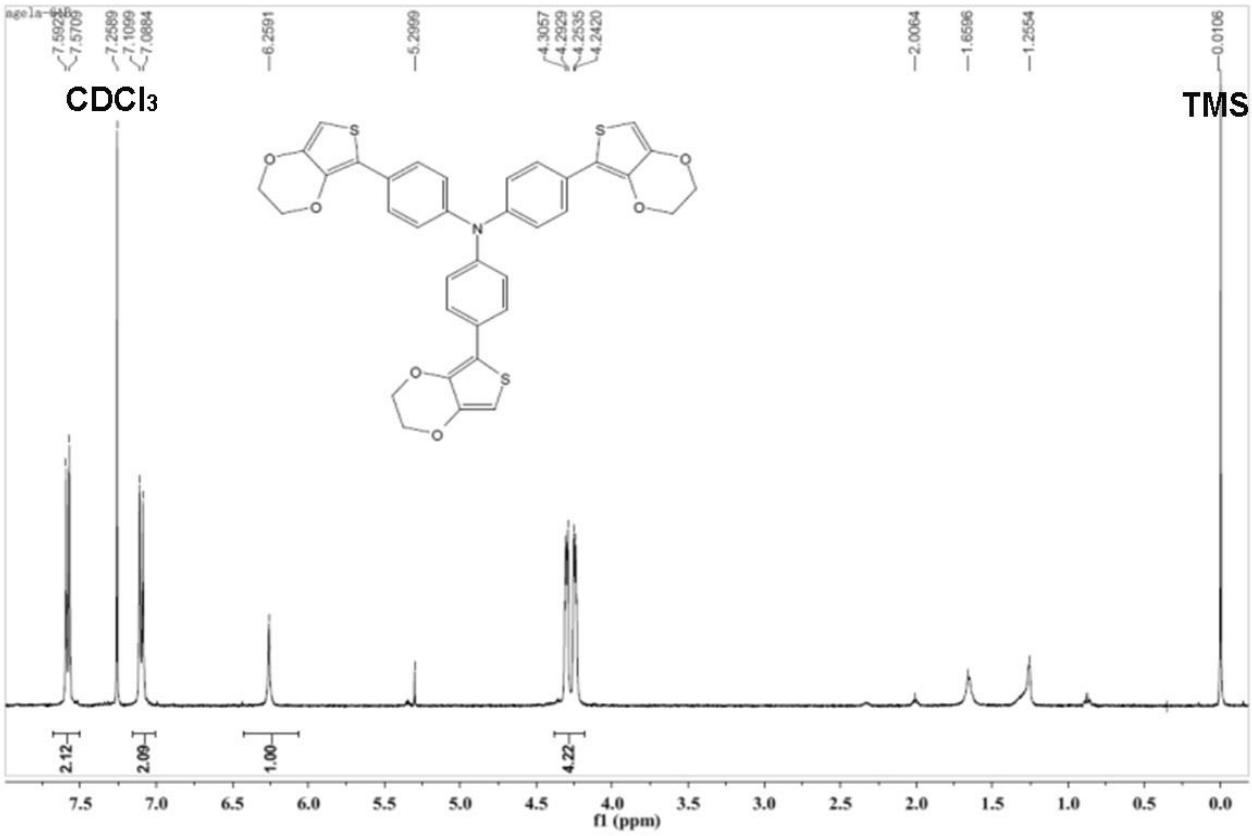

Figure 50. ^{1}H NMR ($CDCl_3$, 400 MHz) spectrum of **TEPA** monomer.

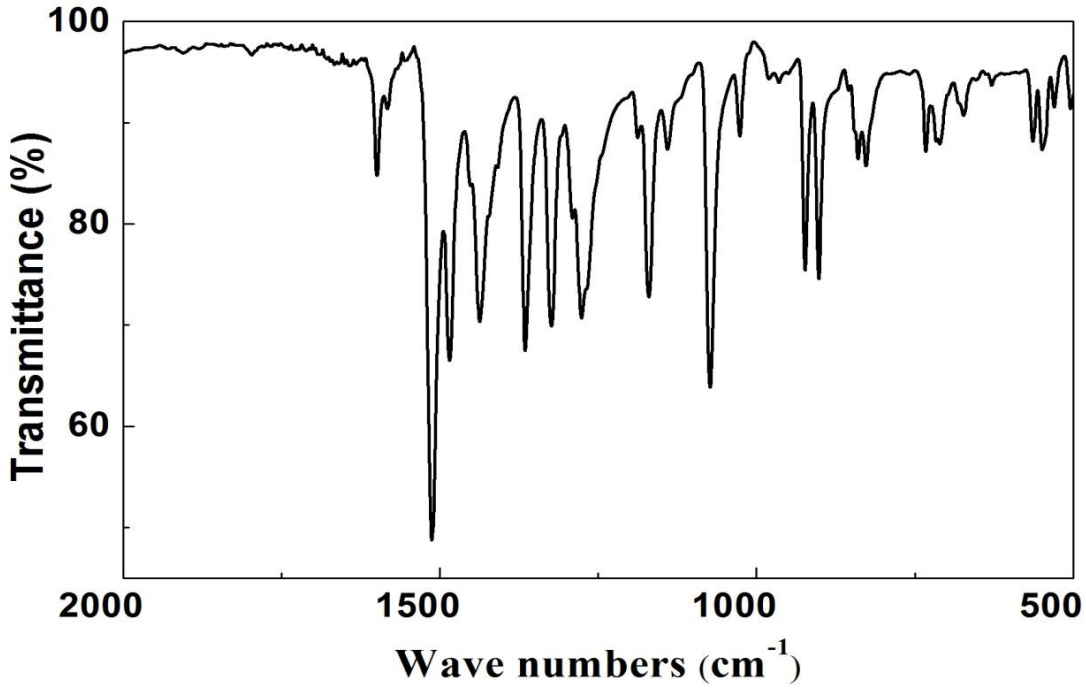

Figure 51. The FT-IR spectra of **TEPA.**

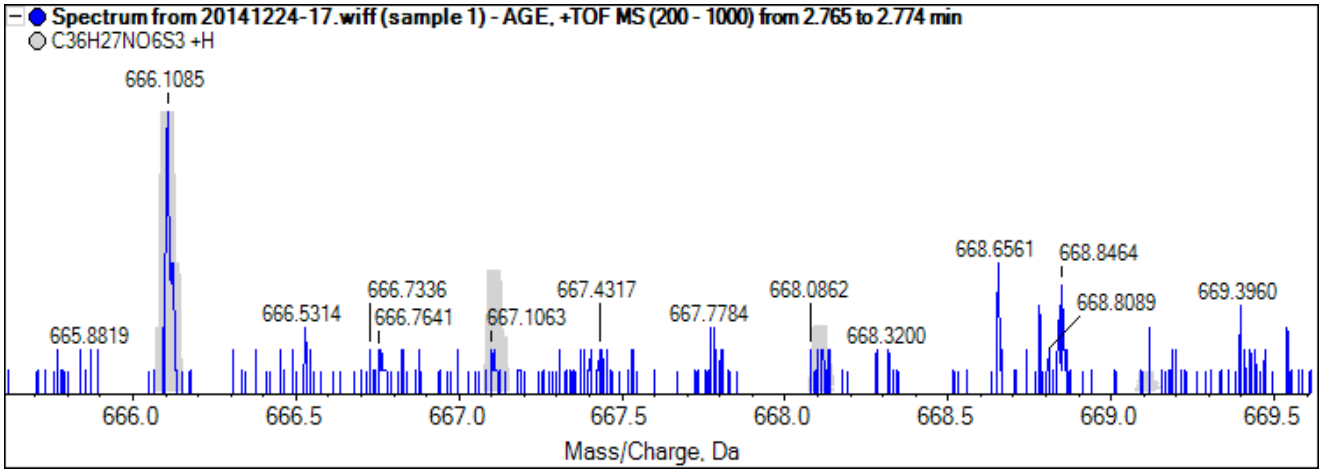

Formula	Intensity	Threshold	Expected m/z	Found at m/z	Error (ppm)
C36H27NO6S3	540	100	666.1073	666.1085	1.8

Figure 52. Mass spectrum and theoretical simulation of **TEPA.**

Yellow sheet-like crystals of **TEPA** suitable for single-crystal X-ray diffraction measurements were grown by slow evaporation from a CH_2Cl_2/CH_3CN (1:1, by volume) solution at room temperature. sXRD analysis was carried out at T= 293(2) K on an Oxford Diffraction Gemini four-circle diffractometer, equipped with a Ruby CCD detector and using graphite-monochromatized Mo-Kα radiation. Data reduction included intensity integration, background and Lorentz-polarization correction performed with the CrysAlisPrO Version 1.171.37.35 software package (Agilent Technologies, 2014). The structures were solved by direct methods and then refined with full-matrix least-square methods using SHELXL-2014 program, with all non-hydrogen atoms being refined anisotropically. A summary of the crystal data, collection parameters and refinement is given in **Table 17** and selected bond lengths (Å) and angles (°) as well as hydrogen-bonding geometries are listed in **Table 18** and **Table 19**. The dihedral angles between the two aromatic rings of **TEPA** molecule were calculated using the Diamond software. The calculated dihedral angles are summarized in **Table 20**.

Table 17. Details of the structure solution and refinement of **TEPA**.

Compound	TEPA
Chemical formula	$C_{36}H_{27}NO_6S_3$
FW	665.76
Crystal system	Monoclinic
Space group	$P2_1/c$
a (Å)	10.6825 (4)
b (Å)	15.4602 (9)
c (Å)	55.789 (3)
β(°)	93.021 (5)
V (Å^3)	9201.0 (8)
Z	12
Calculated Density (Mg/m^3)	1.442
Absorption coefficient(mm^{-1})	0.292
reflections collected	33718
independent reflections (R_{int})	16191 (0.076)
$R1[I>2\sigma(I)]$	0.088
*wR*2 (all data)	0.198

Table 18. Selected bond lengths (Å) and angles (º) of **TEPA**.

Bond	Distance	Bond	Distance
S1A—C1A	1.667 (13)	S1H—C6H	1.729 (11)
S1A—C6A	1.720 (11)	S1H—C1H	1.743 (13)
S1B—C1B	1.702 (12)	S1I—C1I	1.720 (13)
S1B—C6B	1.765 (11)	S1I—C6I	1.741 (11)
S1C—C6C	1.738 (11)	N1—C12B	1.419 (12)
S1C—C1C	1.745 (13)	N1—C12A	1.426 (14)
S1D—C1D	1.718 (13)	N1—C12C	1.447 (13)
S1D—C6D	1.746 (11)	N2—C12F	1.398 (12)
S1E—C1E	1.703 (13)	N2—C12E	1.410 (12)
S1E—C6E	1.719 (10)	N2—C12D	1.445 (13)
S1F—C6F	1.665 (11)	N3—C12H	1.416 (14)
S1F—C1F	1.685 (12)	N3—C12I	1.424 (13)
S1G—C1G	1.732 (12)	N3—C12G	1.447 (13)
S1G—C6G	1.742 (11)		
Atoms	Angles	Atoms	Angles

C12B—N1—C12A	121.6 (9)	C12E—N2—C12D	119.1 (9)
C12B—N1—C12C	118.5 (10)	C12H—N3—C12I	118.6 (10)
C12A—N1—C12C	119.8 (9)	C12H—N3—C12G	120.9 (10)
C12F—N2—C12E	122.2 (9)	C12I—N3—C12G	118.6 (10)
C12F—N2—C12D	118.7 (9)		

Table 19. Hydrogen-bonding geometry (Å,º) of **TEPA**.

D—H···A	D—H	H···A	D···A	D—H···A
C1B—H1BA···O2Ei	0.93	2.54	3.429 (16)	161.1
C1F—H1FA···O3	0.93	2.63	3.533 (16)	162.7
C1G—H1GA···O2Iii	0.93	2.65	3.549 (15)	162.8
C3A—H3AA···O4iii	0.97	2.48	3.286 (16)	140.0
C3B—H3BB···O15iv	0.97	2.48	3.279 (15)	139.2
C3D—H3DB···O1Iv	0.97	2.36	3.268 (17)	155.3
C3F—H3FA···O2Aiii	0.97	2.65	3.392 (16)	133.1
C3H—H3HA···O1Evi	0.97	2.43	3.345 (17)	156.3

Symmetry codes: (i) x, y−1, z; (ii) −x+1, y+1/2, −z+1/2; (iii) −x+1, −y+1, −z; (iv) x+1, y, z; (v) x+1, y+1, z; (vi) x−1, y−1, z.

Table 20. Calculated dihedral angle (°) of **TEPA** over all three independent molecules in unit cell.

	Name	Dihedral angle/°
between two phenyl groups of **TPA** core	1-1pp	60.7(6)
	1-2pp	74.5(3)
	1-3pp	70.2(5)
	2-1pp	60.2(2)
	2-2pp	73.8(1)
	2-3pp	68.8(3)
	3-1pp	59.9(2)
	3-2pp	73.9(5)
	3-3pp	66.5(3)
between a phenyl group and a combined thiophene ring from **EDOT** group	1-1pt	21.9(4)
	1-2pt	18.6(4)
	1-3pt	23.1(5)
	2-1pt	21.9(3)
	2-2pt	20.7(2)
	2-3pt	23.3(2)
	3-1pt	22.9(4)
	3-2pt	20.4(3)
	3-3pt	20.8(4)

As depicted in **Figure 53**, molecules of **TEPA** have a propeller-like **TPA** core with each 'blade' being an **EDOT** group and with the central N-atom being nearly trigonal planar [C-N-C over the three independent molecules being in the range of 118.5(10)-122.2(9)^{o}]. The carbon atoms at the 2-position of the thiophene rings of the **EDOT** groups are bonded to the para position of the triphenylamine groups of the **TPA** core. As shown in **Figure 54**, C—H···O intermolecular hydrogen bonds connect adjacent molecules and form two-dimensional layers within the lattice, which further extend into a 3D supramolecular structure through Van der Waals interactions (**Figure 55**). As shown in **Figure 56**, molecules of **TEPA** have a highly distorted arrangement. The three phenyl groups of the **TPA** core within individual molecules are not in the same plane, with the dihedral angles between the neighboring phenyl groups of **TPA** core being in the range of 59.9-74.5^{o} (**Figure 56a**). In addition, the phenyl and thiophene rings are also not co-planar, with the dihedral angles between these rings being in the range of 18.6-23.3^{o} (**Figure 56b**). These features are important because, in general, planarity and the resulting conjugation are strongly related to the band gap and conductivity of polymers, while the planarity of monomer units determines the planarity of the conjugated polymer to a large extent, small conformational differences may produce large band-gap effects in conjugated polymers [151-154]. The structure of the **TEPA** monomer is therefore not only related to the conformation of **PTEPA** but also to its physical properties.

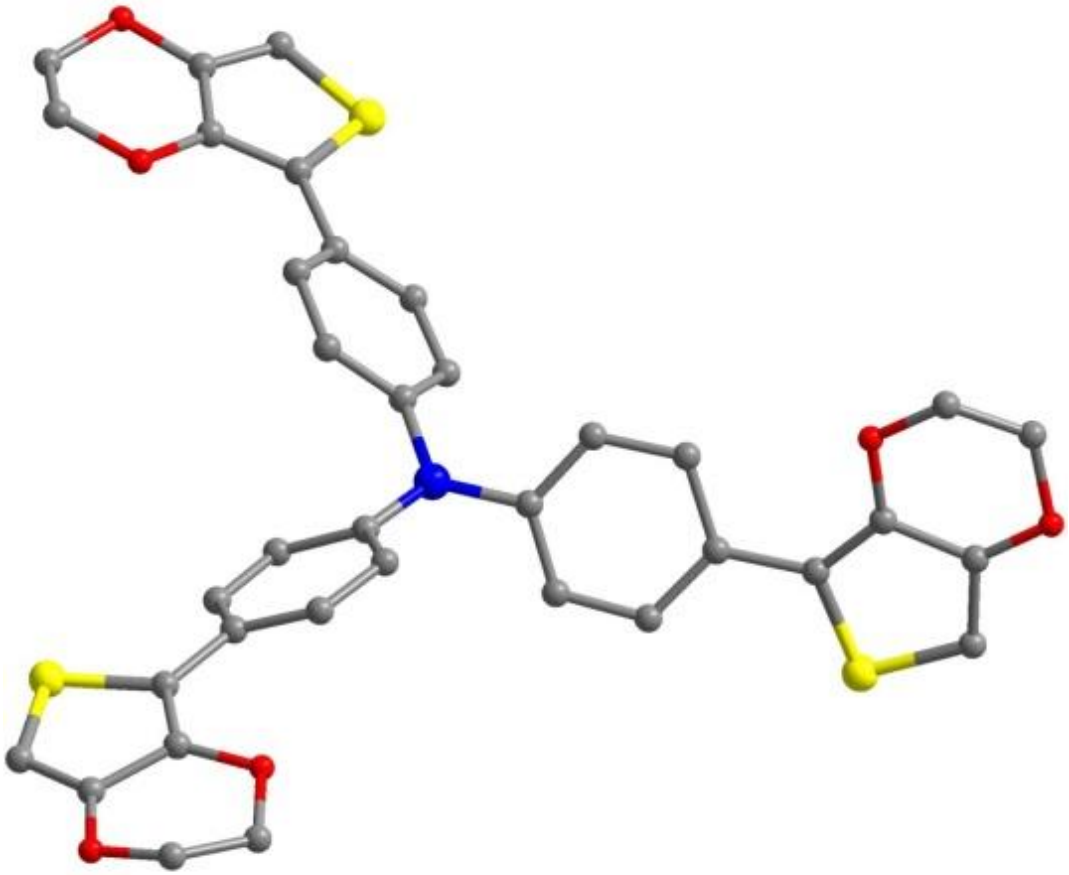

Figure 53. Molecular structure of **TEPA**, H-atoms have been omitted for clarity (red = O, blue = N, gray = C, yellow = S), and only one of the three independent molecules in the unit cell is shown.

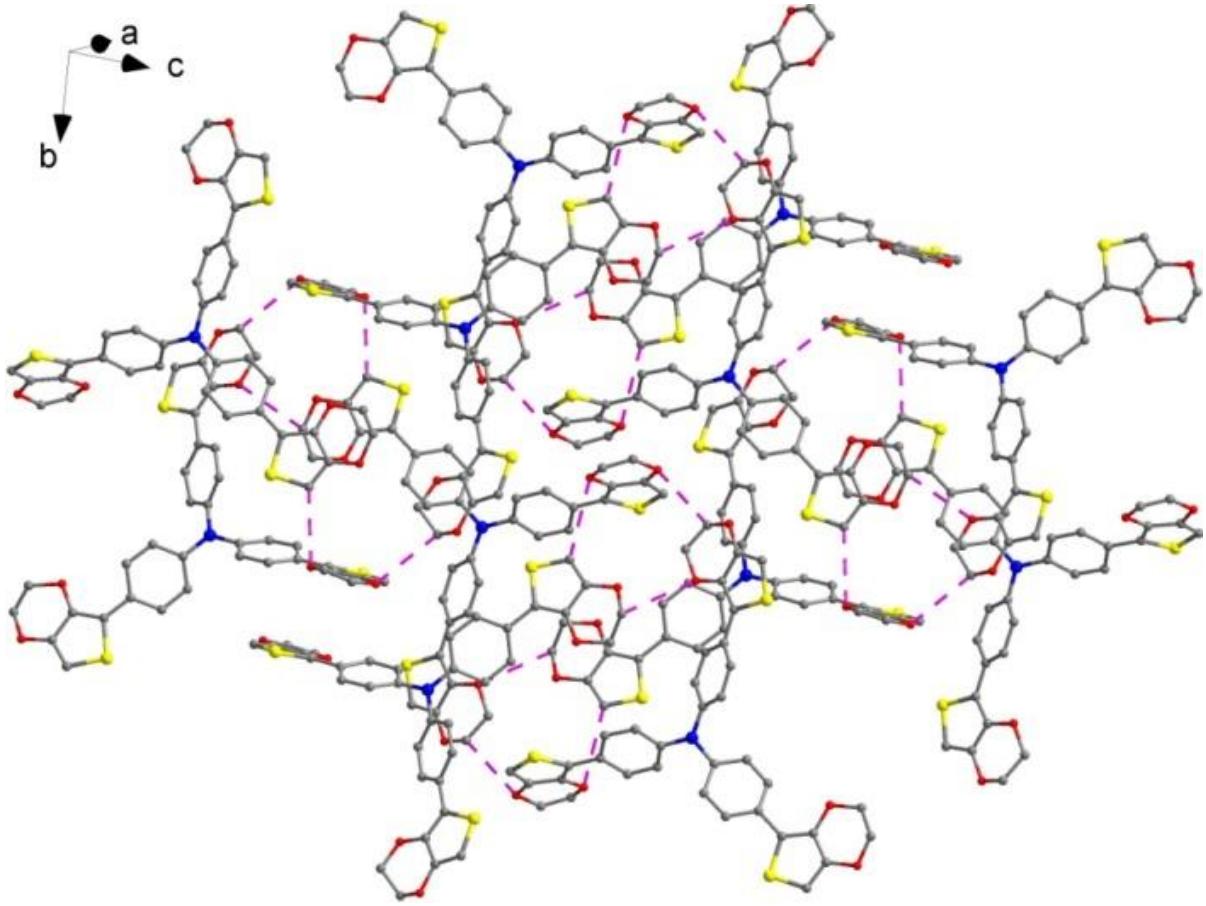

Figure 54. Two-dimensional layers of **TEPA** molecules linked by C—H···O intermolecular hydrogen bonds.

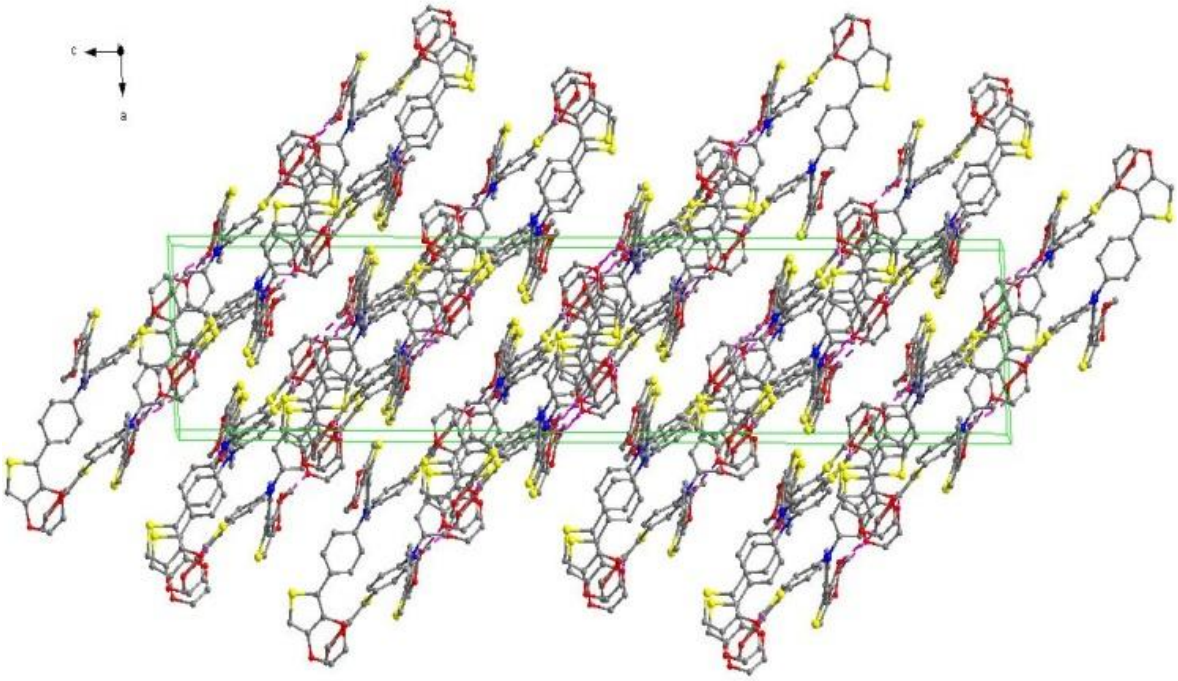

Figure 55. Molecular packing of **TEPA**.

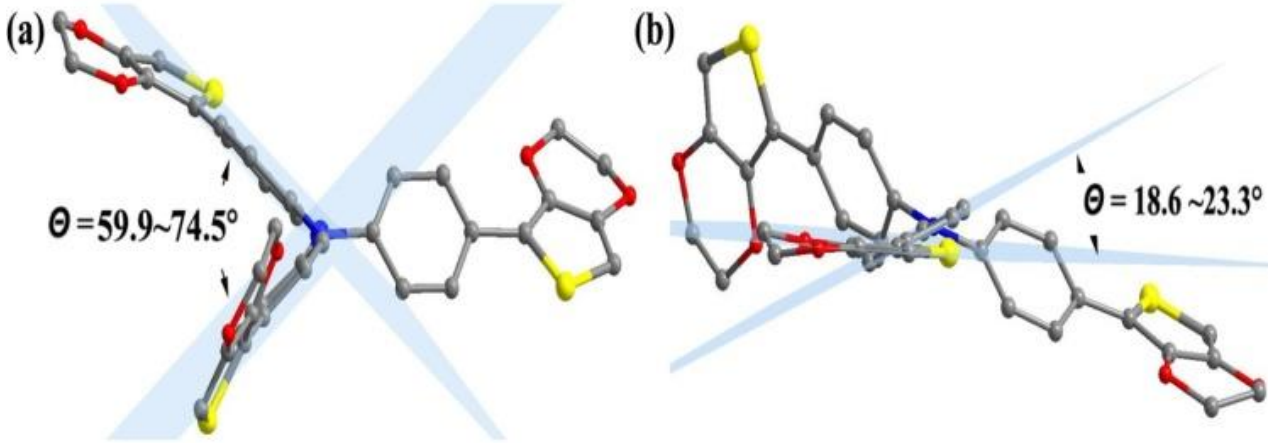

Figure 56. Key dimensions of the **TEPA** monomer units, indicating the distortion of the polymer building blocks.

In some previous reports, due to the lack of accurate structural informations, monomeric units have been approximated to completely planar, 'star-shaped' building blocks [155-157]. As a result, it has been assumed that the highly porous polymers observed result from the aggregation of monomers into cyclic units which build together into planar, honey-comb arrangements e.g. in poly[1,3,5-tris(4-diphenylamino-phenyl)benzene] which has been shown to possess a highly porous structure. As represented in **Figure 57**, the **TEPA** monomer is in fact not a completely planar building block but is slightly pyramidalised at the central N1 atom with respect to the terminal C atoms (C1A, C1B, C1C), which will form C-C bonds to other monomer units upon polymerisation, the distances from the central N atoms to the terminal C atoms over all three independent molecules in the unit cell are in the range of 0.808-0.817 nm, while the associated C-N-C angles are in the range of 117.4-122.9°.

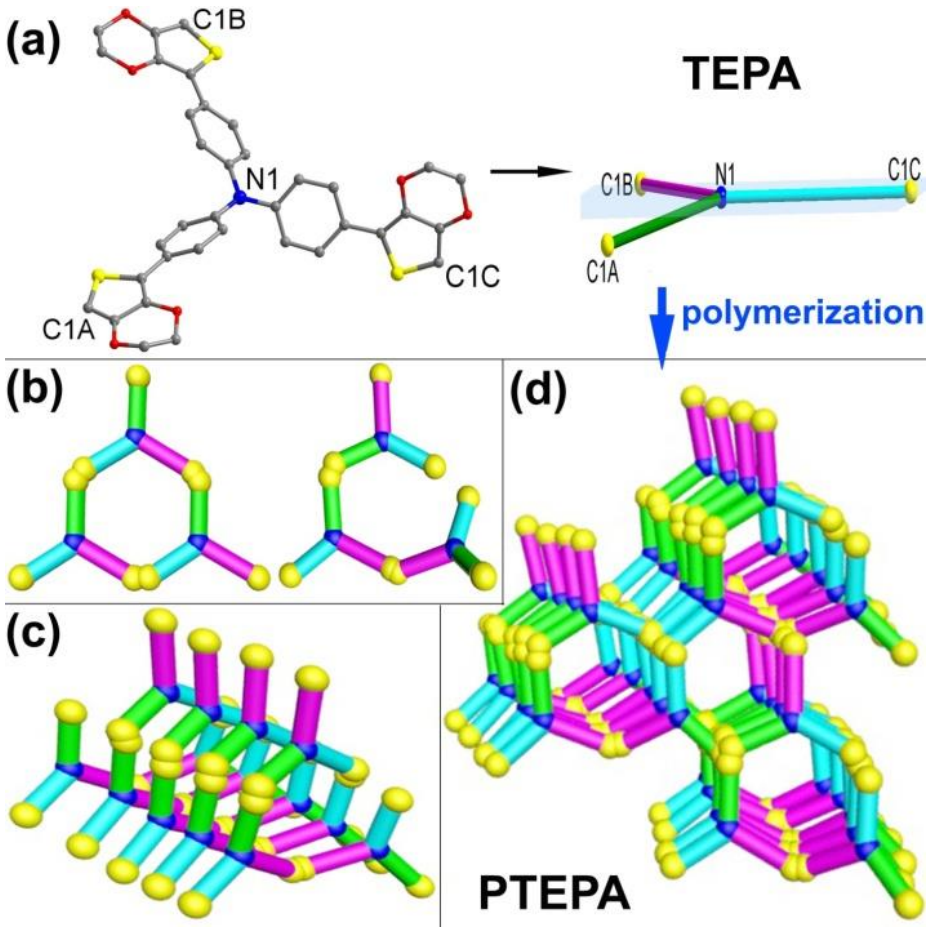

Figure 57. (a) Schematic representation of the **TEPA** monomer as a building block, (b) two possible assemblies of **PTEPA**, (c) a possible spiral channel of **PTEPA**, (d) a possible porous polymer structure of **PTEPA**.

Figure 57 shows two possible assemblies of **TEPA**, although it is possible to assemble a nanoring through three connected **TEPA** molecules (shown on the left of **Figure 57b**) which would form the previously proposed honeycomb sheet arrangement, the inherent distortion of the building blocks of **TEPA** are, we believe, more likely to result in the formation polymer chains (**Figure 57b**, right). In this case polymerization of **TEPA** would result in irregular spiral channels (**Figure 57c**) instead of the ordered columnar channels which would occur in a honeycomb structure. As shown in **Figure 57d**, cross-linking of this arrangement will give a three-dimensional porous dendritic structure. As the degree of polymerization

increases, the effect of the bifurcation and distortion of **PTEPA** will be accumulated throughout the structure of the polymer, while the pores and channels in **PTEPA** will be also gradually twisted and blocked by the external branches. This less porous structure is consistent with porosity measurements of **PTEPA** (see section 4.2.3.2). It was reported that Polytriphenylamine (**PTPA**) displays negligible microporous structure with a very small surface area, which, it was proposed, may be due to the difficulty in building a porous honeycomb structure using a monomer with shorter connecting groups. Based on this hypothesis, we speculate that the structure of **PTPA** contains similar twisted pores and channels to that proposed for **PTEPA**.

4.2.3 Preparation and properties of conjugated polymers

4.2.3.1 Preparation and properties of P(F-TH) and P(F-TH:EDOT)

The conjugated polymer film of **P(F-TH)** was prepared via constant potential polymerization onto the ITO substrate at 1.9V vs Ag/AgCl. Electrochemical polymerization was performed in 0.1 M $TBAPF_6$/ CH_3CN containing 0.03 $mol \cdot L^{-1}$ **F-TH** and the amount of electricity accumulated on the films of ITO glass (0.9 cm × 2.6 cm) was 0.06 C using a three-electrode system with Ag/AgCl reference electrode and Pt sheet counter electrode. After that, **P(F-TH)** was dedoped at -0.6 V for 1 minute.

The film of **P(F-TH:EDOT)** was prepared via constant potential copolymerization of the **F-TH** and **EDOT** monomers onto the ITO substrate at 1.4V. This electrochemical copolymerization was performed in 0.1 M $LiClO_4$ / CH_3CN solution containing 5.0 $mmol \cdot L^{-1}$ **F-TH**, 5.0 $mmol \cdot L^{-1}$ **EDOT,** and the amount of electricity accumulated on the films of ITO glass (0.9 cm × 2.6 cm) was 0.05 C using a three-electrode system with Ag/AgCl reference electrode and Pt sheet counter electrode. After that the **P(F-TH:EDOT)** film was dedoped at -0.8 V.

The film of **PEDOT** for comparison was also prepared via constant potential copolymerization of the **EDOT** monomers onto the ITO substrate at 1.4V. Electrochemical polymerization was performed in 0.1 M $LiClO_4$/ CH_3CN containing 5.0 mmol·L^{-1} **EDOT,** and the amount of electricity accumulated on the films of ITO glass (0.9 cm × 2.6 cm) was 0.05 C using a three-electrode system with Ag/AgCl reference electrode and Pt sheet counter electrode. After that, the **PEDOT** film was dedoped at -0.8 V.

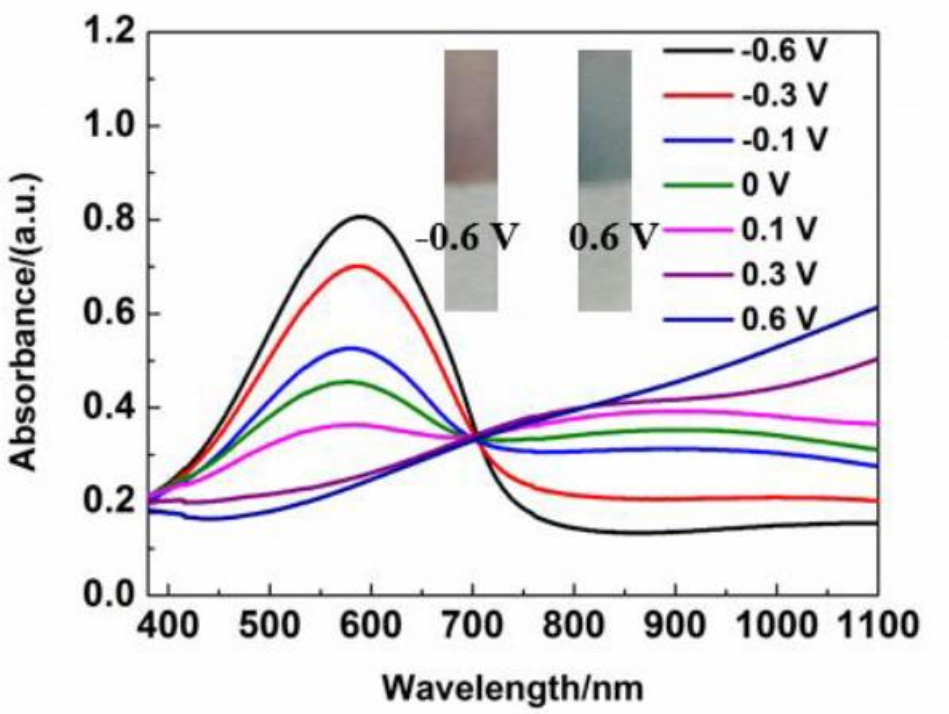

Figure 58. Optical absorption spectrum of **P(F-TH)** under different potentials (-0.6~0.6V).

Visible and NIR transmission spectra of **P(F-TH)** at different potentials (-0.6 to 0.6 V) are shown in **Figure 58**. **P(F-TH)** is a cathodically-colored film with a color change from brown at -0.6 V to sky-blue in the oxidized state at 0.6 V. In the neutral state, the visible absorption band of **P(F-TH)** centered around 590 nm is attributed to the π-π* transition. As the potential increases to the oxidized state, the visible absorption band of **P(F-TH)** gradually decreases, but a new **NIR** absorption related to the electronic transition of the polaron and the dipolaron of the doped ions strengthens.

Due to the molecular structure of **F-TH**, we found it is very difficult to obtain good homopolymer film from **F-TH** through electrochemical polymerization, which prompted us to consider about the copolymerization of **F-TH** with **EDOT**. In another aspect, the presence of **F-TH** units will affect the electro-optical properties of obtained film. In an initial study, copolymer **P(F-TH:EDOT)** films were prepared by electrochemical polymerization.

As shown in **Figure 59**, both **P(F-TH:EDOT)** and **PEDOT** films' surface have a fibril morphology, but the fibers in **P(F-TH:EDOT)** are generally thinner than those in **PEDOT**. Besides, fibers in **PEDOT** are partly agglomerated together and form a rough surface with disordered pores (**Figure 59a**, **Figure 59b**). In **P(F-TH:EDOT)**, the reticular fibers formed a loose sponge-like nanoporous network, which is more favorable for ions insertion and extraction (**Figure 59c** and **Figure 59d**).

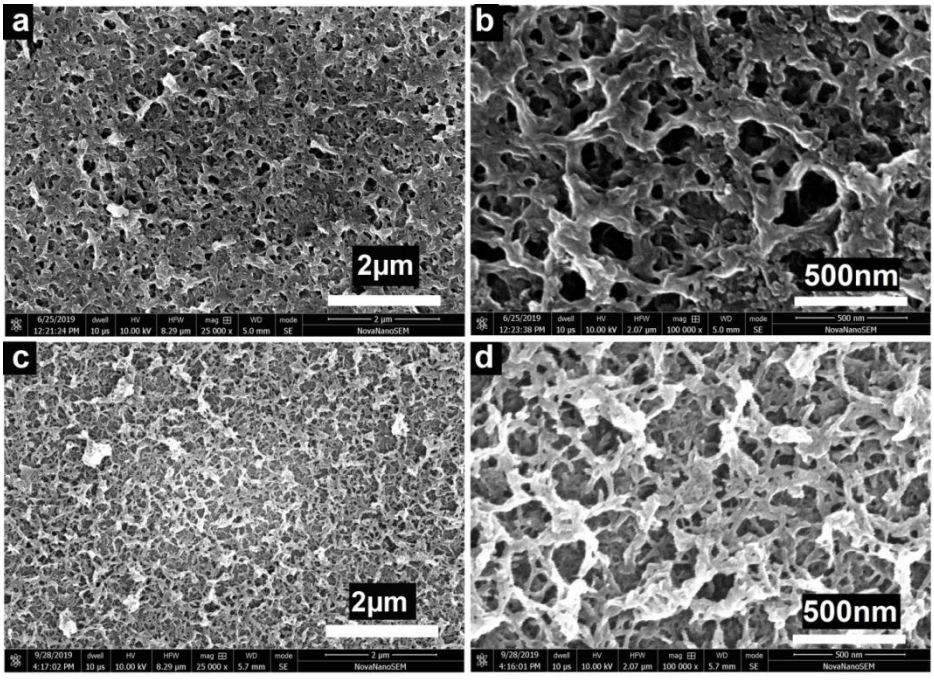

Figure 59. SEM images of **PEDOT** taken at a magnification of (a) 25k and (b) 100k; SEM images of **P(F-TH:EDOT)** taken at a magnification of (c) 25k and (d) 100k.

In order to evaluate their properties, the **P(F-TH:EDOT)** and **PEDOT** films were electrodeposited onto **ITO** coated glass having dimensions of 2.6 cm × 0.9 cm at a

constant potential of 1.4 V *versus* Ag/AgCl and passing charge of 0.05 C to form films with an average thickness of ~86.9 nm for **P(F-TH:EDOT)** and ~85.3 nm for **PEDOT**. As shown in **Figure 60**, water and acetonitrile droplet contact angle measurements performed on **P(F-TH:EDOT)** and **PEDOT** films revealed significant differences in the wettability. **P(F-TH:EDOT)** exhibits a contact angle with water of 56.9° (**Figure 60a**) larger than that of **PEDOT** (33.5°, **Figure 60b**), indicating that **P(F-TH:EDOT)** has a reduced hydrophilicity compared to **PEDOT**. According to previous reports, most **EDOT**-containing polymers are sensitive to moisture in their neutral state, **P(F-TH:EDOT)** with reduced hydrophilicity is expected to increase its resistance to environmental moisture. On the other hand, **P(F-TH:EDOT)** exhibits a contact angle with acetonitrile of 10.9° (**Figure 60c**), smaller than that of **PEDOT** (25.3°, **Figure 60d**), indicating that **P(F-TH:EDOT)** has a better oleophilic wetting behavior than **PEDOT.** Wettability has an important impact on electrode materials' electrochemical performance. Although few studies mentioned the relationship of electrochromic properties with electrical contacting behavior of electrode-electrolyte interfaces in electrochromic conjugated polymers, it has been widely studied in batteries and supercapacitors that wettability of electrodes to electrolyte is strongly related with the capacity and high-rate dischargeability. To date, lots of researches have been focused on improving the electrode-electrolyte wettability to enhance the utilization of electrode capacity and decrease electrolyte resistance. It can be inferred that the enhanced wettability of **P(F-TH:EDOT)** to acetonitrile probably will be beneficial to improve the electrochromic performance of **P(F-TH:EDOT)** in the electrolyte of acetonitrile.

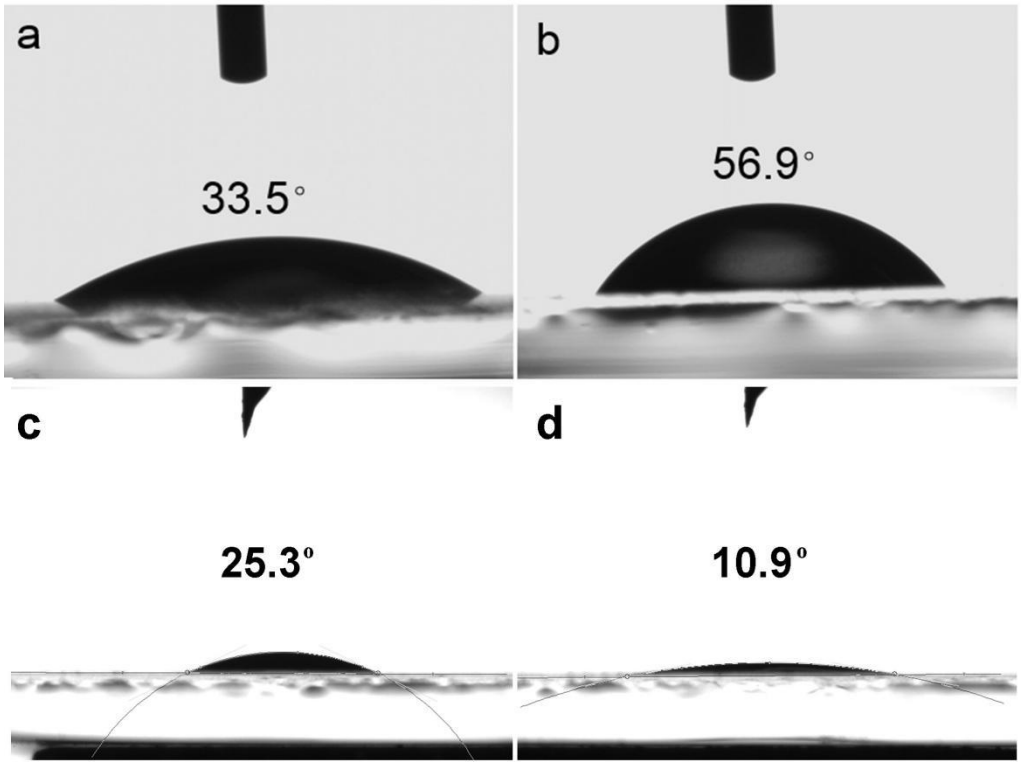

Figure 60. Water droplet contact angles of (a) **PEDOT** and (b) **P(F-TH:EDOT)**, CH_3CN droplet contact angle of (c) **PEDOT** and (d) **P(F-TH:EDOT)**.

P(F-TH:EDOT) and **PEDOT** exhibit similar electrochemical behavior in 0.1 mol·L^{-1} $LiClO_4/CH_3CN$ solution. As shown in Fig. 61a, cyclic voltammetry (CV) curve of **P(F-TH:EDOT)** displays two oxidation peaks ($E_{p,a}$ = 0.30 V and $E_{p,a}$' = 1.10 V) and a reduction peak ($E_{p,c}$ = -0.74 V) similar to the CV curve of **PEDOT** displaying also two oxidation peaks ($E_{p,a}$ = 0.30 V and $E_{p,a}$' = 1.21V) and a reduction peak ($E_{p,c}$ = -0.69 V). The first oxidation peak of **P(F-TH:EDOT)** and **PEDOT** appears at the same potential, but both the second oxidation peak and the reduction peak of **P(F-TH:EDOT)** were shifted to a lower potential ($E_{p,a}$' = 1.21→1.10 V, $E_{p,c}$ = -0.69 V→-0.74 V) compared to that of **PEDOT**. Besides, **P(F-TH:EDOT)** exhibited substantially larger current density than **PEDOT**, proving that **P(F-TH:EDOT)** has higher electrochemical activity in comparison with **PEDOT**. As shown in Fig. 61b, **P(F-TH:EDOT)** film is stable and preserves its electroactivity at high scan rates. The

peak current densities $j_{p,a}$, $j_{p,a}$' and $j_{p,c}$, were all proportional to the scan rate, which indicated that the electrochemical processes are non-diffusion controlled.

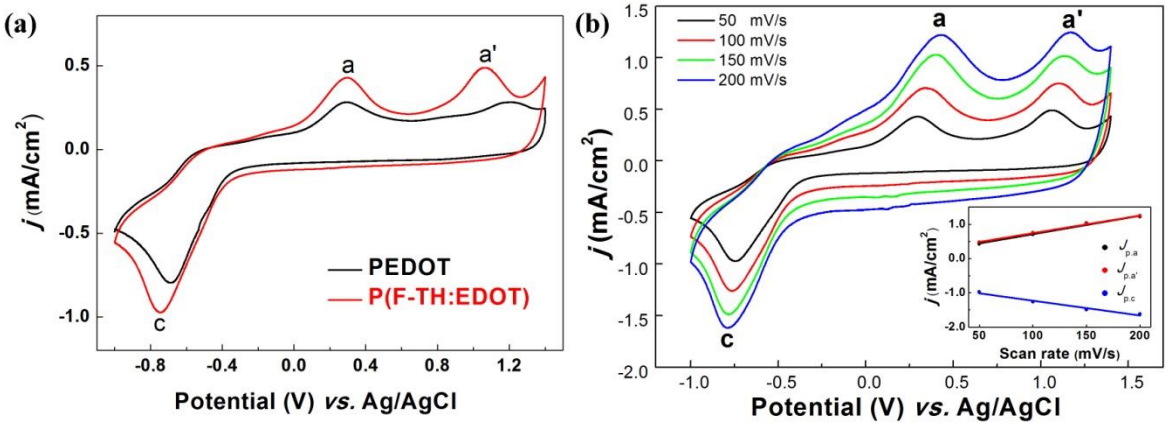

Figure 61. (a) CV curves of the **P(F-TH:EDOT)** (red) and **PEDOT** (black) at a scan rate of 50 mV·s^{-1} in 0.1 mol·L^{-1} $LiClO_4/CH_3CN$ solution; (b) CV curves of the **P(F-TH:EDOT)** at different scan rate in 0.1 mol·L^{-1} $LiClO_4/CH_3CN$ solution and plots of the peak currents in different scan rate (insert).

Nyquist representation of the impedance spectra of **P(F-TH:EDOT)** and **PEDOT** films modified electrodes were collected in the frequency range of 10^5 - 1Hz in 0.1 mol·L^{-1} $LiClO_4/CH_3CN$ solution (**Figure 62**). In the high frequency range, the spectra include semicircles which are attributed to the processes at the ITO/film and film/solution interfaces, while the low frequency part corresponds to the charge transport processes in the bulk of the film. The impedance spectra could be fitted using the equivalent circuit shown in **Figure 62b.** The circuit can be decomposed in three elements connected in series: (i) the cell resistance R_s, (ii) the impedance at the electrode/solution interface modelled by a parallel combination of the charge transfer resistance R and a capacitance C_i, and (iii) the impedance associated to the charge transport in the bulk of the film composed of a parallel combination of a constant phase element CPE_F and a Warburg element W_F. The charge transfer resistance of **P(F-TH:EDOT)** is 20.6 Ω lower that of **PEDOT** (28.9 Ω), which confirms that **P(F-TH:EDOT)** film is more efficient and faster to exchange ions with the solution. In

addition, W_F value for **P(F-TH:EDOT)** is higher than that of **PEDOT**, which can be attributed to the faster ion diffusion coefficient in **P(F-TH:EDOT)** film. These results are probably due to the enhanced wettability to electrolyte solution and the sponge-like nanoporous network of **P(F-TH:EDOT)** which supplies sufficient ion-transfer highways to promote the electrolyte penetration.

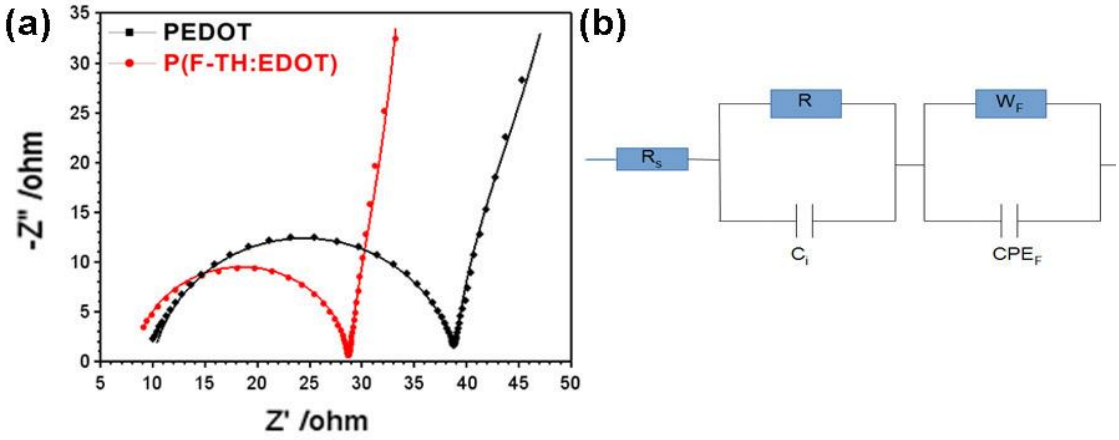

Figure 62. (a) Nyquist plots of the impedance spectra of **P(F-TH:EDOT)** (red) and **PEDOT** (black) modified electrodes measured in 0.1 mol·L^{-1} $LiClO_4/CH_3CN$, (b) Equivalent circuit used to fit the spectra.

Visible and NIR transmission spectra of **P(F-TH:EDOT)** and **PEDOT** films at different potentials (-0.8 to 0.8 V) are shown in **Figure 63**. As determined by the onset of the π-π* transition, the **P(F-TH:EDOT)** films obtained under these conditions has a band gap of ca. 1.61 eV (771 nm), slightly larger than that of **PEDOT** films (1.53 eV, 809 nm). Similar to **PEDOT**, **P(F-TH:EDOT)** is a cathodically-colored film with a color change from deep blue at -0.8 V to transmissive sky-blue in the oxidized state at 0.8 V. In the neutral state, the visible absorption band of **P(F-TH:EDOT)** centered at 616 nm is attributed to the π-π* transition, which is a bit blue-shifted compared with that of **PEDOT** (620 nm). As the potential increases to the oxidized state, the visible absorption of **P(F-TH:EDOT)** gradually decreases, but a new NIR absorption related to the electronic transition of the polaron and the

dipolaron of the doped ions strengthens.

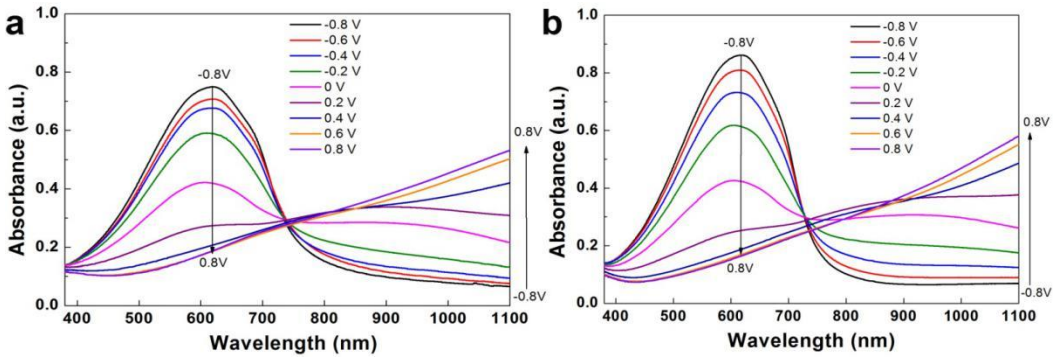

Figure 63. Spectroelectrochemical spectra of (a) **PEDOT** and (b) **P(F-TH:EDOT)** with different applied potentials between -0.8 V and 0.8 V.

Coloration efficiency (CE) is one of the most important characteristics for ECPs. Calculating on the basis of **Figure 64a** and **Figure 64b**, the CE value of **P(F-TH:EDOT)** achieves up to 167.9 cm^2/C, 55% higher than that of **PEDOT (**108.1 cm^2/C, ESI**).** As shown in **Figure 64c** and **Figure 64d**, **P(F-TH:EDOT)** exhibits improved electrochromic properties with higher optical contrast (55% at 616nm) and shorter coloring time (0.70s) compared to **PEDOT** (43% optical contrast at 620nm, 1.57s coloring time). These phenomena may be also attributed to the enhanced wettability to electrolyte solution of **P(F-TH:EDOT)**.

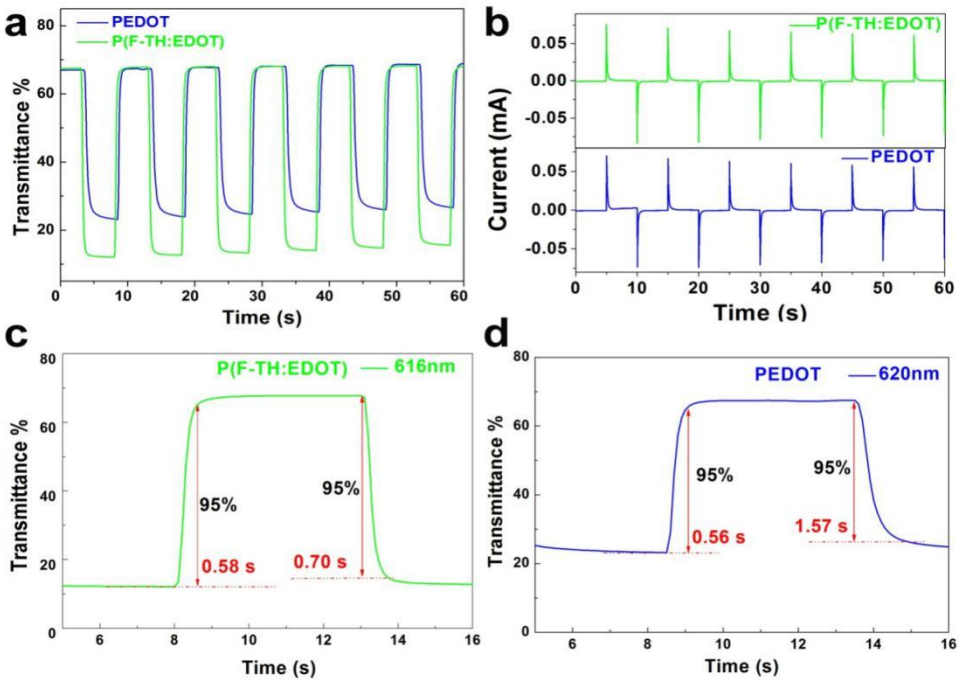

Figure 64. The simultaneous monitoring of (a) transmittance and (b) switching current for **P(F-TH:EDOT)** film (green) monitored at 616 nm and **PEDOT** film (blue) monitored at 620 nm, switching response for (c) **P(F-TH:EDOT)** and (d) **PEDOT** films monitored at corresponding wavelengths in 0.1 mol·L^{-1} $LiClO_4/CH_3CN$ solution between their neutral (-0.8 V) and oxidized (0.8 V) states at 5 s intervals.

4.2.3.2 Preparation and properties of PTEPA

Dendritic homopolymer and copolymer films based on **TEPA** have been synthesized via electropolymerization in previous reports [150]. But all of these polymers exhibit insolubility in conventional organic solvents, which introduces difficulties for large-scale production. Microemulsion polymerization has been regarded as a simple and reliable process for preparation of nanostructured conjugated ploymers and oligomers [158-161]. In this work, **PTEPA** powder was prepared via micelle-induced self-assembly and in situ polymerization of **TEPA** monomers. As a surfactant, dodecyltrimethylammonium bromide (**DTAB**) forms micelles between the stirred aqueous and organic biphasic system during the microemulsion polymerization,

TEPA diffuses into the micelles, where the oxidizing agent oxidizes it and subsequent polymerization occurs. The detail of the preparation process as follows:

0.2 g **DTAB** and 12 mL of 0.4 mol/L $FeCl_3$ aqueous solution were mixed and stirred for 1 h at room temperature in a two-necked round bottom flask equipped with a dropping funnel. Subsequently, the **TEPA** monomer (1 mmol) was dissolved in 13 mL CH_2Cl_2, which was added dropwise to the previous solution with vigorous stirring. After polymerization for 18 h, the organic phase was decanted and washed several times with distilled water to remove the organic solvent. The powder of **PTEPA** produced was finally washed with methanol to wash out unreacted monomer and dried under vacuum at room temperature.

As shown in **Figure 65**, the obtained **PTEPA** powder is composed of irregular nanoparticles, most of which loosely agglomerated together. Nitrogen adsorption-desorption experiments were conducted to further explore the microstructure of the **PTEPA**. As presented in **Figure 65d**, the **PTEPA** exhibits a type IV isotherm with hierarchical pore structure: an obvious hysteresis loop between the sorption curve and the desorption curve suggests the presence of mesopores. A significant rise in the sorption curve in the high pressure region ($0.80 < P/P_0 < 0.95$) indicates the presence of macropores, and a sharp uptake at low pressures ($P/P_0 < 0.01$) is a characteristic feature for microporous materials. The Brunauer–Emmett–Teller (**BET**) surface area of **PTEPA** calculated in the low pressure region ($0.009 < P/P_0 < 0.05$) of the isotherm is 67 m^2/g, and the total pore volume was calculated as 0.25 cm^3/g ($P/P_0 = 0.992$) for **PTEPA**. Pore size distributions calculated from desorption branches by the Barrett-Joyner-Halenda (BJH) model are given in **Figure 65e**. **PTEPA** display typical hierarchical pore size distribution with a highest peak centering at ca. 1.94 nm, a lower peak centering at ca. 7.98 nm and micropores smaller than 1.53 nm. The

average pore radius is 6.8 nm. In addition, micropore distribution of **PTEPA** analyzed by the Horvath-Kawazoe method (**Figure 65f**) reveals that **PTEPA** has a narrow micropore size distribution with median pore width of 1.07 nm. These results prove that **PTEPA** is nanoporous, which is in accord with the schematic polymer structure of **PTEPA**. The macropores and mesopores in **PTEPA** are mainly derived from the removed solvent and surfactant after polymerization, while the micropores stem from the porous framework of **PTEPA**. Inherent nanopores make the numerous active sites of **PTEPA** accessible by electrolyte ions during electrochemical processes. This may benefit the performance in electrical energy storage systems.

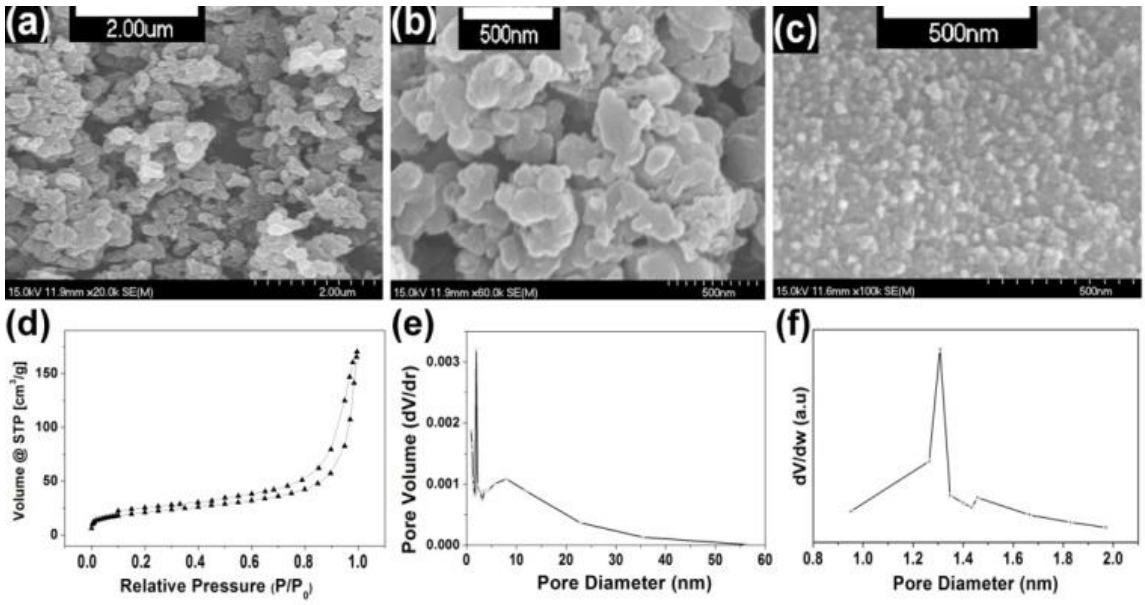

Figure 65. SEM images of **PTEPA** powder taken at a magnification of (a) 20k and (b) 60k; (c) SEM image of a **PTEPA** film; (d) Nitrogen adsorption–desorption isotherms of **PTEPA** powder; (e) BJH pore size distribution from the desorption isotherms of **PTEPA**; (f) microporous pore size distribution in PTEPA calculated from the adsorption isotherms.

The electrochemical energy storage performances of a **PTEPA** electrode as the cathode was investigated in a 2032 coin-type half-cell. As shown in **Figure 66a**, CV profiles of the electrode exhibit pairs of broad redox peaks located at 3.69 V *vs.* Li/Li^+ (oxidation) and 3.37 V *vs.* Li/Li^+ (reduction). The separation of the redox

waves in **PTEPA** is approximately 0.32 V, which is a slightly narrower than that previously reported for the polytriphenylamine (**PTPA**) electrode (0.34 V). The symmetric peak shape of the oxidation and reduction peaks of **PTEPA** demonstrates its capacitance characteristic. The charge-discharge behavior of the **PTEPA** electrode was explored at 20 mA/g between 2.5 V and 4.3 V. As shown in **Figure 66b**, the **PTEPA** electrode exhibits a discharge capacity of 89.5 mAh/g in the initial cycle with two sloping voltage stages. The high voltage stage between the voltage of 4.1 V and 3.3 V is attributed to the redox reaction of **TPA** moieties of the **PTEPA**, which provides discharge capacity of about 62 mAh/g, while the other lower stage between 2.8 V and 2.6 V is probably related to the **EDOT** moieties, which provides a discharge capacity of about 27.5 mAh/g. Compared with other reported active materials, **PTEPA** exhibits a more sloping discharge curve without a stable discharge voltage plateau, which indicates that it is more suitable for applications in SCs than in batteries. The cycling performance of the **PTEPA** electrode was examined at a constant current of 20 mA/g during a 50 cycle test and the results are shown in **Figure 66c**. It is found that the discharge capacity of **PTEPA** decreases from its initial 89.5 mAh/g to 84.9 mAh/g after 50 cycles, with about a 5% loss of capacity. The stability upon cycling of the **PTEPA** electrode was found to be better than that of **PTPA** electrodes reported in the literature [155,156]. The relatively stable cycling performance of **PTEPA** can be attributed to its nanoporous structure which reduced potential electrochemical decomposition and morphological change during the repeated charge-discharge processes. As shown in **Figure 66d**, **PTEPA** exhibits relatively low coulombic efficiency in the initial charge-discharge process that is related to formation of an solid electrolyte interface (SEI) membrane on the lithium anode. With increase in cycling, the coulombic efficiency increased, reaching 98.3% at the 50th cycle. This increase can be attributed to a improved wetting of the

electrodes and to an improvement of the SEI properties upon cycling.

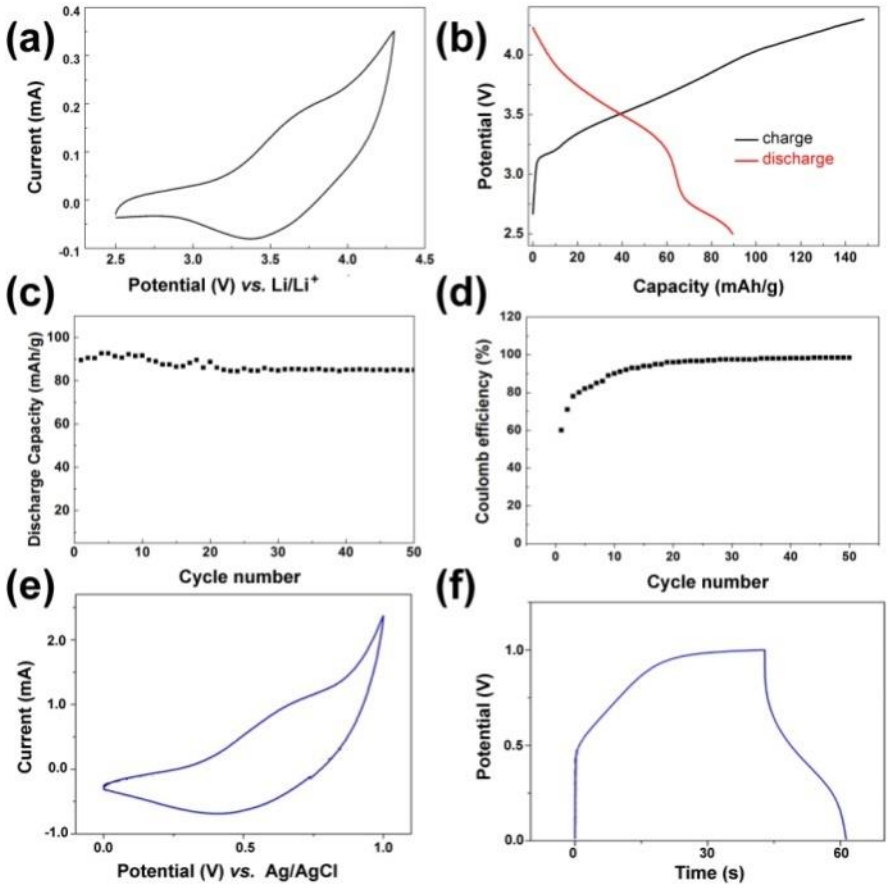

Figure 66. (a) CV curve of the **PTEPA** electrode in $LiPF_6$ EC/DMC (v/v, 1:1) electrolyte versus Li/Li^+, at a scan rate of 1 mV/s; (b) Initial charge-discharge curves of the **PTEPA** electrode at a current density of 20 mA/g; (c) Cycling stability of the **PTEPA** electrode at a current density of 20 mA/g; (d) Coulombic Efficiency of the **PTEPA** electrode; (e) CV curve of the **PTEPA** film in 1 mol/L H_2SO_4 aqueous solution versus Ag/AgCl, at a scan rate of 100 mV/s (f) GCD curves of the **PTEPA** film in 1 mol/L H_2SO_4 aqueous solution at approximately 10 A/g.

Electrochemical measurements show that the **PTEPA** film on ITO exhibits mainly a Faradaic pseudocapacitive behavior in 1M H_2SO_4 aqueous solution. As shown in **Figure 66e**, CV profiles of the **PTEPA** electrode exhibit a pair of broad redox waves centered at 0.67 V *vs.* Ag/AgCl (oxidation) and 0.39 V *vs.* Ag/AgCl (reduction), with good reversibility. As shown in **Figure 66f**, the galvanostatic charge-discharge profiles show a significant IR drop at the beginning of the discharge process,

followed by slow discharge process (0.8 V to 0.2 V), the potential sharply reverts to the original value afterward. The coulombic efficiency of the **PTEPA** film is about 43%. However, since the thin **PTEPA** film is easily detached from the ITO substrate during the charge and discharge process, it is difficult to determine the film mass and to calculate specific capacity accurately.

Spectroelectrochemical analysis was used to study the electrochromic properties of the **PTEPA** films on **ITO**. Visible and **NIR** transmission spectra of the **PTEPA** film at different potentials (-0.5 to 1.0 V) are shown in **Figure 67**. When a -0.5 V voltage was applied, the **PTEPA** film in its reduced state exhibited a yellow-green color with two absorption bands. The absorption band centered at 440 nm was attributed to the π–π* transition and the broad absorption band between 560 nm and 1050 nm was assigned to the charge transfer band from the **TPA** moiety to the **EDOT** moiety. Upon increasing the applied potential, the intensity of absorption peak around 440 nm was decreased, while the broad absorption peak at higher wavelength increases, leading to a color change to steel-blue at the fully oxidized state (1.0 V).

In order to characterize the optical contrast (ΔT%) and switching properties of the **PTEPA** film, dynamic electrochromic experiments were studied at 440 nm and 660 nm. The square wave potential method was used between −0.4 V and 1.0 V at regular intervals of 5 s. As shown in **Figure 67b**, the ΔT% was found to be 23.97% at 440 nm and 14.29% at 660 nm, which were are slightly lower than that of electroploymerized **PTEPA** films (26.84% at 448 nm and 17.03% at 660 nm). The coloration efficiency values of **PTEPA** film are calculated to be 80.6 cm^2/C at 440 nm and 122.8 cm^2/C at 660 nm, respectively. In addition, the switching time of the **PTEPA** film was found to be 0.96 s for coloring and 1.89 s for bleaching at 440 nm (**Figure 67c**), and 0.67 s for coloring and 2.89 s for bleaching at 660 nm (**Figure 67d**). These times are longer compared to electroploymerized **PTEPA** film. These

phenomena can be attributed to the relatively low polymerization degree of the drop-casted film. The reasonable optical contrast and the fast switching properties make **PTEPA** a promising electrochromic material and will be beneficial to its application in electrochromic supercapacitors (ECSCs).

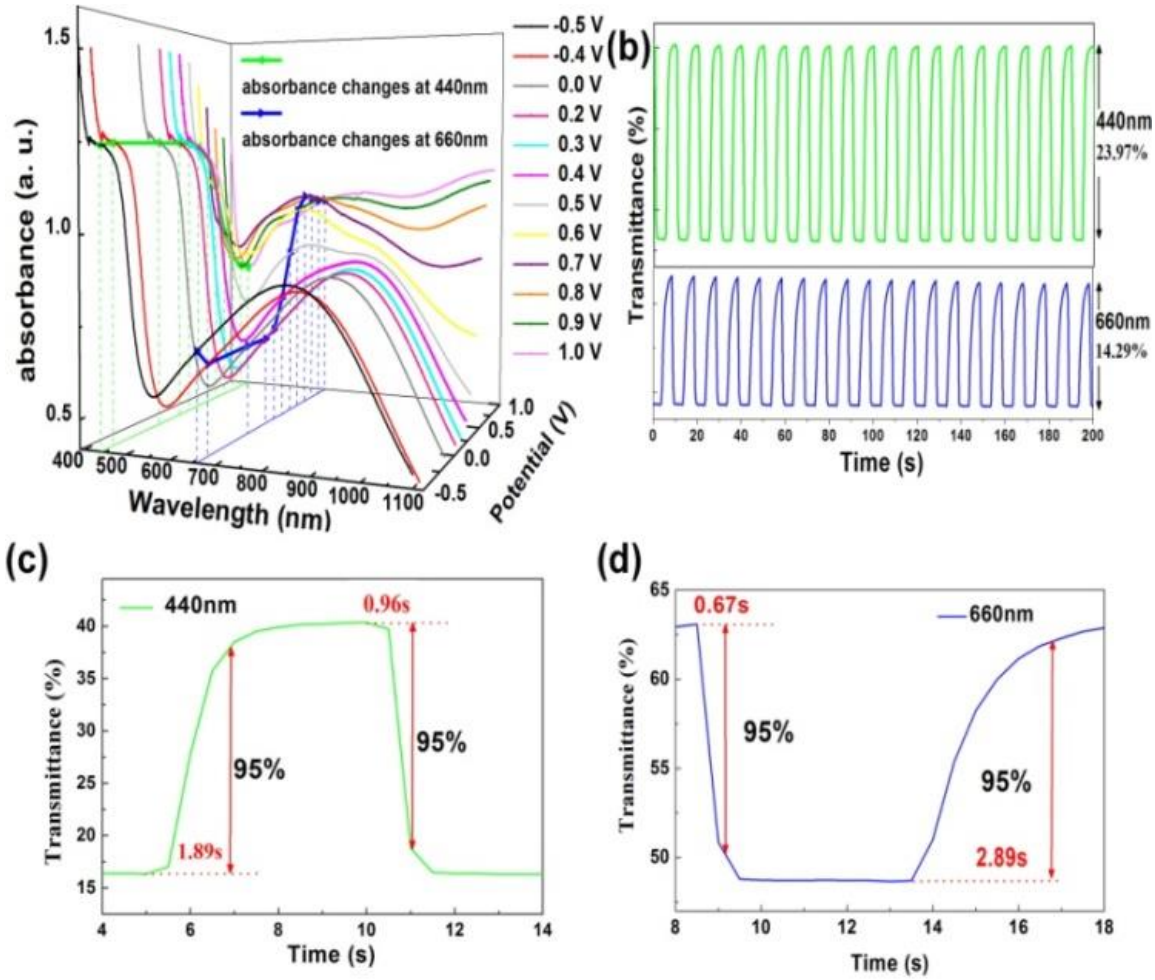

Figure 67. (a) Spectroelectrochemical spectra of **PTEPA** films with different applied potentials between -0.4 V and 1.0 V; (b) Transmittance-time profiles of **PTEPA** films at 440 nm and 660 nm between -0.4 and 1.0 V with a residence of 5 s; (c) Switching response for **PTEPA** films monitored at 440 nm; (d) Switching response for **PTEPA** films monitored at 660 nm.

4.2.3.3 Preparation and properties of nanostructured PEDOT film

3,4-ethylenedioxythiophene (**EDOT**), which can be easily polymerized into electroactive polymer films adhering on an electrode surface through electrochemical

polymerization or copolymerization reactions, has been widely considered to be an ideal building block for electrochromic conjugated polymers [162]. Its homopolymer, poly(3,4-ethylenedioxythiophene) (**PEDOT**) is a famous commercially-available electrochromic conjugated polymer featuring cathodically coloring from light blue to deep blue with excellent electrochemical stability and low energy gap.

Generally, electrochromic **PEDOT** film can be directly polymerized in an organic solution on the surface of conductive substrates, such as platinum discs, FTO or ITO glass. In the processes of electropolymerizations, the polymerization conditions (e.g. solvents, supporting electrolytes, electroploymerization potential, temperature and so on) will strongly influence the structure and properties of **PEDOT** [163-165].

Ionic liquids (ILs) are usually fluid at room temperature, completely composed of ions. Besides the properties (e.g. viscosity, density, melting point and hydrophobicity) of ILs can be adjusted through changing the combination of anions and cations [166]. Recently, ILs have been widely used in electropolymerization of conductive polymers, as a electrolyte component, due to their unique characteristics [167]. Herein, a series of **PEDOT** nanostructured films were prepared using different organic solvents, electrolytes and ionic liquids, the influences of solvents and different types of electrolytes on the electrochromic performance of **PEDOT** were further investigated.

SEM images of **PEDOT** films grown in different electrolyte (0.1 mol/L bis[(trifluoromethyl)sulfonyl]imide (**BMIMTf$_2$N**), 0.1 mol/L 1-Butyl-3-methylimidazolium tetrafluoroborate (**BMIMBF$_4$**), 0.1 mol/L tetraethylammonium tetrafluoroborate (**TEATFB**); 0.1 mol/L tetraethylammonium hexafluorophosphate (**TEAPF$_6$**), 0.1 mol/L tetrabutylammonium hexafluorophosphate (**TBAPF$_6$**), 0.1 mol/L tetrabutylammonium periodate (**TBAP**)) and solvent (methylene dichloride DCM) and acetonitrile (ACN)) are shown in **Figure 68.**

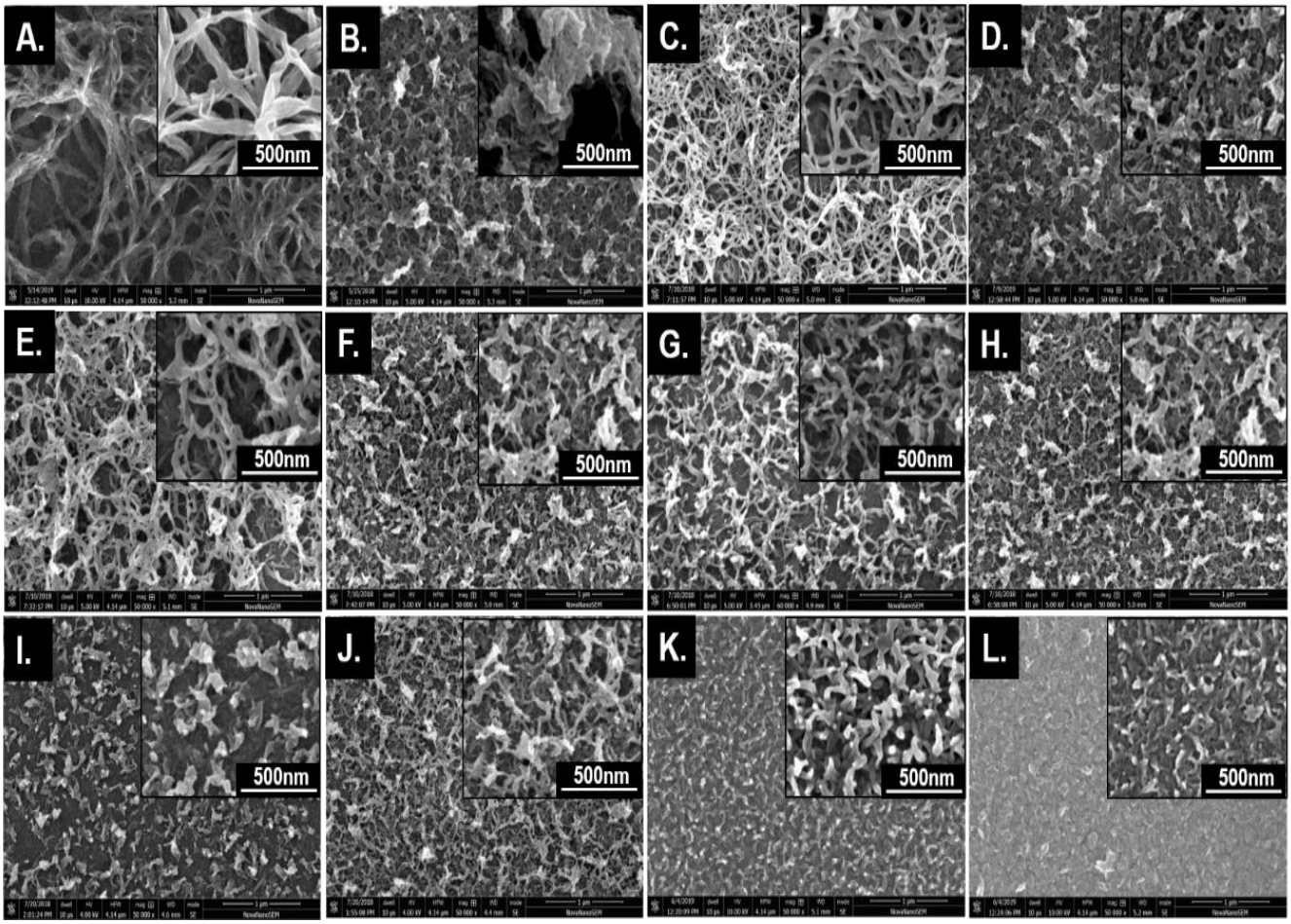

Figure 68. SEM images of **PEDOT** films grown in the solvent of DCM (A,C,E,G,I,K) and ACN (B,D,F,H,J,L) with the electrolyte of 0.1mol/L $BMIMTf_2N$ (A, B); $BMIMBF_4$ (C, D); TEATFB (E, F); $TEAPF_6$ (G, H); $TBAPF_6$ (I, J) and TBAP (K, L).

As shown in **Figure 68 (A, C, E, G, I, K)**, all the **PEDOT** films grown in DCM show twisted nanofibers structure, which is significant different with the **PEDOT** films grown in **ACN** (**Figure 68B, D, F, H, J, L**). As a solvent, DCM solvent exhibit greater volatility and smaller viscosity than that of ACN, which accelerates the diffusion of ions, making **EDOT** form a longer tubular fiber structure on the surface of the working electrode. Besides, with the participation of ionic liquid of $BMIMTf_2N$, the **PEDOT** film (**Figure 68A**) shows larger porosity than other films which may be owing to the larger anion of **$BMIMTf_2N$**.

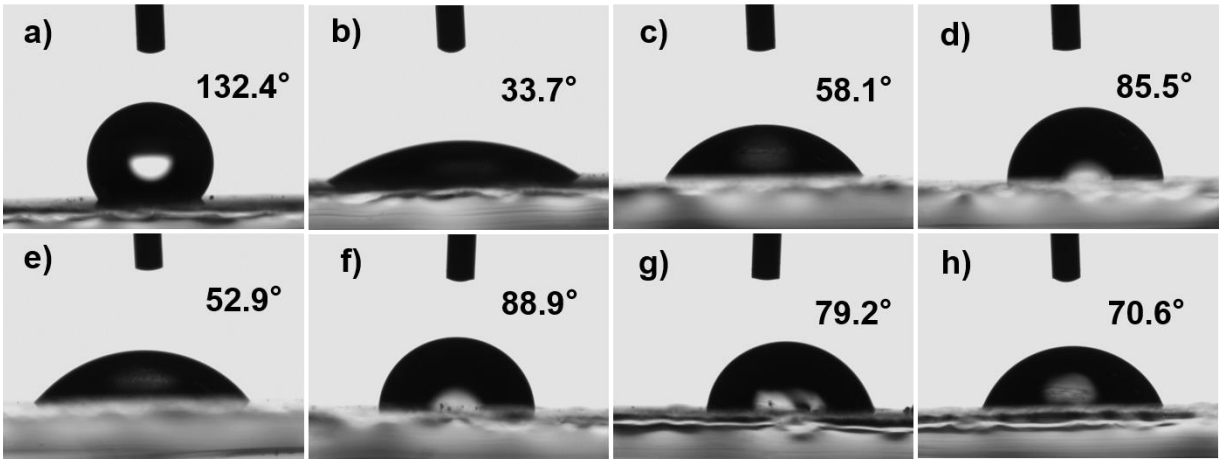

Figure 69. Water droplet contact angles of **PEDOT** films prepared in the solvent of ACN (e-h) or DCM (a-d) with 0.1 mol/L BMIMTf2N (a, e); BMIMBF4 (b, f); TEATFB (c, g) and $TEAPF_6$ (d, h).

As shown in Figure 69, in order to further study the influences of electrolytes and solvents on electropolymerization of **PEDOT** films, water droplet contact angles on the surface of **PEDOT** films were measured using 5μl of water drops. The **PEDOT** film (**Figure 69a**) obtained in the $BMIMTf_2N$/DCM has strong hydrophobicity with 132.4° water contact angle, but the **PEDOT** film (**Figure 69b**) obtained in the $BIMMBF_4$/DCM exihit significant hydrophilicity with 33.7° water contact angle. As shown in **Figure 68**, The morphology of these two **PEDOT** films are similar. Thus, we assume that the anion such as BF_4^-, PF_6^- play an important role in the hydrophilic and hydrophobic properties of films.

4.2.4 Hybrid materials based on POTs and conjugated polymers

4.2.4.1 Preparation and properties of inorganic/organic composite film PEDOT:Ce@TiO_2

As shown in **Figure 70**, an inorganic/organic composite film **PEDOT:Ce@TiO_2** was prepared through drop casting-secondary polymerization method using the mixture solution of **PEDOT** oligomer and a cerium-containing **POT-12** $[Ti_8O_7(HOEt)(OEt)_{21}Ce]$.

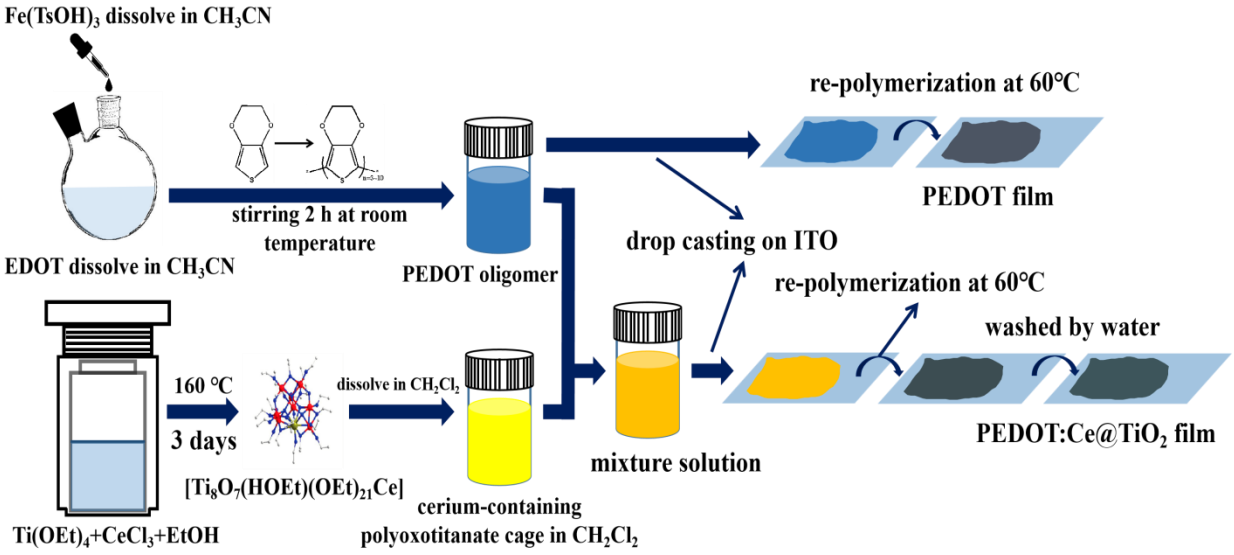

Figure 70. Schematic illustration of preparation of PEDOT:Ce@TiO_2 film.

The preparation details are described as follows:

1. Preparation of **PEDOT** oligomer solution

0.67 g (5 mmol) **EDOT** was dissolved in 50 mL acetonitrile and placed it in a round-bottomed flask. Iron(III) p-toluenesulfonate (1.14 g, 2 mmol) was dissolved in 50 mL acetonitrile and then slowly dropped into the round bottom flask filled with **EDOT** solution. After stirred 2 hours at room temperature, the mixture gradually turns to dark blue, the **PEDOT** oligomer solution is prepared.

2. Preparation of **POT-12/DCM** solution

The **POT-12** crystals of [$Ti_8O_7(HOEt)(OEt)_{21}Ce$] were obtained through the solvothermal reaction of the mixture containing tetraethyl titanate (3.5 mL, 15.4 mmol), anhydrous cerium chloride (0.246g, 1 mmol) and anhydrous ethanol (7 mL) into the autoclave. the mixture heated to 150 ºC for 2 days gave a light yellow solution, and orange **POT-12** crystals of [$Ti_8O_7(HOEt)(OEt)_{21}Ce$] were obtained from the yellow solution through slowly evaporate the solvent at room temperature. Dissolving 0.5 g POT crystals in 10 mL DCM we can prepare a 0.03 mol/L POT/

DCM solution.

3. Preparation of **PEDOT:Ce@TiO$_2$** film

PEDOT oligomer solution and **POT-12/DCM** solution were mixed in a volume ratio of 1:1, the mixture was drip coating on the ITO surface, and dried at 60 ^{o}C for 2 h. After washed with deionized water, and dried again at 60 ^{o}C, the **PEDOT:Ce@TiO$_2$** film was prepared.

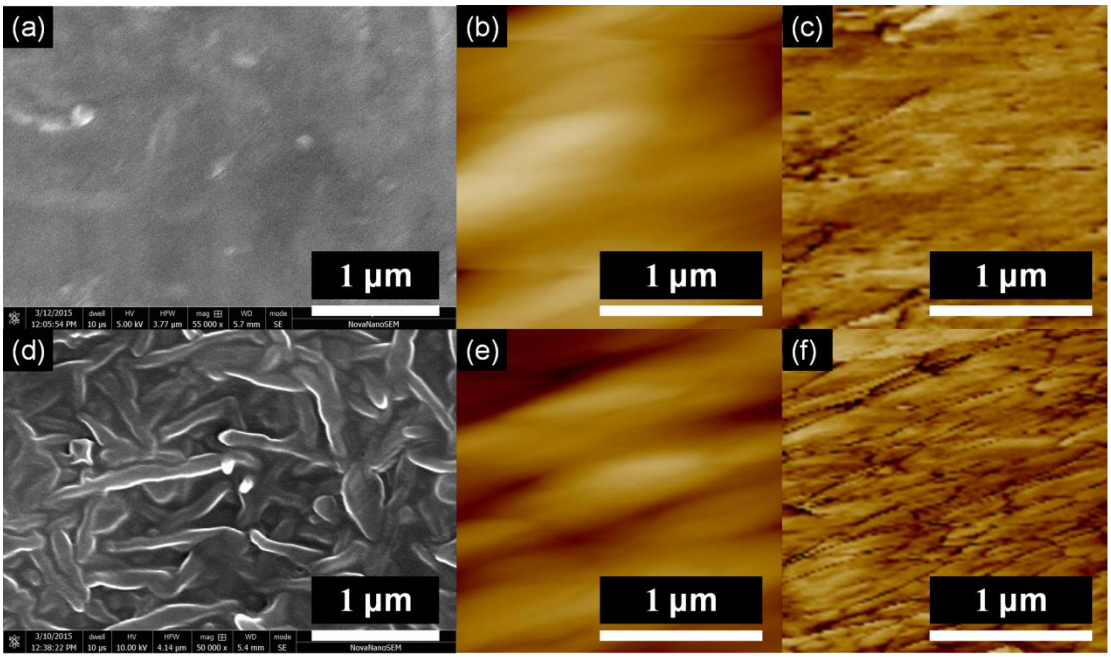

Figure 71. (a) SEM image, (b) AFM height sensor image, (c) AFM tapping phase image of **PEDOT** film; (d) SEM image, (e) AFM height sensor image, (f) AFM tapping phase image of **PEDOT:Ce@TiO$_2$** film.

As shown in **Figure 71**, **PEDOT:Ce@TiO$_2$** film has a special nanostructure with "gully-like" rough surface morphology. The surface roughness, Ra of **PEDOT:Ce@TiO$_2$** measured by Atomic force microscopy (AFM) is 25.43 nm, which is significantly higher than that of **PEDOT** (Ra = 13.39 nm), indicating that **Ce@TiO$_2$** has a significant influence on the surface morphology of **PEDOT:Ce@TiO$_2$**. The difference between light and dark caused by the height

difference cannot be observed in AFM phase diagram of **PEDOT:Ce@TiO$_2$** film (**Figure 71f**), which can be inferred that there is no obvious phase separation in this film.

As shown in **Figure 72**, **PEDOT:Ce@TiO$_2$** exhibits strong hydrophobicity while good wettability to acetonitrile solution.

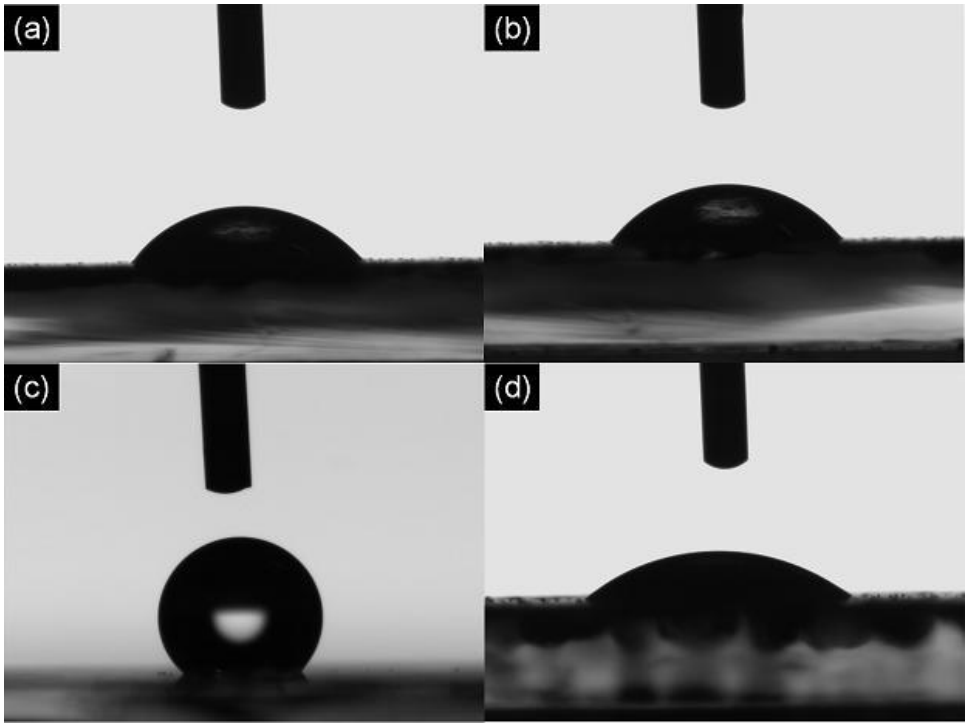

Figure 72. Images of water droplets on the surfaces of (a) **PEDOT** film and (c) **PEDOT:Ce@TiO$_2$** film; Images of ACN droplets on the surfaces of (b) **PEDOT** film and (d) **PEDOT:Ce@TiO$_2$** film.

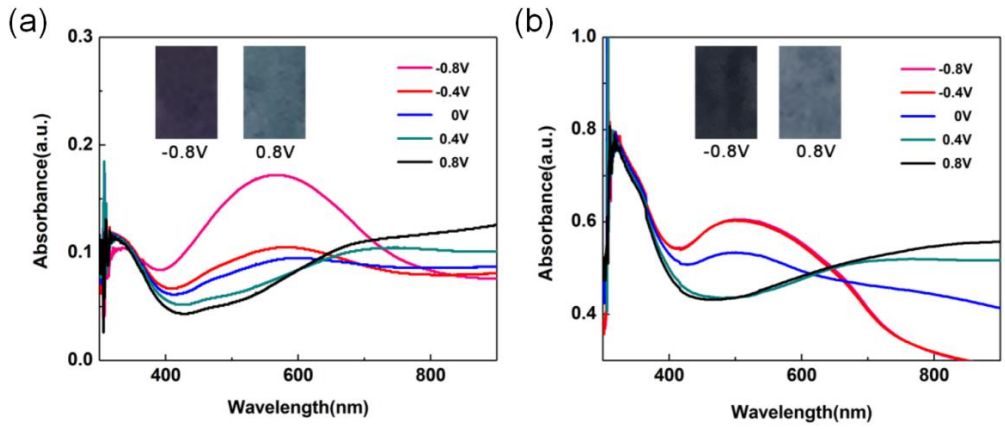

Figure 73. UV-Vis spectra and optical photos (insert) of films under different potential, (a) **PEDOT,** (b) **PEDOT:Ce@TiO$_2$**.

As shown in **Figure 73**, **PEDOT:Ce@TiO$_2$** film can be used as cathodically electrochromic film like **PEDOT** film. As shown in **Figure 74**, **PEDOT:Ce@TiO$_2$** shows larger electrochemical activity compare to **PEDOT** as supercapacitor electrode materials. The mass specific capacitance of **PEDOT:Ce@TiO$_2$** film is 71.2 F/g at a current density of 1 A/g, which is 1.7 times higher than that of the **PEDOT** film.

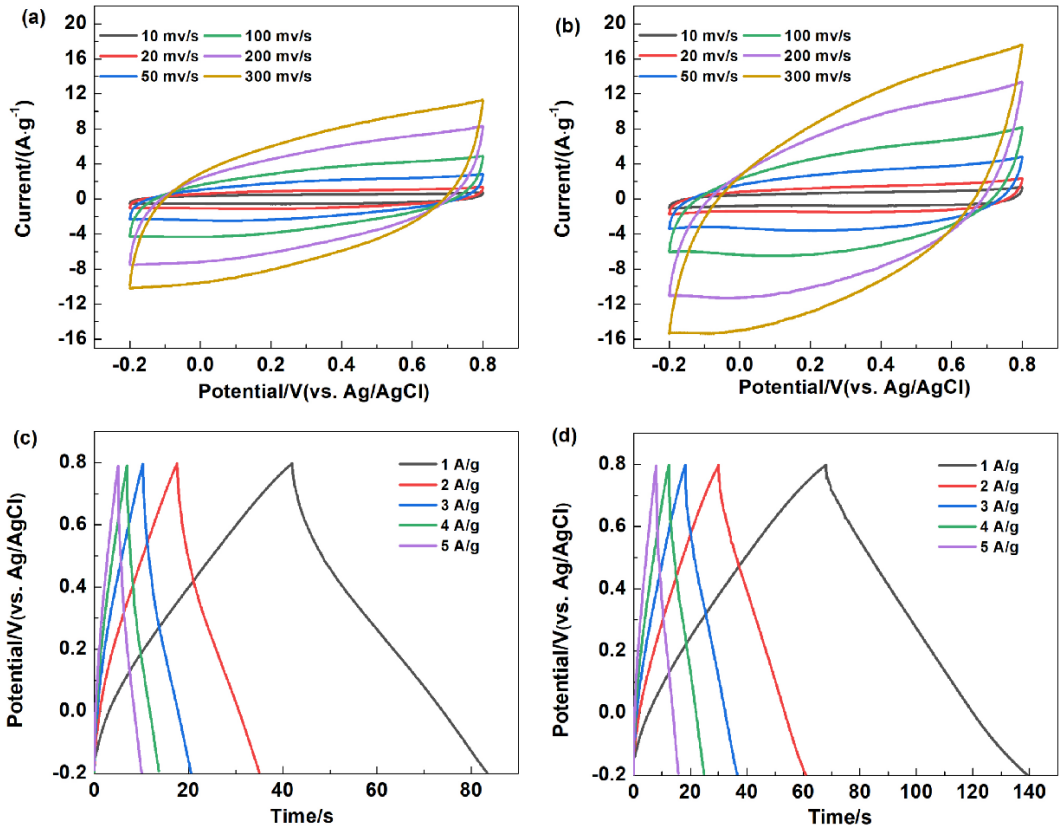

Figure 74. CV curves of (a) **PEDOT** and (b) **PEDOT:Ce@TiO$_2$**, galvanostatic charge/discharge curves of (c) **PEDOT** and (d) **PEDOT:Ce@TiO$_2$**.

4.2.4.2 Preparation and properties of inorganic/organic composite film Poly-(TEPA-POT-4)

The composite **Poly-(TEPA-POT-4)** film was prepared via constant potential

polymerization of the **POT-4** and **TEPA** monomers onto the ITO substrate at 1.7V. Electrochemical copolymerization was performed in a solution of 0.1 M $TBAPF_6$/ DCM containing 4.0 mM **POT-4** and 4.0 mM **TEPA**. Before **Poly-(TEPA-POT-4)** was dedoped at -0.6 V for 1 minute, the amount of electricity accumulated on the films of ITO glass (4 cm × 0.9 cm) is 0.04 C in a three-electrode system with the reference electrode of Ag/AgCl and the counter electrode a platinum sheet.

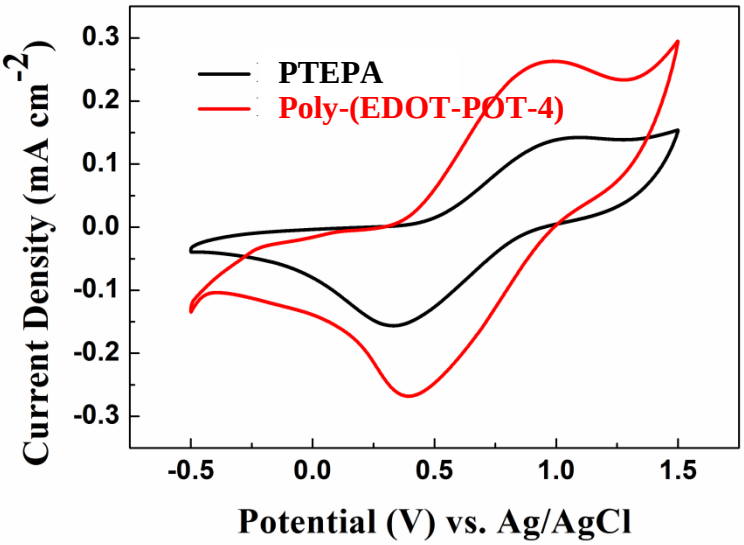

Figure 75. CV curves of **PTEPA** and **Poly-(TEPA-POT-4)** films in 0.1 mol·L^{-1} $TBAPF_6$/DCM at scan rate of 100 mV·s^{-1}.

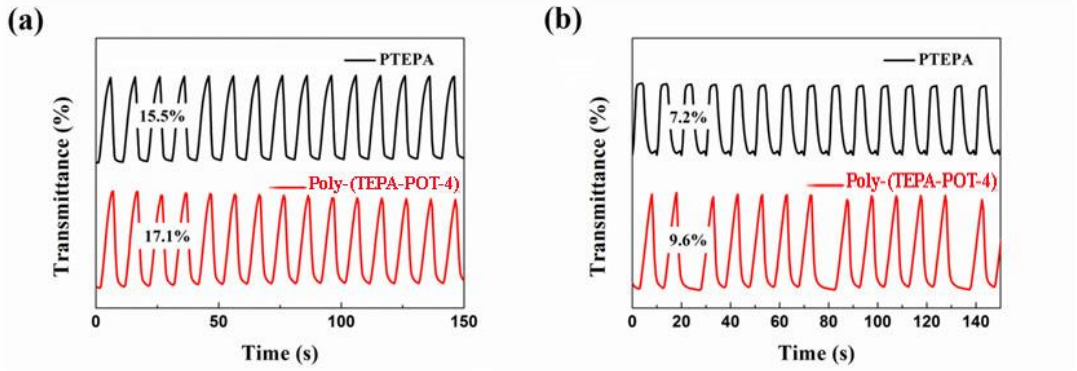

Figure 76. (a) Optical contrast of the film **PTEPA** at 450.2 nm and film **Poly-(TEPA-POT-4)** at 449.4 nm; (b) Optical contrast of the film **PTEPA** at 693.4 nm and film **Poly-(TEPA-POT-4)** at 694.4 nm.

As shown in **Figure 75**, the electrochemical behavior of **PTEPA** film **Poly-(TEPA-POT-4)** film were compared in 0.1 mol/L $TBAPF_6$/DCM solution. CV curves were measured in the voltage range of -0.5~1.5 V and the sweep speed of 100 mV/s. **Poly-(TEPA-POT-4)** film has larger current density and bigger cyclic voltammetry curve area than that of **PTEPA** film. Besides, compared with the **Poly-(TEPA-POT-4)** film (the potential of oxidation peak is 1.06 V and reduction peak is 0.33 V), the **Poly-(TEPA-POT-4)** film also has a lower oxidation peak potential (0.98 V) and a higher reduction peak potential (0.39 V). As shown in **Figure 76**, **Poly-(TEPA-POT-4)** film shows higher contrast and better electrochromic performance than that of **PTEPA** film.

4.2.4.3 Preparation and properties of hybrid film Poly-(EDOT-POT-1)

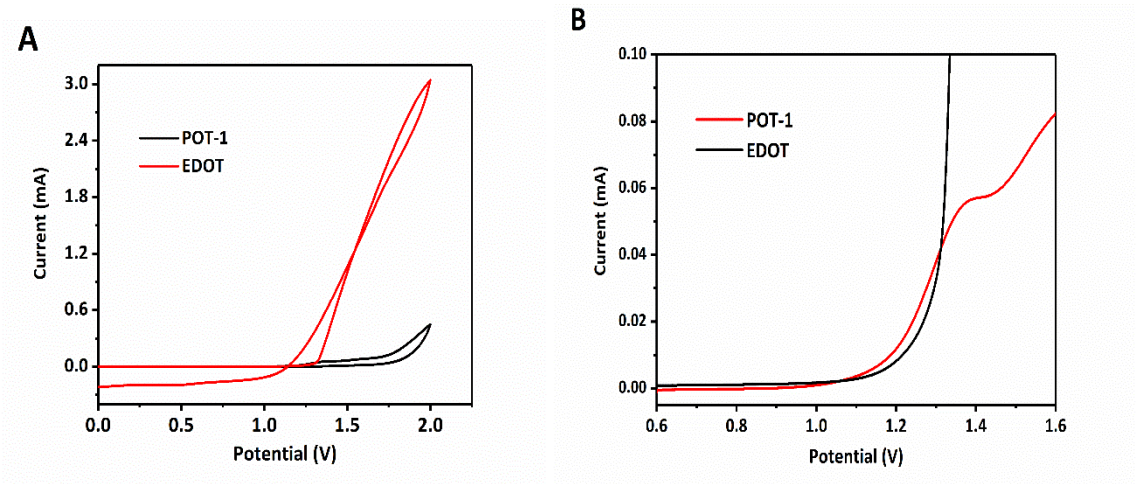

Figure 77. (A) First cycle of CV curve of **POT-1** (red curve) and (B) linear sweep voltammetry curve of **EDOT** (black curve) in 0.1 M $TBAPF_6$/DCM solution at a scan rate of 50 mV s^{-1} with the Ag/AgCl as reference electrode and the platinum sheet as counter electrode.

As shown in **Figure 77**, cyclic voltammetry (**CV**) curves of **POT-1** in a DCM

solution of 0.1 M tetrabutylammonium hexafluorophosphate ($TBAPF_6$) exhibit an irreversible multistage oxidation process with initial oxidation potential at 1.05 V, very close to that of 3,4-ethylenedioxythiophene (**EDOT**). The similarity of the initial oxidation potentials was propitious for the controllable formation of the copolymers [168]. **Poly-(EDOT-POT-1)** film was prepared via constant potential copolymerization of the **POT-1** and **EDOT** comonomers onto the ITO substrate at 1.7V. Electrochemical copolymerization was performed in a solution of 0.1 M **$TBAPF_6$/DCM** containing 4.0 mM **POT-1** and 4.0 mM **EDOT**. Before **Poly-(EDOT-POT-1)-1** was dedoped at -0.8 V, the amount of electricity accumulated on the films of ITO glass (4 cm × 0.9 cm) is 0.04 C in a three-electrode system with the reference electrode of Ag/AgCl and the counter electrode a platinum sheet.

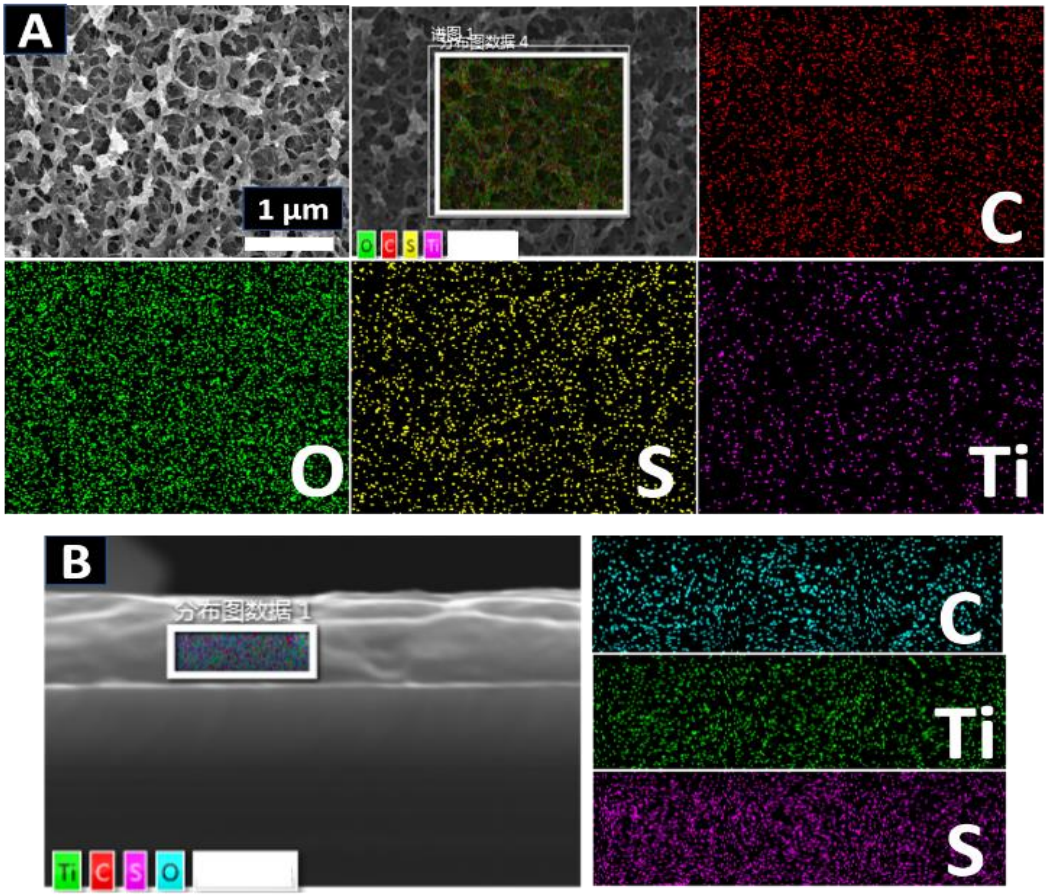

Figure 78. SEM and elemental mapping of plane (A) and section (B) of the **Poly-(EDOT-POT-1)** film.

Energy dispersive spectroscopy (EDS) and X-ray photoelectron spectroscopy (XPS) show that **Poly-(EDOT-POT-1)** contains 2.05-3.45% atom% Ti. As shown in **Figure 78**, elemental mapping indicates that Ti atoms are dispersed homogeneously in the matrix. **Poly-(EDOT-POT-1)** is a stable film where the dispersion of Ti in **Poly-(EDOT-POT-1)** was not changed even after soaked in **DCM** for 2 weeks. Like reported **PEDOT/TiO_2** composites, **Poly-(EDOT-POT-1)** have strong hydrophobic surface. Compared with other reported **PEDOT/TiO_2** nanostructured composite films, **Poly-(EDOT-POT-1)**, which possesses good homogeneity and high dispersion of the Ti_xO_y units, it can be assumed that they should have broad applications in the fields of optoelectronics, electrochromism and energy storage; a proposition that was then tested by further experiments.

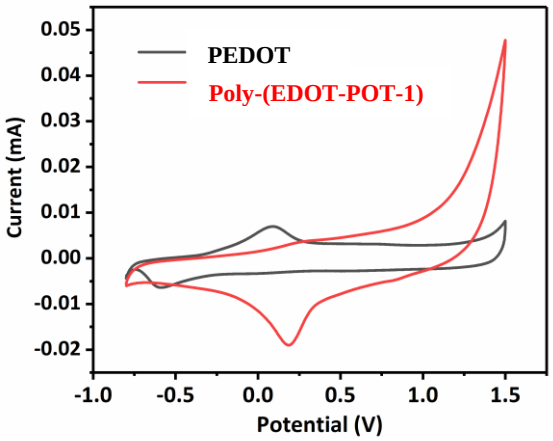

Figure 79. CV curves of **Poly-(EDOT-POT-1)** and **PEDOT** films on the surface of the glassy carbon electrode in 0.1 mol/L $TBAPF_6$/DCM at scan rate of 10 mV/s.

As shown in **Figure 79**, CV curves of **Poly-(EDOT-POT)-1** and **PEDOT** films on a glassy carbon electrode were tested in a three-electrode system with Ag/AgCl as the reference electrode. The **PEDOT** film exhibits a redox pair (E_{pc}= -0.59 V, E_{pa}= 0.09

V) in the potential range from -0.80 to 1.50 V, while there is only one significant reduction peak around 0.20 V for the film of **Poly-(EDOT-POT-1)** at a scan rate of 10 mV/s.

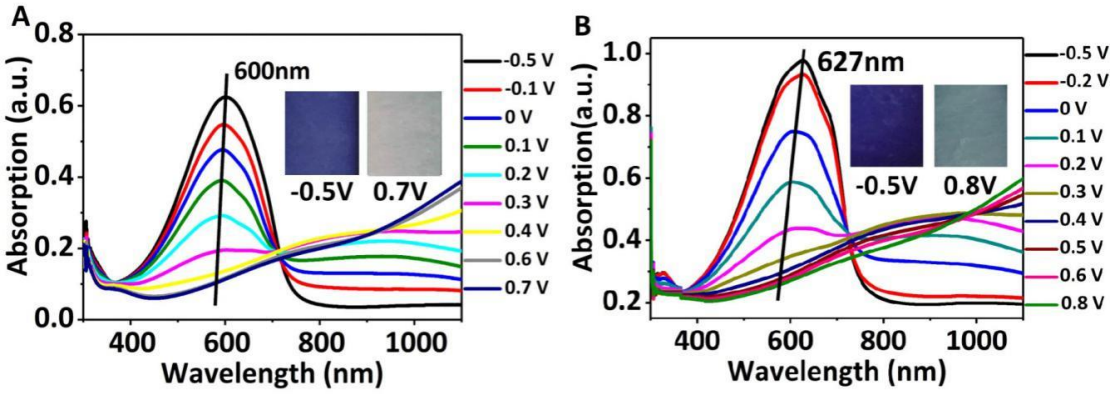

Figure 80. UV–vis spectra of (A) **Poly-(EDOT-POT-1)** and (B) **PEDOT** at applied voltages between -0.8 V and 1.2 V in 0.1 M TBAH/DCM solution (insets are the photographs of the corresponding polymer films on ITO glass).

Using the same deposition potential and polymerization conditions, the average thickness of the **Poly-(EDOT-POT-1)** film is ca. 1.8 times that of the **PEDOT** film. Visible and NIR transmission spectra of **Poly-(EDOT-POT-1)** and **PEDOT** on ITO at different potentials are shown in **Figure 80**. Like **PEDOT**, **Poly-(EDOT-POT-1)** is a cathodically-colored material with a color change from dark blue (colored state) at −0.5 V to light-blue (bleached state) at 0.7 V. In the colored state, the visible absorption band of **Poly-(EDOT-POT-1)** (600 nm) is blue shifted compared with that of **PEDOT** (627 nm), which must be due to the attachment of **POT-1** to the conjugated backbone. As shown in **Figure 81**, **Poly-(EDOT-POT-1)** exhibits improved electrochromic properties with larger optical contrast (53.0%) and shorter coloring time (1.36 s) compared to **PEDOT** (50.7% optical contrast, 1.59s coloring time), which may be due to the nanoporous structure of **Poly-(EDOT-POT-1)**. These superior characteristics are significant as **PEDOT,** to our knowledge, is the only

commercially-available polymeric organic material used in electrochromic applications, such as smart windows.

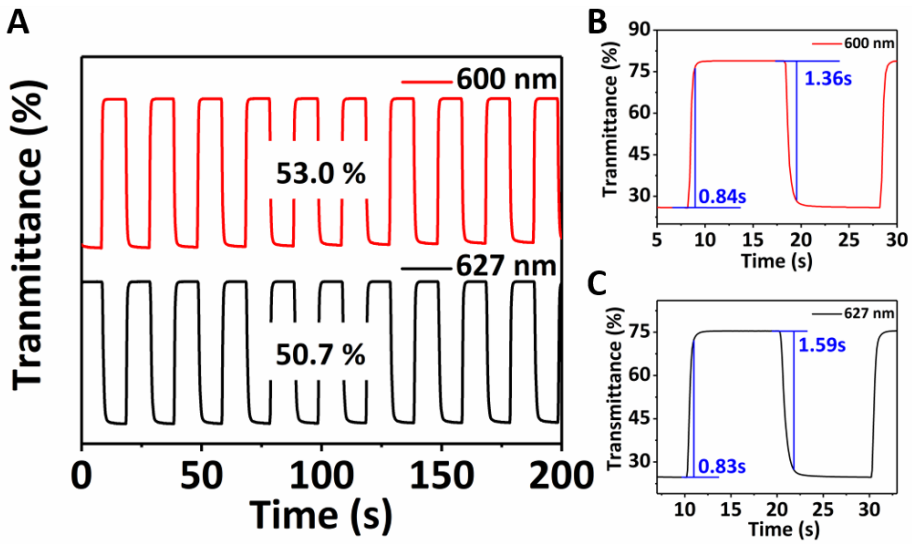

Figure 81. Optical contrast of the **Poly-(EDOT-POT-1)** (red curve) polymer films monitored between -0.5 V and 0.7 V and the **PEDOT** (black curve) films monitored between -0.5 V and 0.8 V in 0.1 M TBAH/DCM solution with a residence time of 10 s (A); Electrochromic switching response of **Poly-(EDOT-POT-1)** (B) and **PEDOT** (C).

Poly-(EDOT-POT-1) was further tested as an electrode material for a supercapacitor in a three-electrode system using 0.1 M $LiClO_4$/ACN as the electrolyte. As shown in **Figure 82**, CV curves of **Poly-(EDOT-POT-1)** and **PEDOT** both exhibit a quasi-rectangular shape at sweep rates from 10 to 300 mV/s, but the specific capacitance of **Poly-(EDOT-POT-1)** is larger than that of **PEDOT** especially at higher scanning rate. Charge-discharge curves at current densities between 1A/g and 5 A/g display regular-triangular shapes and no obvious voltage drop can be observed at the beginning of the discharge process for both the **Poly-(EDOT-POT-1)** and **PEDOT** electrodes, indicating ideal capacitor behaviour. It is noteworthy that the specific capacitance of **Poly-(EDOT-POT-1)** is 102.5 F/g at a current density of 1 A/g and is much higher than that of bare **PEDOT** (75.8 F/g). With increase of current densities to 5 A/g, the

specific capacitance of **Poly-(EDOT-POT-1)** decreases to 94.1 F/g, 34% higher than that of **PEDOT** (70.3 F/g). These values are in good agreements with those estimated from electrochemical impedance spectroscopy (**Figure 83**). By fitting the impedance spectra, the specific capacitance of **Poly-(EDOT-POT-1)** at -0.1V was found to be around 90 F/g while that for of **PEDOT** is around 51 F/g.

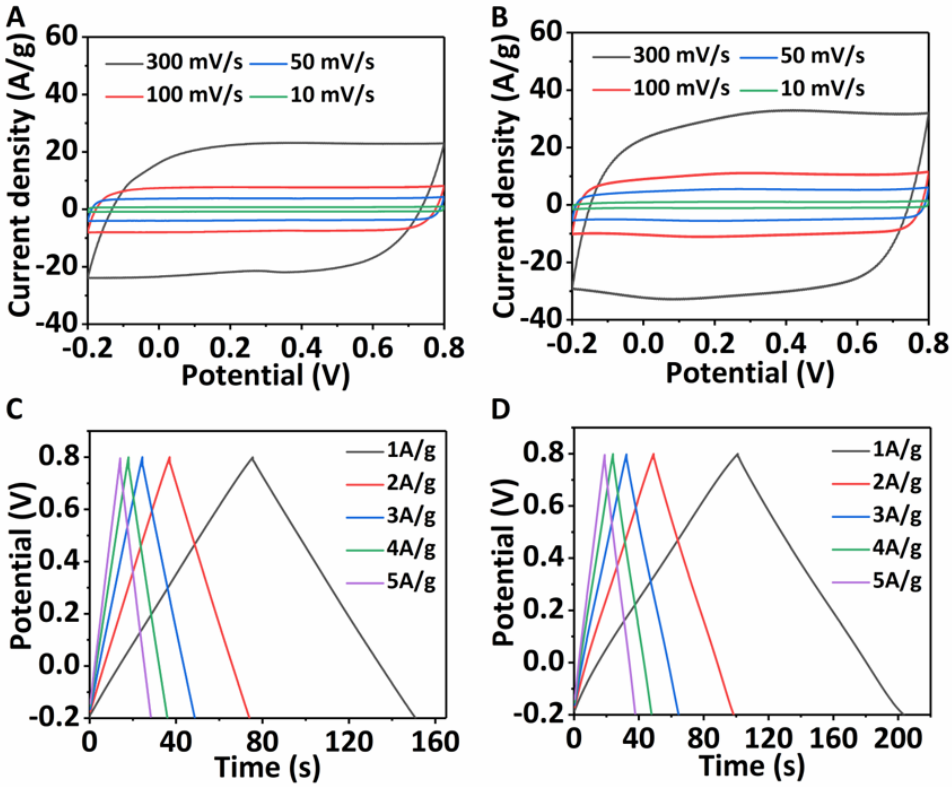

Figure 82. CV curves of **PEDOT** (A) and **Poly-(EDOT-POT-1)** (B); galvanostatic charge/discharge curves of **PEDOT** (C) and **Poly-(EDOT-POT-1)** (D).

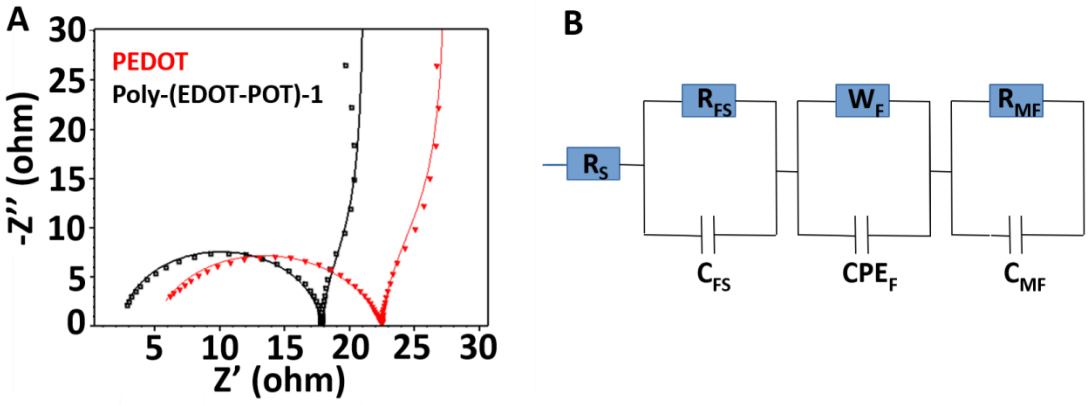

Figure 83. Nyquist plots of the impedance spectra of **PEDOT** (red) and **Poly-(EDOT-POT-1)** (black)

modified electrodes measured in 0.1M $LiClO_4$ acetonitrile solution at -0.156 V and -0.110 V respectively. The symbols represent the experimental data and the solid lines the fit of the experimental data (A). Equivalent circuit used to fit the spectra (B).

4.2.4.4 Preparation and properties of hybrid film Poly-(H_2T_2P-POT-1)

Our group took advantage of the reactivity of oxidized porphyrins to develop an easy and original method of porphyrin electropolymerization [169-171]. In the past two decades, our group have developed effective methods to obtain organic/inorganic hybrid materials as well as polymeric materials based on **POMs** and porphyrins. It had been found that many of these hybrid materials are able to photocatalytically reduce metallic ions, NO_x or CO_2. In these hybrid materials, the porphyrin sub-units were used as photosensitizers capable of delivering electrons to the strongly oxidant **POMs** under light irradiation. The reduced **POMs** can then catalyse reductions, while the porphyrins can be regenerated in the presence of a reversible sacrificial electron donor [172-183].

To the best of our knowledge, there have been no published article reporting the organic/inorganic hybrid materials based on **POTs** and porphyrins. Given this outcome, the scarcity of **POT**-based polymers for photocurrent generation, and our ongoing interest in photocatalytic **POM**-polymer conjugates under UV and visible light irradiation, we decided to prepare and evaluate the efficiency of hybrid film **Poly-(H_2T_2P-POT-1)** which was obtained from porphyrins and **POT-1** for photocurrent generation.

As shown in **Scheme 1, Poly-(H_2T_2P-POT-1)** was synthesized by our electropolymerization method, which involved radical coupling reaction between oxidazed **POT-1**$^{\bullet+}$ to an electro-generated monooxidized radical cation porphyrin **$ZnT_2P^{\bullet+}$** (**Scheme 2**). As soon as the iterative scans were performed at a potential in the anodic part sufficiently high to allow the formation of the porphyrin radical cation **$ZnT_2P^{\bullet+}$**, the formation of a conducting film of **Poly-(ZnT_2P-POT-1)** coating on

working electrode was observed. Because H^+ are relased during the electropolymerization, the last step corresponds to the dematallation of the **ZnT$_2$P** giving the free base porphyrin.

Please note that the encapsulation of the **ZnT$_2$P** in the **POT-1** based polymer could also occur. The difficult polymerization of the **POT-1** cluster in the absence of **EDOT** seems to show the presence of radical coupling and to be in the favor of the mechanism suggested in **Scheme 2**. Further work will be needed to prove this claim.

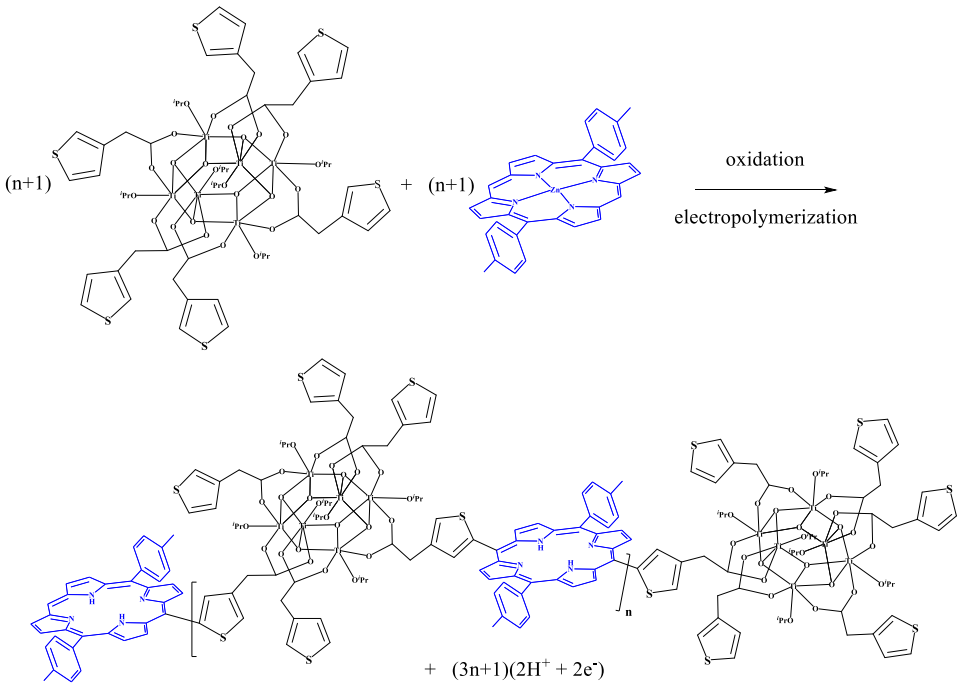

Scheme 1. Synthetic route for the formation of new hybrid copolymer films **Poly-(H$_2$T$_2$P-POT-1)**. We have visualized so as to be clear the reaction of only two thiophene groups for **POT-1**.

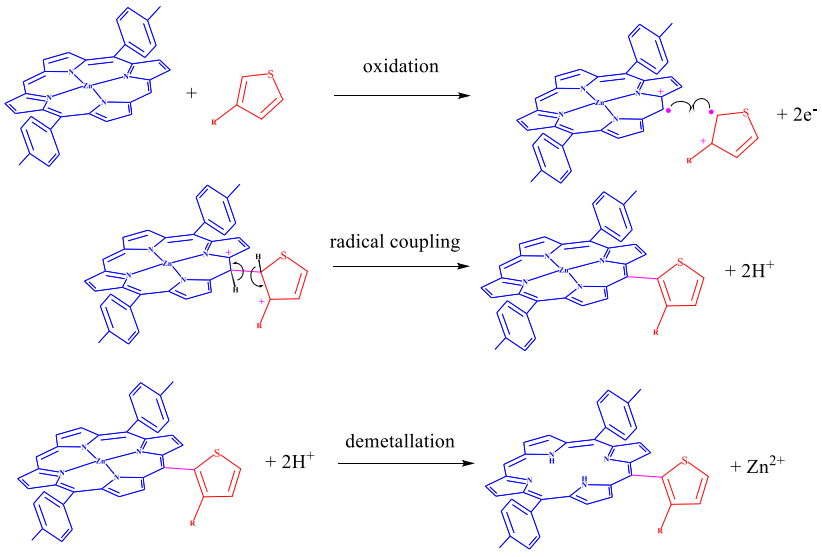

Scheme 2. Mechanism proposed for the formation of new hybrid copolymer films **Poly-(H_2T_2P-POT-1)**. We have visualized so as to be clear the reaction of only one radical coupling between **POT-1**$^{\bullet+}$ and **$ZnT_2P^{\bullet+}$.**

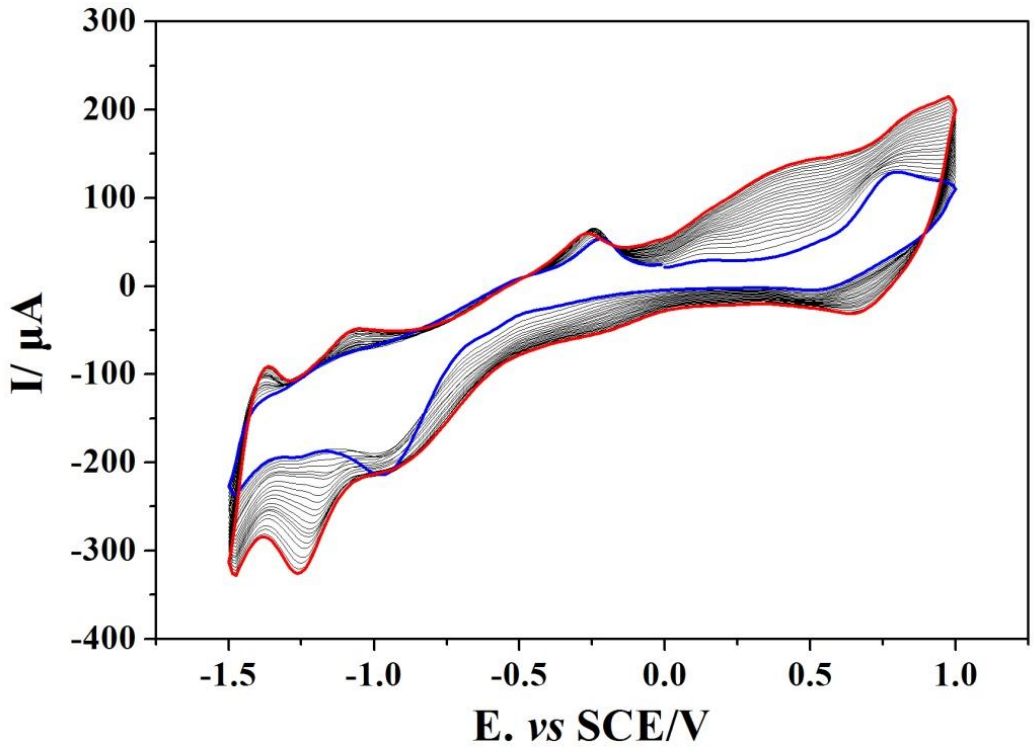

Figure 84. Cyclic voltammograms recorded during 25 iterative scans conducted between -1.50 V and +1.00 V vs. SCE in a 1,2-$C_2H_4Cl_2$/CH_3CN (7/3) solution of **ZnT_2P** (0.25 mmol L^{-1}) in the presence of **POT-1** (0.25 mmol L^{-1}) and NBu_4PF_6 (0.1 mol L^{-1}). WE: ITO. S = 1 cm^2, v = 0.1 V s^{-1}. Blue curve: first scan (n = 1), red curve: final scan (n = 25).

As shown in **Figure 84**, the electropolymerization process were carried out under conditions similar to those previously reported [182,183], by iterative scans between −1.50 and +1.00 V *versus* SCE in 0.1 mol L^{-1} solutions of tetrabutylammonium hexafluorophosphate (NBu_4PF_6) in 1,2-$C_2H_4Cl_2$/CH_3CN (7/3) containing **ZnT_2P** (0.25 mmol L^{-1}) and **POT-1** (0.25 mmol L^{-1}) under argon atmosphere.

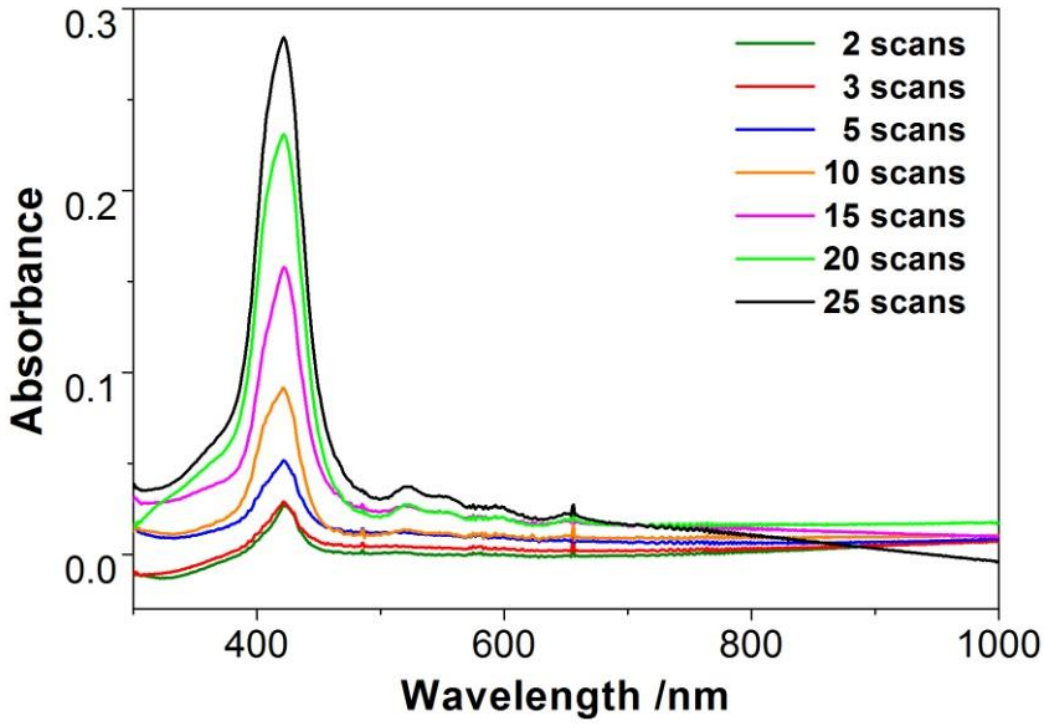

Figure 85. UV-visible-NIR absorption spectra of **Poly-(H_2T_2P-POT-1)** onto ITO with different numbers of iterative scans between -1.50 and +1.00 V vs. SCE (v=100 mVs^{-1}). Only one side is covered by ITO.

As shown in **Figure 85**, UV-visible-NIR spectra on ITO electrodes coated with the copolymer have been measured at various thickness. The absorption intensity of the chromophores increases linearly with iterative scan number. It must be noted that four Q bands have been observed between 500 nm – 700 nm showing the presence of the free base porphyrin 5,15-tolyl-porphyrin (**H_2T_2P**). It can be probably explained by the demetallation of the metalloporphyrin **ZnT_2P** giving **H_2T_2P** during the electropolymerization with the release of H^+.

Figure 86 shows the typical current-potential curves of **Poly-(H_2T_2P-POT-1)** thin films on ITO electrodes obtained in 5 mM I_2/0.5 M I^- aqueous solution. The equilibrium potential of I_3^-/I^- redox couple in solution is taken as reference potential at 0 V in the cyclic voltammograms. The curve obtained in the absence of

illumination was analysized firstly (black line). For bare ITO electrode, almost no Faradaic current is observed between -0.3 V and 0.3 V, revealing the slow I^- oxidation and I_3^- reduction kinetics on ITO [184]. However, the I^- oxidation and I_3^- reduction currents are significantly enhanced on the ITO modified by **Poly-(H_2T_2P-POT-1)**. For the I^- oxidation, anodic current peak at ca. 0.14 V is observed, but further studies are required to explain why the oxidation current goes through a maximum. The current-potential curve measured under visible light illumination and potentiodynamic condition are also plotted in **Figure 86** (red line), and the photocurrent response in the potentiostatic mode at 0 V under on-off light illumination cycles is shown in **Figure 87**. The thickness of the **Poly-(H_2T_2P-POT-1)** films is of great importance to optimize the generation of photocurrent under visible illumination with an increase of the intensity of the photocurrent *versus* the number of iterative scan.

Under visible light, the open circuit potential increases of ca. 40 mV. Above this potential, the I^- oxidation current becomes predominant owing to the high I^- concentration in solution, impeding thus further increase of the photovoltage. For potentials below the OCP, a negative photocurrent is observed, the photocurrent at 0 V of the **Poly-(H_2T_2P-POT-1)** thin film reaching ca. -45 µA cm^{-2} (potentiostatic experiment) or -90 µAcm^{-2} (in the CV). The photoelectrochemistry test results indicated that the films obtained have good electrochemical and photochemical properties. Impedance properties of such material need to be measured. Electrochemistry quartz crystal microbalance (EQCM), AFM, XRD and XPS analyses need also to be achieved and are under work. Electrochromic properties and electricity storage capacities need also to be measured.

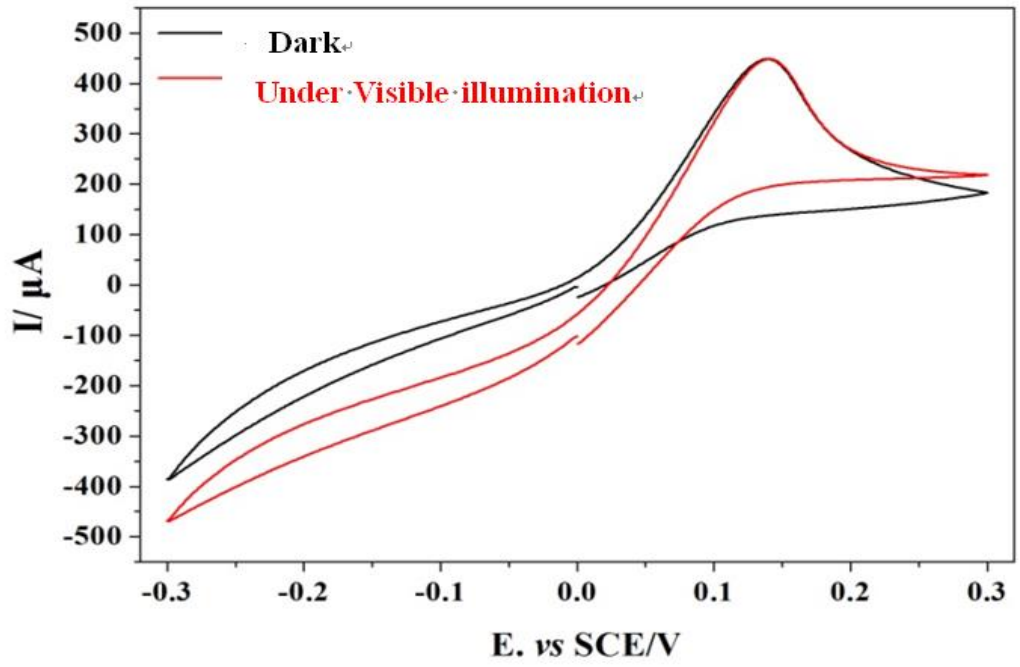

Figure 86. Potential-current curves of **Poly-(H_2T_2P-POT-1)** films measured in the dark or under visible illumination using 300 W arc Xenon lamp and a long pass filter (λ > 400 nm).

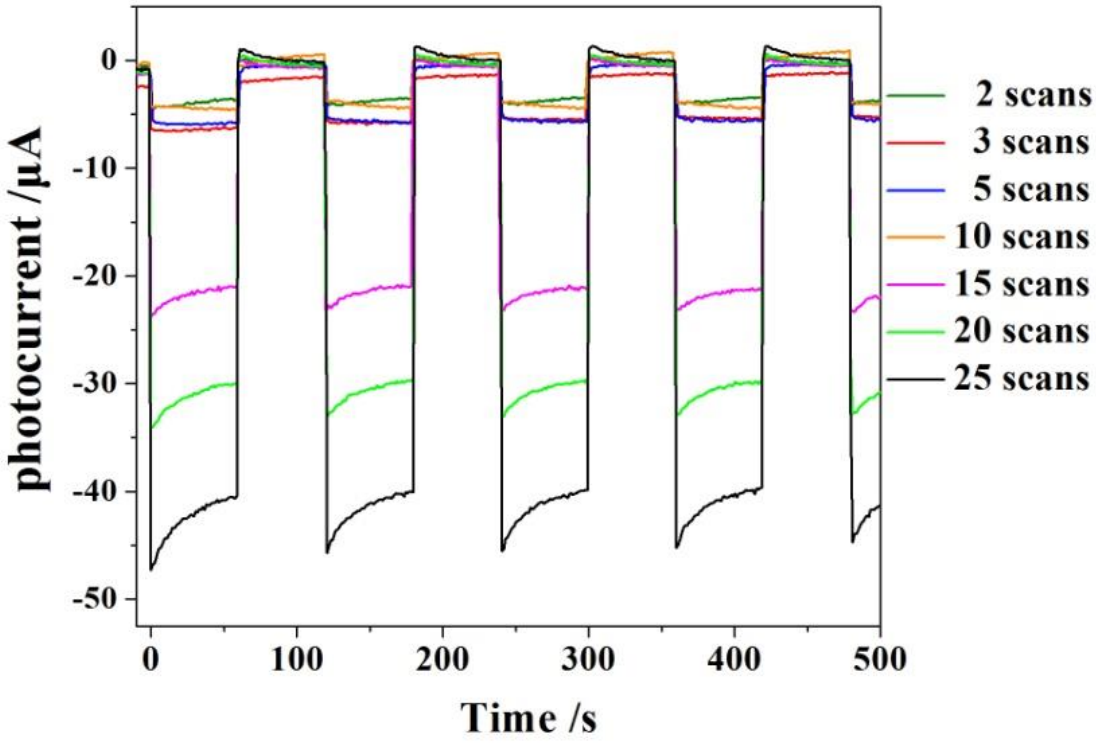

Figure 87. Photoelectrochemical response of **Poly-(H_2T_2P-POT-1)** films obtained with various iterative scans.

4.3 Conclusions

In conclusion, we developed new synthesis methods of organic monomers **F-TH** and **TEPA**. Thereafter, conjugated polymers such as **P(F-TH)**, **P(F-TH:EDOT)**, **PTEPA** and **PEDOT** were prepared. All of these polymers exhibit significant electrochromic properties and have good electricity storage capacities. We further introduced different POTs into conjugated polymers and obtain a series of inorganic/organic hybrid materials which have improved electrochemical performances. Especially, **Poly-(EDOT-POT-1)** films have promising electrochromic properties and electricity storage capacities, this material can be used as electrode material in ECSC.

Preliminary results presented at the end of this chapter have shown that hybrid free base porphyrin/POT copolymer, namely **Poly-(H_2T_2P-POT-1)** can be prepared from zinc 5,15-ditolylporphyrin and **POT-1** subunits. **Poly-(H_2T_2P-POT-1)** films exhibit good photocurrent generation behavior. It will be a good candidate for the development of photovoltaic devices.

Summary and Scope of Further Work

5.1 Summary

The present study has been carried out with the objective to design, synthesize and characterize series of new functional material based on **POTs**. We tried to study the intrinsic links among micro-structures and electrochemical properties of **POTs** based material, develop controllable synthesis technologies and obtain **POTs** based materials with excellent overall performance.

The important results of the present thesis investigation can be summarized as follow:

1. Through solvothermal and solvent diffusion methods, we synthesized twelve different **POTs** with different formula and structure have been successfully synthesized and structural determined.
2. Based on obtained **POTs**, we further prepared a series of novel materials. **C@TiO$_2$** composite materials can be used as electrode materials for Li-ion battery and supercapacitor because of their excellent electricity storage capacity. **PEDOT:Ce@TiO$_2$**, **Poly-(TEPA-POT-4)**, have strong hydrophobic surface and exhibit promising electrochromic properties.
3. The 3D nanoporous film **Poly-(EDOT-POT-1)** is a promising electrode material suitable for fast-ion transport and exhibits improved electrochromic properties and 35% higher capacitance (102.5 F/g) compared to **PEDOT** (75.8 F/g) at a current density of 1 A/g. The improved performance of the hybrid organic-inorganic material **Poly-(EDOT-POT-1)** over the parent organic polymer **PEDOT** potentially opens up a new avenue of research in this area,

with implications to a range of existing functional organic polymers.

4. **Poly-(H_2T_2P-POT-1)** films exhibit good photocurrent generation behavior, and the control of the thickness of the **Poly-(H_2T_2P-POT-1)** films is of great importance to optimize the generation of photocurrent under visible illumination.

5.2 Scope of Further Work

1. The synthesis method of **Poly-(H_2T_2P-POT-1)** films could be further improved. The mechanism of the electropolymerization needs further investigation. The photo-electrochemistry properties of **Poly-(H_2T_2P-POT-1)** will be fully studied in future**.** the overall conversion efficiency η of the sealed cell using **Poly-(H_2T_2P-POT-1)** as electrode materials also to be studied.
2. Although we have explored the incorporation of the polymerizable ligand into **POTs**. Till now we only obtain 4 polymerizable **POTs** monomers. We will try to obtain more **POTs** monomers especially heterometallic **POTs** monomers in future.
3. As homogeneous hybrid materials, **POTs** grafting conjugate polymers are expected to solve or significantly decrease those problems caused by uneven dispersion and heterogeneity interfaces in conventional composite materials. More experiments are waiting for us to prove the advantages of this kind of hybrid matrials.

General conclusion

The objective of the present thesis was to design and prepare inorganic-organic hybrid materials based on **POTs**. In this thesis, we designed, synthesized and characterized a series of novel materials based on **POTs**:**TiO_2/C** composite materials; **$CeTi_xO_y$/PEDOT** composites as well as new copolymer materials **Poly-(EDOT-POT-1)** and **Poly-(ZnT_2P-POT-1)**. We studied the intrinsic links among micro-structures and electrochemical properties of these novel materials.

In chapter II, a series of POTs with different nuclearity have been synthesized and structurally characterized. **POT-1**, **POT-2**, **POT-3**, **POT-4** are functional ligands modified **POTs** while **POT-6**, **POT-8**, **POT-9**, **POT-10, POT-11** are metal doped POTs. Their structural diversity and adjustable coordination sites make them promising as nanosized precursors or building blocks for novel materials.

In chapter III, using **POT-5** as precursor, as series of **C@TiO_2** composite materials were obtained through calcined in nitrogen flow or air flow at different temperature. The **C@TiO_2** composites calcined in nitrogen named **N800**. Compare with other **C@TiO_2** composites calcined in nitrogen (**N1000**, **N900**, **N800**, **N700**, **N600**, **N500**, **N400**, **N300**) and air (**K300**, **K400**, **K500**, **K600**, **K700**, **K800**, **K900**, **K1000**), **N800** exhibits excellent electrochemical performance, which is mainly attributed to the following aspects: the nanoporous structure that can increase the contact area between the electrolyte and the electrode and shorten the transmission distance of lithium ions which ensures rapid charge-discharge performance.

In chapter IV, new synthesis method for hybrid materials based on **POT** and conducting polymers (CPs) were developed. CPs such as **P(F-TH)**, **P(F-TH:EDOT)**, **PTEPA** and **PEDOT** exhibit significant electrochromic properties and have good electricity storage capacities. Different **POTs** are further cooperated into **CPs** and a series of inorganic/organic hybrid materials with improved electrochemical performances were obtained. Especially, **Poly-(EDOT-POT-1)** films have promising electrochromic properties and electricity storage capacities, this material can be used as electrode material in ECSC, **Poly-(H_2T_2P-POT-1)** films exhibit good photocurrent generation behavior, which worth further study.

Further research will be focused on the investigation of the electropolymerization of **Poly-(ZnT_2P-POT-1)**, try to obtain more **POTs** monomers especially heterometallic **POTs** monomers to prepare more novel hybrid materials, characterize their physical and

chemical properties and find their advantages and potencial applications.

List of Publications

Publications in Journals

1. “Conjugated hybrid films based on a new polyoxotitanate monomer”, G. Liu, X. Yang, A. Bonnefont, **Y. Lv***, J. Chen, W. Dan, Z. Chen, L. Ruhlmann*, D. S. Wright, C. Zhang*, *Chemical Communications*, **2018**, *54, 14132-14135. Corresponding author.*

2. “A New Polyethylene Composite Material Based on Nano Silver Particels Loaded Graphene Oxide”, F. Zhang, K. Zhang, M. Zhou, C. Chen, Z. Cai, G. Wei, X. Jiang, C. Zhang, L. Ruhlmann, **Y. Lv***, *Journal Inorganic Materials*; **2019**, *34(6), 633-640. Corresponding author.*

3. “Preparation and electrochemical properties of a new multifunctional inorganic/organic composite film”, J. Chen, P. Ma, C. Zhang, L. Ruhlmann, **Y. Lv***, *Journal Inorganic Materials*; **2020**, *35(2), 217-223. Corresponding author.*

4. “Recycling Iron-Containing Sludges from the Electroflocculation of Printing and Dyeing Wastewater into Anode Materials for Lithium‐Ion Batteries”, G. Liu, Y. Shen, P. Ma, S. Zhao, A. Bonnefont, **Y. Lv*** C. Wang, L. Ruhlmann,* C. Zhang*, *ChemSusChem*; **2020**, *13, 3469– 3478. Corresponding author.*

5. “An Efficient Electrochromic Supercapacitor Based on Solution-Processable Nanoporous Poly{tris[4-(3,4-ethylenedioxythiophene)phenyl]amine}”, **Y. Lv**, X. Yang, W. Du, P. Ma, H. Wang, A. Bonnefont, D. S. Wright,* L. Ruhlmann,* C. Zhang*, *ChemSusChem*; **2020**, *13, 3844– 3854.*

6. “Fluorinated Oleophilic Electrochromic Copolymer Based on 3-(N-Trifluoroacetamido)thiophene and 3,4-Ethylenedioxythiophene (EDOT)”, H. Wang, Y. Shen, P. Ma, A. Bonnefont, **Y. Lv***, L. Ruhlmann,*H. Ni, W. Liu, C. Zhang*, *ChemElectroChem*; **2020**, *7, 3038–3043. Corresponding author.*

Presentations in conferences:

1. A series of novel electrochromic materials based on polyoxotitanate clusters grafting thiophene conjugate polymers, Yiyao Shen, Laurent Ruhlmann and Yaokang Lv, The 32nd Chinese Chemical Society (CCS) Congress, April 19-21, 2021, Zhuhai, Guangdong, P. R. China.

References

1. Issawi C. *The 1973 oil crisis and after*. J Post Keynes Econ. 1978; 1(2): 3−26.

2. Finlan A. *The Gulf War 1991*. Oxford: Osprey Publishing; 2003.

3. Hall, D. O., Mynick, H. E., & Williams, R. H. (1991). Cooling the greenhouse with bioenergy. *Nature*, 353(6339), 11-12.

4. Rogelj, J., Huppmann, D., Krey, V., Riahi, K., & Meinshausen, M. (2019). A new scenario logic for the paris agreement long-term temperature goal. *Nature*, 573(7774), 357-363.

5. MIT Energy initiative, *The future of solar energy*. (2019) http://energy.mit.edu/research/future-solar-energy/.

6. Zhang, H. , Lu, Y. , Han, W. , Zhu, J. , & Huang, W. (2020). Solar energy conversion and utilization: towards the emerging photo-electrochemical devices based on perovskite photovoltaics. *Chemical Engineering Journal*, 393, 124766.

7. Fujishima, A., & Honda, K. (1972). Electrochemical photolysis of water at a semiconductor electrode. *Nature*, 238(5358), 37-38.

8. A, J, & Nozik. (1978). Photoelectrochemistry: applications to solar energy conversion. *Annual Review of Physical Chemistry*, 29, 189.

9. Adam, & Heller. (1984). Hydrogen-evolving solar cells. *Science*, 233, 1141.

10. Getoff, N. (1990). Photoelectrochemical and photocatalytic methods of hydrogen production: a short review. *International Journal of Hydrogen Energy*, 15(6), 407-417.

11. (a) G Pleskov, I͡U. V. (I͡Uriĭ Viktorovich). (1990). *Solar energy conversion : a photoelectrochemical approach*. Springer-Verlag; (b) Gao, L., Cui, Y., Vervuurt, R. H., van Dam, D., van Veldhoven, R. P., Hofmann, J. P., Bol, A.

A., Haverkort, J. E. M., Notten, P. H. L., Bakkers, E. P. A. M. & Hensen, E. J. M. (2016). High-efficiency InP-based photocathode for hydrogen production by interface energetics design and photon management. *Advanced Functional Materials*, 26(5), 679-686.

12. Gao L., Cui Y., Vervuurt R. H. J., Dm D. V., Rene P. J., Veldhoven V., Hofmann J. P., Ageeth A., Bol J. E., Haverkort M., Peter H. L., Notten E., Bakkers P. A. M. & Hensen, E. J. (2016). High‐efficiency InP‐based photocathode for hydrogen production by interface energetics design and photon management. *Advanced Functional Materials*, 26(5), 679-686.

13. Shi, D., Zheng, R., Sun, M. J., Cao, X., Sun, C. X., Cui, C. J., Liu, C. S., Zhao, J. & Du, M. (2017). Semiconductive Copper (I)–Organic Frameworks for Efficient Light‐Driven Hydrogen Generation Without Additional Photosensitizers and Cocatalysts. *Angewandte Chemie*, 129(46), 14829-14833.

14. Zheng, L., Teng, F., Ye, X., Zheng, H., & Fang, X. (2020). Photo/electrochemical applications of metal sulfide/TiO_2 heterostructures. *Advanced Energy Materials*, 10(1), 1902355.

15. REN21. *Renewables 2020 global status report.* https://www.ren21.net/wp-content/uploads/2019/05/gsr_2020_full_report_en.pdf Published June, 2020. Accessed February 27, 2021.

16. Zhang, Y., Gevorgian, V., Wang, C., Lei, X., Chou, E., Yang, R., Li, Q. & Jiang, L. (2017). Grid-level application of electrical energy storage: Example use cases in the United States and China. *IEEE Power and Energy Magazine*, 15(5), 51-58.

17. Dunn, B., Kamath, H., & Tarascon, J. M. (2011). Electrical energy storage for the grid: a battery of choices. *Science*, 334(6058), 928-935.

18. Choi, J. W., & Aurbach, D. (2016). Promise and reality of post-lithium-ion batteries with high energy densities. *Nature Reviews Materials*, 1(4), 1-16.

19. Lu, Y., Zhang, Q., Li, L., Niu, Z., & Chen, J. (2018). Design strategies toward

enhancing the performance of organic electrode materials in metal-ion batteries. *Chem*, 4(12), 2786-2813.

20. Xie, J., Gu, P., & Zhang, Q. (2017). Nanostructured conjugated polymers: toward high-performance organic electrodes for rechargeable batteries. *ACS Energy Letters*, 2(9), 1985-1996.

21. Sharma, K., Arora, A., & Tripathi, S. K. (2019). Review of supercapacitors: Materials and devices. *Journal of Energy Storage*, 21, 801-825.

22. Borenstein, A., Hanna, O., Attias, R., Luski, S., Brousse, T., & Aurbach, D. (2017). Carbon-based composite materials for supercapacitor electrodes: a review. *Journal of Materials Chemistry A*, 5(25), 12653-12672.

23. Snook, G. A., Kao, P., & Best, A. S. (2011). Conducting-polymer-based supercapacitor devices and electrodes. *Journal of power sources*, 196(1), 1-12.

24. Lukatskaya, M. R., Kota, S., Lin, Z., Zhao, M. Q., Shpigel, N., Levi, M. D., Halim, J., Taberna, P.-L., Barsoum, M. W., Simon, P., & Gogotsi, Y. (2017). Ultra-high-rate pseudocapacitive energy storage in two-dimensional transition metal carbides. *Nature Energy*, 2(8), 1-6.

25. Granqvist, C. G. (2005). Electrochromic devices. *Journal of the European Ceramic Society*, 25(12), 2907-2912.

26. Mortimer, R. J. (2011). Electrochromic materials. Annual review of materials research, 41, 241-268.

27. Rosseinsky, D. R., & Mortimer, R. J. (2001). Electrochromic systems and the prospects for devices. *Advanced Materials*, 13(11), 783-793.

28. Li, H., McRae, L., Firby, C. J., Al-Hussein, M., & Elezzabi, A. Y. (2018). Nanohybridization of molybdenum oxide with tungsten molybdenum oxide nanowires for solution-processed fully reversible switching of energy storing smart windows. *Nano Energy*, 47, 130-139.

29. Wang, X., Chen, K., de Vasconcelos, L. S., He, J., Shin, Y. C., Mei, J., & Zhao, K. (2020). Mechanical breathing in organic electrochromics. *Nature communications*, 11(1), 1-10.

30. Cai, G., Darmawan, P., Cheng, X., & Lee, P. S. (2017). Inkjet printed large area multifunctional smart windows. *Advanced Energy Materials*, 7(14), 1602598.

31. Sass, S. L. (1998). The substance of civilization: Materials and human history from the stone age to the age of silicon. Arcade Publishing.

32. Long, D. L., Burkholder, E., & Cronin, L. (2007). Polyoxometalate clusters, nanostructures and materials: From self assembly to designer materials and devices. *Chemical Society Reviews*, 36(1), 105-121.

33. López, X., Carbó, J. J., Bo, C., & Poblet, J. M. (2012). Structure, properties and reactivity of polyoxometalates: a theoretical perspective. *Chemical Society Reviews*, 41(22), 7537-7571.

34. Anyushin, A. V., Kondinski, A., & Parac-Vogt, T. N. (2020). Hybrid polyoxometalates as post-functionalization platforms: from fundamentals to emerging applications. *Chemical Society Reviews*, 49(2), 382-432.

35. Pelaez, M., Nolan, N. T., Pillai, S. C., Seery, M. K., Falaras, P., Kontos, A. G., Dunlop, P. S. M., J. Hamilton, J. W., Byrne, J. A., O'Shea, K., Entezari, M. H. & Dionysiou, D. D. (2012). A review on the visible light active titanium dioxide photocatalysts for environmental applications. *Applied Catalysis B: Environmental*, 125, 331-349..

36. Linsebigler, A. L., Lu, G., & Yates Jr, J. T. (1995). Photocatalysis on TiO_2 surfaces: principles, mechanisms, and selected results. *Chemical reviews*, 95(3), 735-758.

37. Sandell, A., Sanyal, B., Walle, L. E., Richter, J. H., Plogmaker, S., Karlsson, P. G., Borg, A. & Uvdal, P. (2008). Probing and modifying the empty-state threshold of anatase TiO_2: Experiments and ab initio theory. *Physical Review*

B, 78(7), 075113.

38. Li, M., Hebenstreit, W., Gross, L., Diebold, U., Henderson, M. A., Jennison, D. R., Schultz, P.A., & Sears, M. P. (1999). Oxygen-induced restructuring of the TiO_2 (110) surface: a comprehensive study. *Surface Science*, 437(1-2), 173-190.

39. Bai, J., & Zhou, B. (2014). Titanium dioxide nanomaterials for sensor applications. *Chemical reviews*, 114(19), 10131-10176.

40. Rozes, L., & Sanchez, C. (2011). Titanium oxo-clusters: precursors for a Lego-like construction of nanostructured hybrid materials. *Chemical Society Reviews*, 40(2), 1006-1030.

41. Coppens, P., Chen, Y., & Trzop, E. (2014). Crystallography and properties of polyoxotitanate nanoclusters. *Chemical reviews*, 114(19), 9645-9661.

42. Li, N., Matthews, P. D., Luo, H. K., & Wright, D. S. (2016). Novel properties and potential applications of functional ligand-modified polyoxotitanate cages. *Chemical Communications*, 52(75), 11180-11190.

43. Narayanam, N., Fang, W. H., Chintakrinda, K., Zhang, L., & Zhang, J. (2017). Deep eutectic-solvothermal synthesis of titanium-oxo clusters protected by π-conjugated chromophores. *Chemical Communications*, 53(57), 8078-8080.

44. Chambers, M. B., Wang, X., Ellezam, L., Ersen, O., Fontecave, M., Sanchez, C., Rozes, L. & Mellot-Draznieks, C. (2017). Maximizing the photocatalytic activity of metal–organic frameworks with aminated-functionalized linkers: substoichiometric effects in MIL-125-NH2. *Journal of the American Chemical Society*, 139(24), 8222-8228.

45. Lv, Y., Willkomm, J., Steiner, A., Gan, L., Reisner, E., & Wright, D. S. (2012). Encapsulation of a 'naked' Br^- anion in a polyoxotitanate host. *Chemical Science*, 3(8), 2470-2473.

46. Lv, Y., Du, W., Ren, Y., Cai, Z., Yu, K., Zhang, C., Chen, Z. & Wright, D. S.

(2016). An integrated electrochromic supercapacitor based on nanostructured Er-containing titania using an Er (III)-doped polyoxotitanate cage. *Inorganic Chemistry Frontiers*, 3(9), 1119-1123.

47. Benedict, J. B., Freindorf, R., Trzop, E., Cogswell, J., & Coppens, P. (2010). Large polyoxotitanate clusters: well-defined models for pure-phase TiO2 structures and surfaces. *Journal of the American Chemical Society*, 132(39), 13669-13671.

48. Gao, M. Y., Wang, F., Gu, Z. G., Zhang, D. X., Zhang, L., & Zhang, J. (2016). Fullerene-like Polyoxotitanium cage with high solution stability. *Journal of the American Chemical Society*, 138(8), 2556-2559.

49. Fang, W. H., Zhang, L., & Zhang, J. (2016). A 3.6 nm Ti52–oxo nanocluster with precise atomic structure. *Journal of the American Chemical Society*, 138(24), 7480-7483.

50. Fang, W. H., Zhang, L., & Zhang, J. (2018). Synthetic strategies, diverse structures and tuneable properties of polyoxo-titanium clusters. *Chemical Society Reviews*, 47(2), 404-421.

51. Mason, J. A., Darago, L. E., Lukens Jr, W. W., & Long, J. R. (2015). Synthesis and O_2 reactivity of a titanium (III) metal–organic framework. *Inorganic chemistry*, 54(20), 10096-10104.

52. Bueken, B., Vermoortele, F., Vanpoucke, D. E., Reinsch, H., Tsou, C. C., Valvekens, P., De Baerdemaeker, T., Ameloot, R., Kirschhock, C. E., Van Speybroeck, V., Mayer, J. M. & De Vos, D. (2015). A Flexible Photoactive Titanium Metal-Organic Framework Based on a $[Ti^{IV}_3(\mu_3\text{-}O)(O)_2(COO)_6]$ Cluster. *Angewandte Chemie International Edition*, 54(47), 13912-13917.

53. Assi, H., Mouchaham, G., Steunou, N., Devic, T., & Serre, C. (2017). Titanium coordination compounds: from discrete metal complexes to metal–organic frameworks. *Chemical Society Reviews*, 46(11), 3431-3452.

54. Czakler, M., Artner, C., & Schubert, U. (2014). Acetic acid mediated synthesis

of phosphonate-substituted titanium oxo clusters. European journal of inorganic chemistry, 2014(12), 2038.

55. Artner, C., Koyun, A., & Schubert, U. (2015). A heterobimetallic copper–titanium oxo cluster with a new structural motif. Monatshefte für Chemie-Chemical Monthly, 146(11), 1777-1780.

56. Lv, Y., Cheng, J., Matthews, P. D., Holgado, J. P., Willkomm, J., Leskes, M., Steiner, A., Fenske, D., King, T. C., Wood, P. T., Gan, L., Lambert, R. M. & Wright, D. S. (2014). A study of the optical properties of metal-doped polyoxotitanium cages and the relationship to metal-doped titania. *Dalton Transactions*, 43(23), 8679-8689.

57. Gu, Z. G., Zhan, C., Zhang, J., & Bu, X. (2016). Chiral chemistry of metal–camphorate frameworks. *Chemical Society Reviews*, 45(11), 3122-3144.

58. Rocha, J., Carlos, L. D., Paz, F. A. A., & Ananias, D. (2011). Luminescent multifunctional lanthanides-based metal–organic frameworks. *Chemical Society Reviews*, 40(2), 926-940.

59. Zhang, G., Liu, C., Long, D. L., Cronin, L., Tung, C. H., & Wang, Y. (2016). Water-soluble pentagonal-prismatic titanium-oxo clusters. *Journal of the American Chemical Society*, 138(35), 11097-11100.

60. Zhang, G., Hou, J., Tung, C. H., & Wang, Y. (2016). Small Titanium Oxo Clusters: Primary Structures of Titanium (IV) in Water. Inorganic chemistry, 55(7), 3212-3214.

61. Hu, J., Zhan, L., Zhang, G., Zhang, Q., Du, L., Tung, C. H., & Wang, Y. (2016). Effects of substitutional dopants on the photoresponse of a polyoxotitanate cluster. *Inorganic chemistry*, 55(17), 8493-8501.

62. Xiong, W. W., Li, J. R., Hu, B., Tan, B., Li, R. F., & Huang, X. Y. (2012). Largest discrete supertetrahedral clusters synthesized in ionic liquids. *Chemical Science*, 3(4), 1200-1204.

63. Tang, B., & Row, K. H. (2013). Recent developments in deep eutectic solvents in chemical sciences. *Monatshefte für Chemie-Chemical Monthly*, 144(10), 1427-1454.

64. Narayanam, N., Fang, W. H., Chintakrinda, K., Zhang, L., & Zhang, J. (2017). Deep eutectic-solvothermal synthesis of titanium-oxo clusters protected by π-conjugated chromophores. *Chemical Communications*, 53(57), 8078-8080.

65. Chaumont, C., Mobian, P., & Henry, M. (2014). An unprecedented high nuclearity catecholato-based Ti (IV)-architecture bearing labile pyridine ligands. *Dalton Transactions*, 43(9), 3416-3419.

66. Chaumont, C., Huen, E., Huguenard, C., Mobian, P., & Henry, M. (2013). Toward colored reticular titanium-based hybrid networks: Evaluation of the reactivity of the $[Ti_8O_8(OOCCH_2But)_{16}]$ wheel with phenol, resorcinol and catechol. *Polyhedron*, 57, 70-76.

67. Yuan, S., Liu, T. F., Feng, D., Tian, J., Wang, K., Qin, J., Zhang, Q., Chen, Y. P., Bosch, M., Zou, L., Teat, S. J., Dalgarno, S. J. & Zhou, H. C. (2015). A single crystalline porphyrinic titanium metal–organic framework. *Chemical science*, 6(7), 3926-3930.

68. Snoeberger III, R. C., Young, K. J., Tang, J., Allen, L. J., Crabtree, R. H., Brudvig, G. W., Coppens, P., Victor, S. B. & Benedict, J. B. (2012). Interfacial electron transfer into functionalized crystalline polyoxotitanate nanoclusters. *Journal of the American Chemical Society*, 134(21), 8911-8917.

69. Wu, Y. Y., Lu, X. W., Qi, M., Su, H. C., Zhao, X. W., Zhu, Q. Y., & Dai, J. (2014). Titanium–oxo cluster with 9-anthracenecarboxylate antennae: a fluorescent and photocurrent transfer material. *Inorganic chemistry*, 53(14), 7233-7240.

70. Marom, N., Körzdörfer, T., Ren, X., Tkatchenko, A., & Chelikowsky, J. R. (2014). Size effects in the interface level alignment of dye-sensitized TiO_2 clusters. *The journal of physical chemistry letters*, 5(14), 2395-2401.

71. Liu, J. X., Gao, M. Y., Fang, W. H., Zhang, L., & Zhang, J. (2016). Bandgap engineering of titanium–oxo clusters: labile surface sites used for ligand

substitution and metal incorporation. *Angewandte Chemie International Edition*, 55(17), 5160-5165.

72. Lai, Y. H., Lin, C. Y., Lv, Y., King, T. C., Steiner, A., Muresan, N. M., Gan, L., Wright, D. S., & Reisner, E. (2013). Facile assembly of an efficient CoO_x water oxidation electrocatalyst from Co-containing polyoxotitanate nanocages. *Chemical Communications*, 49(39), 4331-4333.

73. Chen, Y., Jarzembska, K. N., Trzop, E., Zhang, L., & Coppens, P. (2015). How does substitutional doping affect visible light absorption in a series of homodisperse Ti_{11} polyoxotitanate nanoparticles?. *Chemistry–A European Journal*, 21(32), 11538-11544.

74. Hu, J., Zhan, L., Zhang, G., Zhang, Q., Du, L., Tung, C. H., & Wang, Y. (2016). Effects of substitutional dopants on the photoresponse of a polyoxotitanate cluster. *Inorganic chemistry*, 55(17), 8493-8501.

75. Liu, S., Hu, W., Nath, J. K., Tong, J., Hou, X., Liu, W., Yang, J. & Liu, B. (2017). $[Ti_{12}In_6O_{18}(OOCC_6H_5)_{30}]$: a multifunctional hetero-polyoxotitanate nanocluster with high stability and visible photoactivity. *Dalton Transactions*, 46(3), 678-684.

76. Zhang, J., Hu, W., Zhang, J., Liu, S., Tong, J., Hou, X., Liu, W., Yang, J. & Liu, B. (2017). Stable Heteropolyoxotitanate Nanocluster for Full Solar Spectrum Photocatalytic Hydrogen Evolution. *The Journal of Physical Chemistry C*, 121(34), 18326-18332.

77. Chen, Y., Sokolow, J., Trzop, E., Chen, Y. S., & Coppens, P. (2013). A large manganese-doped polyoxotitanate nanocluster: $Ti_{14}MnO_{14}(OH)_2(OEt)_{28}$. *Journal of the Chinese Chemical Society*, 60(7), 887-890.

78. Matthews, P. D., King, T. C., & Wright, D. S. (2014). Structure, photochemistry and applications of metal-doped polyoxotitanium alkoxide cages. *Chemical Communications*, 50(85), 12815-12823.

79. Wu, L., Jimmy, C. Y., Zhang, L., Wang, X., & Ho, W. (2004). Preparation of a highly active nanocrystalline TiO_2 photocatalyst from titanium oxo cluster precursor. *Journal of Solid State Chemistry*, 177(7), 2584-2590.

80. Rammal, A., Brisach, F., & Henry, M. (2002). Hydrothermal synthesis of TiO_2 anatase nanocrystals using hexaprismatic-shaped oxo-carboxylate complexes. *Comptes Rendus Chimie*, 5(1), 59-66.

81. Boyle, T. J., Tribby, L. J., Alam, T. M., Bunge, S. D., & Holland, G. P. (2005). Catechol derivatives of Group 4 and 5 compounds. *Polyhedron*, 24(10), 1143-1152.

82. Boyle, T. J., Tyner, R. P., Alam, T. M., Scott, B. L., Ziller, J. W., & Potter, B. G. (1999). Implications for the thin-film densification of TiO_2 from carboxylic acid-modified titanium alkoxides. syntheses, characterizations, X-ray structures of $Ti_3(\mu_3\text{-}O)(O_2CH)_2(ONep)_8$, $Ti_3(\mu_3\text{-}O)(O_2CMe)_2(ONep)_8$, $Ti_6(\mu_3\text{-}O)_6(O_2CCHMe_2)_6(ONep)_6$, $[Ti(\mu\text{-}O_2CCMe_3)(ONep)_3]_2$, and $Ti_3(\mu_3\text{-}O)(O_2CCH_2CMe_3)_2(ONep)_8$ ($ONep=OCH_2CMe_3$). *Journal of the American Chemical Society*, 121(51), 12104-12112.

83. Karatchevtseva, I., Cassidy, D. J., Zhang, Z., Triani, G., Finnie, K. S., Cram, S. L., & Bartlett, C. J. (2008). Crystallization of TiO_2 powders and thin films prepared from modified titanium alkoxide precursors. *Journal of the American Ceramic Society*, 91(6), 2015-2023.

84. Mehner, A., Rüffer, T., Lang, H., Pohlers, A., Hoyer, W., & Spange, S. (2008). Synthesis of Nanosized TiO_2 by Cationic Polymerization of (μ4−oxido)−hexakis (μ−furfuryloxo)−octakis (furfuryloxo)−tetra−titanium. *Advanced Materials*, 20(21), 4113-4117.

85. Liu, J., Cai, Z., Lv, Y., Zhang, Y., Su, C., Ouyang, M., Zhang, C. & Wright, D. S. (2015). From a polyoxotitanium cage to TiO_2/C composites, a novel strategy for nanoporous materials. *Journal of Materials Chemistry A*, 3(5), 1837-1840.

86. Férey, G. (2008). Hybrid porous solids: past, present, future. *Chemical Society Reviews*, 37(1), 191-214.

87. Miele-Pajot, N., Hubert-Pfalzgraf, L. G., Papiernik, R., Vaissermann, J., & Collier, R. (1999). Synthesis and molecular structure of $[Ti_4(OPr^i)_8(\mu, \eta_2\text{-}OCH_2CH{=}CHCH_2O)_2(\mu_3,\eta_2\text{-}OCH_2CH{=}CHCH_2O)_2]$. Application to the

elaboration of low density, microcellular, doped organic materials. *Journal of Materials Chemistry*, 9(12), 3027-3033.

88. Steunou, N., Förster, S., Florian, P., Sanchez, C., & Antonietti, M. (2002). Synthesis of nanostructured polymer-titanium oxide composites through the assembly of titanium-oxo clusters and amphiphilic block copolymers micelles. *Journal of Materials Chemistry*, 12(12), 3426-3430.

89. Fornasieri, G., Rozes, L., Le Calvé, S., Alonso, B., Massiot, D., Rager, M. N., Evain, M., Boubekeur, K. & Sanchez, C. (2005). Reactivity of titanium oxo ethoxo cluster [$Ti_{16}O_{16}(OEt)_{32}$]. Versatile precursor of nanobuilding block-based hybrid materials. *Journal of the American Chemical Society*, 127(13), 4869-4878.

90. Frot, T., Cochet, S., Laurent, G., Sassoye, C., Popall, M., Sanchez, C., & Rozes, L. (2010). $Ti_8O_8(OOCR)_{16}$, a new family of titanium–oxo clusters: potential NBUs for reticular chemistry. *European Journal of Inorganic Chemistry*, 2010(36), 5650-5659.

91. Heinz, P., Puchberger, M., Bendova, M., Baumann, S. O., & Schubert, U. (2010). Clusters for alkyne-azide click reactions. *Dalton Transactions*, 39(33), 7640-7644.

92. Eslava, S., Papageorgiou, A. C., Beaumont, S. K., Kyriakou, G., Wright, D. S., & Lambert, R. M. (2010). Synthesis, characterization, and surface tethering of sulfide-functionalized Ti16-oxo-alkoxy cages. *Chemistry of Materials*, 22(18), 5174-5178.

93. Zhang, G., Kim, G., & Choi, W. (2014). Visible light driven photocatalysis mediated via ligand-to-metal charge transfer (LMCT): an alternative approach to solar activation of titania. *Energy & Environmental Science*, 7(3), 954-966.

94. Chaumont, C., Mobian, P., & Henry, M. (2014). An unprecedented high nuclearity catecholato-based Ti (IV)-architecture bearing labile pyridine ligands. *Dalton Transactions*, 43(9), 3416-3419.

95. Hou, J. L., Luo, W., Wu, Y. Y., Su, H. C., Zhang, G. L., Zhu, Q. Y., & Dai, J. (2015). Two Ti 13-oxo-clusters showing non-compact structures, film

electrode preparation and photocurrent properties. *Dalton Transactions*, 44(46), 19829-19835.

96. Wu, Y. Y., Wang, P., Wang, Y. H., Jiang, J. B., Bian, G. Q., Zhu, Q. Y., & Dai, J. (2013). Metal–phenanthroline fused Ti 17 clusters, a single molecular source for sensitized photoconductive films. *Journal of Materials Chemistry A*, 1(34), 9862-9868.

97. Jarzembska, K. N., Chen, Y., Nasca, J. N., Trzop, E., Watson, D. F., & Coppens, P. (2014). Relating structure and photoelectrochemical properties: electron injection by structurally and theoretically characterized transition metal-doped phenanthroline–polyoxotitanate nanoparticles. *Physical Chemistry Chemical Physics*, 16(30), 15792-15795.

98. Li, N., Matthews, P. D., Leung, J. J., King, T. C., Wood, P. T., Luo, H. K., & Wright, D. S. (2015). Synthesis, structure and properties of the manganese-doped polyoxotitanate cage $[Ti_{18}MnO_{30}(OEt)_{20}(MnPhen)_3]$(Phen= 1, 10-phenanthroline). *Dalton Transactions*, 44(44), 19090-19096.

99. Feldt, S. M., Gibson, E. A., Gabrielsson, E., Sun, L., Boschloo, G., & Hagfeldt, A. (2010). Design of organic dyes and cobalt polypyridine redox mediators for high-efficiency dye-sensitized solar cells. *Journal of the American Chemical Society*, 132(46), 16714-16724.

100. Lin, Y., Zhu, Y. F., Chen, Z. H., Liu, F. H., Zhao, L., & Su, Z. M. (2014). Synthesis, structure, and photocatalytic hydrogen of three environmentally friendly titanium oxo-clusters. *Inorganic Chemistry Communications*, 40, 22-*25*.

101. Wu, Y. Y., Luo, W., Wang, Y. H., Pu, Y. Y., Zhang, X., You, L. S., You, L.-S., Zhu, Q.-Y. & Dai, J. (2012). Titanium–oxo–clusters with dicarboxylates: single-crystal structure and photochromic effect. *Inorganic chemistry*, 51(16), 8982-8988.

102. Dan-Hardi, M., Serre, C., Frot, T., Rozes, L., Maurin, G., Sanchez, C., & Férey, G. (2009). A new photoactive crystalline highly porous titanium (IV) dicarboxylate. *Journal of the American Chemical Society*, 131(31), 10857-10859.

103. Lv, Y., Cai, Z., Yan, D., Su, C., Li, W., Chen, W., Ren, Z., Wei, Y., Ouyang, M., Zhang, C. & Wright, D. S. (2016). Novel Eu-containing titania composites derived from a new Eu (III)-doped polyoxotitanate cage. *RSC advances*, 6(1), 57-60.

104. Mikami, K., Matsumoto, Y., & Xu, L. (2006). Modification of alkoxo ligands of BINOL–Ti ladder: isolation and X-ray crystallographic analysis. *Inorganica chimica Acta*, 359(13), 4159-4167.

105. Ishimoto, R., Kamata, K., Suzuki, K., Yamaguchi, K., & Mizuno, N. (2015). Synthesis and structural characterization of BINOL-modified chiral polyoxometalates. *Dalton Transactions*, 44(24), 10947-10951.

106. Pandiaraju, S., Chen, G., Lough, A., & Yudin, A. K. (2001). Generation of Highly Enantioselective Catalysts from the Pseudoenatiomeric Assembly of BINOL, F_8BINOL, and Ti $(O^iPr)_4$. *Journal of the American Chemical Society*, 123(16), 3850-3851.

107. Balsells, J., Davis, T. J., Carroll, P., & Walsh, P. J. (2002). Insight into the mechanism of the asymmetric addition of alkyl groups to aldehydes catalyzed by titanium− BINOLate species. *Journal of the American Chemical Society*, 124(35), 10336-10348.

108. Corden, J. P., Errington, W., Moore, P., Partridge, M. G., & Wallbridge, M. G. (2004). Synthesis of di-, tri-and penta-nuclear titanium (iv) species from reactions of titanium (iv) alkoxides with 2, 2′-biphenol (H_2L_1) and 1, 1′-binaphthol (H_2L_2); crystal structures of $[Ti_3(\mu_2\text{-}OPr^i)_2(OPr^i)_8L_1]$, $[Ti_3(OPr^i)_6L_{13}]$, $[Ti_5(\mu_3\text{-}O)_2(\mu_2\text{-}OR)_2(OR)_6L_{14}]$ (R= OPr^i, OBu^n) and $[Ti_2(OPr^i)_4L_{22}]$. *Dalton Transactions*, (12), 1846-1851.

109. Schetter, B., Ziemer, B., Schnakenburg, G., & Mahrwald, R. (2008). Tetranuclear BINOL⁻ Titanium Complex in Selective Direct Aldol Additions. *The Journal of Organic Chemistry*, 73(3), 813-819.

110. Mahrwald, R., & Schetter, B. (2006). Unusual highly regioselective direct aldol additions with a moisture-resistant and highly efficient titanium catalyst. *Organic letters*, 8(2), 281-284.

111. Yu, R., Yamashita, Y., & Kobayashi, S. (2009). Titanium (IV)/Tridentate BINOL Derivative as Catalyst for meso - Aziridine Ring - Opening Reactions: High Enantioselectivity, Strong Positive Non - Linear Effect and Structural Characterization. *Advanced Synthesis & Catalysis*, 351(1−2), 147-152.

112. Terada, M., Matsumoto, Y., Nakamura, Y., & Mikami, K. (1999). Molecular assembly of BINOL-Ti complexes into an active μ3-oxo titanium catalyst. *Inorganica Chimica Acta*, 296(1), 267-272.

113. Mikami, K., Ueki, M., Matsumoto, Y., & Terada, M. (2001). Tetranuclear titanium 7, 7′ - modified binaphtholate cluster as a novel chiral Lewis acid catalyst. *Chirality: The Pharmacological, Biological, and Chemical Consequences of Molecular Asymmetry*, 13(9), 541-544.

114. McKeown, N. B. (2010). Nanoporous molecular crystals. *Journal of Materials Chemistry*, 20(47), 10588-10597.

115. Hong, K., Bak, W., & Chun, H. (2014). Robust Molecular Crystals of Titanium (IV)-oxo-Carboxylate Clusters Showing Water Stability and CO_2 Sorption Capability. *Inorganic Chemistry*, 53(14), 7288-7293.

116. (a) Hong, K., & Chun, H. (2013). Nonporous titanium–oxo molecular clusters that reversibly and selectively adsorb carbon dioxide. *Inorganic Chemistry*, 52(17), 9705-9707; (b) Wang, R., Li, Y., Shetye, K., Dutta, T., Jin, L., Li, S., & Peng, Z. (2015). Luminescent Polythiophene−Based Main−Chain Polyoxometalate - Containing Conjugated Polymers with Improved Solar−Cell Performance. European *Journal of Inorganic Chemistry*, 2015(4), 656-663; (c) Matsuse, R., Abe, M., Tomiyasu, Y., Inatomi, A., Yonemura, H., Yamada, S., & Hisaeda, Y. (2013). Metallopolymer Films Exhibiting Three-Color Electrochromism in the UV/Vis and Near-IR Region: Remarkable Utility of Trimetallic Clusters Bearing Thienyl Pendants and Their Mixed-Valent Charge Transfer Transitions. *Journal of Inorganic and Organometallic Polymers and Materials*, 23(1), 136-146; (d) Lv, Y. , Yao, M. , Holgado, J. P. , Roth, T. , Steiner, A. , & Gan, L. , et al. (2013). A low-temperature single-source route to an efficient broad-band cerium(iii) photocatalyst using a bimetallic polyoxotitanium cage. *RSC Advances*, 3, 13659-13662.

117. Sheldrick, G. M. (2015). SHELXT–Integrated space-group and crystal-structure determination. *Acta Crystallographica Section A: Foundations and Advances*, 71(1), 3-8.

118. Day, V. W., Eberspacher, T. A., Klemperer, W. G., & Park, C. W. (1993). Dodecatitanates: a new family of stable polyoxotitanates. *Journal of the American Chemical Socie*ty, 115(18), 8469-8470.

119. Roy, N., Sohn, Y., & Pradhan, D. (2013). Synergy of low-energy {101} and high-energy {001} TiO_2 crystal facets for enhanced photocatalysis. *ACS Nano*, 7(3), 2532-2540.

120. Wang, G., Wang, Q., Lu, W., & Li, J. (2006). Photoelectrochemical study on charge transfer properties of TiO_2-B nanowires with an application as humidity sensors. *The Journal of Physical Chemistry B*, 110(43), 22029-22034.

121. Huang, J. H., Hung, P. Y., Hu, S. F., & Liu, R. S. (2010). Improvement efficiency of a dye-sensitized solar cell using Eu^{3+} modified TiO_2 nanoparticles as a secondary layer electrode. *Journal of Materials Chemistry*, 20(31), 6505-6511.

122. Pan, K., Dong, Y., Tian, C., Zhou, W., Tian, G., Zhao, B., & Fu, H. (2009). TiO2-B narrow nanobelt/TiO_2 nanoparticle composite photoelectrode for dye-sensitized solar cells. *Electrochimica Acta*, 54(28), 7350-7356.

123. Zhu, W., Yang, H., Nakanishi, K., Kanamori, K., & Guo, X. (2015). Sol-gel synthesis of nanocrystal-constructed hierarchically porous TiO_2 based composites for lithium ion batteries. *RSC Advances*, 5(31), 24803-24813.

124. Cheng, Y., Chen, Z., Wu, H., Zhu, M., & Lu, Y. (2016). Ionic Liquid‐Assisted Synthesis of TiO_2-Carbon Hybrid Nanostructures for Lithium‐Ion Batteries. *Advanced Functional Materials*, 26(9), 1338-1346.

125. Gao, L., Li, S., Huang, D., Shen, Y., & Wang, M. (2015). Porous $Li_4Ti_5O_{12}$–TiO_2 nanosheet arrays for high-performance lithium-ion batteries. *Journal of Materials Chemistry A*, 3(18), 10107-10113.

126. Moriguchi, I., Hidaka, R., Yamada, H., Kudo, T., Murakami, H., & Nakashima, N. (2006). A Mesoporous Nanocomposite of TiO_2 and Carbon Nanotubes as a High−Rate Li−Intercalation Electrode Material. *Advanced materials*, 18(1), 69-73.

127. Liu, H., Cao, K., Xu, X., Jiao, L., Wang, Y., & Yuan, H. (2015). Ultrasmall TiO_2 nanoparticles in situ growth on graphene hybrid as superior anode material for sodium/lithium ion batteries. *ACS applied materials & interfaces*, 7(21), 11239-11245.

128. Ye, J., Liu, W., Cai, J., Chen, S., Zhao, X., Zhou, H., & Qi, L. (2011). Nanoporous anatase TiO_2 mesocrystals: additive-free synthesis, remarkable crystalline-phase stability, and improved lithium insertion behavior. *Journal of the American Chemical Society*, 133(4), 933-940.

129. Hochbaum, A. I., & Yang, P. (2010). Semiconductor nanowires for energy conversion. *Chemical Reviews*, 110(1), 527-546.

130. Guo, Y. G., Hu, Y. S., Sigle, W., & Maier, J. (2007). Superior electrode performance of nanostructured mesoporous TiO_2 (anatase) through efficient hierarchical mixed conducting networks. *Advanced Materials*, 19(16), 2087-2091.

131. Zhou, H., Liu, L., Wang, X., Liang, F., Bao, S., Lv, D., Tang, Y., & Jia, D. (2013). Multimodal porous CNT@TiO_2 nanocables with superior performance in lithium-ion batteries. *Journal of Materials Chemistry A*, *1*(30), 8525-8528.

132. Gentili, V., Brutti, S., Hardwick, L. J., Armstrong, A. R., Panero, S., & Bruce, P. G. (2012). Lithium insertion into anatase nanotubes. *Chemistry of Materials*, 24(22), 4468-4476.

133. Zhao, B., Jiang, S., Su, C., Cai, R., Ran, R., Tadé, M. O., & Shao, Z. (2013). A 3D porous architecture composed of TiO_2 nanotubes connected with a carbon nanofiber matrix for fast energy storage. *Journal of Materials Chemistry A*, 1(39), 12310-12320.

134. Yang, Z., Du, G., Meng, Q., Guo, Z., Yu, X., Chen, Z., Guo, T. & Zeng, R.

(2012). Synthesis of uniform TiO_2@carbon composite nanofibers as anode for lithium ion batteries with enhanced electrochemical performance. *Journal of Materials Chemistry*, 22(12), 5848-5854.

135. Wang, W., Tian, M., Abdulagatov, A., George, S. M., Lee, Y. C., & Yang, R. (2012). Three-dimensional Ni/TiO_2 nanowire network for high areal capacity lithium ion microbattery applications. *Nano Letters*, 12(2), 655-660.

136. Luo, Y., Luo, J., Jian, J., Zhou, W., Yang, H., Qi, X., Zhang, H., Fan, H. J., Yu, D. Y. W., Li, C. M. & Yu, T. (2012). Seed-assisted synthesis of highly ordered TiO_2@α-Fe_2O_3 core/shell arrays on carbon textiles for lithium-ion battery applications. *Energy & Environmental Science*, 5(4), 6559-6566.

137. Wang, W., Sa, Q., Chen, J., Wang, Y., Jung, H., & Yin, Y. (2013). Porous TiO_2/C nanocomposite shells as a high-performance anode material for lithium-ion batteries. *ACS applied materials & interfaces*, 5(14), 6478-6483.

138. Sordello, F., Zeb, G., Hu, K., Calza, P., Minero, C., Szkopek, T., & Cerruti, M. (2014). Tuning TiO_2 nanoparticle morphology in graphene–TiO 2 hybrids by graphene surface modification. *Nanoscale*, 6(12), 6710-6719.

139. Simon, P., & Gogotsi, Y. (2008). Graphene-based supercapacitor with an ultrahigh energy density. *Nature Materials*, 7, 845-854.

140. Guo, Q., Zhao, X., Li, Z., Wang, D., & Nie, G. (2020). A novel solid-state electrochromic supercapacitor with high energy storage capacity and cycle stability based on poly (5-formylindole)/WO_3 honeycombed porous nanocomposites. *Chemical Engineering Journal*, 384, 123370.

141. Bi, Z., Li, X., Chen, Y., He, X., Xu, X., & Gao, X. (2017). Large-scale multifunctional electrochromic-energy storage device based on tungsten trioxide monohydrate nanosheets and prussian white. *ACS Applied Materials & Interfaces*, 9(35), 29872-29880.

142. Cai, G., Darmawan, P., Cheng, X., & Lee, P. S. (2017). Inkjet printed large area multifunctional smart windows. *Advanced Energy Materials*, 7(14), 1602598.

143. Guo, Q., Li, J., Zhang, B., Nie, G., & Wang, D. (2019). High-performance asymmetric electrochromic-supercapacitor device based on poly (indole-6-carboxylicacid)/TiO_2 nanocomposites. *ACS Applied Materials & Interfaces*, 11(6), 6491-6501.

144. Guo, Q., Zhao, X., Li, Z., Wang, B., Wang, D., & Nie, G. (2020). High performance multicolor intelligent supercapacitor and its quantitative monitoring of energy storage level by electrochromic parameters. *ACS Applied Energy Materials*, 3(3), 2727-2736.

145. Wang, R., Li, Y., Shetye, K., Dutta, T., Jin, L., Li, S., & Peng, Z. (2015). Luminescent Polythiophene−Based Main−Chain Polyoxometalate−Containing Conjugated Polymers with Improved Solar−Cell Performance. *European Journal of Inorganic Chemistry*, 2015(4), 656-663.

146. Wu, H., Yang, H. K., & Wang, W. (2016). Covalently-linked polyoxometalate–polymer hybrids: optimizing synthesis, appealing structures and prospective applications. *New Journal of Chemistry*, 40(2), 886-897.

147. Heinemann, F. W., Hartung, H., Dehne, H., & Scheunemann, A. (1995). Thiooxalic acid 2-amide-1-hydrazide-2-hydrazone. *Acta Crystallographica Section C: Crystal Structure Communications*, 51(3), 442-445.

148. Kim, K. H., Han, Y. K., & Jung, J. (2005). Basis set effects on relative energies and HOMO–LUMO energy gaps of fullerene C 36. *Theoretical Chemistry Accounts*, 113(4), 233-237.

149. Fleming, I. (2011). *Molecular orbitals and organic chemical reactions.* John Wiley & Sons.

150. Chahma, M. H., Gilroy, J. B., & Hicks, R. G. (2007). Linear and branched electroactive polymers based on ethylenedioxythiophene–triarylamine conjugates. *Journal of Materials Chemistry*, 17(45), 4768-4771.

151. Janzen, D. E., Burand, M. W., Ewbank, P. C., Pappenfus, T. M., Higuchi, H., Filho S., D. A., Young V. G.; Brédas J. & Mann, K. R. (2004). Preparation and characterization of π-stacking quinodimethane oligothiophenes. Predicting semiconductor behavior and bandwidths from crystal structures and molecular

orbital calculations. *Journal of the American Chemical Society*, 126(46), 15295-15308.

152. Poverenov, E., Sheynin, Y., Zamoshchik, N., Patra, A., Leitus, G., Perepichka, I. F., & Bendikov, M. (2012). Flat conjugated polymers combining a relatively low HOMO energy level and band gap: polyselenophenes versus polythiophenes. *Journal of Materials Chemistry*, 22(29), 14645-14655.

153. Hwang, H., Kim, Y., Kang, M., Lee, M. H., Heo, Y. J., & Kim, D. Y. (2017). A conjugated polymer with high planarity and extended π-electron delocalization via a quinoid structure prepared by short synthetic steps. *Polymer Chemistry*, 8(2), 361-365.

154. Wijsboom, Y. H., Patra, A., Zade, S. S., Sheynin, Y., Li, M., Shimon, L. J., & Bendikov, M. (2009). Controlling Rigidity and Planarity in Conjugated Polymers: Poly (3, 4‐ethylenedithioselenophene). *Angewandte Chemie*, 121(30), 5551-5555.

155. Chen, Z., Li, W., Dai, Y., Xu, N., Su, C., Liu, J., & Zhang, C. (2018). Conjugated microporous polymer based on star-shaped triphenylamine-benzene structure with improved electrochemical performances as the organic cathode material of Li-ion battery. *Electrochimica Acta*, 286, 187-194.

156. Su, C., Yang, F., Ye, Y., Xu, L., Wang, L., & Zhang, C. (2013). Poly [tris (thienylphenyl) amine] derivatives as a performance-improved cathode material for lithium ion batteries. *Journal of The Electrochemical Society*, 160(11), A2021.

157. Dai, Y., Li, W., Chen, Z., Zhu, X., Liu, J., Zhao, R., Wright D. S., Noori A., Mousavi M. F., & Zhang, C. (2019). An air-stable electrochromic conjugated microporous polymer as an emerging electrode material for hybrid energy storage systems. *Journal of Materials Chemistry A*, 7(27), 16397-16405.

158. Yoon, H., Chang, M., & Jang, J. (2007). Formation of 1D poly (3, 4‐ethylenedioxythiophene) nanomaterials in reverse microemulsions and their application to chemical sensors. *Advanced Functional Materials*, 17(3), 431-436.

159. Jones, B. H., & Lodge, T. P. (2012). Nanocasting nanoporous inorganic and organic materials from polymeric bicontinuous microemulsion templates. *Polymer Journal*, 44(2), 131-146.

160. Jang, J., Bae, J., & Park, E. (2006). Selective Fabrication of Poly (3, 4‐ethylenedioxythiophene) Nanocapsules and Mesocellular Foams Using Surfactant‐Mediated Interfacial Polymerization. *Advanced Materials*, 18(3), 354-358.

161. Ren, L., Zhang, G., Li, H., Hu, D., & Dou, S. (2019). Electrode materials based on micro-emulsion polymerized polyaniline and their capacitive property. *Int. J. Electrochem. Sci*, 14, 238-249.

162. Liu, X., Hu, Y., Shen, L., Zhang, G., Cao, T., Xu, J., Zhao, F., Hou, J., Liu, H. & Jiang, F. (2018). Novel copolymers based on PEO bridged thiophenes and 3, 4-ethylenedioxythiophene: Electrochemical, optical, and electrochromic properties. *Electrochimica Acta*, 288, 52-60.

163. Chiang, T. Y., Huang, M. C., & Tsai, C. H. (2014). The effects of solvent on the electrochromic properties of poly (3, 4-ethylenedioxythiophene). *RSC Advances*, 4(41), 21201-21207.

164. Tseng, C. Y., Hu, C. W., Huang, K. C., Chang, L. C., Vittal, R., & Ho, K. C. (2013). Ion transport across the film of poly (5, 6-dimethoxyindole-2-carboxylic acid) in relation to its electrochromic switching: An electrochemical quartz crystal microbalance study. *Electrochimica Acta*, 101, 232-237.

165. Cysewska, K., Karczewski, J., & Jasiński, P. (2015). Influence of electropolymerization conditions on the morphological and electrical properties of PEDOT film. *Electrochimica Acta*, 176, 156-161.

166. Rogers, R. D. (2007). Reflections on ionic liquids. *Nature*, 447(7147), 917-918.

167. Lu, W., Fadeev, A. G., Qi, B., Smela, E., Mattes, B. R., Ding, J., Geoffrey, M. S., Mazurkiewicz, J., Zhou, D., W. G. Gordon, MacFarlane D. R., Forsyth S.

A., & Forsyth, M. (2002). Use of ionic liquids for π-conjugated polymer electrochemical devices. *Science*, 297(5583), 983-987.

168. Gaupp, C. L., & Reynolds, J. R. (2003). Multichromic copolymers based on 3, 6-bis(2-(3,4-ethylenedioxythiophene))-N-alkylcarbazole derivatives. *Macromolecules*, 36(17), 6305-6315.

169. Ruhlmann, L., Schulz, A., Giraudeau, A., Messerschmidt, C., & Fuhrhop, J. H. (1999). A polycationic zinc-5, 15-dichlorooctaethylporphyrinate-viologen wire. *Journal of the American Chemical Society*, 121(28), 6664-6667.

170. Ruhlmann, L., Hao, J., Ping, Z., & Giraudeau, A. (2008). Self-oriented polycationic copolymers obtained from bipyridinium meso-substituted-octaethylporphyrins. *Journal of Electroanalytical Chemistry*, 621(1), 22-30.

171. Huo, Z., Gisselbrecht, J. P., Farha, R., Goldmann, M., Saint-Aman, E., Bucher, C., & Ruhlmann, L. (2014). Alternating electro-copolymerization of zinc-β-octaethylporphyrin with a flexible bipyridinium. *Electrochimica Acta*, 122, 108-117.

172. Allain, C., Favette, S., Chamoreau, L. M., Vaissermann, J., Ruhlmann, L., & Hasenknopf, B. (2008). *Hybrid organic–inorganic porphyrin–polyoxometalate complexes*.

173. Schaming, D., Allain, C., Farha, R., Goldmann, M., Lobstein, S., Giraudeau, A., Hasenknopf, B. & Ruhlmann, L. (2010). Synthesis and photocatalytic properties of mixed polyoxometalate− porphyrin copolymers obtained from Anderson-type polyoxomolybdates. *Langmuir*, 26(7), 5101-5109.

174. Costa-Coquelard, C., Sorgues, S., & Ruhlmann, L. (2010). Photocatalysis with polyoxometalates associated to porphyrins under visible light: an application of charge transfer in electrostatic complexes. *The Journal of Physical Chemistry A*, 114(22), 6394-6400.

175. Schaming, D., Costa-Coquelard, C., Lampre, I., Sorgues, S., Erard, M., Liu, X., J. Liu, L. Sun, J. Canny, R. Thouvenot, Ruhlmann, L. (2010). Formation of a new hybrid complex via coordination interaction between 5, 10, 15-tritolyl-20-(4-and 3-pyridyl) porphyrin or 5, 10, 15-triphenyl-20-(4-pyridyl) porphyrin

and the α-$[MSiW_{11}O_{39}]_6^-$ Keggin-type polyoxometalate (M= Co^{2+} and Ni^{2+}). *Inorganica Chimica Acta*, 363(10), 2185-2192.

176. Costa-Coquelard, C., Sorgues, S., & Ruhlmann, L. (2010). Photocatalysis with polyoxometalates associated to porphyrins under visible light: an application of charge transfer in electrostatic complexes. *The Journal of Physical Chemistry A*, 114(22), 6394-6400.

177. Ahmed, I., Wang, X., Boualili, N., Xu, H., Farha, R., Goldmann, M., & Ruhlmann, L. (2012). Photocatalytic synthesis of silver dendrites using electrostatic hybrid films of porphyrin–polyoxometalate. *Applied Catalysis A: General*, 447, 89-99.

178. Ahmed, I., Farha, R., Goldmann, M., & Ruhlmann, L. (2013). A molecular photovoltaic system based on Dawson type polyoxometalate and porphyrin formed by layer-by-layer self assembly. *Chemical Communications*, 49(5), 496-498.

179. Allain, C., Schaming, D., Karakostas, N., Erard, M., Gisselbrecht, J. P., Sorgues, S., Lampre, I.; Ruhlmann, L. & Hasenknopf, B. (2013). Synthesis, electrochemical and photophysical properties of covalently linked porphyrin–polyoxometalates. *Dalton Transactions*, 42(8), 2745-2754.

180. Azcarate, I., Ahmed, I., Farha, R., Goldmann, M., Wang, X., Xu, H., Hasenknopf, B., Lacôte, E. & Ruhlmann, L. (2013). Synthesis and characterization of conjugated Dawson-type polyoxometalate–porphyrin copolymers. *Dalton Transactions*, 42(35), 12688-12698.

181. Ahmed, I., Farha, R., Huo, Z., Allain, C., Wang, X., Xu, H., Goldmann, M.， Hasenknopf, B. & Ruhlmann, L. (2013). Porphyrin–polyoxometalate hybrids connected via a Tris-alkoxo linker for the generation of photocurrent. *Electrochimica Acta*, 110, 726-734.

182. Azcarate, I., Huo, Z., Farha, R., Goldmann, M., Xu, H., Hasenknopf, B., E. Lacte & Ruhlmann, L. (2015). Generation of Photocurrent by Visible‐Light Irradiation of Conjugated Dawson Polyoxophosphovanadotungstate–Porphyrin Copolymers. *Chemistry–A European Journal*, 21(22), 8271-8280.

183. Huo, Z., Zang, D., Yang, S., Farha, R., Goldmann, M., Hasenknopf, B., Xu, H & Ruhlmann, L. (2015). Synthesis and characterization of Lindqvist-type polyoxometalate–porphyrin copolymers. *Electrochimica Acta*, 179, 326-335.

184. Boudiaf, M., Liang, Y., Lamare, R., Weiss, J., Ibrahim, H., Goldmann, M., Bentouhami, E., Badets V., Choua S., Breton N. L., Bonnefont A. & Ruhlmann, L. (2019). Stable isoporphyrin copolymer: Electrochemical mechanism and behavior and photovoltaic properties. *Electrochimica Acta*, 309, 432-449.

Appendixs

Table S1. Selected bond lengths (Å) and angles (°) of **POT-1**.

Bond	Distance	Bond	Distance
Ti(1)-O(7)	1.7762(13)	Ti(1)-O(1)	2.0588(14)
Ti(1)-O(12)	1.8806(13)	Ti(1)-O(5)	2.0630(14)
Ti(1)-O(10)	1.9020(13)	Ti(1)-O(11)#1	2.1747(13)
Ti(2)-O(8)	1.7703(14)	Ti(2)-O(4)	2.0507(13)
Ti(2)-O(11)	1.8896(13)	Ti(2)-O(6)#1	2.0609(14)
Ti(2)-O(10)	1.9037(13)	Ti(2)-O(12)#1	2.1683(13)
Ti(02)-O(9)	1.7506(14)	Ti(02)-O(3)#1	2.0605(14)
Ti(02)-O(11)	1.8947(13)	Ti(02)-O(2)#1	2.0726(14)
Ti(02)-O(12)	1.9025(13)	Ti(02)-O(10)#1	2.1629(13)
Atoms	Angle	Atoms	Angle
O(7)-Ti(1)-O(12)	102.92(6)	O(10)-Ti(1)-O(5)	161.49(6)
O(7)-Ti(1)-O(10)	95.70(6)	O(1)-Ti(1)-O(5)	77.93(6)
O(12)-Ti(1)-O(10)	103.27(6)	O(7)-Ti(1)-O(11)#1	173.25(6)
O(7)-Ti(1)-O(1)	93.87(6)	O(12)-Ti(1)-O(11)#1	77.77(5)
O(12)-Ti(1)-O(1)	158.81(6)	O(10)-Ti(1)-O(11)#1	77.65(5)
O(10)-Ti(1)-O(1)	87.59(6)	O(1)-Ti(1)-O(11)#1	87.07(5)
O(7)-Ti(1)-O(5)	96.72(6)	O(5)-Ti(1)-O(11)#1	90.01(5)
O(12)-Ti(1)-O(5)	87.24(6)	O(8)-Ti(2)-O(11)	102.30(6)
O(8)-Ti(2)-O(10)	104.02(6)	O(10)-Ti(2)-O(6)#1	157.62(6)
O(11)-Ti(2)-O(10)	101.66(6)	O(4)-Ti(2)-O(6)#1	77.65(5)
O(8)-Ti(2)-O(4)	91.38(6)	O(8)-Ti(2)-O(12)#1	178.69(6)
O(11)-Ti(2)-O(4)	161.38(6)	O(11)-Ti(2)-O(12)#1	77.75(5)
O(10)-Ti(2)-O(4)	86.93(6)	O(10)-Ti(2)-O(12)#1	77.23(5)
O(8)-Ti(2)-O(6)#1	92.59(6)	O(4)-Ti(2)-O(12)#1	88.29(5)
O(11)-Ti(2)-O(6)#1	89.05(6)	O(6)#1-Ti(2)-O(12)#1	86.09(5)
O(9)-Ti(02)-O(11)	102.78(6)	O(12)-Ti(02)-O(2)#1	161.42(6)
O(9)-Ti(02)-O(12)	100.13(6)	O(3)#1-Ti(02)-O(2)#1	76.75(6)
O(11)-Ti(02)-O(12)	101.97(6)	O(9)-Ti(02)-O(10)#1	177.50(6)
O(9)-Ti(02)-O(3)#1	93.61(6)	O(11)-Ti(02)-O(10)#1	78.10(5)
O(11)-Ti(02)-O(3)#1	157.90(6)	O(12)-Ti(02)-O(10)#1	77.39(5)
O(12)-Ti(02)-O(3)#1	89.43(6)	O(3)#1-Ti(02)-O(10)#1	86.16(5)
O(9)-Ti(02)-O(2)#1	93.17(6)	O(2)#1-Ti(02)-O(10)#1	89.20(5)
O(11)-Ti(02)-O(2)#1	87.51(6)		

Table S2. Selected bond lengths (Å) and angles (º) of **POT-2**.

Bond	Distance	Bond	Distance
Ti1—O13	1.775 (6)	Ti2—O9	1.987 (5)
Ti1—O6	1.810 (5)	Ti2—O3	2.044 (5)
Ti1—O12	1.991 (5)	Ti3—O11	1.788 (5)
Ti1—O5	1.992 (5)	Ti3—O10	1.796 (5)
Ti1—O4	2.062 (5)	Ti3—O12	2.018 (5)
Ti1—O2	2.130 (5)	Ti3—O9	2.019 (5)
Ti2—O8	1.761 (7)	Ti3—O5	2.022 (4)
Ti2—O7	1.782 (6)	Ti3—O1	2.146 (5)
Ti2—O5	1.850 (5)		
O13—Ti1—O6	97.5 (3)	S2—C9—H9	124.5
O13—Ti1—O12	97.9 (2)	C12—C11—O6	108.6 (11)
O6—Ti1—O12	103.3 (2)	C12—C11—C13	114.0 (10)
O13—Ti1—O5	96.8 (2)	O6—C11—C13	110.2 (9)
Atoms	Angle	Atoms	Angle
O6—Ti1—O5	165.6 (2)	O8—Ti2—O7	115.9 (3)
O12—Ti1—O5	76.7 (2)	O8—Ti2—O5	116.4 (3)
O13—Ti1—O4	91.1 (2)	O7—Ti2—O5	127.4 (3)
O6—Ti1—O4	91.4 (2)	O8—Ti2—O9	100.7 (3)
O12—Ti1—O4	161.6 (2)	O7—Ti2—O9	96.8 (3)
O5—Ti1—O4	86.28 (19)	O5—Ti2—O9	79.1 (2)
O13—Ti1—O2	174.9 (2)	O8—Ti2—O3	90.4 (2)
O6—Ti1—O2	83.4 (2)	O7—Ti2—O3	87.0 (2)
O12—Ti1—O2	86.8 (2)	O5—Ti2—O3	87.2 (2)
O5—Ti1—O2	82.2 (2)	O9—Ti2—O3	165.2 (2)
O4—Ti1—O2	83.89 (19)	O10—Ti3—O5	96.3 (2)
O11—Ti3—O10	95.6 (2)	O12—Ti3—O5	75.43 (19)
O11—Ti3—O12	104.0 (2)	O9—Ti3—O5	74.5 (2)
O10—Ti3—O12	96.8 (2)	O11—Ti3—O1	85.5 (2)
O11—Ti3—O9	103.5 (2)	O10—Ti3—O1	178.6 (2)
O10—Ti3—O9	95.5 (2)	O12—Ti3—O1	83.8 (2)
O12—Ti3—O9	148.5 (2)	O9—Ti3—O1	83.4 (2)
O11—Ti3—O5	168.0 (2)	O5—Ti3—O1	82.53 19)

Table S3. Selected bond lengths (Å) and angles (°) of **POT-3**.

Bond	Distance	Bond	Distance
Ti1—O2	1.8017 (19)	Ti2—O6	1.9779 (19)
Ti1—O7	1.8314 (19)	Ti2—O9	2.0040 (19)
Ti1—O1	1.9641 (18)	Ti3—O13	1.8133 (19)
Ti1—O5	2.0233 (18)	Ti3—O3	1.8291 (19)
Ti1—O6	2.0320 (19)	Ti3—O1	1.9721 (17)
Ti1—O8	2.1012 (19)	Ti3—O9	2.004 (2)
Ti2—O11	1.7722 (19)	Ti3—O4	2.0321 (19)
Ti2—O19	1.782 (2)	Ti3—O12	2.1230 (19)
Ti2—O1	1.9378 (18)		
Atoms	Angle	Atoms	Angle
O2—Ti1—O7	95.14 (8)	O11—Ti2—O19	105.39 (10)
O2—Ti1—O1	170.41 (8)	O11—Ti2—O1	143.70 (9)
O7—Ti1—O1	94.29 (8)	O19—Ti2—O1	110.86 (9)
O2—Ti1—O5	94.02 (8)	O11—Ti2—O6	96.65 (9)
O7—Ti1—O5	93.81 (8)	O19—Ti2—O6	104.02 (10)
O1—Ti1—O5	87.10 (7)	O1—Ti2—O6	76.80 (7)
O2—Ti1—O6	102.26 (8)	O11—Ti2—O9	94.33 (9)
O7—Ti1—O6	95.88 (8)	O19—Ti2—O9	102.11 (10)
O1—Ti1—O6	74.97 (7)	O1—Ti2—O9	76.42 (7)
O5—Ti1—O6	160.18 (7)	O6—Ti2—O9	147.73 (8)
O2—Ti1—O8	84.44 (8)	O1—Ti3—O9	75.66 (7)
O7—Ti1—O8	178.13 (8)	O13—Ti3—O4	90.04 (8)
O1—Ti1—O8	86.19 (7)	O3—Ti3—O4	94.45 (8)
O5—Ti1—O8	84.41 (8)	O1—Ti3—O4	87.84 (7)
O6—Ti1—O8	85.99 (8)	O9—Ti3—O4	161.87 (8)
O13—Ti3—O3	95.97 (9)	O13—Ti3—O12	174.47 (8)
O13—Ti3—O1	97.02 (8)	O3—Ti3—O12	85.20 (8)
O3—Ti3—O1	166.81 (8)	O1—Ti3—O12	82.09 (8)
O13—Ti3—O9	99.28 (9)	O9—Ti3—O12	85.82 (8)
O3—Ti3—O9	99.95 (8)	O4—Ti3—O12	84.47 (8)

Table S4. Selected bond lengths (Å) and angles (°) of **POT-4**.

Bond	Distance	Bond	Distance
Ti1—O9	1.787 (2)	Ti3—O8	1.787 (2)
Ti1—O1	1.849 (2)	Ti3—O1	1.836 (2)
Ti1—O11	1.966 (2)	Ti3—O7	1.966 (2)
Ti1—O16	2.015 (3)	Ti3—O10	2.024 (2)
Ti1—O2	2.067 (2)	Ti3—O2	2.050 (2)
Ti1—O6	2.145 (2)	Ti3—O3	2.163 (2)
Ti2—O13	1.778 (3)	Ti4—O14	1.780 (3)
Ti2—O12	1.816 (3)	Ti4—O15	1.800 (3)
Ti2—O10	2.014 (2)	Ti4—O16	2.009 (2)
Ti2—O5	2.051 (3)	Ti4—O4	2.053 (3)
Ti2—O2	2.063 (2)	Ti4—O2	2.054 (2)
Ti2—O11	2.084 (2)	Ti4—O7	2.105 (2)
Atoms	Angle	Atoms	Angle
O9—Ti1—O1	98.94 (11)	O8—Ti3—O1	102.21 (11)
O9—Ti1—O11	105.87 (11)	O8—Ti3—O7	104.86 (11)
O1—Ti1—O11	92.08 (10)	O1—Ti3—O7	92.55 (11)
O9—Ti1—O16	98.52 (11)	O8—Ti3—O10	98.35 (11)
O1—Ti1—O16	101.64 (11)	O1—Ti3—O10	100.33 (10)
O11—Ti1—O16	149.76 (10)	O7—Ti3—O10	150.39 (10)
O9—Ti1—O2	174.62 (11)	O8—Ti3—O2	174.38 (11)
O1—Ti1—O2	80.57 (10)	O1—Ti3—O2	81.32 (10)
O11—Ti1—O2	79.51 (10)	O7—Ti3—O2	79.20 (9)
O16—Ti1—O2	76.4 (1)	O10—Ti3—O2	76.59 (9)
O9—Ti1—O6	92.96 (11)	O8—Ti3—O3	89.91 (10)
O1—Ti1—O6	167.14 (10)	O1—Ti3—O3	167.31 (10)
O11—Ti1—O6	79.92 (10)	O7—Ti3—O3	80.55 (10)
O16—Ti1—O6	81.25 (10)	O10—Ti3—O3	81.37 (10)
O2—Ti1—O6	88.04 (9)	O2—Ti3—O3	86.91 (9)
O13—Ti2—O12	97.86 (12)	O14—Ti4—O15	98.51 (14)
O13—Ti2—O10	100.59 (11)	O14—Ti4—O16	99.58 (12)
O12—Ti2—O10	98.32 (11)	O15—Ti4—O16	99.72 (12)
O13—Ti2—O5	90.08 (11)	O14—Ti4—O4	90.09 (12)
O12—Ti2—O5	95.16 (11)	O15—Ti4—O4	94.46 (12)
O10—Ti2—O5	161.45 (10)	O16—Ti4—O4	161.40 (11)
O13—Ti2—O2	96.67 (11)	O14—Ti4—O2	96.52 (12)
O12—Ti2—O2	165.26 (11)	O15—Ti4—O2	164.94 (12)
O10—Ti2—O2	76.52 (9)	O16—Ti4—O2	76.81 (10)

O5—Ti2—O2	87.27 (10)	O4—Ti4—O2	86.38 (10)
O13—Ti2—O11	170.05 (12)	O14—Ti4—O7	169.67 (12)
O12—Ti2—O11	88.97 (11)	O15—Ti4—O7	89.20 (12)
O10—Ti2—O11	85.47 (9)	O16—Ti4—O7	85.79 (10)
O5—Ti2—O11	82.08 (10)	O4—Ti4—O7	82.42 (10)
O2—Ti2—O11	76.94 (9)	O2—Ti4—O7	76.00 (9)

Table S5. Selected bond lengths (Å) and angles (°) of **POT-5**.

Bond	Distance	Bond	Distance
Ti1—O1	2.005(2)	Ti1—O3	2.057(3)
Ti1—O2	1.784(1)	Ti1—O4	2.086(2)
Ti1—Cl1	2.243(3)	Ti1—Cl2	2.275(4)
Atoms	Angle	Atoms	Angle
Cl1—Ti1—Cl2	97.71(5)	Ti1—O2—Ti1	137.0(2)

Table S6. Selected bond lengths (Å) and angles (°) of **POT-6**.

Bond	Distance	Bond	Distance
I1—In1	2.7466 (16)	Ti1—O10	1.741 (13)
I2—In1	2.7414 (17)	Ti1—O21	1.783 (13)
In1—O12	2.206 (11)	Ti1—O15	1.977 (13)
In1—O15	2.218 (12)	Ti1—O17	2.016 (12)
In1—O22	2.236 (10)	Ti1—O1	2.115 (11)
In1—O1	2.251 (10)	Ti1—O22	2.190 (12)
Ti2—O23	1.723 (13)	Ti2—O17	2.013 (12)
Ti2—O14	1.790 (12)	Ti2—O22	2.106 (11)
Ti2—O12	2.006 (12)	Ti2—O1	2.203 (11)
Atoms	Angle	Atoms	Angle
O12—In1—O15	133.3 (4)	O12—In1—I2	112.0 (3)
O12—In1—O22	69.0 (4)	O15—In1—I2	97.8 (3)
O15—In1—O22	70.8 (4)	O22—In1—I2	100.7 (3)
O12—In1—O1	73.1 (4)	O1—In1—I2	163.1 (3)
O15—In1—O1	69.3 (4)	O12—In1—I1	99.8 (3)
O22—In1—O1	65.3 (4)	O15—In1—I1	110.9 (3)
O22—In1—I1	160.8 (3)	I2—In1—I1	98.04 (5)
O1—In1—I1	96.8 (3)		

Table S7 Selected bond lengths (Å) and angles (°) of **POT-7**.

Bond	Distance	Bond	Distance
Ti1—O4	1.764 (6)	Ti1—Cl1	2.753 (3)
Ti1—O5	1.790 (7)	Ti2—O8	1.765 (7)
Ti1—O1	1.932 (6)	Ti2—O6	1.784 (7)
Ti1—O3	2.006 (6)	Ti2—O1	1.944 (5)
Ti1—O2	2.036 (7)	Ti2—O7	2.030 (8)
Ti2—Cl1	2.742 (3)	Ti2—O2	2.041 (8)
Ti3—O9	1.767 (7)	Ti3—O7	2.028 (7)
Ti3—O10	1.791 (7)	Ti3—O3	2.031 (7)
Ti3—O1	1.951 (6)	Ti3—Cl1	2.762 (3)
Atoms	Angle	Atoms	Angle
O4—Ti1—O5	99.9 (3)	O8—Ti2—O6	100.5 (4)
O4—Ti1—O1	101.6 (3)	O8—Ti2—O1	100.0 (3)
O5—Ti1—O1	158.5 (3)	O6—Ti2—O1	159.5 (3)
O4—Ti1—O3	102.7 (3)	O8—Ti2—O7	103.1 (4)
O5—Ti1—O3	101.0 (3)	O6—Ti2—O7	101.6 (3)
O1—Ti1—O3	73.6 (3)	O1—Ti2—O7	74.3 (3)
O4—Ti1—O2	101.1 (3)	O8—Ti2—O2	101.2 (4)
O5—Ti1—O2	102.6 (3)	O6—Ti2—O2	101.6 (3)
O1—Ti1—O2	73.9 (3)	O1—Ti2—O2	73.6 (3)
O3—Ti1—O2	142.8 (3)	O7—Ti2—O2	142.5 (3)
O4—Ti1—Cl1	176.6 (3)	O8—Ti2—Cl1	175.3 (3)
O5—Ti1—Cl1	83.3 (2)	O6—Ti2—Cl1	84.1 (2)
O1—Ti1—Cl1	75.21 (17)	O1—Ti2—Cl1	75.32 (18)
O3—Ti1—Cl1	77.60 (18)	O7—Ti2—Cl1	76.3 (2)
O2—Ti1—Cl1	77.0 (2)	O2—Ti2—Cl1	77.2 (2)
O9—Ti3—O10	99.9 (4)	O1—Ti3—O3	72.6 (2)
O9—Ti3—O1	102.0 (3)	O7—Ti3—O3	141.5 (3)
O10—Ti3—O1	158.0 (3)	O9—Ti3—Cl1	176.6 (3)
O9—Ti3—O7	102.6 (3)	O10—Ti3—Cl1	83.3 (2)
O10—Ti3—O7	102.3 (3)	O1—Ti3—Cl1	74.73 (17)
O1—Ti3—O7	74.2 (3)	O7—Ti3—Cl1	75.81 (19)
O9—Ti3—O3	103.0 (3)	O3—Ti3—Cl1	77.00 (18)
O10—Ti3—O3	101.1 (3)		

Table S8 Selected bond lengths (Å) and angles (°) of **POT-8**.

Bond	Distance	Bond	Distance
Br1—Co1	2.4433 (10)	Ti1—O5	1.768 (4)
Co1—O3	1.990 (4)	Ti1—O7	1.918 (4)
Co1—O2	2.024 (4)	Ti1—O4	1.943 (3)
Co1—O4	2.045 (3)	Ti1—O1	1.982 (3)
Co1—O1	2.311 (3)	Ti1—O6	2.057 (4)
Ti3—O12	1.787 (4)	Ti1—O8	2.060 (4)
Ti3—O13	1.793 (4)	Ti2—O10	1.747 (4)
Ti3—O3	1.955 (4)	Ti2—O9	1.781 (4)
Ti3—O1	1.983 (3)	Ti2—O2	1.924 (4)
Ti3—O11	2.116 (4)	Ti2—O6	1.972 (4)
Ti3—O7	2.192 (4)	Ti2—O1	2.024 (4)
Atoms	Angle	Atoms	Angle
O3—Co1—O2	115.97 (17)	O5—Ti1—O7	106.35 (18)
O3—Co1—O4	117.05 (15)	O5—Ti1—O4	97.49 (16)
O2—Co1—O4	101.04 (15)	O7—Ti1—O4	96.48 (15)
O3—Co1—O1	74.12 (13)	O5—Ti1—O1	174.40 (18)
O2—Co1—O1	71.78 (14)	O7—Ti1—O1	79.25 (15)
O4—Co1—O1	71.70 (13)	O4—Ti1—O1	81.43 (14)
O3—Co1—Br1	105.58 (11)	O5—Ti1—O6	98.80 (17)
O2—Co1—Br1	110.17 (11)	O7—Ti1—O6	153.07 (16)
O4—Co1—Br1	106.71 (10)	O4—Ti1—O6	89.52 (15)
O1—Co1—Br1	177.80 (10)	O1—Ti1—O6	75.72 (14)
O5—Ti1—O8	90.36 (16)	O10—Ti2—O9	99.6 (2)
O7—Ti1—O8	87.66 (16)	O10—Ti2—O2	111.9 (2)
O4—Ti1—O8	169.68 (17)	O9—Ti2—O2	94.93 (18)
O1—Ti1—O8	90.11 (15)	O10—Ti2—O6	117.67 (19)
O6—Ti1—O8	82.64 (15)	O9—Ti2—O6	94.53 (18)
O2—Ti2—O6	126.90 (17)	O12—Ti3—O13	98.13 (19)
O10—Ti2—O1	96.0 (2)	O12—Ti3—O3	97.45 (18)
O9—Ti2—O1	164.26 (19)	O13—Ti3—O3	97.44 (18)
O2—Ti2—O1	80.52 (15)	O12—Ti3—O1	99.03 (17)
O6—Ti2—O1	76.72 (14)	O13—Ti3—O1	162.66 (18)
O3—Ti3—O1	82.80 (14)	O3—Ti3—O11	167.05 (15)
O12—Ti3—O11	91.54 (17)	O1—Ti3—O11	86.61 (14)
O13—Ti3—O11	90.45 (17)	O12—Ti3—O7	170.06 (17)
O13—Ti3—O7	89.72 (17)	O1—Ti3—O7	72.95 (14)
O3—Ti3—O7	87.50 (15)	O11—Ti3—O7	82.27 (14)

Table S9. Selected bond lengths (Å) and angles (°) of **POT-9**.

Bond	Distance	Bond	Distance
Ce1—O2	2.178 (4)	Ce1—O3	2.438 (4)
Ce1—O1	2.183 (4)	Ce1—O6	2.442 (5)
Ce1—O4	2.368 (4)	Ce1—Cl1	2.8382 (18)
Ce1—O5	2.396 (4)	Ce1—Cl2	2.8555 (17)
Ti1—O9	1.768 (6)	Ti1—O5	1.978 (5)
Ti1—O8	1.775 (6)	Ti1—O7	2.024 (5)
Ti1—O2	1.963 (4)	Ti1—Cl1	2.9420 (3)
Ti2—O10	1.773 (5)	Ti2—O7	2.035 (5)
Ti2—O11	1.789 (5)	Ti2—Cl1	2.899 (2)
Ti2—O2	1.956 (4)	Ti2—O3	1.974 (4)
Ti3—O13	1.760 (6)	Ti3—O6	1.974 (5)
Ti3—O14	1.791 (5)	Ti3—O12	2.037 (5)
Ti3—O1	1.952 (4)	Ti3—Cl2	2.876 (2)
Ti4—O15	1.769 (5)	Ti4—O4	1.986 (5)
Ti4—O16	1.779 (6)	Ti4—O12	2.026 (5)
Ti4—O1	1.951 (4)	Ti4—Cl2	2.923 (2)
Atoms	Angle	Atoms	Angle
O2—Ce1—O1	133.61 (15)	O2—Ce1—O6	149.58 (15)
O2—Ce1—O4	83.21 (15)	O1—Ce1—O6	64.56 (15)
O1—Ce1—O4	65.56 (15)	O4—Ce1—O6	125.69 (16)
O2—Ce1—O5	65.10 (16)	O5—Ce1—O6	99.61 (17)
O1—Ce1—O5	83.49 (15)	O3—Ce1—O6	113.26 (16)
O4—Ce1—O5	94.79 (16)	O2—Ce1—Cl1	69.92 (11)
O2—Ce1—O3	64.69 (15)	O1—Ce1—Cl1	133.58 (12)
O1—Ce1—O3	149.47 (14)	O4—Ce1—Cl1	153.06 (11)
O4—Ce1—O3	99.13 (16)	O5—Ce1—Cl1	72.70 (12)
O5—Ce1—O3	125.47 (15)	O3—Ce1—Cl1	71.44 (12)
O6—Ce1—Cl1	80.60 (12)	O5—Ce1—Cl2	152.66 (12)
O2—Ce1—Cl2	133.91 (11)	O3—Ce1—Cl2	81.10 (11)
O1—Ce1—Cl2	69.27 (11)	O6—Ce1—Cl2	71.28 (12)
O4—Ce1—Cl2	72.30 (11)	Cl1—Ce1—Cl2	128.41 (6)
O9—Ti1—O8	101.1 (3)	O10—Ti2—O11	101.1 (2)
O9—Ti1—O2	105.2 (2)	O10—Ti2—O2	104.9 (2)
O8—Ti1—O2	153.7 (3)	O11—Ti2—O2	153.9 (2)
O9—Ti1—O5	102.0 (3)	O10—Ti2—O3	102.2 (2)
O8—Ti1—O5	97.9 (2)	O11—Ti2—O3	99.0 (2)
O2—Ti1—O5	77.54 (18)	O2—Ti2—O3	78.24 (17)

O9—Ti1—O7	103.0 (3)	O10—Ti2—O7	101.9 (2)
O8—Ti1—O7	98.9 (3)	O11—Ti2—O7	97.7 (2)
O2—Ti1—O7	74.52 (18)	O2—Ti2—O7	74.43 (18)
O5—Ti1—O7	146.4 (2)	O3—Ti2—O7	147.3 (2)
O10—Ti2—Cl1	175.87 (19)	O3—Ti2—Cl1	76.34 (15)
O11—Ti2—Cl1	82.96 (18)	O7—Ti2—Cl1	77.99 (16)
O2—Ti2—Cl1	71.09 (13)	O13—Ti3—O14	102.2 (3)
O13—Ti3—O1	102.5 (2)	O14—Ti3—Cl2	83.9 (2)
O14—Ti3—O1	155.1 (2)	O1—Ti3—Cl2	71.43 (13)
O13—Ti3—O6	101.8 (3)	O6—Ti3—Cl2	77.12 (15)
O14—Ti3—O6	100.0 (2)	O12—Ti3—Cl2	77.71 (15)
O1—Ti3—O6	78.33 (18)	O15—Ti4—O16	103.6 (3)
O13—Ti3—O12	101.1 (3)	O15—Ti4—O1	102.5 (2)
O14—Ti3—O12	97.5 (2)	O16—Ti4—O1	153.9 (2)
O1—Ti3—O12	74.33 (18)	O15—Ti4—O4	102.8 (2)
O6—Ti3—O12	147.5 (2)	O16—Ti4—O4	97.6 (2)
O13—Ti3—Cl2	173.9 (2)	O1—Ti4—O4	77.67 (18)
O15—Ti4—Cl2	172.8 (2)	O15—Ti4—O12	101.9 (3)
O16—Ti4—Cl2	83.66 (19)	O16—Ti4—O12	98.8 (2)
O1—Ti4—Cl2	70.30 (12)	O1—Ti4—O12	74.58 (19)
O4—Ti4—Cl2	75.84 (13)	O4—Ti4—O12	146.09 (19)
O12—Ti4—Cl2	76.72 (14)		

Table S10. Selected bond lengths (Å) and angles (º) of **POT-10**.

Bond	Distance	Bond	Distance
Cu1—O2	1.908 (4)	Ti1—O3	1.787 (4)
Cu1—O15	1.916 (3)	Ti1—O2	1.902 (4)
Cu1—O32	1.973 (4)	Ti1—O4	1.963 (4)
Cu1—O33	1.977 (4)	Ti1—O1	1.972 (4)
Ti2—O7	1.773 (4)	Ti1—O6	2.009 (4)
Ti2—O9	1.791 (4)	Ti1—O5	2.080 (4)
Ti2—O2	1.916 (4)	Ti3—O10	1.807 (4)
Ti2—O8	1.967 (4)	Ti3—O13	1.852 (4)
Ti2—O1	2.084 (4)	Ti3—O9	1.870 (4)
Ti4—O19	1.763 (4)	Ti3—O11	2.008 (4)
Ti4—O13	1.791 (4)	Ti3—O12	2.138 (4)
Ti4—O15	1.924 (4)	Ti3—O14	2.151 (4)
Ti4—O18	1.969 (4)	Ti5—O21	1.791 (4)
Ti4—O16	2.074 (4)	Ti5—O15	1.898 (4)

Ti6—O23	1.797 (4)	Ti5—O16	1.937 (4)
Ti6—O4	1.929 (4)	Ti5—O4	1.981 (4)
Ti6—O5	1.968 (4)	Ti5—O6	2.030 (5)
Ti6—O20	1.972 (4)	Ti5—O20	2.092 (4)
Ti6—O24	2.004 (4)	Ti7—O25	1.762 (4)
Ti6—O22	2.005 (4)	Ti7—O17	1.886 (3)
Ti8—O27	1.762 (4)	Ti7—O26	1.909 (4)
Ti8—O16	1.884 (4)	Ti7—O22	1.952 (4)
Ti8—O24	1.917 (4)	Ti7—O24	1.963 (4)
Ti8—O18	1.933 (4)	Ti9—O29	1.776 (4)
Ti8—O26	1.959 (4)	Ti9—O11	1.954 (4)
Ti10—O30	1.771 (4)	Ti9—O12	1.954 (4)
Ti10—O14	1.935 (4)	Ti9—O18	1.961 (4)
Ti10—O11	1.946 (4)	Ti9—O28	2.015 (4)
Ti10—O8	1.972 (4)	Ti9—O26	2.024 (4)
Ti10—O28	2.019 (5)	Ti11—O1	1.845 (4)
Ti10—O17	2.043 (4)	Ti11—O22	1.923 (4)
Ti11—O8	1.938 (4)	Ti11—O17	1.978 (4)
Ti11—O31	1.775 (4)		

Atoms	Angle	Atoms	Angle
O2—Cu1—O15	97.50 (15)	O2—Cu1—O33	88.36 (16)
O2—Cu1—O32	168.92 (18)	O15—Cu1—O33	172.26 (17)
O15—Cu1—O32	90.06 (15)	O32—Cu1—O33	83.45 (16)

Table S11. Selected bond lengths (Å) and angles (º) of **POT-11**.

Bond	Distance	Bond	Distance
Ti1—O4	1.809 (11)	Ti2—O6	1.623 (14)
Ti1—O2	1.892 (14)	Ti2—O1iii	1.875 (15)
Ti1—O3	1.955 (10)	Ti2—O2iv	1.970 (14)
Ti1—O1	1.957 (15)	Ti2—O2	2.073 (13)
Ti1—O5i	1.993 (13)	Ti2—O1	2.089 (12)
Ti1—O5	2.069 (14)	Ti4—O10	1.766 (8)
Ti3—O9	1.721 (9)	Ti4—O11viii	1.863 (9)
Ti3—O7v	1.938 (6)	Ti4—O7	1.911 (6)
Ti3—O7	1.938 (6)	Ti4—O7ix	1.911 (6)
Ti3—O8	1.941 (3)	Ti4—O8vi	1.977 (9)
Ti3—O8vi	1.941 (3)	Co1—O12	1.908 (6)
Ti5—O12	1.798 (9)	Co1—O11	1.920 (7)

Ti5—O11	2.015 (3)	Co1—O7	1.997 (7)
Ti5—O11viii	2.015 (3)	Co1—I2	2.638 (3)
Ti5—O7x	2.037 (6)	Ti5—O7	2.037 (6)

Atoms	Angle	Atoms	Angle
O4—Ti1—O2	96.7 (6)	O6—Ti2—O1iii	119.2 (7)
O4—Ti1—O3	173.5 (8)	O6—Ti2—O2iv	117.3 (6)
O2—Ti1—O3	88.2 (5)	O1iii—Ti2—O2iv	88.3 (6)
O4—Ti1—O1	96.6 (6)	O6—Ti2—O2	97.4 (7)
O2—Ti1—O1	86.5 (6)	O1iii—Ti2—O2	141.6 (5)
O3—Ti1—O1	87.9 (6)	O2iv—Ti2—O2	84.5 (6)
O4—Ti1—O5i	95.4 (7)	O6—Ti2—O1	100.2 (6)
O2—Ti1—O5i	89.5 (6)	O1iii—Ti2—O1	83.5 (6)
O3—Ti1—O5i	80.4 (6)	O2iv—Ti2—O1	140.6 (5)
O1—Ti1—O5i	167.7 (5)	O2—Ti2—O1	78.7 (6)
O4—Ti1—O5	96.8 (6)	O9—Ti3—O7v	105.4 (3)
O2—Ti1—O5	166.1 (5)	O9—Ti3—O7	105.4 (3)
O3—Ti1—O5	78.5 (6)	O7v—Ti3—O7	93.3 (4)
O1—Ti1—O5	88.7 (6)	O9—Ti3—O8	105.3 (3)
O5i—Ti1—O5	92.5 (9)	O7v—Ti3—O8	80.4 (3)
O10—Ti4—O11viii	107.4 (4)	O7—Ti3—O8	149.3 (3)
O10—Ti4—O7	107.40 (18)	O9—Ti3—O8vi	105.3 (3)
O11viii—Ti4—O7	89.0 (2)	O7v—Ti3—O8vi	149.3 (3)
O10—Ti4—O7ix	107.40 (18)	O7—Ti3—O8vi	80.4 (3)
O11viii—Ti4—O7ix	89.0 (2)	O8—Ti3—O8vi	89.8 (5)
O7—Ti4—O7ix	144.1 (4)	O12—Ti5—O11	103.3 (2)
O10—Ti4—O8vi	109.4 (4)	O12—Ti5—O11viii	103.3 (2)
O11viii—Ti4—O8vi	143.2 (3)	O11—Ti5—O11viii	153.3 (5)
O7—Ti4—O8vi	80.2 (2)	O12—Ti5—O7x	105.92 (19)
O7ix—Ti4—O8vi	80.2 (2)	O11—Ti5—O7x	81.5 (3)
O12—Co1—O11	102.9 (3)	O11viii—Ti5—O7x	91.2 (3)
O12—Co1—O7	103.4 (3)	O12—Ti5—O7	105.92 (19)
O11—Co1—O7	95.3 (3)	O11—Ti5—O7	91.2 (3)
O12—Co1—I2	121.4 (3)	O11viii—Ti5—O7	81.5 (3)
O11—Co1—I2	112.8 (2)	O7x—Ti5—O7	148.2 (4)
O7—Co1—I2	117.2 (2)		

Abstract

Functional materials play a vital role and have important scientific significance for researches to meet the worldwide demand for effient and environmentally-friendly technologies and devices for energy conversion and storage. The well-known material, has been widely used in photocatalysis, sensors, solar cells, lithium-ion batteries and other fields. Polyoxotitanates (**POTs**) containing well-defined ratios of Ti atoms to the dopant metals and/or organic ligands are very interesting since these **POTs** are potential single source precursors to useful materials such as metal-doped TiO_2 with structurally well-defined models for metal-mediated photocatalysis.

In this work, eleven different **POTs** with different formula and structure have been successfully synthesized and structurally determined. Thereafter, a series of novel materials were prepared based on these original **POTs**. Composite materials **C@TiO$_2$** can be used as electrode materials for Li-ion battery and supercapacitor because of their excellent electricity storage capacity. **PEDOT:Ce@TiO$_2$**, **PTEPA-Ti**, **Poly-(EDOT-POT-1)** have strong hydrophobic surface and exhibit promising electrochromic properties. Especially, the 3D nanoporous film **Poly-(EDOT-POT)-1** obtained using $Ti_6O_6(TA)_6(iPrO)_6$) (**POT-1**, TA = thiophen-3-acetate) is a promising electrode material suitable for fast-ion transport and exhibits improved electrochromic properties and 35% higher capacitance (102.5 F/g) compared to **PEDOT** (75.8 F/g) at a current density of 1 A/g. The improved performance of the hybrid organic-inorganic material **Poly-(EDOT-POT)-1** over the parent organic polymer **PEDOT** potentially opens up a new avenue of research in this area, with implications to a range of existing functional organic polymers. **Poly-(EDOT-POT-1)** can be used in electrochromic devices such as electrochromic supercapacitor. Besides, one hybrid polymer with porphyrin and **POT-1** subunit has been obtained. The film **Poly-(H_2T_2P-POT-1),** exhibits good photocurrent generation behavior, and the control of the thickness of the **Poly-(H_2T_2P-POT-1)** film is of great importance to optimize the generation of photocurrent under visible illumination. But the overall conversion efficiency of the sealed cell remains to be studied.

Our work in this thesis will pave the way to fabricate promising electrochromic materials with excellent integrated performance and expand the applications of **POTs.**

Résumé

Les matériaux fonctionnels jouent un rôle vital et ont une importance scientifique importante pour les recherches visant à répondre à la demande mondiale de technologies et de dispositifs efficaces et respectueux de l'environnement pour la conversion et le stockage de l'énergie. Des matériaux bien connus ont été largement utilisé en photocatalyse, dans le domaine des les capteurs et des cellules solaires, et des batteries lithium-ion. Parmis eux, les polyoxotitanates (**POT**) contenant des rapports bien définis d'atomes de Ti et de métaux dopants et/ou de ligands organiques sont très intéressants car ils sont des précurseurs potentiels pour former des matériaux dopés tels que le TiO_2 avec des applications en photocatalyse pour la remédiation des métaux.

Dans ce travail, douze clusters **POT** ont été synthétisés avec succès et déterminés structurellement. Par la suite, une série de nouveaux matériaux ont été préparés sur la base de ces **POT** originaux. Les matériaux composites **C@TiO$_2$** peuvent être utilisés comme matériaux d'électrode pour batterie Li-ion et supercondensateur en raison de leur excellente capacité de stockage d'électricité. **PEDOT:Ce@TiO$_2$**, **PTEPA-Ti**, **Poly-(EDOT-POT-1)** ont une forte surface hydrophobe et présentent des propriétés électrochromes prometteuses. En particulier, le film nanoporeux 3D **Poly-(EDOT-POT)-1**, obtenu à partir de $Ti_6O_6(TA)_6(iPrO)_6$) (**POT-1**, TA = thiophène-3-acétate) est un matériau d'électrode prometteur adapté au transport d'ions rapides et présente des propriétés électrochromes améliorées et une capacité supérieure de 35 % (102,5 F/g) par rapport au **PEDOT** (75,8 F/g) pour une densité de courant de 1 A/g. L'amélioration des performances du matériau hybride organique-inorganique **Poly-(EDOT-POT)-1** par rapport au polymère organique parent **PEDOT** ouvre potentiellement une nouvelle voie de recherche dans ce domaine, avec des implications pour une gamme de polymères organiques fonctionnels existants. **Poly-(EDOT-POT)-1** peut être utilisé dans des dispositifs électrochromes tels que les supercondensateurs électrochromes. Enfin, un copolymère à base de porphyrine et du **POT-1** a été obtrnu. Le film **Poly-(ZnT_2P-POT-1)** présente un bon comportement de génération pour la génération de photocourant. Le contrôle de l'épaisseur des films **Poly-(H_2T_2P-POT-1)** est d'une grande importance pour optimiser la génération de photocourant sous éclairage visible. Mais le rendement global de conversion de la cellule scellée reste à étudier.

Notre travail dans cette thèse ouvrira la voie à la fabrication de matériaux électrochromes prometteurs avec d'excellentes performances intégrées et étendra les applications des **POT**.